

**Dental morphology and mechanical efficiency during
development in a hard object feeding primate
(*Cercocebus atys*)**

Karen Rose Swan

PhD in Medical Sciences

The University of Hull and The University of York

The Hull York Medical School

February 2016

Abstract

Teeth play a prominent role in food acquisition and processing by providing the working surfaces to initiate and propagate fracture. Variation in the shape and size of teeth has therefore naturally been associated with various dietary adaptations. However, few studies have actually tested the functional consequences of tooth form on food breakdown. The work presented in this thesis uses a combination of shape quantification and physical testing to further our understanding of the relationship between dental occlusal morphology and food breakdown in the dietary specialisation hard object feeding. The sooty mangabey, *Cercocebus atys*, is a primate that specialises in hard object feeding throughout its life, and so presents an interesting study group that will be of focus in this thesis. Individual cusps which vary in angle and bluntness performed differently (in terms of force, energy, duration and fragmentation) during food breakdown physical testing. Therefore trade-offs in dental occlusal morphology may have to occur when optimising for more than one performance criteria. This may in part explain the diversity of tooth form observed in hard object feeders. The morphology of *C. atys* molars changes considerably with age due to wear, with high sharp cusps in the juveniles wearing down to produce dentine pools surrounded by an enamel ridge in older individuals. Given the considerable change in dental occlusal morphology due to wear, performance is minimally effected in hard hollow object feeding, this is particularly relevant for the dietary ecology of *C. atys* suggesting functional equivalence in the tooth as it wears. This study reveals a complex relationship between dental occlusal morphology and dietary ecology.

List of contents

ABSTRACT	1
LIST OF FIGURES	6
LIST OF TABLES	15
ACKNOWLEDGEMENTS.....	17
AUTHOR'S DECLARATION.....	18
CHAPTER 1: INTRODUCTION AND LITERATURE REVIEW	19
1.1. Introduction.....	19
1.2. Food processing and mastication.....	20
1.2.1. The masticatory apparatus.....	20
1.2.2. The masticatory cycle	20
1.3. Physical properties of foods	21
1.3.1. Stress and strain	21
1.3.2. Internal properties	23
1.3.3. External properties	28
1.4. Dental form and function	28
1.4.1. Basic tooth structure.....	29
1.4.2. Tooth types.....	30
1.4.3. Dental form	30
1.4.4. Dental replacement and wear	32
1.4.5. Dental function and food fracture	37
1.4.6. Quantification of dental function	39
1.5. Relationship between dental form and diet	39
1.5.1. Occlusal surface area (crown size).....	40
1.5.2. Cusp morphology	40
1.6. Hard object feeding.....	42
1.6.1. Diet and feeding ecology of <i>Cercocebus atys</i>	44
1.7. Aims and objectives	48

CHAPTER 2: CUSP DESIGN AND OPTIMALITY IN HARD OBJECT FEEDERS 49

2.1. Introduction..... 49

2.1.1. Quantifying the mechanical performance of teeth 49

2.1.2. Cusp form and function..... 50

2.1.3. Tooth form and food processing in hard object feeders 51

2.1.4. Mechanical performance indicators 52

2.1.5. Aims and objectives 55

2.2. Materials and methods 57

2.2.1. Cusp design and manufacture 57

2.2.2. Hard object design and manufacture 65

2.2.3. Experimental design and analysis 69

2.3. Results 78

2.3.1. Hollow hard object breakdown: mechanical performance indicators 78

2.3.2. Solid hard object breakdown: mechanical performance indicators 99

2.4. Discussion 111

2.4.1. Does cusp morphology affect the mechanical performance of hollow hard object breakdown? 111

2.4.2. Which cusp morphology is most optimal for hollow hard object breakdown? 115

2.4.3. Does cusp morphology affect the mechanical performance of solid hard object breakdown?.... 116

2.4.4. Which cusp morphology is most optimal for solid hard object breakdown? 118

2.4.5. Summary of findings..... 118

2.4.6. General discussion and application of results for further study 119

2.5. Conclusions..... 122

CHAPTER 3: QUANTIFICATION OF DENTAL WEAR IN A DEVELOPMENTAL SAMPLE OF A HARD OBJECT FEEDING PRIMATE (*CERCOCEBUS ATYS*)..... 123

3.1. Introduction..... 123

3.1.1. Dental wear and masticatory efficiency 124

3.1.2. Quantification of gross occlusal wear 126

3.1.3. Aims and objectives 128

3.2. Materials and method..... 130

3.2.1. Sample..... 130

3.2.2. Percentage dentine exposure 134

3.2.3.	Dental wear rate	135
3.2.4.	Quantification of cusp radius of curvature and angle.....	136
3.2.5.	Concavity/convexity profiling.....	139
3.3.	Results	143
3.3.1.	What is the pattern of wear on the M ₁ over the lifetime of <i>C. atys</i> ?	143
	Does the functional shape of the M ₁ changes as the tooth wears in <i>C.atys</i> ?.....	149
3.3.2.	How does the rate of wear in a M ₁ tooth of <i>C. atys</i> compare to other primate species?	157
3.4.	Discussion	159
3.4.1.	What is the pattern of wear on the M ₁ over the lifetime of <i>C. atys</i> ?	159
3.4.2.	Does the functional shape of the M ₁ change as the tooth wears in <i>C. atys</i> ?.....	161
3.4.3.	How does the rate of wear in a M ₁ tooth of <i>C. atys</i> compare to other primate species?	162
3.5.	Conclusions.....	163

CHAPTER 4: THE EFFECT OF DENTAL WEAR ON THE MECHANICAL PERFORMANCE OF A HARD OBJECT FEEDER (*CERCOCEBUS ATYS*).....164

4.1.	Introduction.....	164
4.1.1.	Feeding and development in <i>C. atys</i>	164
4.1.2.	Ontogenetic changes of the masticatory apparatus in <i>Cercocebus atys</i>	165
4.1.3.	Dental wear, form and function in <i>C. atys</i>	166
4.1.4.	Aims and objectives	167
4.2.	Materials and methods	169
4.2.1.	Design and manufacture of dental models	169
4.2.2.	Design and manufacture of hard food objects.....	178
4.2.3.	Experimental procedure to test mechanical performance of dental models	178
4.2.4.	Data analysis	178
4.3.	Results	179
4.3.1.	Cusp optimality in <i>C. atys</i> : Hollow hard object breakdown.....	180
4.3.2.	Cusp optimality in <i>C. atys</i> : Solid hard object breakdown	184
4.3.3.	Mechanical implications of dental wear in <i>C. atys</i> : Hollow hard object breakdown	187
4.3.4.	Mechanical implications of dental wear in <i>C. atys</i> : Solid hard object breakdown.....	192
4.3.5.	The effect of 1 cusp arrangement on mechanical performance: Hollow hard object breakdown	199
4.3.6.	The effect of 1 cusp arrangement on mechanical performance: Solid hard object breakdown	201
4.3.7.	The effect of 4 cusp arrangement on mechanical performance: Hollow hard object breakdown	203

4.3.8. The effect of 4 cusp arrangement on mechanical performance: Solid hard object breakdown ...	204
4.4. Discussion	206
4.4.1. Is a single unworn cusp of <i>C. atys</i> optimised for hard object feeding?	206
4.4.2. Are there any differences in mechanical performance between different crown morphologies produced through wear when used to break hard food items?.....	208
4.4.3. The effect of cusp placement	213
4.5. Conclusions	214
CHAPTER 5: CONCLUDING REMARKS	215
5.1. Implications and directions for future research.....	216
REFERENCES	217
APPENDIX A: CHAPTER 2	229
APPENDIX B: CHAPTER 3	257
APPENDIX C: CHAPTER 4	266

List of figures

Figure 1.1 Diagram illustrating the different phases of the power stroke during the masticatory cycle. ...	21
Figure 1.2 The three basic types of loading	22
Figure 1.3 Theoretical stress-strain curves	23
Figure 1.4 The toughness and Young's modulus values for a variety of different food types.	27
Figure 1.5 The basic structure of a mammalian tooth	29
Figure 1.6 An example of a mammalian dental arcade.	30
Figure 1.7 An example of a left upper and lower cuspal arrangement seen in mammalian molars	31
Figure 1.8 Image displaying a small example of the diversity in postcanine teeth that can be observed in mammals.....	32
Figure 1.9 Dental wear of the M2 tooth in the Milne-Edwards' sifaka (<i>Propithecus edwardsi</i>).	32
Figure 1.10 Radius of curvature comparison	34
Figure 1.11 An example of a tooth surface used in DNE analyses	36
Figure 1.12 Diagram illustrating how similar DNE scores can be generated from different shapes.....	36
Figure 1.13 Schematic representation of the three basic tooth designs used for fracturing food.	37
Figure 1.14 Schematic diagram of a sharp cusp that has a small area of initial contact.....	38
Figure 1.15 Schematic diagram comparing the build-up of strain energy in a homogenous food item when indented by a cusp with a wide angle and a cusp with an acute angle for a given load.....	38
Figure 1.16 Images displaying some of the diversity of teeth found in a range of hard object feeding mammals.....	43
Figure 1.17 The morphology of a sample of <i>Sacoglottis gabonensis</i> seeds	45
Figure 1.18 Image of an adult female <i>C. atys</i> processing a <i>Sacoglottis gabonensis</i> seed	47
Figure 2.1 Image of a hominin dental row cast compressed onto a hollow acrylic hemisphere.	50
Figure 2.2 Schematic diagram illustrating the relationship between cusp morphology and force.	53
Figure 2.3 Schematic diagram illustrating the relationship between cusp morphology and duration	54
Figure 2.4 2D sketches of the four basic triangular templates used to construct the hypothetical cusps ...	57
Figure 2.5 Diagram displaying the blunting distances used to fit a curve, which altered the level of bluntness in each group of angles	58
Figure 2.6 Diagram displaying the three coordinates used to fit a parabolic curve to the triangle.....	58
Figure 2.7 Surface area of each cusp as measured 1mm from the tip.	59
Figure 2.8 An example of the final design of a cusp model	62
Figure 2.9 Graph displaying peak force to break plaster domes plotted against repeat number for A30 aluminium cusp model.....	63
Figure 2.10 Graph displaying peak force to break plaster domes plotted against repeat number for A60 aluminium cusp model.....	63
Figure 2.11 An example of the deformation of the aluminium tip after 20 compression tests using plaster of Paris hard domes	64
Figure 2.12 Stainless steel cusp models used in study	65
Figure 2.13 Brittle objects used previously to investigate tooth form and mechanical performance.....	66
Figure 2.14 2D sketches and dimensions of hard objects used in this study	67
Figure 2.15 Orientation of the 3D printed layers	67

Figure 2.16 Images taken of the solid 3D printed domes after being soaked in dye solution for 3 different durations (15min, 30min, 60min).	68
Figure 2.17 Photographs of the hollow and solid 3D printed domes.	68
Figure 2.18 Experimental set up for compression tests.	70
Figure 2.19 Design of alignment dome	70
Figure 2.20 Alignment of test objects.	71
Figure 2.21 Pattern of hollow dome breakdown using model C120 as an example.	72
Figure 2.22 Energy measurements for hollow dome breakdown.	72
Figure 2.23 Pattern of solid dome breakdown using model C120 as an example.	73
Figure 2.24 Energy measurement for solid food breakdown.	73
Figure 2.25 Sieve stack and meshes contained within	74
Figure 2.26 Examples of fragments for each size category	75
Figure 2.27 Examples of the fracture patterns observed during hollow hard object breakdown	78
Figure 2.28 Boxplots illustrating the effect of angle and bluntness on the force required to initiate fracture in hollow hard objects.	79
Figure 2.29 The force required to initiate fracture in hollow hard objects in relation to the radius of curvature of the cusp tips	80
Figure 2.30 Boxplots illustrating the effect of angle and bluntness on the energy expended at initial fracture in hollow hard objects.	81
Figure 2.31 Energy expended at initial fracture of hollow hard objects in relation to the radius of curvature of the cusp tips	81
Figure 2.32 Boxplots illustrating the effect of angle and bluntness on time required to initiate fracture in hollow hard objects.	82
Figure 2.33 Time required to initiate fracture in hollow hard objects in relation to the radius of curvature of the cusp tips.	83
Figure 2.34 Boxplots illustrating the effect of angle and bluntness on the surface area of the cusp in contact with the dome at initial fracture of hollow hard objects.	84
Figure 2.35 Surface area of the cusp tip at the initial fracture of hollow hard objects in relation to the radius of curvature of the cusp tips	84
Figure 2.36 Schematic representation of the average level of displacement of each cusp model into the hollow dome at the point of initial fracture (the red area represents the surface area in contact with the dome).	85
Figure 2.37 Bivariate plot of mean force and energy to initiate fracture in a hollow hard object for each cusp design	86
Figure 2.38 Bivariate plot of mean force and time to initiate fracture in a hollow hard object for each cusp design.	87
Figure 2.39 Boxplots illustrating the effect of angle and bluntness on the maximum force required to break the hollow hard objects.	88
Figure 2.40 Maximum force required to break hollow hard objects in relation to the radius of curvature of the cusp tips	89
Figure 2.41 Boxplots illustrating the effect of angle and bluntness on the energy expended at peak force to break the hollow hard objects	90

Figure 2.42 Energy expended at peak force to break hollow hard objects in relation to the radius of curvature of the cusp tips	91
Figure 2.43 Boxplots illustrating the effect of angle and bluntness on the time it takes to reach peak force to break hollow hard objects.	92
Figure 2.44 Time at peak force to break hollow hard objects in relation to the radius of curvature of the cusp tips.	93
Figure 2.45 Boxplots illustrating the effect of angle and bluntness on the surface area of the cusp to break hollow hard objects.....	94
Figure 2.46 Surface area of cusp in contact with the dome at peak force to break hollow hard objects in relation to the radius of curvature of the cusp tips	95
Figure 2.47 Schematic representation of the average level of displacement of each cusp model into the hollow dome at peak force.....	96
Figure 2.48 Bivariate plot of mean force and energy to break a hollow hard object for each cusp design	97
Figure 2.49 Bivariate plot of mean force and time to break a hollow hard object for each cusp design....	98
Figure 2.50 Examples of the two extremes in fragmentation observed during the breakdown of solid hard objects.....	99
Figure 2.51 Boxplots illustrating the effect of angle and bluntness on the maximum force required to break the solid hard objects.	100
Figure 2.52 Maximum force required to break solid hard objects in relation to the radius of curvature of the cusp tips	100
Figure 2.53 Boxplots illustrating the effect of angle and bluntness on the energy expended at peak force to break the solid hard objects.	101
Figure 2.54 Energy expended at maximum force required to break solid hard objects in relation to the radius of curvature of the cusp tips	102
Figure 2.55 Boxplots illustrating the effect of angle and bluntness on the time it takes to reach maximum force to break solid hard objects.	103
Figure 2.56 Time taken to reach the maximum force required to break solid hard objects in relation to the radius of curvature of the cusp tips.....	104
Figure 2.57 Boxplots illustrating the effect of angle and bluntness on the fragmentation of solid hard objects.....	105
Figure 2.58 Fragmentation of solid hard objects in relation to the radius of curvature of the cusp tips...	106
Figure 2.59 Boxplots illustrating the effect of angle and bluntness on the surface area of the cusp to break the solid hard objects.	107
Figure 2.60 Surface area in contact with the dome at peak force to break solid hard objects in relation to the radius of curvature of the cusp tips.	107
Figure 2.61 Schematic representation of the average level of displacement of each cusp model into the solid dome at peak force.	108
Figure 2.62 Bivariate plot of mean force and energy to break a solid hard object for each cusp design..	109
Figure 2.63 Bivariate plot of mean force and time to break a solid hard object for each cusp design	110
Figure 2.64 Bivariate plot of mean force and fragmentation index to break a solid hard object for each cusp design	110
Figure 2.65 Examples of both modes of fracture exhibited during hollow hard object breakdown.....	112

Figure 2.66 Example of one of the hollow domes compressed by B60	112
Figure 2.67 Diagram illustrating the contact between the E120 model and a hollow hemisphere.....	113
Figure 2.68 Bivariate plot showing the displacement at the initial fracture of a hollow hard object against the radius of curvature value of each cusp design.	114
Figure 2.69 Bivariate showing the displacement at peak force to break a hollow hard object against the radius of curvature value of each cusp design.	115
Figure 2.70 Examples of the two different modes of fracture exhibited during solid hard food breakdown	116
Figure 2.71 Bivariate plot showing the displacement at peak force to break a solid hard object against the radius of curvature value of each cusp design.	117
Figure 2.72 Cusp designs that were most optimal to initiate fracture and break hollow and solid hard food items.	119
Figure 2.73 Image of a stainless steel B30 cusp with a deformed tip.....	121
Figure 3.1 An unworn and worn <i>C.atys</i> first molar and examples of adult molar cusp diversity in primates with different diets.....	123
Figure 3.2 Mandibles of <i>C.atys</i> showing examples of the state of dental eruption for each developmental stage used in the study	132
Figure 3.3 Illustration of the measurements used to estimate percentage of dentine exposure	134
Figure 3.4 The cusps of a lower <i>C.atys</i> M1 that were quantified in this study using radius of curvature and angle measurements.....	136
Figure 3.5 Demonstration of the process used to orientate the M ₁ tooth to a flat plane.....	137
Figure 3.6 Image displaying the outline of the cusp base that was used to take major and minor cross sections of the cusp.....	138
Figure 3.7 Image illustrating the analysis of cusp morphology.....	138
Figure 3.8 Basic bowl shape used in pilot study to investigate the effects of orientation and simplification on mean curvature	140
Figure 3.9 The rotation of the model by 45° to examine the effect of orientation on mean curvature.	140
Figure 3.10 An illustration of the simplification process used in Avizo 8.0 (FEI).....	141
Figure 3.11 A comparison of the two shapes used to investigate sensitivity to mesh simplification.	142
Figure 3.12 Images of dental wear in stage 1 individuals.	143
Figure 3.13 Images of dental wear in stage 2 individuals.	144
Figure 3.14 Schematic demonstrating the order of cusp elimination in a <i>C.atys</i> M ₁	144
Figure 3.15 Images of dental wear in stage 3 individuals.	145
Figure 3.16 Images of dental wear in stage 4 individuals.	145
Figure 3.17 Percentage of dentine exposure of the M ₁ for each developmental stage.	146
Figure 3.18 Percentage of dentine exposure of the M ₂ for each developmental stage.	148
Figure 3.19 Diagram of a M1 tooth in lateral view.	149
Figure 3.20 Diagrams displaying the two extremes of radius of curvature values recorded from the cusp cross sections of the sample.....	150
Figure 3.21 Stage 0 mean curvature colour map	152
Figure 3.22 Stage 1 mean curvature colour maps.	152
Figure 3.23 Stage 2 mean curvature colour maps	153

Figure 3.24 Stage 3 mean curvature colour maps	154
Figure 3.25 Stage 4 mean curvature colour maps.	154
Figure 3.26 Examples of the histograms showing the percent frequency of mean curvature values from each developmental stage.	156
Figure 3.27 Major axis regression of the wear on M_2 and M_1	157
Figure 3.28 An interspecific comparison of the major axis lines for dental wear rate	158
Figure 3.29 Casts of the postcanine dental row (lower, left) of four different female yellow baboon (<i>Papio cynocephalus</i>) individuals from the Amboseli basin that represent different age groups.....	160
Figure 4.1 Diagram illustrating the changes in craniofacial form in <i>C. atys</i> during development.	165
Figure 4.2 Developmental changes in the masticatory apparatus in <i>C. atys</i>	166
Figure 4.3 Series of 5 cusps used by Crofts and Summers (2014) to investigate the effects of concavity and convexity to fracture brittle snail shells.	167
Figure 4.4 Design and dimensions of <i>C.atys</i> cusp model.....	170
Figure 4.5 <i>C.atys</i> cusp model where a CAD file was CNC machined in stainless steel	170
Figure 4.6 Intercuspal measurements from an unworn <i>C.atys</i> M_1	171
Figure 4.7 The creation of a hypothetical crown with 4 cusps.	172
Figure 4.8 Simulation of cusp loss due to dental wear.	173
Figure 4.9 Single cusped models used to investigate the effect of cusp position on food breakdown	173
Figure 4.10 Measurements of the enamel ridge taken from an image of specimen C13.22.	174
Figure 4.11 Hollowed out cylinder used to construct the ridged model.	175
Figure 4.12 Construction of the ridge model.....	175
Figure 4.13 Design and dimensions of the ridged model	175
Figure 4.14 Flat version of the ridged model.	176
Figure 4.15 Base used to attach the crowns to the universal testing machine.	176
Figure 4.16 Stainless steel crown models used to investigate the effects of dental wear on mechanical performance in <i>C.atys</i>	176
Figure 4.17 The final designs of the dental models used to investigate the effects of dental wear in <i>C.atys</i>	177
Figure 4.18 Bivariate plot of mean force and time to initiate fracture in a hollow hard object for each cusp design.....	180
Figure 4.19 Bivariate plot of mean force and energy to initiate fracture in a hollow hard object for each cusp design.	181
Figure 4.20 Bivariate plot of mean force and time to break a hollow hard object for each cusp design..	182
Figure 4.21 Bivariate plot of mean force and energy to break a hollow hard object for each cusp design	183
Figure 4.22 Bivariate plot of mean force and time to break a solid hard object for each cusp design	184
Figure 4.23 Bivariate plot of mean force and energy to break a solid hard object for each cusp design..	185
Figure 4.24 Bivariate plot of mean force and fragmentation index to break a solid hard object for each cusp design.	186
Figure 4.25 Comparison of fragmentation behaviour of hollow domes.....	187
Figure 4.26 Boxplot displaying the peak force required to break a hollow hard object for each wear state shown in blue. The force required to initiate fracture for the 1 cusp model is shown in purple.	188

Figure 4.27 Boxplot displaying the energy required at peak force to break a hollow hard object for each wear state shown in blue. The force required to initiate fracture for the 1 cusp model is shown in purple.....	189
Figure 4.28 Boxplot displaying the time required at peak force to break a hollow hard object for each wear state shown in blue. The force required to initiate fracture for the 1 cusp model is shown in purple.....	190
Figure 4.29 Boxplot displaying the contact surface area of each crown at peak force to break (blue) and initiate fracture (purple) in a hollow hard food object.....	191
Figure 4.30 Comparison of fragmentation behaviour of solid domes.....	192
Figure 4.31 Boxplot displaying the maximum force required to break a solid hard object for each wear state.....	193
Figure 4.32 Boxplot displaying the energy required at peak force to break a solid hard object for each wear state.....	194
Figure 4.33 Boxplot displaying the time required at peak force to break a solid hard object for each wear state.....	195
Figure 4.34 Examples of the extremes in fragmentation produced by the ridge model.....	196
Figure 4.35 Boxplot displaying the degree of fragmentation of a solid hard object for each wear state..	197
Figure 4.36 Boxplot displaying the contact surface area of each crown at peak force to break a solid hard food object.....	198
Figure 4.37 Examples of the hollow domes fractured by the 1 cusp model (lateral) and 1 cusp (central).....	199
Figure 4.38 A comparison of the results between the single cusp models for each of the mechanical performance criteria and surface area.....	200
Figure 4.39 Examples of the solid domes fractured by the 1 cusp model (lateral) and 1 cusp (central) model.....	201
Figure 4.40 A comparison of the results between the single cusp models for each of the mechanical performance criteria and surface area to break a solid hard object.....	202
Figure 4.41 A comparison of the results between the 4 cusp models of different cuspal positions to break a hollow hard object for each of the mechanical performance criteria and surface area.....	203
Figure 4.42 A comparison of the results between the 4 cusp models of different cuspal positions to break a solid hard object for each of the mechanical performance criteria and surface area.....	205
Figure 4.43 Diagram predicting two different ways the hollow dome could fracture depending on the crown model used for compression.....	209
Figure 4.44 The orientation of <i>C. atys</i> molar teeth in centric occlusion where the lingual cusps form the first point of contact.....	210
Figure 4.45 The eruption of the permanent mandibular P4 during stage 2 development.....	210
Figure 4.46 Diagram displaying a comparison of the placement of the ridge model on the dome.....	212
Figure 4.47 Chipping fracture that occurred when a single cusp was positioned laterally to the centre of the dome.....	214
Figure A.1 B60 hollow hard object breakdown images.....	230
Figure A.2 Consistency of repeats for B60 based on force at initial fracture and peak force to break a hollow dome.....	230

Figure A.3 B60 solid hard object breakdown images	231
Figure A.4 Consistency of repeats for B60 to break down a solid dome in terms of peak force and fragmentation.....	231
Figure A.5 C60 hollow hard object breakdown images	232
Figure A.6 Consistency of repeats for C60 based on force at initial fracture and peak force to break a hollow dome	232
Figure A.7 C60 solid hard object breakdown images	233
Figure A.8 Consistency of repeats for C60 to break down a solid dome in terms of peak force and fragmentation.....	233
Figure A.9 D60 hollow hard object breakdown images	233
Figure A.10 Consistency of repeats for D60 based on force at initial fracture and peak force to break a hollow dome	234
Figure A.11 D60 solid hard object breakdown images	234
Figure A.12 Consistency of repeats for D60 to break down a solid dome in terms of peak force and fragmentation.....	235
Figure A.13 E60 hollow hard object breakdown images	235
Figure A.14 Consistency of repeats for E60 based on force at initial fracture and peak force to break a hollow dome.	236
Figure A.15 E60 solid hard object breakdown images.....	236
Figure A.16 Consistency of repeats for E60 to break down a solid dome in terms of peak force and fragmentation.....	237
Figure A.17 B90 hollow hard object breakdown images	237
Figure A.18 Consistency of repeats for B90 based on force at initial fracture and peak force to break a hollow dome.	238
Figure A.19 B90 solid hard object breakdown images	238
Figure A.20 Consistency of repeats for B90 to break down a solid dome in terms of peak force and fragmentation.....	239
Figure A.21 C90 hollow hard object breakdown images	239
Figure A.22 Consistency of repeats for C90 based on force at initial fracture and peak force to break a hollow dome	240
Figure A.23 C90 solid hard object breakdown images	240
Figure A.24 Consistency of repeats for C90 to break down a solid dome in terms of peak force and fragmentation.....	241
Figure A.25 D90 hollow hard object breakdown images.....	241
Figure A.26 Consistency of repeats for D90 based on force at initial fracture and peak force to break a hollow dome.	242
Figure A.27 D90 solid hard object breakdown images.	242
Figure A.28 Consistency of repeats for D90 to break down a solid dome in terms of peak force and fragmentation.....	243
Figure A.29 E90 hollow hard object breakdown images.	243
Figure A.30 Consistency of repeats for E90 based on force at initial fracture and peak force to break a hollow dome.	244

Figure A.31 E90 solid hard object breakdown images.....	244
Figure A.32 Consistency of repeats for E90 to break down a solid dome in terms of peak force and fragmentation.....	245
Figure A.33 B120 hollow hard object breakdown images	245
Figure A.34 Consistency of repeats for B120 based on force at initial fracture and peak force to break a hollow dome	246
Figure A.35 B120 solid hard object breakdown images	246
Figure A.36 Consistency of repeats for B120 to breakdown a solid dome in terms of peak force and fragmentation.....	247
Figure A.37 C120 hollow hard object breakdown images	247
Figure A.38 Consistency of repeats for C120 based on force at initial fracture and peak force to break a hollow dome.	248
Figure A.39 C120 solid hard object breakdown images	248
Figure A.40 Consistency of repeats for C120 to break down a solid dome in terms of peak force and fragmentation.....	249
Figure A.41 D120 hollow hard object breakdown images	249
Figure A.42 Consistency of repeats for D120 based on force at initial fracture and peak force to break a hollow dome.	250
Figure A.43 D120 solid hard object breakdown images	250
Figure A.44 Consistency of repeats for D120 to break down a solid dome in terms of peak force and fragmentation.....	251
Figure A.45 E120 hollow hard object breakdown images	251
Figure A.46 Consistency of repeats for E120 based on force at initial fracture and peak force to break a hollow dome.	252
Figure A.47 E120 solid hard object breakdown images.....	252
Figure A.48 Consistency of repeats for E120 to break down a solid dome in terms of peak force and fragmentation.....	253
Figure B.1 Stage 0 mean curvature histogram	262
Figure B.2 Stage 1 mean curvature histograms.....	262
Figure B.3 Stage 2 mean curvature histograms.....	263
Figure B.4 Stage 3 mean curvature histograms.....	264
Figure B.5 Stage 4 mean curvature histograms.....	265
Figure C.1 <i>C.atys</i> cusp hollow hard object breakdown images.....	266
Figure C.2 Consistency of repeats for the <i>C.atys</i> cusp dental model to break down a hollow hard object.	266
Figure C.3 <i>C.atys</i> cusp solid hard object breakdown images	267
Figure C.4 Consistency of repeats for the <i>C.atys</i> cusp model to break down a solid hard object.	267
Figure C.5 4 cusps hollow hard object breakdown images.	268
Figure C.6 Consistency of repeats for the 4 cusp dental model to break down a hollow hard object	268
Figure C.7 4 cusps solid hard object breakdown images	269
Figure C.8 Consistency of repeats for the 4 cusp dental model to break down a solid hard object	269
Figure C.9 3 cusps hollow hard object breakdown images.	270

Figure C.10 Consistency of repeats for the 3 cusp dental model to break down a hollow hard object	270
Figure C.11 3 cusps solid hard object breakdown.....	271
Figure C.12 Consistency of repeats for the 3 cusp dental model to break down a solid hard object	271
Figure C.13 2 cusps hollow hard object breakdown images.	272
Figure C.14 Consistency of repeats for the 2 cusp dental model to break down a hollow hard object	272
Figure C.15 2 cusps solid hard object breakdown images.	273
Figure C.16 Consistency of repeats for the 2 cusp dental model to break down a solid hard object	273
Figure C.17 1 cusp hollow hard object breakdown images.....	274
Figure C.18 Consistency of repeats for the 1 cusp dental model to break down a hollow hard object	275
Figure C.19 1 cusp solid hard object breakdown images	276
Figure C.20 Consistency of repeats for the 1 cusp dental model to break down a solid hard object	276
Figure C.21 0 cusps hollow hard object breakdown images	277
Figure C.22 Consistency of repeats for the 0 cusps dental model to break down a hollow hard object...	277
Figure C.23 0 cusps solid hard object breakdown images.	278
Figure C.24 Consistency of repeats for the 0 cusp dental model to break down a solid hard object	278
Figure C.25 0 ridge hollow hard object breakdown images.....	279
Figure C.26 Consistency of repeats for the 0 ridge dental model to break down a hollow hard object ...	279
Figure C.27 0 ridge solid hard object breakdown images.	280
Figure C.28 Consistency of repeats for the 0 ridge dental model to break down a solid hard object.....	280
Figure C.29 Ridged hollow hard object breakdown images	281
Figure C.30 Consistency of repeats for the ridge dental model to break down a hollow hard object	282
Figure C.31 Ridge solid hard object breakdown images.....	283
Figure C.32 Consistency of repeats for the ridged dental model to break down a solid hard object.....	283
Figure C.33 1 cusp (central) hollow hard object breakdown images	284
Figure C.34 Consistency of repeats for the 1 cusp (central) dental model to break down a hollow hard object	284
Figure C.35 1 cusp (central) solid hard object breakdown images.....	285
Figure C.36 Consistency of repeats for the 1 cusp (central) dental model to break down a solid hard object	285
Figure C.37 4 cusps (intercuspal distance) hollow hard object breakdown images	286
Figure C.38 Consistency of repeats for the 4 cusp (intercuspal) dental model to break down a hollow hard object	286
Figure C.39 4 cusps (intercuspal distance) solid hard object breakdown images	287
Figure C.40 Consistency of repeats for the 4 cusp (intercuspal distance) dental model to break down a solid hard object.....	287

List of tables

Table 1.1 Dietary profile of <i>C.atys</i>	44
Table 1.2 Shore-D hardness and Young’s modulus values for the main hard foods (<i>Sacoglottis gabonensis</i> and <i>Coula edulis</i>) consumed by <i>C.atys</i> in the wild.....	46
Table 1.3 Percentage of feeding actions associated with the hard foods <i>Sacoglottis gabonensis</i> and <i>Coula edulis</i>	47
Table 2.1 Dimensions of cusp designs used in study, which varied in angle, bluntness and radius of curvature at the acting point	60
Table 2.2 Cusp morphospace created by altering the angle and bluntness of a cone	61
Table 2.3 A comparison of the mechanical properties of stainless steel and aluminium	64
Table 2.4 Young’s modulus of the 3D print material.....	69
Table 2.5 Results of peak force (N) recorded to break solid domes using C60 cusp tip to examine inter- and intraobserver reliability.	77
Table 2.6 Examples of radius of curvature values recorded from the postcanine teeth of extant and extinct hard object feeders.	120
Table 3.1 Developmental stages used in study based on the eruption sequence in <i>Cercocebus atys</i>	131
Table 3.2 Table displaying information for each <i>C. atys</i> specimen in the sample	133
Table 3.3 Sample size for each eruption stage for both M1 and M2 teeth that were used to estimate PDE and dental wear rate.	135
Table 3.4 Results of pilot study examining the effects of orientation and simplification of a simple curved dome model on mean curvature values.....	141
Table 3.5 Averages and standard deviations of the percentage of dentine exposure on the M ₁ for each developmental stage.	147
Table 3.6 Averages and standard deviations of the percentage of dentine exposure on the M ₂ for each developmental stage.	148
Table 3.7 Radius of curvature values for the cross sections of the minor and major axis of each cusp ...	150
Table 3.8 Angle values for the cross sections of the minor and major axis of each cusp.....	151
Table 3.9 Equations of the Major Axis from Model II regression for each species	158
Table A.1 Averages and standard deviations of the surface area, displacement, force, energy and duration measurements at the point of initial fracture of the hollow hard objects for each cusp design (N=10)	254
Table A.2 Averages and standard deviations of the surface area, displacement, force, energy and duration measurements at peak force to break hollow hard objects for each cusp design (N=10)	255
Table A.3 Averages and standard deviations of the surface area, displacement, force, energy and duration measurements at peak force to break solid hard objects for each cusp design (N=10).....	256
Table B.1 Resolution of the CT scans used to reconstruct virtual dental models for each <i>C.atys</i> specimen.	257
Table B.2 Stage of eruption for both upper and lower dentition of each <i>C.atys</i> specimen included in chapter 3	258
Table B.3 Data on occlusal wear for each specimen.....	261

Table C.1 Averages and standard deviations of the results for each crown design to break down a hollow hard object.	288
Table C.2 Averages and standard deviations of the results for each crown design to break down a solid hard object.	289

Acknowledgements

Firstly, I would like to thank my supervisors Dr Laura Fitton and Dr Samuel Cobb for their continuous guidance, encouragement and support, without which this project would not have been possible. I would also like to thank the chair of my thesis advisory panel Prof Paul O'Higgins for helpful advice and discussion throughout the course of the project.

I am extremely grateful to the HYMS administrative staff: Roxana Freeman, Gill Pulpher, Elaine Brookes, Heather Milnes, Kit Fan and Victoria Hill for their help when needed and assistance in purchasing the various consumables and equipment.

Throughout the project there have been a number of people who have helped along the way with technical assistance. To name a few: David Moir and the team at Star Prototype, Paul Elliot and the green chemistry department (University of York), Robert Egginton (Mecmesin), Sue Taft (University of Hull) and Mr. Fitton.

I would like to thank my colleagues and dear friends at HYMS for helpful suggestions, interesting discussions and for making my time at York an enjoyable one: Dr Hester Baverstock, Dr Viviana Toro Ibacache, Dr Miguel Prôa, Dr Jason Dunn, Dr Phil Cox, Ricardo Godinho, Andrew McIntosh, Phil Morris, Han Cao, Olivia Smith, Edwin Dickinson, and Aoibheann Nevin. I also thank Dr Michael Berthaume for stimulating conversations on teeth and the world of fracture mechanics, and Dr Julie Lawrence for her advice when needed and friendship.

I would like to give a special mention to my brother, Dr Andrew Swan, not only for kindly letting me stay with him during my write up period but also for his invaluable mathematical advice and late night discussions.

Lastly, I would like to thank my parents and Greg for their unwavering support and love. Words cannot express my love and gratitude.

Author's declaration

I confirm that this work is original and that if any passage(s) or diagram(s) have been copied from academic papers, books, the internet or any other sources these are clearly identified by the use of quotation marks and the reference(s) is fully cited. I certify that, other than where indicated, this is my own work and does not breach the regulations of HYMS, the University of Hull or the University of York regarding plagiarism or academic conduct in examinations. I have read the HYMS Code of Practice on Academic Misconduct, and state that this piece of work is my own and does not contain any unacknowledged work from any other sources.

Chapter 1: Introduction and literature review

1.1. Introduction

The consumption of food is vital for an individual's survival in order to provide the necessary fuel for maintenance, growth and development, reproduction and thermoregulation. While some foodstuffs, such as the fleshy mesocarp of fruits, have evolved to encourage consumption for the purpose of seed dispersal, most foods are designed not to be eaten (Corlett and Lucas, 1990, Kinzey, 1992, Lucas, 2004). Plants and animals contain a variety of different mechanical and chemical defences to minimise their destruction. However, just as plant and animal prey have evolved mechanisms for defence, predators have evolved counter strategies to overcome them.

Mammals present a vast array of anatomical specialisations, which enable them to access food resources. The teeth, in particular, play a prominent role in food acquisition and processing by providing the working surfaces to initiate and propagate fracture. Variation in the shape and size of teeth have therefore naturally been associated with various dietary adaptations (e.g. Kay, 1975, Kay and Hylander, 1978, Hartstone-Rose and Wahl, 2008). However, few studies have actually tested the functional consequences of tooth form on food breakdown.

The work presented in this thesis uses a combination of shape quantification and physical testing to further our understanding on the relationship between tooth form and food breakdown in the dietary specialisation hard object feeding. The sooty mangabey, *Cercocebus atys*, is a primate that specialises in hard object feeding throughout ontogeny, therefore presents an interesting study group that will be of focus in this thesis. The following sections of this chapter will present core topics relating to dental form and function, and the feeding behaviour of *C. atys*.

1.2. Food processing and mastication

There are two main methods of intraoral food processing in mammals: incision (where foods are initially broken down to fit within the mouth) and mastication (the mechanism by which foods are mechanically broken down into smaller pieces) (Ungar, 2010). Collaboratively these form a primary stage of the digestive system. In relation to endothermy in mammals, mastication is particularly beneficial as the comminution of foods increases the amount of exposed surface area for digestive enzymes to act on. As a result, a more efficient chemical digestion can be achieved thus compensating for a high metabolic rate (Karasov et al., 1986, Fritz et al., 2009).

1.2.1. The masticatory apparatus

The intraoral processing of foods is carried out by a series of anatomical structures that are collectively known as the masticatory apparatus. These include the jaw bones, temporomandibular joints, ligaments, masticatory muscles, and dentition. The lower jaw, or mandible, is the mobile element of the skull that articulates to the temporal bone of the cranium via the temporomandibular joints (TMJ) whereas the upper jaw (maxilla), which contains the upper teeth, is immobile. During the feeding process, food is broken between the upper and lower sets of dentition whilst a group of bilateral muscles work in concert to move the mandible and generate bite forces. The muscles that act to open the jaw include the lateral pterygoid and digastric whereas those that close the jaw include the masseter, temporalis and medial pterygoid. At the same time as particle reduction, the solid food is transformed into a soft mass called a bolus that is eventually swallowed and transported to the stomach (Hiimeae, 2000, Lucas, 2004).

1.2.2. The masticatory cycle

Mastication is predominately a unilateral process where the sides of the skull alternate in the roles of working and balancing. This system allows for a more efficient means of bite force generation by concentrating forces to one location at a time under controlled movements of the jaw (Crompton and Hiimeae, 1970, Lieberman, 2011). Throughout this process, food is broken down by an intricate pattern of jaw movements and tooth-food-tooth interaction (Hiimeae, 2000). A common approach to describe and understand the process of mastication is to divide it into three strokes: preparatory, power and recovery. At the beginning of the cycle the jaw is positioned at the point of widest opening (i.e. maximum gape) and moved upwards forming the preparatory stroke. Food is then broken down at the power stroke where forces are transmitted via tooth-food-tooth contact. This stroke can be further divided into two phases that proceed and follow

centric occlusion of the teeth (Figure 1.1). At Phase I, the lower teeth and jaw move upward, anteriorly and medially into centric occlusion and at Phase II the lower teeth and jaw move medially, anteriorly and downward out of centric occlusion. This cycle is then completed by the recovery stroke where the jaw moves downwards (Butler, 1952, Kay and Hiimae, 1974, Ross, 2000).

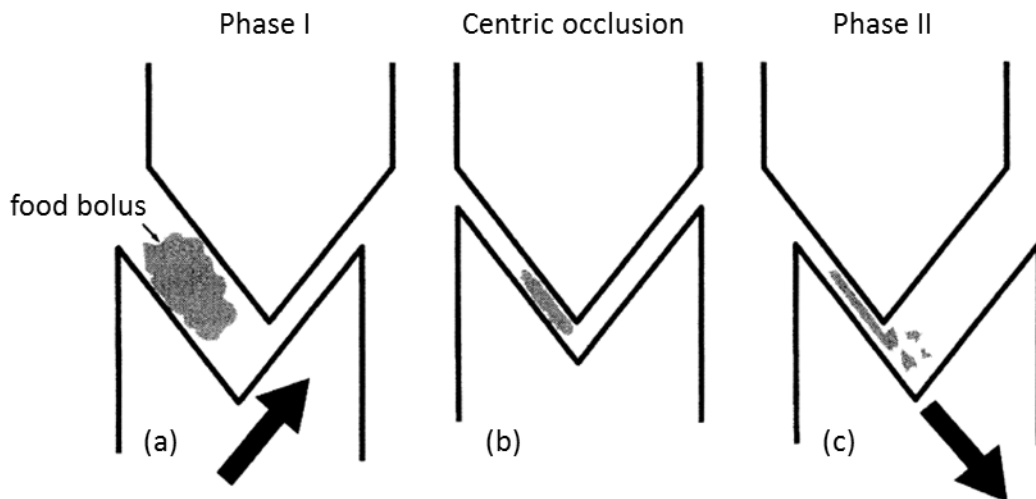


Figure 1.1 Diagram illustrating the different phases of the power stroke during the masticatory cycle where the postcanine teeth move in and out of occlusion. From Ross (2000).

1.3. Physical properties of foods

During food breakdown, teeth interact directly with food by applying the forces that initiate and propagate fracture (i.e. generate new surfaces). How well the food is subsequently broken down is highly influenced by the physical properties of the food item, which can be divided into internal and external properties based on the binary model established by Lucas (2004). The internal properties refer to food's resistance to fracture, whereas the external properties refer to the form and extent of the surface (Lucas, 2004). Both of these properties will be discussed below, however first an introduction to the concepts of stress and strain will be provided, which are central to the understanding of food physical properties, fracture mechanics and food breakdown.

1.3.1. Stress and strain

Stress can be defined as the amount of force applied to a material per unit area and is typically measured in N/m^2 or Pa. The application of stress can be induced in several different ways including tensile stress (perpendicular away from object, Figure 1.2a), compressive stress (perpendicular towards object, Figure 1.2b), and shear stress (horizontal, Figure 1.2c). Strain on the other hand is the deformation of an object and

can be calculated by dividing the amount of change in dimension by the original dimension and has no units (Lucas, 2004, Kerr, 2010).

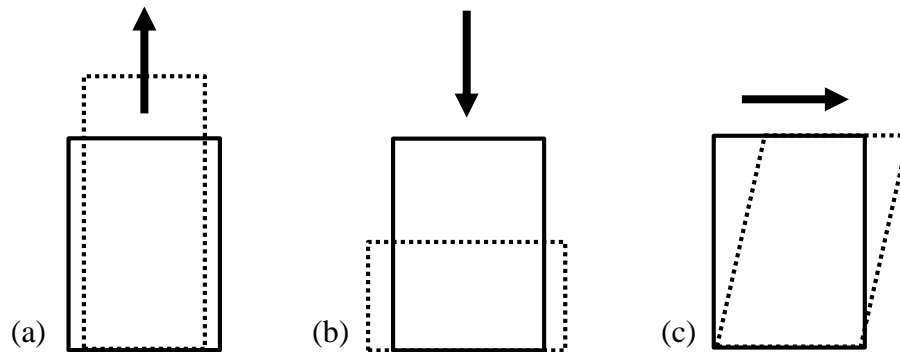


Figure 1.2 The three basic types of loading: (a) tension, (b) compression and (c) shear. Arrows represent the direction of loading. Solid lines represent the original undeformed shape and dotted lines represent the deformed shape. Adapted from Lucas (2004).

As a result of the different loading conditions (e.g. tension, compression, shear), a range of different mechanical properties can subsequently be measured. This is typically achieved using force-displacement and stress-strain curves, which are broken into elastic and plastic regions (Figure 1.3a). The elastic region refers to the first part of the stress-strain curve where deformation is reversible following the withdrawal of an applied force, and the material returns to its original shape. Generally this part of the graph is linear (Hookean) as displayed in Figure 1.3. Once the material has reached its elastic limit, it enters the plastic region where deformation is now permanent. The amount of stress required for this transition is known as the yield stress (or strength, see section 1.3.2.3 p. 25).

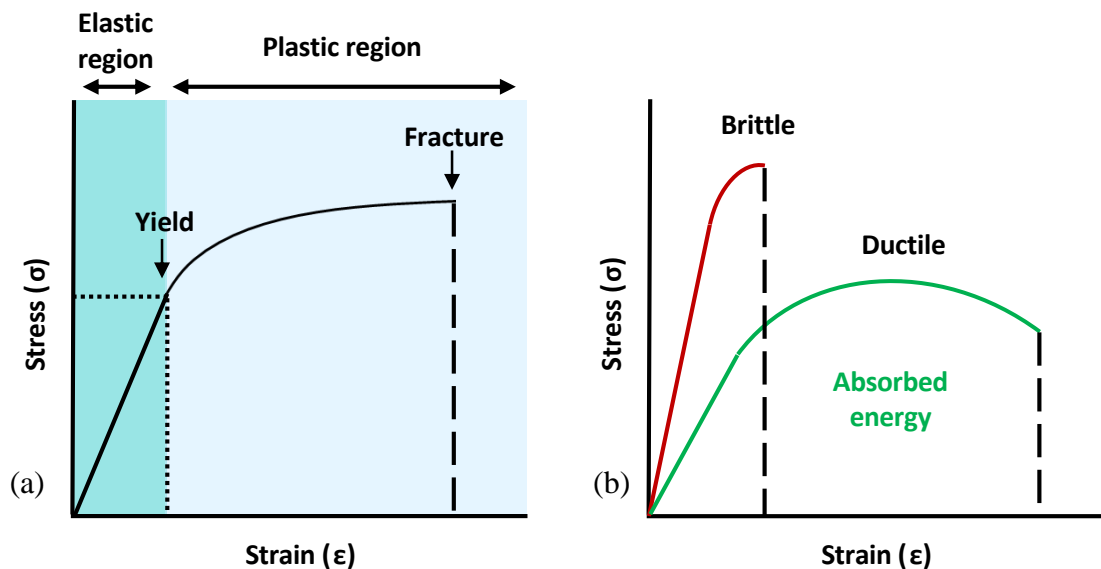


Figure 1.3 Theoretical stress-strain curves: Stress-strain curves can be generated once a material has been loaded, which have an elastic and plastic region (a). These curves vary between brittle and ductile materials where brittle materials fail under high stresses with little plastic deformation and ductile materials fail under high strain with higher amounts of plastic deformation (b).

Within the plastic range, the behaviour of a material can be classed as either brittle or ductile (Figure 1.3b). In the case of brittle materials, fracture occurs soon after the point of yield with very little deformation. Due to the high amount of stress and fast nature, this type of fracture has sometimes been described as “catastrophic” (Strait, 1997). In contrast, ductile materials undergo substantial amounts of plastic deformation often at high strains preceding ultimate fracture (breakage). In terms of energy expenditure, ductile fracture is far more costly for an organism as energy is wasted in deformation. Therefore in order to fracture foods into smaller particles, brittle fracture is considered more beneficial (although a higher amount of generated force may initially be required). However, an exception to this generalization is present in some herbivores that actually benefit from the plastic deformation of foods so as to increase the surface area for enzymes to act on and cause maximum possible damage (Sanson, 2006).

1.3.2. Internal properties

The internal properties, also known as mechanical properties, describe how a material behaves under load (Berthaume, 2016). Over the years, a growing number of researchers have been interested in the internal properties of foods for the study of feeding strategies and adaptations (e.g. Kinzey and Norconk, 1990, Hill and Lucas, 1996, Yamashita, 1996a, 1996b, 1998a, 2009, 2012, Agrawal et al., 1997, Elgart-Berry, 2004, Lambert et al., 2004, Williams et al., 2005, Wright, 2005, Dominy et al., 2008, Taylor et al., 2008, Vogel et al., 2008, 2014, Lucas et al., 2009, Wiczowski, 2009,

Daegling et al., 2011, Norconk and Veres, 2011a, Venkataraman et al., 2014), and plant defences (e.g. Choong et al., 1992, Lucas et al., 2000). The main mechanical properties of interest in relation to food fracture are the Young's modulus, toughness, strength and hardness; many of which can be measured both in the laboratory and in the field (Darvell et al., 1996, Lucas et al., 2001, Lucas, 2004).

1.3.2.1. Young's modulus

Young's modulus (also known as elastic modulus or modulus of elasticity) measures the resistance of a material to deform within its elastic range (i.e. stiffness) (Strait, 1997). In terms of a stress-strain curve, it is the slope of the elastic portion of the graph, therefore can be defined as the ratio of stress to strain (equation 1.1):

$$\text{Young's modulus } (E) = \frac{\text{Stress } (\sigma)}{\text{Strain } (\varepsilon)} \quad (1.1)$$

As strain is dimensionless, E is commonly measured in the same units as stress (N/m^2 or Pa) where a high value is associated with stiff materials (Vincent, 1990). To estimate Young's modulus, a specimen is typically loaded under compression or tension. Alternatively, 3-point or 4-point bending tests may also be utilized (Lucas, 2004, Yamashita et al., 2009).

1.3.2.2. Toughness

Toughness (R), or energy release rate (G) (see Berthaume, 2016), is the resistance of a material to crack propagation and is measured as the amount of energy required to propagate a crack in a given material, typically in J m^{-2} (Atkins and Mai, 1979, Lucas, 2004, Lucas et al., 2008, Lucas et al., 2012). There are a variety of methods used to quantify toughness, most of which depend on a pre-existing crack or notch. Commonly, a notch is induced on the material where a crack will spread during the test (Lucas, 2004). One method, called a 'wedge test', is based on this idea and employs a blade, which is driven into the material thus propagating a crack that divides the object into two pieces in a stable manner. Subsequently, the crack area is estimated as the depth of the wedge penetration after the start of the test. Toughness can then be calculated by dividing the area under the force-deformation curve by the product of wedge displacement (crack depth) and initial width of the object (Vincent et al., 1991, Lucas, 2004, Vogel et al., 2008). Following the same principle, a notch test (similar to 3-point bending) and wire test can also be used (Lucas, 2004, Lucas et al., 2012).

In the case of materials such as leaves and shoots, scissor tests are often utilized to measure toughness (Lucas, 2004). This test is particularly beneficial with thin and flat materials as it allows for crack growth to be directed and controlled as much as possible. In order to fracture and measure toughness, food is placed between open scissor blades that are mounted to a portable universal tester (Darvell et al., 1996, Lucas et al., 2001). Toughness is then estimated as the work done to fracture divided by the area of cut. Friction of the blades must be considered and accounted for during this test (Lucas, 2004). Alternatively, a trouser test may be performed but is only effective with materials that will not deflect cracks (Lucas, 2004). This test involves attaching two ‘trouser legs’ of a plant material to grips that are then pulled apart. Although such a means of fracture has been regarded as less controlled than a scissors test as tearing of the material is largely dictated by composition and heterogeneity of the material (Yamashita et al., 2009). However Berthaume (2016) advises that caution must be upheld when interpreting toughness values due to inconsistencies in measurement and the methodologies used in both engineering and biology. Therefore the toughness of foods may not be directly comparable between different studies.

1.3.2.3. Strength

Strength is the ability of a material to withstand stress without failure or plastic deformation. There are several different aspects of strength, which generally refer to different points on a stress-strain curve. Fracture strength is the amount of stress at crack initiation, yield strength is the amount of stress at point of transition between elastic to plastic, and ultimate strength is the maximum stress experienced prior to fracture, which is indicated as the highest point on a stress-strain curve (Strait, 1997, Lucas, 2004, Berthaume, 2016). Materials that are considered as ‘strong’ are generally able to withstand high amounts of stress whilst weak materials deform under low stress loads (Strait, 1997).

1.3.2.4. Hardness

Despite such accustomed and widespread use, the term ‘hard’ is often difficult to pin down in definition as there does not appear to be a consistent or unanimous understanding of what it actually means. As raised by several researchers (Evans and Sanson, 2005a, Lucas et al., 2009, Berthaume, 2016), there are a large amount of studies that conflict in definition and vary in methodologies used. To add to the confusion, it has also been suggested that hardness is a result of multiple different mechanical properties including stiffness, toughness and strength (Strait, 1993).

The most concise definition can be found in engineering and material sciences where hardness (H) is defined as the resistance of a material to indentation (Lawn and Marshall, 1979, Lucas, 2004, Lucas et al., 2009, Yamashita et al., 2009). Following this definition, hardness is measured using indentation tests such as a ‘Vicker’s indentation’ test (Shahdad et al., 2007, Lucas et al., 2009). This type of mechanical test is reasonably simplistic in methodology and involves the impression of an indenter into the surface of an object under a known load and then withdrawn. A quantification of hardness can then be drawn where the force of indentation (F) is divided by the projected area of indentation (A) (Lucas, 2004):

$$\text{Hardness} = \frac{F}{A} \tag{1.2}$$

Several studies have also attempted to document the hardness of dietary items in conjunction with behavioural observations when studying animals *in situ*. Indentation tests are often impractical in field studies therefore alternative methods are sought that are based on similar principles. For instance, portable agricultural fruit testers and valve spring testers have been used to measure the puncture resistance of fruit pericarp and the crushing resistance of seeds (Kinzey and Norconk, 1990, Yamashita, 1996b, Lambert et al., 2004, Wieczkowski, 2009). However, as noted by Berthaume (2016) hardness cannot accurately be considered as a mechanical property as the value will vary based on what is being used to indent the material.

1.3.2.5. Internal properties of foods and dietary categories

It is apparent that foods can vary in a number of different internal properties. However what does this all mean in terms of diet? Traditionally, animals have been categorised based on the foods they eat the most (e.g. Fleagle, 1988). For example, animals that predominately feed on fruit are labelled as “frugivores”, leaves “folivores”, grasses “graminivores”, insects “insectivores”, saps and gums “gummivores”, and meat “carnivores”. Although these terms offer a simple mode of reference, they can be extremely misleading as they do not indicate the internal properties of the foods (Yamashita, 1996b). For instance, two separate species may both be classed as frugivores regardless of the fact that one consumes soft ripe fruits and the other specialises on hard unripe fruits. When accounting for the properties of toughness and Young’s modulus, Lucas (2004) demonstrates that food types can be highly variable and often overlap between dietary categories (Figure 1.4).

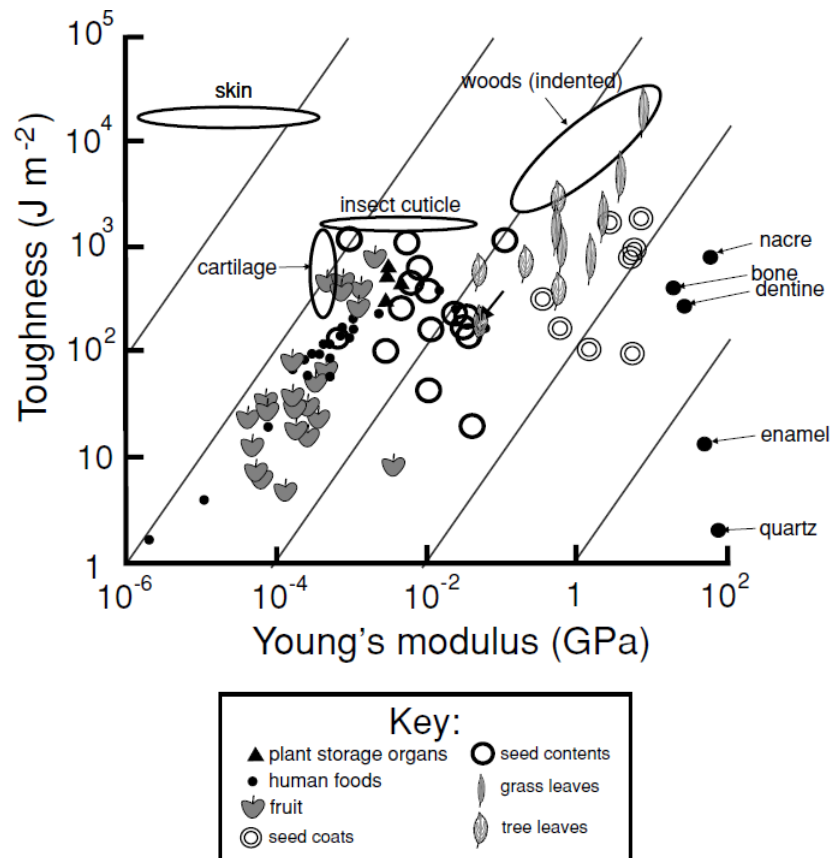


Figure 1.4 The toughness and Young's modulus values for a variety of different food types. Foods vary in mechanical properties within dietary categories and often overlap between different food types. From Lucas (2004).

To complicate matters, different parts of the same food item can exhibit a huge amount of variation in mechanical properties. For example, the seed casing of the *Sacoglottis gabonensis* fruit are extremely hard with a high young's modulus but are also structurally tough as a result of a honeycomb textured interior. Furthermore the seeds encased within are relatively soft, thus a single food item can present a wide range of properties that vary in extent (Daegling et al., 2011). Additionally, in the case of many biomaterials, it is also important to consider that extraneous factors may further influence fracture properties such as age, water content and position in the plant (Ungar, 2010). Therefore the measurement of mechanical properties is often not straight forward. A lot more work needs to be done in this area to improve the accuracy and repeatability of the methods yet much of the groundwork has been set, which has greatly increased our knowledge on food breakdown (see Berthaume (2016) for a detailed review on the topic).

1.3.3. External properties

In addition to internal properties, foods also vary in external properties, which typically refer to the geometry (size and shape) and surface texture (stickiness and abrasiveness) (Lucas, 2004). The geometry of food items refer to the extent of the food surface area and are indicated by the size, shape and volume of food particles. Surface area and volume are directly related with the probability of contact between the surfaces of food and tooth. Generally, the larger the food particle the more likely the particle is to be broken down by the teeth (Lucas and Luke, 1983). The size of the food also appears to play a central role in food placement during the initial stages of ingestion in some animals. For example, Yamashita (2003) found that lemurs (*Lemur catta* and *Propithecus v. verreauxi*) tend to ingest small leaves, flowers and fruit with their anterior teeth, whereas larger food items are ingested posteriorly where higher bite forces can be applied. Shape similarly impacts the rate of food break down but also affects the internal properties of a material by influencing the direction of stresses and strains within a food particle (Ungar, 2010).

The external texture of a food surface generally affects the rate of mastication. One form of texture is stickiness, which is a product of the materials intrinsic surface properties and saliva. This surface property is primarily involved with the process of bolus formation, which has important implications for swallowing and the way food is distributed across the tooth row (Ungar, 2010). For example, foods that are sticky such as fruit or animal tissue tend not to extend along the tooth row. In this case, a greater emphasis is placed on the most central part of the postcanine area where the majority of food particles are broken down. As a result of this, a wide and short dental arcade with small teeth is most suited for the mastication of these types of foods. In contrast, foods that are less sticky such as leaves are less able to form a food bolus therefore do spread along the tooth row and are suited for a long narrow dental row with large teeth (Lucas, 2004). Abrasiveness on the other hand has a long term impact on dental structures throughout an individual's lifetime. Foods with rough textures create wear on the tooth surface which accumulatively causes a decline in the rate of mastication (Lucas, 2004). The impact of this type of food texture on dental morphology and mechanical function will be discussed more fully in chapter 3.

1.4. Dental form and function

Teeth play a prominent role in the fracture and fragmentation of foods by providing the surface of contact where forces are transmitted onto the food item. Given this close

interaction with food, it is unsurprising that dental form is highly associated with diet where teeth must be well equipped for the breakdown of certain foods. Among mammals, there exist a wide range of dental forms, both between species and also within the mouth of a single individual. The first part of this section provides an overview on the basic form of teeth, which is followed by a review on how the variation in dental form is related to function.

1.4.1. Basic tooth structure

A typical mammalian tooth consists of both a crown and one or more roots. The crown is the visible part of the tooth that protrudes above the gum line while the roots are embedded into bony sockets (alveoli) of the upper and lower jaw bones. The structure of the tooth is composed of three layered tissues; enamel, dentine and pulp. Enamel, which forms the outermost layer, is a highly mineralized tissue that provides the working surface of the tooth whereas the dentine below is the main structural tissue. Underlying the dentine and at the core of the crown and root is the pulp chamber, which is a soft tissue containing nerves and blood vessels. The root of the tooth is attached and supported within the jaw by periodontal ligaments, which contain important stretch receptors that provide sensory feedback during dental loading (Figure 1.5) (Hillson, 2005, Ungar, 2010).

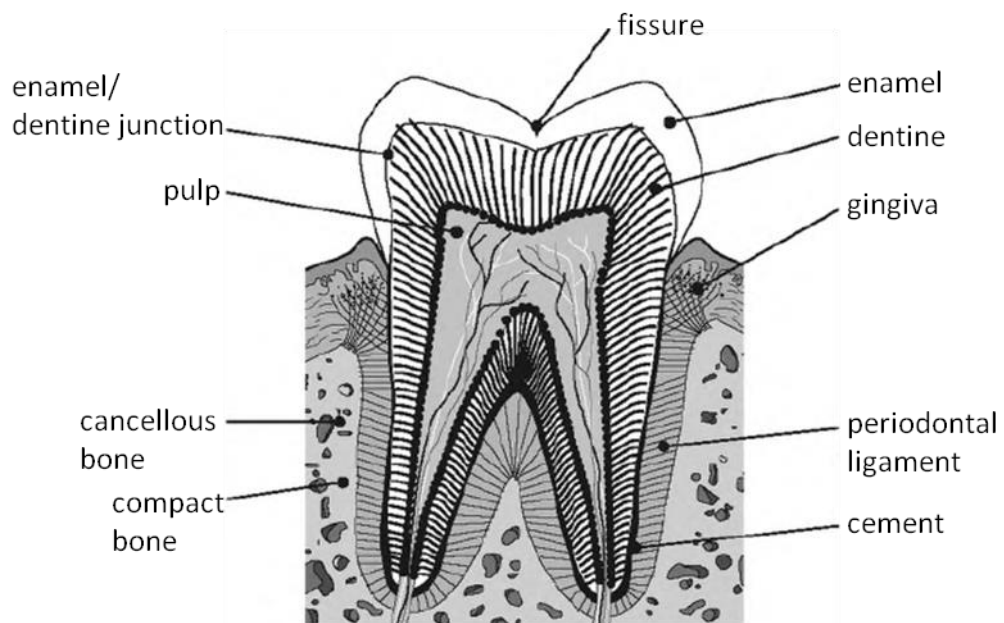


Figure 1.5 The basic structure of a mammalian tooth using a human molar as an example. From Lucas (2004).

1.4.2. Tooth types

The teeth are arranged in a dental row that typically contains four types of teeth, which are morphologically and functionally distinguishable. These include incisors, canines, premolars and molars. These dental types can be broadly divided based on the position in the mouth into anterior (incisors and canines), which are more mesial, and postcanine teeth (premolars and molars), which are more distal (Figure 1.6). The incisors are of the foremost position of the upper and lower jaws that usually exhibit one cusp and one root. The anterior teeth are generally associated with ingestive behaviours, which involve the preparation of food items prior to mastication. For example, the anterior teeth may be used for reducing the size of food to fit in the mouth, gripping foods, separating food from non-foods (e.g. stripping leaves from branches, peeling, scraping) and killing prey. However, they are also known to be used for a variety of non-food related functions across mammals including digging, grooming, social display and fighting (Ungar, 2010). In contrast, premolars and molars constituting the postcanine teeth are much more restricted to the role of fracturing and fragmenting foods, particularly during mastication.

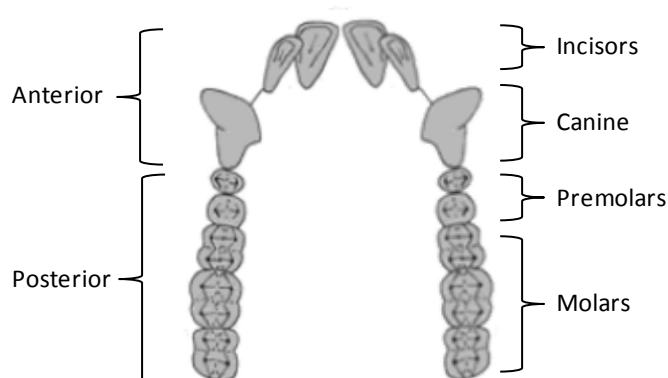


Figure 1.6 An example of a mammalian dental arcade. Image is based on the upper dentition of a macaque (*Macaca fascicularis*). Adapted from Ungar (2010).

1.4.3. Dental form

The division of roles along the dental row is greatly reflected in the shapes of teeth. The anterior teeth in mammals are generally simplistic in morphology where the incisors are short and pointed or flat and spatulate, and the canines are conical, usually protruding higher than the rest of the dentition (Lucas, 2004). In contrast, the postcanine teeth are often much more complex in morphology for roles such as crushing, shearing and grinding foods. On the occlusal (biting) surface of teeth there can exist a number of different features. The pointed elevated features are known as cusps. In terms of tooth function, the morphology of cusps are of particular relevance as it is the cusps that often

form the first point of contact with food, thus have important implications on the mechanics of food breakdown (Lucas et al., 2002). Although the incisors and canines are typically unicuspid, the postcanine teeth often exhibit multiple cusps on a single surface where low rounded cusps are referred to as bunodont (Figure 1.7) (Hillson, 2005).

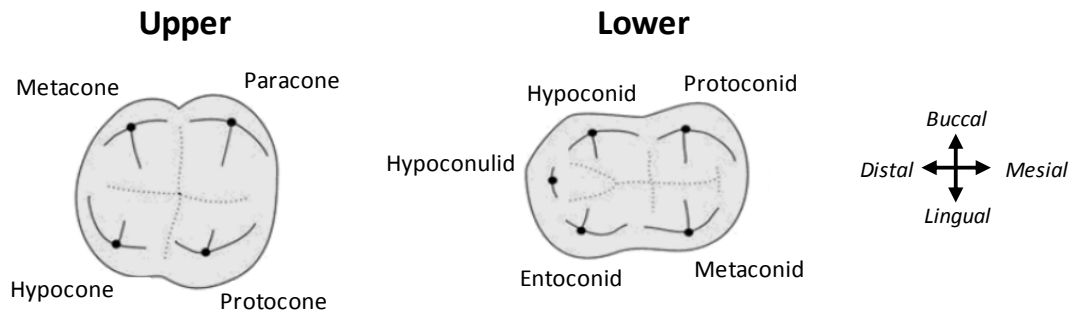


Figure 1.7 An example of a left upper and lower cuspal arrangement seen in mammalian molars. Image is based on a gibbon molar (*Hylobates lar*). Directions of the tooth are indicated where buccal= facing towards the cheek, lingual=facing towards the tongue, mesial=facing towards the median sagittal plane and distal=facing away from the median sagittal plane. Adapted from (Ungar, 2010).

Multiple cusps are frequently joined by crests or ridges, which create sharp cutting edges. In many animals these are expressed as (-lophs), which fuse the cusps together in parallel folds (Hillson, 2005). In between the cusps and crests can exist numerous concave elements such as basins, grooves and fissures. All of these features vary in extent and morphology across mammals and represent a vast array of dietary adaptations. A small snapshot of this diversity is displayed in Figure 1.8.

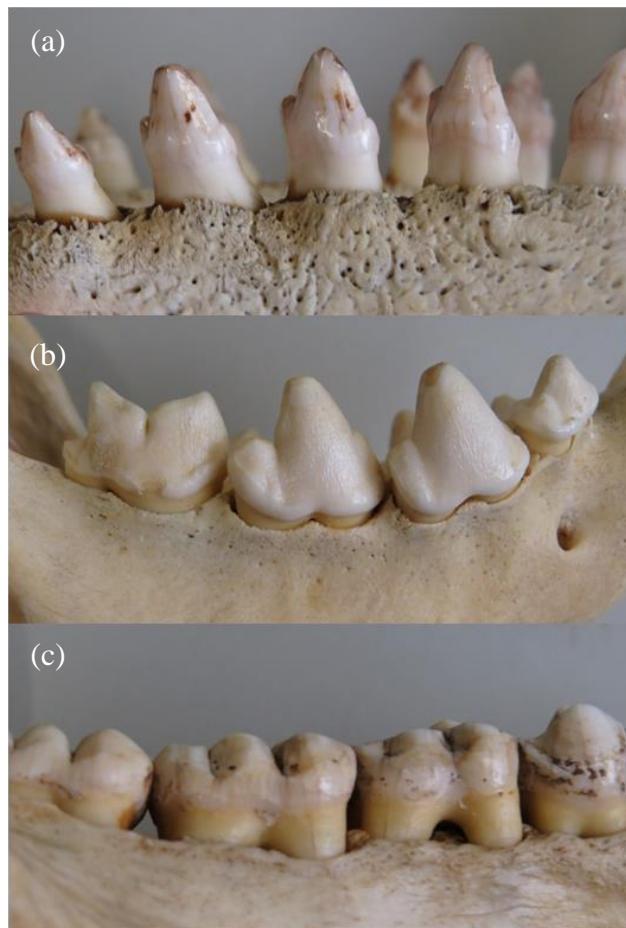


Figure 1.8 Image displaying a small example of the diversity in postcanine teeth that can be observed in mammals; (a) Elephant seal (*Mirounga sp.*), (b) Striped hyena (*Hyaena hyaena*), (c) Western gorilla (*Gorilla gorilla*). Specimens housed at the Leeds Discover Centre, U.K. Photographs: Karen Swan.

1.4.4. Dental replacement and wear

The features of teeth not only vary along the dental row and between different species, but also throughout life. The majority of mammals have two sets of the dentition, where the primary deciduous dentition is replaced by the permanent dentition during development (Hillson, 2005). However, the protective enamel cap is non-regenerative. As a result of the interaction between the opposing teeth, food items and extraneous grit, the enamel can wear away, exposing the underlying dentine (Figure 1.9) (Ungar, 2015). This can have drastic repercussions on the form of teeth, which will be explored in more depth in chapter 3.



Figure 1.9 Dental wear of the M2 tooth in the Milne-Edwards' sifaka (*Propithecus edwardsi*) where dentine exposure is indicated in orange. Adapted from King et al. (2005).

1.4.4.1. Quantification of dental form

The size and shapes of teeth are often used to inform phylogeny, life history and diet (Kay and Hylander, 1978, Fleagle and McGraw, 1999, Fleagle and McGraw, 2002, King et al., 2005). Therefore the quantification of dental form has become a great area of interest. Over the years, a number of different methods have been developed to quantify the shapes of teeth (Evans, 2013). However not all are applicable to all tooth types and wear stages. Furthermore not all are directly useful for inferring functionality. A number of different approaches are outlined and discussed below.

One of the earliest metrics used to differentiate teeth into dietary categories is the shearing quotient (SQ), which was first developed by Kay and colleagues (Kay, 1978, 1984, Kay and Covert, 1984). This method involves summing the length of mesiodistal shearing crests on unworn molar teeth. The SQ is then calculated from the deviation of the total sum of crest lengths from a regression line of summed crest lengths. Generally, this technique has successfully distinguished folivorous and insectivorous primates, that have high SQ values, from frugivorous primates, that have low SQ values (Kay and Covert, 1984, Anthony and Kay, 1993, Meldrum and Kay, 1997, Ungar, 1998). Furthermore within frugivores, hard object specialists have been distinguished from those that consume softer fruits based on SQ values (Anthony and Kay, 1993, Meldrum and Kay, 1997). However, unfortunately this method is largely restricted to unworn teeth due to the lack of homology as the crests are obliterated as a result of wear (Dennis et al., 2004).

Radius of curvature (R) has commonly been used to quantify the sharpness of cusp tips and has been used to investigate dietary adaptations in mammals (Yamashita, 1998a, Evans, 2005, Evans and Sanson, 2005b, Hartstone-Rose and Wahl, 2008, Berthaume, 2014). By definition this metric is the radius of a circle that best fits a two dimensional curve, where a high R value indicates sharper cusps and a low R value indicates blunter cusps. Additionally this is also the inverse of curvature ($1/R$) (Figure 1.10).

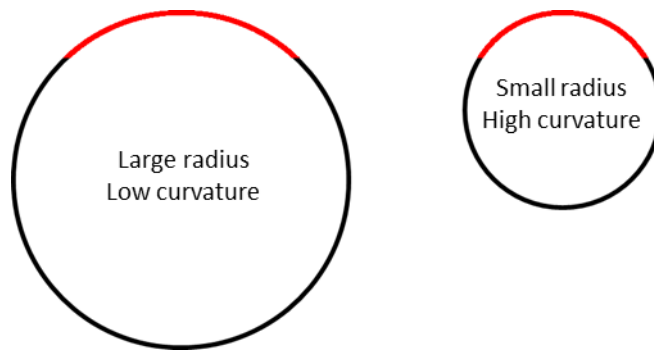


Figure 1.10 Radius of curvature comparison illustrating an arc with a large radius of curvature and an arc with a small radius of curvature. (Arcs in red).

An interesting study by Evans (2005) that examines tooth wear in microchiropterans found that cusp tips classed with the least amount of wear had a significantly higher sharpness than worn specimens indicated by a smaller radius of curvature. However, similar to the shearing quotient, radius of curvature can be highly difficult to measure in worn teeth as the cusps start to flatten and/or undergo cavitation of the tips (Kay and Hiiemae, 1974, Berthaume, 2014).

This so-called ‘worn tooth conundrum’ (Ungar and M’Kirera, 2003) has triggered the onset of a new wave of dental metrics that have collectively been referred to as ‘dental topographic analysis’ (Zuccotti et al., 1998, Ungar and Williamson, 2000, Bunn et al., 2011). These methods, as the name suggests, work off the topography of the tooth surface thus avoid any problems associated with homology as it is independent of landmarks. Some of the first dental topographic techniques were developed using Geographic Information Systems (GIS) software where teeth are examined as topographic landscapes with cusps and basins analogous to mountains and valleys (Ungar and Williamson, 2000). From this a wide range of measures can be extracted including average slope (steepness of the surface), angularity (surface jaggedness), relief index and basin volume (Ungar and Williamson, 2000, Dennis et al., 2004, Venkataraman et al., 2014).

One of the most well used dental topographic techniques is the relief index (RFI) first pioneered by Ungar and Williamson (2000) that measures occlusal relief. RFI is essentially the ratio of 3D surface area to 2D surface area of the occlusal table, where greater occlusal relief is indicated by a higher relief index. Previous research suggests that RFI can be used to differentiate broad dietary categories in primates despite differences in dental wear (M’Kirera and Ungar, 2003, Boyer, 2008, Bunn et al., 2011, Godfrey et al., 2012). Furthermore several studies have also used this technique to

investigate patterns of wear between and within species (Dennis et al., 2004, Ulhaas et al., 2004, King et al., 2005). For example Dennis et al. (2004) found the occlusal relief of mantled howling monkey molars to consistently decrease over time. Although RFI does capture one aspect of the tooth that changes with wear, it does not provide any information on specific shapes changes that can be directly related to the mechanical breakdown of foods. For instance, hypothetically the occlusal relief may change throughout the wear process yet some shape aspects (e.g. crest sharpness) may stay roughly the same.

An additional dental topographic technique is orientation patch count (OPC), which measures dental complexity by calculating the number of patches or “tools” on the tooth surface. Using this method, Evans et al. (2007) found that they were able to detect a dietary signal despite differences in phylogeny between rodents and carnivorans, where herbivorous species exhibited a higher degree of complexity. However, similar to RFI, this method does not provide an idea of the shape of the individual features on the surface; rather it is used for providing an estimate of the number of features.

Recently, Bunn et al. (2011) introduced the use of Dirichlet normal energy (DNE) as a new dental topographic technique. Subsequently this method has been popularised and used in multiple dental morphology studies with the added advantages that it is independent of position, orientation, scale and landmarks (Bunn et al., 2011, Godfrey et al., 2012, Ledogar et al., 2013, Winchester et al., 2014). This method is typically applied to computer-generated polygon meshes (Figure 1.11a) and essentially quantifies the ‘curviness’ of a shape by measuring the deviation of a surface from planar, or in other words, how much a surface bends. In order to investigate curvature, the normal map of the surface mesh is examined where a normal direction is assigned to each point (Figure 1.11b). DNE aims to quantify how much the angle of the normal changes as you move a small distance away from each point. Based on individual calculations from the normals, the surface energy can be estimated for each triangle, which is then used to provide a sum of energy for the whole surface.

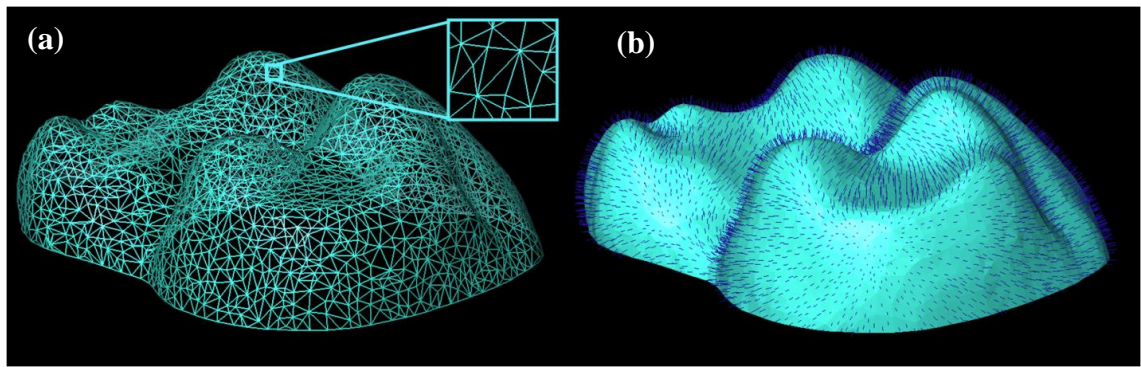


Figure 1.11 An example of a tooth surface used in DNE analyses; (a) shows the polygon mesh comprised of triangular faces and (b) shows the normals on the tooth surface that lie perpendicular to the tangent plane.

In terms of its application in anthropology, DNE has been reported to successfully infer diet between different primate species (e.g. Bunn et al., 2011). However it is worth considering that as DNE is based on the sum values across the entire topographic surface it could lead to misleading interpretations as different shapes could potentially produce a similar overall DNE score. For example, a shape with a single steep peak (Figure 1.12a) could potentially produce a similar DNE score to a shape with two lower peaks (Figure 1.12b). However, the surface energy can be viewed as a colour map on the tooth surface, where differences in curvature can be observed.

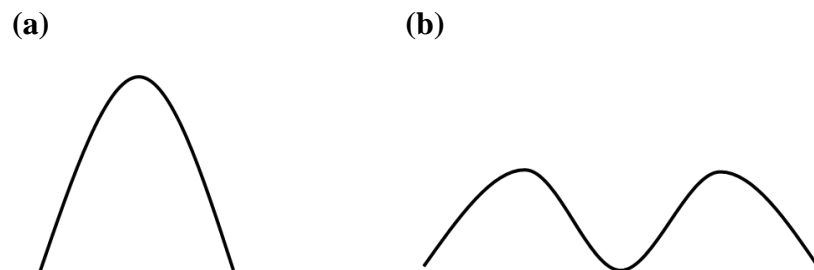


Figure 1.12 Diagram illustrating how similar DNE scores can be generated from different shapes where a single steep peak (a) and two lower peaks (b) could potentially produce the same DNE score as DNE is calculated as a sum from the entire tooth surface.

An additional topographic method involves measuring the degree of concavity and convexity on the surface, which has been used previously to quantify the shape of the enamel-dentine junction (Guy et al., 2013). As dental wear involves the loss of enamel tissue forming concavities where dentine is revealed, this method shows promising application for comparisons of dental form between species and during dental wear and is discussed further in chapter 3.

1.4.5. Dental function and food fracture

From the methods mentioned above, it is clear that there are many different aspects of tooth shape that potentially vary with diet and wear. However, the quantification of shape does not provide an indication of *how* teeth work and *why* teeth are shaped the way they are. There are two main functions of teeth; for guiding chewing, where the shapes of teeth form an interlocking system that limit masticatory movements during chewing, and for the fracture and fragmentation of foods (Ungar, 2015). These correspond to Evans and Sanson's (2006) "geometry of occlusion" and "geometry of function" respectively. Whilst acknowledging that the shapes of teeth are influenced by masticatory movements as the teeth move in and out of occlusion, the main focus of this thesis is on how the shapes of teeth affect food breakdown.

A common approach in dental functional morphology is to view teeth as tools (Lucas, 1979, Lucas and Luke, 1984, Evans, 2005). Intuitively, comparisons have been drawn between bunodont molars and mortar-and-pestles where cusps fit into opposing basins for grinding foods (Figure 1.13a) (Lucas, 1979, Kay and Hiiemae, 1974). Similarly the carnassials of carnivore teeth have been likened to scissors where blades move against each other to slice foods apart (Figure 1.13c) (Osborn and Lumsden, 1978). By simplifying teeth down to basic shapes allows for predictions to be made on food fracture based on engineering principles.

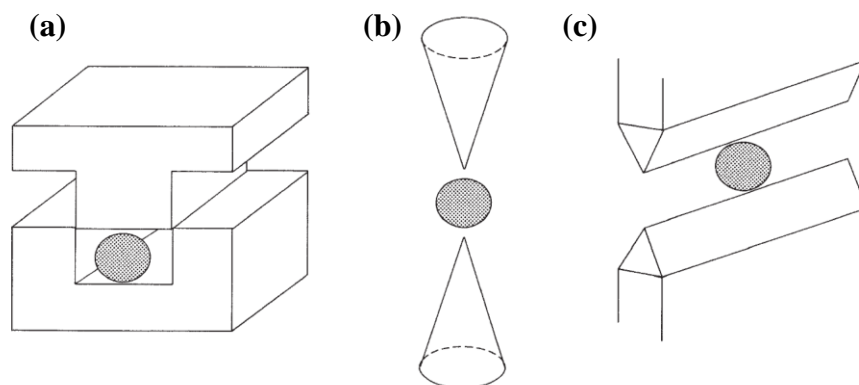


Figure 1.13 Schematic representation of the three basic tooth designs used for fracturing food: (a) mortar-and-pestle, (b) points, (c) blades. From Strait (1997).

1.4.5.1. Crack initiation and propagation

Food items can be mechanically protected in two different ways; to resist crack initiation and to resist crack growth (propagation). The goal of teeth, therefore, is to overcome these defences. How well a tooth is able to achieve this is greatly dependent on its geometry and the physical properties of the food in question (see section 1.3).

The ability to initiate fracture is largely determined by the degree of stiffness and strength of the food item where high values of both these properties require a large amount of stress to generate fracture (Lucas, 1979, Strait, 1997, Lucas, 2004). The most effective way to build up stress concentrations in a material is to use an indenter with the smallest possible area of contact thereby increasing the stress or force per unit area (pressure) for a given load (Figure 1.14). In the case of teeth, a sharp cusp would therefore be most efficient for this purpose.



Figure 1.14 Schematic diagram of a sharp cusp that has a small area of initial contact, therefore maximises the amount of pressure when in contact with a food item. From Strait (1997).

An alternative method to concentrate stress is to use a cusp or blade with a wide subtended angle, i.e. a wedge. By increasing the angle of contact, provides a more efficient means of building up strain energy in the food item as the food item is wedged apart, thus requiring a smaller level of displacement to promote fracture (Figure 1.15) (Vincent, 1990, Lucas and Teaford, 1994, Strait, 1997).

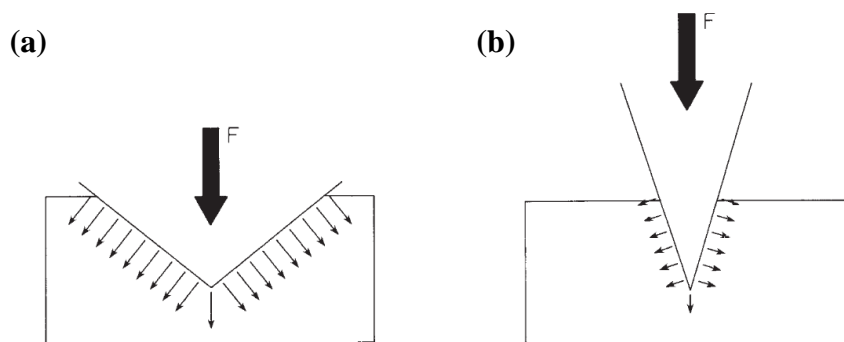


Figure 1.15 Schematic diagram comparing the build-up of strain energy in a homogenous food item when indented by a cusp with a wide angle (a) and a cusp with an acute angle (b) for a given load (F). Relative lengths of the smaller arrows indicate the strain energy magnitudes. From Strait (1997).

How cracks subsequently spread within an object is largely determined by a materials relative toughness, which is the resistance to crack propagation (Lucas, 2004, Sanson,

2006). In terms of brittle materials, once a force is applied to the object, energy is absorbed up until the point of crack initiation. Once a critical (Griffith) crack length has been produced, the crack is then self-propagating as the absorbed energy is released; in other words, the material shatters. However, stress does not build up as readily in ductile materials, instead the material plastically deforms. In this case, fracture must be continuously driven as cracks are not self-propagating (Strait, 1997). The internal structure of some materials are designed to resist crack propagation at a molecular level by hindering or preventing cracks from growing (Atkins and Mai, 1985, Sanson, 2006). For example, in plants the resistance to crack propagation can be enhanced by structures that interrupt the growth of cracks thus increasing overall toughness (Sanson, 2006). This can be achieved by venation patterns that create a heterogeneous structure. In terms of tooth design, a blade would be most suitable to cause the material to subdivide rather than a point (cusp) that is likely to only puncture the food item.

1.4.6. Quantification of dental function

There are several different methods used to investigate dental function in relation to food breakdown. Basic schematics and mathematical models (as presented above from Strait 1997) can help with our basic comprehension of the process. By combining observations made on tooth morphologies with functional principles from engineering, Evans and Sanson (2003, 2006) were able to construct ‘ideal’ cutting teeth, which were found to be comparable to real mammalian tooth forms. To extend on this research, several studies have attempted to simulate the interaction between teeth and food. For example, Berthaume et al. (2010, 2013) uses finite element analysis to map the stress and strain distributions of a computer modelled food object when in contact with teeth. Alternatively, several studies have used physical testing where dental replicas are created and loaded under compression onto a food object (Evans and Sanson, 1998, Berthaume et al., 2010, Crofts and Summers, 2014). The latter approach is adopted throughout this thesis and is reviewed further in chapter 2.

1.5. Relationship between dental form and diet

The shapes of teeth clearly hold important implications on the mechanics of food breakdown. This has led to many researchers to study certain aspects of teeth that can be directly related to function such as the occlusal surface area of the crown (Demes and Creel, 1988) and the morphology of cusps (Yamashita, 1998a, Hartstone-Rose and Wahl, 2008, Berthaume, 2014), which will be discussed below.

1.5.1. Occlusal surface area (crown size)

As crown size is highly variable among mammals, many researchers have attempted to relate occlusal surface area to variations in biting force and the mechanical properties of food (Kay, 1975, 1978, Lucas et al., 1986a, Demes and Creel, 1988). Correlates between stress resistant diets and increased crown sizes have been found (Demes and Creel, 1988, Spencer, 2003, Lucas, 2004), suggesting increased surface area may relate to the tooth's ability to resist high magnitude and/or high frequency loading forces. Furthermore, tooth crown size has also previously been suggested to be related to energy requirements where the total intake of food an animal needs dictates the required size of the tooth (Pilbeam and Gould, 1974, Gould, 1975). However, to date, no critical relationship between postcanine tooth size and body size have been found (Lucas, 2004).

1.5.2. Cusp morphology

Cusps play an integral role in food breakdown; therefore it is not surprising that cusp form is often associated with various dietary adaptations (Bunn and Ungar, 2009). Previous research has shown that by altering the morphology of a single cusp and changing the surface area of contact can have a significant impact on mechanical performance (Evans and Sanson, 1998). A population notion in the study of teeth in primates holds that insectivores and folivores have high cusps and sharp crests for the puncture of exoskeletons and shearing tough vegetation, in contrast, frugivores and hard object feeders tend to have blunter, flatter cusps associated with crushing and grinding motions (Rosenberger and Kinzey, 1976, Seligsohn and Szalay, 1978, Bunn et al., 2011).

Previously research into cusp morphology and function has focussed on the sharpness of cusp tips which is measured using the radius of curvature (R) (see section 1.4.4.1). Several studies have attempted to relate this dental metric to diet but have produced seemingly mixed results. One study by Hartstone-Rose and Wahl (2008) suggests that cusp radius of curvature is associated with diet, especially in extreme dietary specializations such as durophagy. In this study R values were measured in minimally worn cusps of the postcanine teeth in carnivorans, which were divided into groups based on carcass processing behaviours (meat, meat/non-vertebrate, non-vertebrate, and durophage). The results indicated that R values were consistently larger in the teeth of durophagous specialists and that this group was successfully distinguished from other groups which were much more similar in R values. Yamashita (1998a) partially

supports this finding. When relating cusp radius of curvature to the mechanical properties of foods in lemur diets, a discrepancy was found between the upper and lower second molars. In the upper second molars, a positive correlation was found between increasing radius of curvature (increased bluntness) of the cusp tips and dietary hardness and a negative correlation between cusp bluntness and shear strength. However the opposite pattern was found for the lower second molars. The exact reason for why this might be is unclear but the author postulates several factors that may influence cusp tip sharpness such as the type of fit within the opposing basin and crest length. Further to this another complication in interpreting the results is that certain dental forms may be equally functional for different food types. For instance Lucas and Teaford (1994) suggest that the bilophodont molars of colobines form a tool kit of cusps and crests that collaboratively function for both the consumption of soft brittle leaves and tough seeds. Furthermore the lemur species *P.d. edwardsi* and *L. rubriventer* have been documented to exhibit two very different dental morphologies yet both consume a hard diet (Yamashita, 1998b). Therefore, several different forms may be suitable for the same type of mechanical breakdown.

A later study by Berthaume (2014) presents an additional perspective on this debate when examining cusp radius of curvature as a dietary correlate in extant great apes. Given that other metrics of sharpness, such as crest sharpness and length, have previously been associated with folivorous primates it was hypothesised that folivores will have sharper cusps tips (higher R values) than frugivores. Interestingly, the results indicate that frugivores and folivores can be successfully distinguished based on cusp radius of curvature whilst accounting for phylogenetic similarities. However, contrary to initial expectations, folivores were shown to exhibit consistently duller cusps (lower R values) than frugivores. Based on this finding it is argued that radius of curvature does not directly relate to a functional advantage in food item breakdown. Rather, duller cusps, when worn expose comparatively more surface area for cutting through tough vegetation than their sharper counterparts. This study yields several important findings. Firstly, it demonstrates that the radius of curvature is significantly different between folivorous and frugivorous apes, and secondly it raises an interesting concept that the shapes of cusps may indirectly impose a functional advantage through wear. However this conclusion may not be clear-cut. The sharpness of the crests or acuteness of the angles on the surface may be more relevant for a specialisation in folivory rather than the sharpness of the cusp tip. As the jaw moves laterally, sharp crests may be more

effective at the breakdown of leaves rather than sharp points that when indented would only puncture such a tough material. It may also be the case that a blunter cusp is actually more optimal for a folivorous diet but it has yet to be experimentally tested.

In terms of mechanical performance, the occlusal morphology of several extinct hominin species has been physically tested to break down hard brittle food items (Berthaume et al., 2010). In this study physical replicas of the postcanine dental rows were used to fracture an artificial hard food object. Based on the displacement at fracture, the radius of curvature was measured on the cusp of each tooth that first contacted the food item. The results were found to be inconsistent with any functional hypotheses regarding cusp sharpness as significant differences in fracture force were found between species with similar R values. They therefore concluded that the blunt teeth in species considered as hard object feeders were likely to be selected to prevent the crown from failing. However it is worth noting that this study does not account for the fact that multiple cusps were in contact with the food object at the same time. It could, for instance, be the pattern or combination of cusps that is having an effect, something which is later explored further in an additional paper (Berthaume et al., 2013). Furthermore, the teeth from different species were at different wear states, which could potentially affect any interpretations when relating to adaptations to a certain diet as mechanical performance could vary throughout ontogeny.

1.6. Hard object feeding

Of a central focus to this thesis is hard object feeding or durophagy, which is a dietary specialisation that involves the breakdown of hard, mechanically resistant food items. The term 'hard' has been used to describe a broad scope of foods including; the shells of crustaceans and molluscs (Herrel and Holanova, 2008, Constantino et al., 2011), fruit pericarp (Kinzey and Norconk, 1990), bamboo (Figueirido et al., 2013), bone (Figueirido et al., 2013), certain insects (Freeman, 1979, Santana et al., 2012) and the endocarp and kernel of various nuts and seeds (Iwano, 1991, Daegling et al., 2011). These foods are typically stress-limited; a type of mechanical defence used by some plants and animals to avoid being consumed. In terms of mechanical properties, this is usually achieved by a high yield stress, or a high value of the square root of toughness multiplied by Young's modulus (ER)^{0.5}, which help prevent cracks from forming within the structure (Lucas, 2004). In order to overcome such mechanical defences a high level of stress is required to initiate fracture and induce failure, both of which is likely to warrant special adaptations of the masticatory complex.

Interestingly, within durophagous mammals there exists a vast array of dental morphologies (Figure 1.16). This includes the high blade-like premolar teeth of hyenas used to crack open bones (Figure 1.16d) (Van Valkenburgh, 1996, 2007), and the low bulbous postcanine teeth of sea otters used to crush molluscs (Figure 1.16c) (Constantino et al., 2011). Variation in shape is also observed based on the types of teeth used during hard object feeding. For example some hard object feeders use opposing postcanine dental rows with complex surfaces to crush the food objects (Figure 1.16a,c) whereas others use the anterior unicuspid teeth to puncture the food item (Figure 1.16b) (Norconk and Veres, 2011b). The fact that such shape variation exists among hard object feeders implies that several different tooth forms are functional for feeding on obdurate food items. However why there exists such a diversity of tooth forms in durophagous species and whether some shapes are more optimal than others is a complex topic that has remained relatively unexplored.



Figure 1.16 Images displaying some of the diversity of teeth found in a range of hard object feeding mammals; (a) giant panda (*Ailuropoda melanoleuca*), (b) monk saki (*Pithecia monachus*), (c) sea otter (*Enhydra lutris*), (d) spotted hyena (*Crocota crocuta*). Images from Myers et al. (2016).

1.6.1. Diet and feeding ecology of *Cercocebus atys*

The sooty mangabey, situated on the Western coast of Africa, is a terrestrial forager that is well known for habitually feeding on hard food items (Daegling et al., 2011). The main study site for this species is the Taï National Park in the Côte d'Ivoire, which consists mostly of dense evergreen forest (McGraw, 1998, Range and Noë, 2002, McGraw and Zuberbühler, 2007). In recent years McGraw and co-workers have greatly developed our understanding in the feeding ecology of *Cercocebus atys* by providing detailed descriptions of diet, food processing and tooth use in the wild (McGraw et al., 2007, McGraw et al., 2011, Daegling et al., 2011, McGraw et al., 2014). These studies show that the dietary range of *C.atys* is relatively narrow being largely composed of nuts/seeds, fruits and invertebrates (Table 1.1).

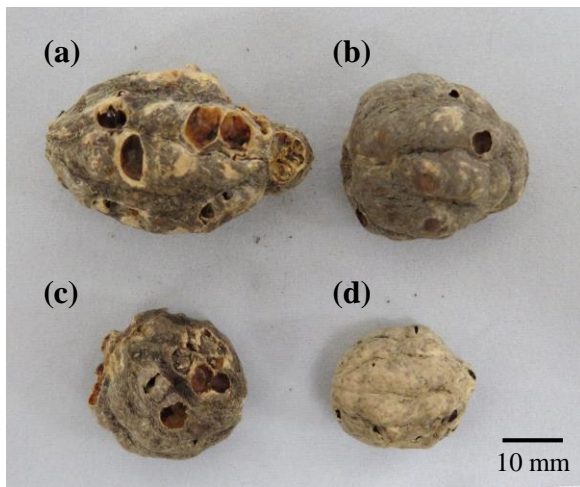
Table 1.1 Dietary profile of *C.atys* from the Taï forest, Côte d'Ivoire, West Africa. Data was collected over a period of 14 months providing a total of 9689 feeding actions. From McGraw et al. (2011).

Food item	Food type	% of total feeding actions (N=9689)
<i>Sacoglottis gabonensis</i>	seed	51.9
Invertebrates	animal	13.01
<i>Dialium aubrevillei</i>	fruit/seed	7.40
<i>Anthonata fragrans</i>	seed	3.50
Fungi	fungi	3.40
<i>Scytopetalum tieghemii</i>	fruit	1.60
<i>Spondianthus preussi</i>	fruit	1.60
<i>Erythrophleum mannii</i>	fruit	1.60
<i>Parinari excelsa</i>	fruit	1.40
<i>Diospyros sanzaminika</i>	fruit	1.30
<i>Xylopiastrum taiense</i>	fruit	1.20
Other (<1% for each food)	fruit, leaf, seed, root	5.69
Unknown	Unknown	6.40

The hardest component of the *C.atys* diet is the endocarp of *Sacoglottis gabonensis* that must be broken in order to access the seeds within (McGraw et al., 2011). All sympatric cercopithecine species have been known to consume the flesh of the *S.gabonensis* fruit (McGraw et al., 2007, McGraw et al., 2011), however few are able to penetrate its highly stress resistant endocarp, thus presenting an excellent dietary niche to be

exploited. In addition to being very hard, the casings are also large measuring on average 24mm and 32mm along the major and minor axis respectively (N=9) (Daegling et al., 2011). Figure 1.17 (a-d) shows the variation in the shape and size of the seed casings in a small sample of *S. gabonensis*, which have been collected by researchers working in the Tai forest (van Casteren, A. 2015: pers. comm.). The internal architecture within the endocarp consists of 1-3 oblong seeds measuring c.15mm x 3mm, which are surrounded by resinous cavities (Figure 1.17c,d) (Dounias, 2008).

External morphology:



	Length (mm)	Width (mm)
(a)	43.5	23.5
(b)	30.7	23.8
(c)	25.2	21.3
(d)	23.1	18.0

Internal morphology:

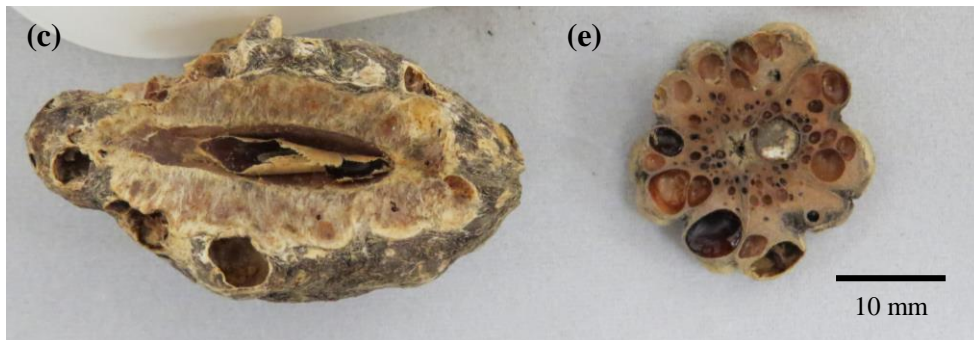


Figure 1.17 The morphology of a sample of *Sacoglottis gabonensis* seeds where a-d shows the external morphology with accompanying dimensions, and c-d shows the internal morphology. Note the damage to the specimen c, which has been cracked open by *C.atys* to extract the kernels within (van Casteren, A. 2015: pers. comm.). Photographs: Karen Swan.

An additional hard food item in the *C.atys* diet includes the endocarp of *Coula edulis*, which is roughly spherical in shape, measures 30-40mm in diameter and contains a single kernel (Boesch and Hedwige, 1982, McGraw et al., 2011). Both *C.edulis* and *S.gabonensis* seeds have been known to be consumed by chimpanzees, however it is worth noting that although physically much larger than *C.atys*, they must resort to tool

use by adopting a hammer and anvil to open the seed casings (Boesch and Hedwige, 1982). The hardness and Young's modulus of these hard food items are presented in Table 1.2.

Table 1.2 Shore-D hardness and Young's modulus values for the main hard foods (*Sacoglottis gabonensis* and *Coula edulis*) consumed by *C.atys* in the wild. Values for almond nuts and coconut husks are also included for comparison. From Pampush et al. (2011).

Food item	Hardness (Shore-D)	Young's modulus (MPa)
<i>Sacoglottis gabonensis</i>	78.3 ± 10.19	285.31 ± 109.51
<i>Coula edulis</i>	65.6 ± 8.31	331.91 ± 155.60
Almond nut	16.78 ± 1.58	30.74 ± 7.44
Coconut husk	75.2 ± 8.60	1067.10 ± 146.62

Along with *Coula edulis* the endocarp of *S.gabonensis* is characteristically processed using a distinctive a postcanine crushing behaviour described by McGraw et al. (2011). The anterior dentition is first used to scrape any unwanted material and to attempt to puncture the seed casing. Postcanine crushing may then occur by adopting a wide gape, placing the endocarp behind the canine and performing a single or succession of powerful isometric bites to shatter the item (Figure 1.18). Any indigestible fragments are then discarded and the food masticated using the postcanine dentition or stored in cheek pouches for later consumption (McGraw et al., 2011, Daegling et al., 2011). A later study by Morse et al. (2013) suggests that the P4 and M1 are predominately used in this postcanine crushing behaviour due to an unusually high amount of wear on these teeth in comparison to the others along the row.

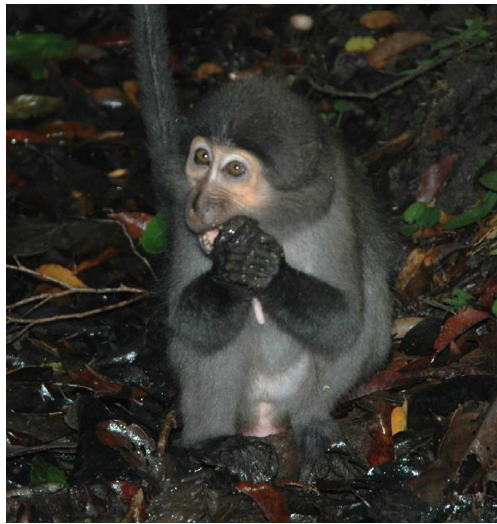


Figure 1.18 Image of an adult female *C.atys* processing a *Sacoglottis gabonensis* seed using characteristic postcanine crushing. From Daegling et al (2011).

Despite differences in body size, adult males and females, and non-adults (younger than 6 years old or pre M3 eruption) most frequently consume the seeds of *Sacoglottis gabonensis* out of all the foods in their diet (Table 1.3) (McGraw et al., 2011). Therefore as a species, *Cercocebus atys* can confidently be classed as a habitual hard object feeder regardless of sex and age class. To process such mechanically demanding foods over the course of a life time it is essential that the teeth are functional despite the inevitable effects of wear. This then raises the important question of whether the wear process maintains the shapes of teeth in *C.atys* such as the case of many folivorous primates (Ungar and M'Kirera, 2003, Dennis et al., 2004, King et al., 2005, Bunn and Ungar, 2009, Cuozzo et al., 2014, Venkataraman et al., 2014).

Table 1.3 Percentage of feeding actions associated with the hard foods *Sacoglottis gabonensis* and *Coula edulis*. Comparisons are made between adult females and males, and adults and non-adults. Data from McGraw et al. (2011).

	Percentage of feeding actions (%)			
	Adult females	Adult males	Adults	Non-adults
<i>Sacoglottis gabonensis</i>	49	62.3	51.2	69.4
<i>Coula edulis</i>	0.26	1.63	0.49	0.86

1.7. Aims and objectives

This thesis will examine how dental form and function affect the breakdown of hard brittle food items. In particular, the consequence of dental wear will be investigated in *C. atys*, a hard object feeding primate where the adults and juveniles both consume the same stress resistant food despite considerable differences in masticatory form and dental wear. Differences in dental topography during wear in this species will be quantified and related to its dietary ecology. The effect of changes in form on function will also be assessed using a novel combination of physical replicas of cusps, teeth, 3D printed hard food objects and physical testing. The results of the subsequent studies should further our understanding of the relationship between dentition and hard object feeding.

The aims of this thesis are to:

1. To investigate how cusp morphology may be optimised for hard object feeding.
2. To quantify dental wear in a hard object feeding primate, *C. atys*.
3. To measure how these variations in form during dental wear in *C. atys* may impact functionality.

Chapter 2: Cusp design and optimality in hard object feeders

2.1. Introduction

Teeth play a vital role in food acquisition and processing by providing the main points of contact between the masticatory apparatus and the food object. Therefore it is unsurprising that the shapes of dental structures have frequently been associated with different dietary specializations where teeth are viewed as tools, specially designed for the breakdown of certain foods (Lucas, 1979, Lucas and Luke, 1984, Evans, 2005). Although previous research has found correlations between tooth shape and diet, these studies tend to assume rather than demonstrate how certain dental features may confer a functional advantage (e.g. Kay, 1975, Kay and Hylander, 1978). As food reduction is predominately a mechanical process, it makes sense to measure performance of teeth using mechanical parameters (Spears and Crompton, 1996b). This study therefore aims to examine how the shapes of teeth may be optimised for a single dietary strategy, hard object feeding, based on various mechanical performance indicators.

2.1.1. Quantifying the mechanical performance of teeth

In order to examine the relationship between dental form and function, previous studies have attempted to simulate the interaction between teeth and food in a controlled laboratory setting. This typically involves loading physical models of teeth under compression to fracture a food object. Depending on the aims of the study, a range of data can then be extracted such as information on force, displacement, time, energy, and the fracture and fragmentation patterns of the test object. The results based on this experimental setup has been used previously to analyse the mechanics of bladed teeth (Anderson and LaBarbera, 2008, Anderson, 2009), serrated teeth (Abler, 1992), specializations to hard object feeding (Berthaume et al., 2010, Crofts and Summers, 2014), puncture ability of teeth (Freeman and Weins, 1997, Freeman and Lemen, 2006, Evans and Sanson, 1998), bite force (Lucas et al., 1994) and for the use in experimental dentistry studies (Slagter et al., 1992, Sui et al., 2006, Melani et al., 2012).

Previously, Berthaume (2010) has used mechanical simulations of tooth-food contact to investigate whether the occlusal morphology of early hominins species represent an adaptation to hard object feeding (Figure 2.1). Using metal casts of teeth to fracture

brittle acrylic hemispheres they found no evidence to support a functional adaptation of the teeth to break down hard foods. However, it is extremely difficult to examine the precise relationship between tooth form and function of natural teeth where the occlusal surface is highly complex, often exhibiting multiple cusps that vary in morphology at different wear states. The use of a dental row further complicates matters by providing contact by several teeth of different morphologies.



Figure 2.1 Image of a hominin dental row cast compressed onto a hollow acrylic hemisphere used in Berthaume et al. (2010).

The complexity of naturally occurring dentition has led some researchers to model teeth as basic shapes in order to obtain a deeper understanding between tooth geometry and the fracture of foods (Evans and Sanson, 1998, Crofts and Summers, 2014). As cusps play such a prominent role in initiating and propagating fracture in foods (Luke and Lucas, 1983, Lucas, 2004), they provide an excellent opportunity to simplify the tooth and examine how the variation in form of single dental feature may affect food breakdown.

2.1.2. Cusp form and function

The shapes of cusps can vary in main two ways; bluntness and included angle, which can both affect tooth functionality (Evans and Sanson, 1998). Bluntness is the degree of taper, which can be defined as the rate of the decrease in cross sectional area from base to tip (Ungar, 2010). By increasing the bluntness of a cusp, increases the surface area of initial contact therefore produces higher stress in the food item. Similarly, by widening the angle of a cusp will also increase surface area of contact, however, it also has the added effect of building up strain energy by wedging the material apart, thus has to penetrate less of the material to propagate cracks (Vincent, 1990). Using stylized models of cusps to fracture insects, Evans and Sanson (1998) were able to show that

both these shape parameters influence the initial and maximum force and energy required to penetrate.

Furthermore, both of these shape variables independently affect the radius of curvature (i.e. radius of the circle of best fit) of the cusp tip, which has commonly been used to quantify cusps to investigate dietary adaptations (Yamashita, 1998a, Hartstone-Rose and Wahl, 2008, Berthaume et al., 2010, Berthaume, 2014). To date, there has been some confusion surrounding the relationship between cusp radius of curvature and diet (see section 1.5.2 p. 40), therefore by accounting for both angle and bluntness when studying cusp form may help clarify exactly how cusp shape may affect mechanical breakdown. In relation to hard object feeding, teeth are used to fracture highly stress-resistant food items; therefore the potential for cusps to alleviate some of the mechanical demands of such a diet may play an important role.

2.1.3. Tooth form and food processing in hard object feeders

As discussed in chapter 1, the teeth of hard object feeders present an extraordinary array of dental morphologies. Previously, Crofts and Summers (2014) investigated the effect of crown morphology observed in durophagous organisms, to fracture snail shells. They found that teeth with a tall, skinny cusp were the best performers based on the force at fracture, which were similar in form to the teeth of sculpin fish (*Asemichthys taylori*) that are used to puncture snail shells in the wild (Norton, 1988). However, they note that additional factors may be influencing tooth form in durophagous species as there exist many different tooth morphologies in nature - none of which conform to their proposed optimal shape.

Variation in tooth form may partly be explained by a disparity in dental function among hard object feeders. There are two main ways in which the teeth are used to process foods. The first of these refers to *food access* whereby an object must be fractured or prised open in order to access the food within. This feeding behaviour is typically associated with the breakage of mechanically protective layers such as shells and seed casings that act to deter predators. Once the layer has been broken, the food within can be then be consumed. An example of hard object feeding for food access can be drawn from observations of pitheciine primates including *Pithecia* and *Chiropotes* spp. that use their canines to puncture highly resistant husks of unripe fruits to extract the highly nutritious and often softer seeds within (Kinzey and Norconk, 1990, Norconk and Veres, 2011b). It is important to add that this behaviour is not restricted to anterior

teeth. For instance, sooty mangabeys are known to use their premolar and molar teeth to fracture highly stress resistant endocarps to access the seeds within (Daegling et al., 2011, McGraw et al., 2011).

The second way in which the teeth may be used in a hard object feeding behaviour is to break down hard foods for *consumption*. In this case foods have a nutritional value and are comminuted into smaller pieces, which are to be swallowed and digested. For example, spotted hyenas (*Crocuta crocuta*) are infamous hypercarnivores that use their premolar teeth to crack bones, which are then digested thoroughly (Kruuk, 1972, Van Valkenburgh, 2007). Although both food access and consumption may not necessarily be mutually exclusive, it is still important to acknowledge that a distinction in function exists among different hard object feeders that may influence how a tooth may be optimised. Therefore the mechanical barriers such as endocarps and shells may warrant different mechanical requirements to a solid food to be broken down for consumption.

2.1.4. Mechanical performance indicators

One explanation for why Crofts and Summers (2014) found an inconsistency between their proposed optimal tooth shape and those found in nature is that they only used force at fracture to measure optimality. On the contrary, there are many different parameters that may be optimised for during food breakdown which include; force, energy, duration and fragmentation, which are discussed below in relation to cusp shape.

2.1.4.1. Force

Force is a parameter that has been of major interest in studies on the mechanical performance of teeth where optimisation is important for both the access and consumption of foods (Evans and Sanson, 1998, Berthaume et al., 2010, Crofts and Summers, 2014). During food processing forces are generated by the masticatory muscles that are transmitted via the teeth onto the food object. How the teeth are shaped can influence the amount of force required to fracture by determining the amount of pressure (force per unit area) onto the food item (equation 2.1).

$$Pressure = \frac{Force}{Area}$$

(2.1)

Grounded in engineering principals, it is widely acknowledged that by reducing the contact surface area of a structure concentrates stress to a small area thereby increasing

pressure. In terms of cusp morphology, this can be achieved by reducing the angle and increasing the sharpness of the cusp tip, which individually act to minimise the contact surface area (Figure 2.2) (Lucas, 2004). By lowering the forces needed to fracture foods means that less muscle force may be needed during mastication. Furthermore, Strait (1997) suggests that this optimisation may be particularly important for smaller-bodied animals that need to break strong or stiff foods as they have absolutely smaller muscles than larger-bodied animals.

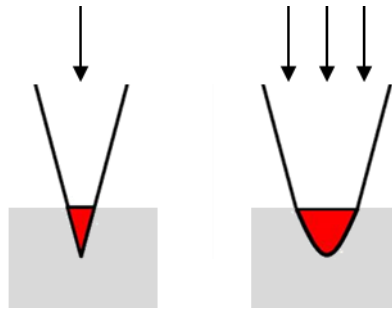


Figure 2.2 Schematic diagram illustrating the relationship between cusp morphology and force. By minimising the surface area of a point minimises the amount of input force (arrows) needed to produce the same pressure. Arrows indicate the direction and magnitude of masticatory forces.

2.1.4.2. Energy

In addition to force, energy has also been regarded as a parameter of great interest when quantifying the mechanical efficiency of food breakdown (Lucas et al., 1994, Evans and Sanson, 1998, Berthaume et al., 2010). Energy is a property that cannot be created but is transferred between objects in many different forms. During food breakdown, mechanical energy is transferred when a force is applied to a food item causing fracture (Berthaume et al., 2010). In this context, energy or “work done” can be mathematically described as the integral of force over distance (equation 2.2) and is typically estimated by calculating the area under the force-displacement graph and measured in N/m or Joules.

$$Work\ done = \int_C F ds$$

(2.2)

In terms of feeding efficiency, the amount of energy obtained from the digestion of foods must always outweigh the amount lost during food processing (Lucas, 1979). Therefore it is vital that energy should be conserved as much as possible during food breakdown. Previous research has found force and energy to be highly correlated where

both measures have been shown to decrease with increasing cusp tip sharpness used to penetrate insects (Evans and Sanson, 1998). In some cases, force has even been used to indirectly infer energy (Crofts and Summers, 2014).

2.1.4.3. Duration

Duration of fracture is an interesting parameter that has previously been neglected by former mechanical studies on tooth form. The time it takes to fracture an object could hold important implications on masticatory efficiency when considering the effects of muscle fatigue, where muscles are unable to maintain a constant force as a result of prolonged contraction (Maton et al., 1992). During the production of sustained bite forces in humans, Maton et al. (1992) demonstrated that the muscles of mastication, specifically the masseter and temporalis, exhibit characteristics of muscle fatigue similar to that of limb muscles. A quick fracture may therefore be beneficial to prevent the muscles wearing and allow for a more efficient force production. In terms of cusp morphology, a quicker fracture may be achieved by a blunter, wider cusp, which promotes crack propagation as a result of a larger contact surface area and distribution of stress on the food item (Lucas, 2004). Therefore the cusp does not need to be displaced far into the object or take as long a time to induce fracture. In contrast, sharp, acute cusps are likely to suppress crack propagation therefore must be displaced further into the object taking a longer duration to initiate fracture (Figure 2.3) (Lucas, 2004).

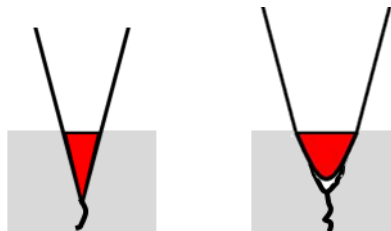


Figure 2.3 Schematic diagram illustrating the relationship between cusp morphology and duration. Sharper, acuter cusps tend to suppress crack growth therefore need to be displaced further into the object thus taking a longer time to induce fracture. In contrast blunter, wider cusps tend to promote crack propagation due to a larger surface area therefore require less displacement and time to fracture.

2.1.4.4. Fragmentation

The quantity and size of particles that food is broken down into is highly important for food consumption as this has a direct impact on the efficiency of digestion (Lucas, 2004, Ungar, 2010). During mastication the teeth act to reduce food, which increases the surface area per unit volume of a solid. By exposing new surface area for enzymes in the gut to act on, a more efficient chemical digestion can be achieved (Lucas, 2004).

Therefore in this criterion, teeth considered as most optimal are those that fragment food into a high number of small particles. Previously, fragmentation has not been explicitly studied in relation to tooth design. However it has been theorized that blunter and wider cusps promote crack propagation as a result of a greater distribution of stress when in contact with a food item (Lucas, 2004). In relation to brittle hard objects, crack growth can lead to the object to shatter into pieces, providing a crack has reached its critical length where it is self-propagating (see section 1.4.5.1 pp. 38-39).

In terms of food access, the degree of fragmentation is considered to be of less importance as the main goal is to break these items to access in order to digest the food within. Interestingly, sea otters have been known to habitually chew shelled prey items as whole (Kenyon, 1969, Vandever, 1969, Calkins, 1978). From scat analyses, it appears that fragments of mollusc shells, and the plates and spines of sea urchins are indeed swallowed and pass through the gastrointestinal tract relatively undigested suggesting that these items are of little nutritional value (Murie, 1940). Alternatively some primate hard object feeders such as *Cercocebus atys* have been known to expel fragments from the oral cavity (Daegling et al., 2011). Based on this behavioural evidence it seems likely that in the case of food access, the shells that are broken are either swallowed (if small enough) or discarded physically prior to ingestion. Therefore there does not seem to be an apparent benefit for optimising for either high degree or low degree of fragmentation, rather, the object just needs to be broken.

2.1.5. Aims and objectives

In order to examine cusp optimality in hard object feeders, a series of stainless steel cusp tips will be created that vary in angle, bluntness and radius of curvature. Each cusp will be mounted to a universal testing machine and used to fracture brittle 3D printed hemispheres representing a hard food object. To account for the distinction between food access and food consumption in hard object feeding two forms of the hemisphere will be made; one hollow to be broken for food access and one solid to be broken for food consumption. Mechanical performance will then be indicated based on the force, energy and duration to fracture the hemispheres. For the solid domes a measure of fragmentation will be also be included in order to assess how well a hard food item is broken down for consumption. To facilitate the interpretation of cusp performance, displacement and surface will also be recorded. The results from these experiments will be used to answer the following research questions:

1. *Does cusp morphology affect the mechanical performance of hollow hard object breakdown?*

It is expected that force and energy will increase with increasing cusp angle, bluntness and radius of curvature due to a greater contact surface area. In contrast, the duration will decrease with increasing cusp angle, bluntness and radius of curvature due to a shorter displacement at fracture.

2. *Which cusp morphology(s) is most optimal for hollow hard object breakdown?*

If cusp morphology is found to affect the mechanical performance to break hollow hard objects, the results of different performance indicators will be compared to assess which cusp is the best overall performer.

3. *Does cusp morphology affect the mechanical performance of solid hard object breakdown?*

Similar to hollow hard object breakdown it is expected that force and energy will increase with increasing cusp angle, bluntness and radius of curvature and duration will decrease with increasing cusp angle, bluntness and radius of curvature. In terms of fragmentation, it is expected that cusps with a larger angle, bluntness and radius of curvature will produce the highest amount of small particles due to the promotion of crack growth in the object.

4. *Which cusp morphology(s) is most optimal for solid hard object breakdown?*

If cusp morphology is found to affect the mechanical performance to break hollow hard objects, the results of different performance indicators will be compared to assess which cusp is the best overall performer.

2.2. Materials and methods

2.2.1. Cusp design and manufacture

The following subsection outlines the design and manufacture of the physical cusp models used to fracture the hard brittle food items.

2.2.1.1. Cusp design

Hypothetical cusp designs were based on those used by Evans and Sanson (1998) to examine the effect of cusp shape on the breakdown of insects. The cusps were idealized so that the geometry was determined by two key dimensions; angle and bluntness. Using the CAD software SolidWorks 2014 (Dassault Systèmes SolidWorks Corp.), 2D sketches were first made of four triangular templates that were of the same height but varied in subtended angle (30° , 60° , 90° and 120°) (Figure 2.4).

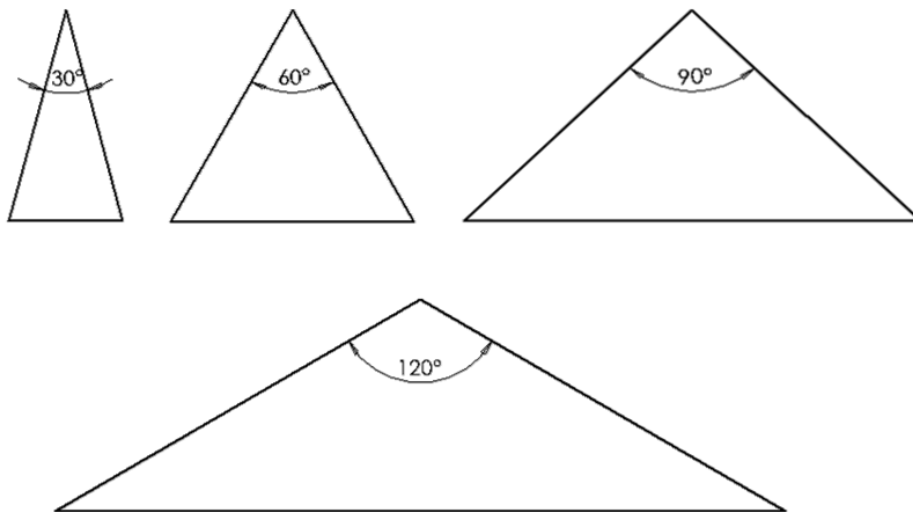


Figure 2.4 2D sketches of the four basic triangular templates used to construct the hypothetical cusps, which measured 30° , 60° , 90° and 120° .

For each template triangle, a blunting series was created by fitting a curve at varying distances from the original triangle tip (A) (Figure 2.5). These distances named as ‘blunting distances’ were predefined as 0.75mm, 1.5mm, 3mm and 6mm from the tip (A) and labelled as B, C, D and E respectively.

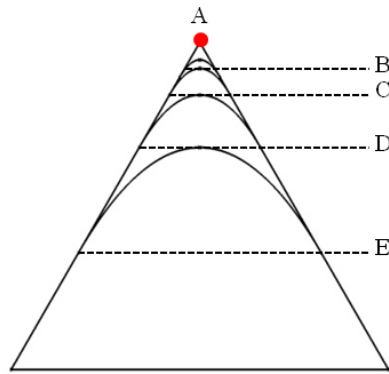


Figure 2.5 Diagram displaying the blunting distances used to fit a curve, which altered the level of bluntness in each group of angles. Blunting distances were B=0.75mm, C=1.5mm, D=3mm and E=6mm from the tip of the triangle (A). A 60° template is used in the example.

In order to construct the triangles with curved tips, a parabola was first drawn onto the triangular template using a tool in SolidWorks 2014 (Dassault Systèmes SolidWorks Corp.) that could be manipulated using three sets of XY coordinates.

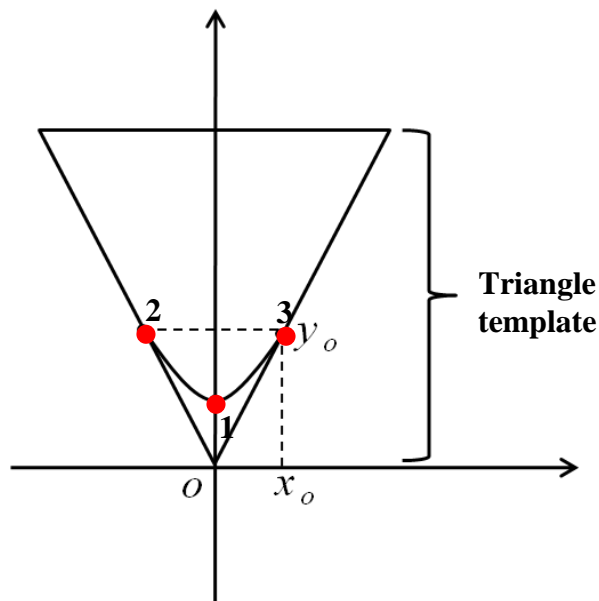


Figure 2.6 Diagram displaying the three coordinates used to fit a parabolic curve to the triangle where Y_0 = blunting distance and X_0 = the point at which the curve and the triangle meet at Y_0 .

The first coordinate (1), the apex of the parabola, was positioned at half the distance between the set blunting distance (Y_0) and the tip of the triangle (Figure 2.6). For example, the apex for a blunting distance of 3mm would be 1.5mm from the tip. The remaining two points (2, 3), which were the start and end of the curve, were positioned at the set blunting distance on the y axis (Y_0) and where the parabola intersected this point on the x axis (X_0), which was calculated using equation 2.3:

$$X_0 = \tan\left(\frac{1}{2} \theta\right) Y_0$$

(2.3)

The 2D sketches were then sectioned in half and revolved on the y axis to create a 3D cone. In total a series of 20 cusp models were created that varied in angle and bluntness that determined the radius of curvature of the tip. When measured at a set distance from the tip, an increase in angle and bluntness ultimately increased the amount of surface area (Figure 2.7). Additionally, in order to compensate for the changes in angle and bluntness, the height and base measurements also varied accordingly (Table 2.1).

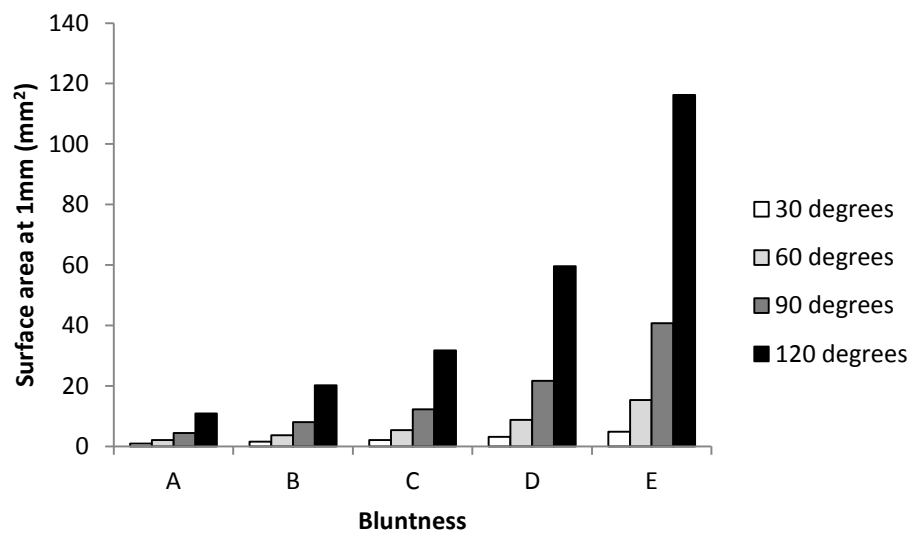






















Figure 2.7 Surface area of each cusp as measured 1mm from the tip.

Table 2.1 Dimensions of cusp designs used in study, which varied in angle, bluntness and radius of curvature at the acting point. Based on these variables the surface area and volume exposed at certain levels of displacements varied accordingly.

Name	Angle (°)	Blunting distance (mm)	Radius of curvature (mm)	Height (mm)	Base Ø (mm)	Surface area at 1mm (mm²)
A30	30	0.00	0.00	9.33	5.00	0.87
B30	30	0.75	0.05	8.96	5.00	1.50
C30	30	1.50	0.11	8.58	5.00	2.09
D30	30	3.00	0.22	7.83	5.00	3.11
E30	30	6.00	0.43	6.33	5.00	4.82
A60	60	0.00	0.00	9.33	10.77	2.09
B60	60	0.75	0.25	8.96	10.77	3.70
C60	60	1.50	0.50	8.58	10.77	5.37
D60	60	3.00	1.00	7.83	10.77	8.79
E60	60	6.00	2.00	6.33	10.77	15.31
A90	90	0.00	0.00	9.33	18.66	4.44
B90	90	0.75	0.75	8.96	18.66	8.05
C90	90	1.50	1.50	8.58	18.66	12.23
D90	90	3.00	3.00	7.83	18.66	21.71
E90	90	6.00	6.00	6.33	18.66	40.68
A120	120	0.00	0.00	9.33	32.32	10.88
B120	120	0.75	2.25	8.96	32.32	20.17
C120	120	1.50	4.50	8.58	32.32	31.73
D120	120	3.00	9.00	7.83	32.32	59.58
E120	120	6.00	18.00	6.33	32.32	116.18

Table 2.2 Cusp morphospace created by altering the angle and bluntness of a cone. Radius of curvature values (R) indicated below each model in mm.

		Blunting distance Y_0 (mm)				
		A (0)	B (0.75)	C (1.5)	D (3)	E (6)
Angle (°)	30	 $R=0$	 $R=0.05$	 $R=0.11$	 $R=0.22$	 $R=0.43$
	60	 $R=0$	 $R=0.25$	 $R=0.5$	 $R=1$	 $R=2$
	90	 $R=0$	 $R=0.75$	 $R=1.5$	 $R=3$	 $R=6$
	120	 $R=0$	 $R=2.25$	 $R=4.5$	 $R=9$	 $R=18$

In order to attach the cusp models to the universal testing machine the final designs were modified to include a cylindrical base at the bottom of the cone (Figure 2.8). A 4mm hole was extruded at the centre of the base so that a 10/32 UNF internal thread could be tapped. This allowed for each cusp model to be consistently placed in the same position for each test run whilst providing an effective method of attachment and detachment to and from the machine.

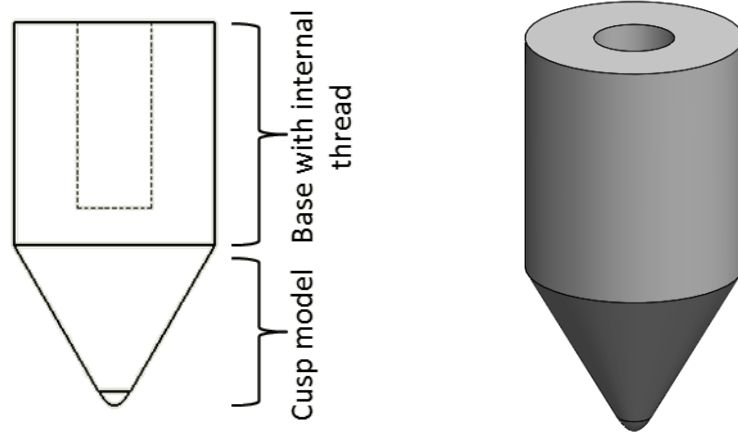


Figure 2.8 An example of the final design of a cusp model where the cusp shape was fitted to a cylindrical base with a 10/32 UNF internal thread that allowed the model to be attached to the machine securely.

2.2.1.2. Cusp manufacture

The final designs were manufactured using Computer Numerical Control (CNC) machining, which involves the use of computers to automate tools such as lathes, drills and saws to produce a physical 3D model from a block of material from a virtual 3D surface. Selective Laser Sintering (SLS) was also considered but was rejected as this method relies on the use of powdered metal, which may impact the structural integrity of the cusp models when subjected to high compressive forces. Furthermore, the resolution of the cusp tips and the quality of the surface were found to be relatively poor in comparison to those made from CNC machining.

2.2.1.3. Cusp model material

Initially the models were manufactured in aluminium, which is a low cost metal that has been used previously in similar experiments to create artificial dental models (Crofts and Summers, 2014). However, from preliminary experiments it was found that this material deforms quite easily when compressed into a hard solid object. When using two of the sharpest cusp models of the series (A30, A60) to fracture plaster of Paris domes ($h=10\text{mm}$, $\text{Ø}=20\text{mm}$) it was noticed that within the first few repeats, the plaster

domes were observed to fracture at considerably lower forces than the subsequent repeats. This suggested that the cusp tip had changed shape to the extent that it was affecting the mechanical performance between repeats.

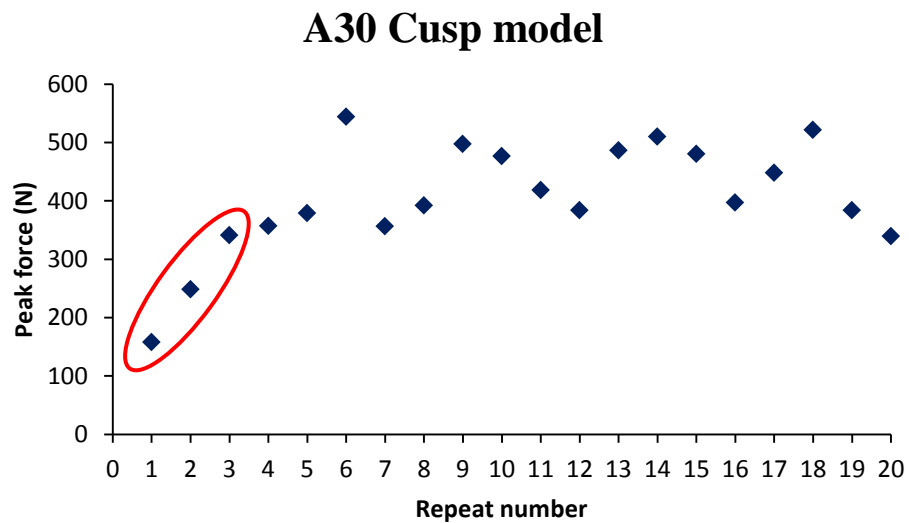


Figure 2.9 Graph displaying peak force to break plaster domes plotted against repeat number for A30 aluminium cusp model.

For the A30 cusp model a steep increase in peak force was observed in the first 3 repeats (Figure 2.9). There then appeared to be an apparent plateau in force where it was likely that the model has stopped deforming.

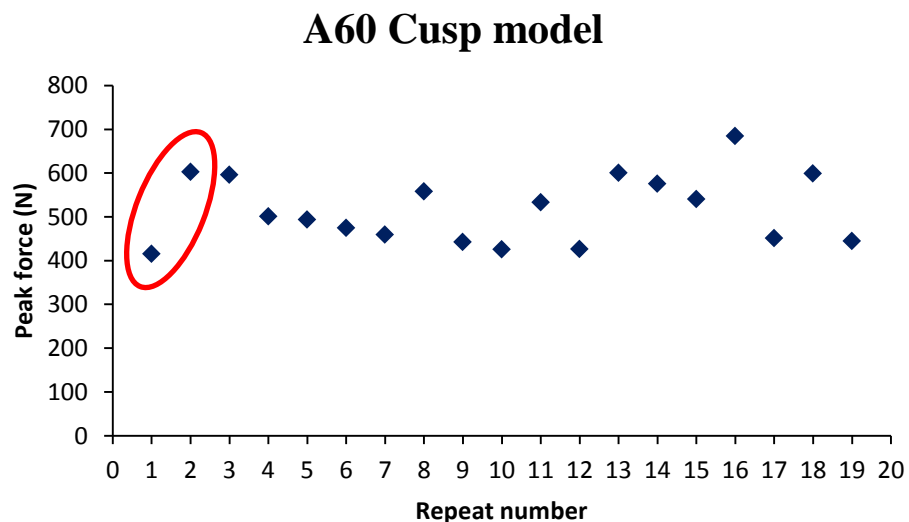


Figure 2.10 Graph displaying peak force to break plaster domes plotted against repeat number for A60 aluminium cusp model.

The A60 model shows similar results although not as extreme as the more acute model A30. Again a rise in peak force can be observed at the second repeat, after which the

results begin to reach a plateau (Figure 2.10). The apparent deformation of the model was confirmed using photographs taken before and after the set of repeats for A60 (Figure 2.11), where the tip had clearly flattened (Figure 2.11b).

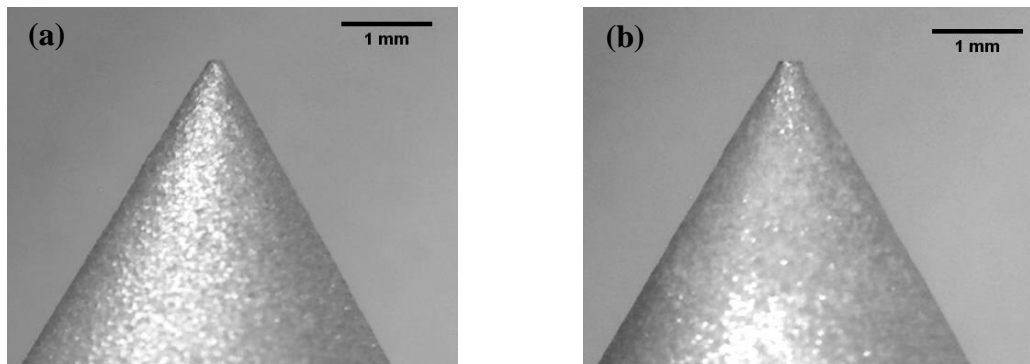


Figure 2.11 An example of the deformation of the aluminium tip after 20 compression tests using plaster of Paris hard domes; (a) A60 aluminium model before compression tests; (b) A60 aluminium model after compression tests.

As this chapter and the remainder of the thesis focuses on how the shapes of teeth affect fracture performance, it was deemed extremely important to ensure that the material used to manufacture the models was not liable to deform when under compression. Consequently it was decided to manufacture the cusp models in stainless steel which has a much higher Young's modulus than aluminium (Table 2.3).

Table 2.3 A comparison of the mechanical properties of stainless steel and aluminium. Mechanical property values from Aerospace Specification Metals Inc. (ASM) data sheets.

Material	Young's modulus (GPa)	Tensile yield strength (MPa)	Hardness (Vickers)	Poisson's ratio
Aluminium 7075-t651	71.7	503	175	0.33
Stainless steel 304	193-200	215	129	0.29

The final cusp models used in the present study were manufactured in stainless steel (SS304) using CNC machining (Star Prototype Manufacturing Co., Ltd). However it was decided to exclude cusps with no bluntness (A) and 30° angles as the cusp tips of these models were considered to be more susceptible to damage due to the fine detail of the shape of the tip.



Figure 2.12 Stainless steel cusp models used in study, which were made in angles of 60°, 90° and 120° (front to back), and blunting distances B, C, D and E (left to right).

2.2.2. Hard object design and manufacture

The following subsection outlines the incentive behind the choice of material, design and manufacture of a hard object, which will be used to compare the mechanical performance of cusps.

2.2.2.1. Choosing a material

The choice of a food test object is extremely important as the internal and external material properties heavily determine the fracture and fragmentation behaviour (Lucas, 2004). As this item is to be used to infer the mechanical efficiency of teeth used in hard object feeding it is important to use a material that reflects the properties of such foods.

In order to achieve this, one approach is to use real hard food items that are known to be consumed by the animal of study in the wild. For example, Lucas et al. (1994) used *Mezzettia parvifloa* and *Macadamia ternifolia* seeds when studying bite force in orangutans. Although the use of such foods is biological relevant they are also likely to be variable in size, shape and internal architecture due to natural variation; factors which may all affect fracture behaviour. Additionally foods such as nuts and seeds may prove difficult to align to certain aspects of teeth due to irregular geometries, thus further impede the reproducibility of the experiment.

Therefore alternatively, other studies have sought to use synthetic materials as a representation of a food object in order to control as much as possible for potential variation in internal and external properties. For example in order to investigate hominin dental morphology and hard object feeding, Berthaume et al. (2010) used hollow acrylic hemispheres to simulate the mechanical properties of a macadamia nut shell (Figure

2.13a). These hemispheres were manufactured as the same shape, size and material using a slow precision casting method. They were then further modified by chilling the domes to -78°C to ensure a consistent brittle failure when loaded in compression. An additional study by Crofts and Summers (2014) adopts a similar approach but utilizes recent advances in 3D printing technology to create a hard brittle food item when examining the mechanical performance of the dentition of durophagous organisms (Figure 2.13b). By CT scanning real snail shells they were able to replicate the exact morphology of a natural prey item yet control for physical properties and increase reproducibility.

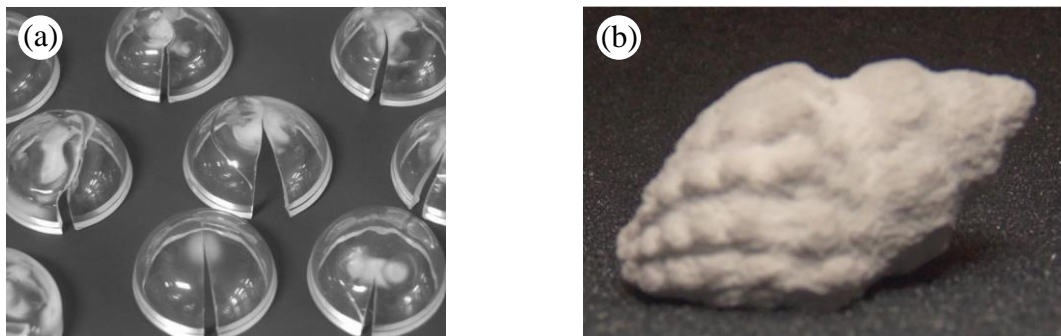


Figure 2.13 Brittle objects used previously to investigate tooth form and mechanical performance; (a) fractured acrylic domes used by Berthaume *et al.* (2010) and (b) a 3D printed shell (*Nucella lamellosa*) derived from CT scans therefore containing both external and internal architecture (Crofts and Summers, 2014).

Based on these past analyses it was decided to use a material that adheres to the aims of the project (i.e. is a hard brittle material) yet can also be standardized in shape, size, homogeneity and mechanical properties so as to increase the reproducibility of the experiment and reduce variation in fracture behaviour between samples. Therefore, following Crofts and Summers (2014) it was decided to use 3D printing.

2.2.2.2. Design of hard object

One of the key advantages of 3D printing is that the size and shape of the object can be controlled for and precisely designed using CAD software. In SolidWorks 2014 (Dassault Systèmes SolidWorks Corp.), two forms of hemispheres were designed; one hollow representing a structure to be fractured for food access (Figure 2.14a), and one solid representing a food to be broken down for consumption (Figure 2.14b). Both variants were the same size in order to isolate the effects of breaking a hollow or solid structure. It is acknowledged that hard food items come in a range of different shapes and sizes. Therefore the simple shape designed in this study was used solely to compare mechanical performance rather than simulate the breakdown of a certain food. Once

designed the sketches were converted into a surface file format (.stl) ready to be 3D printed.

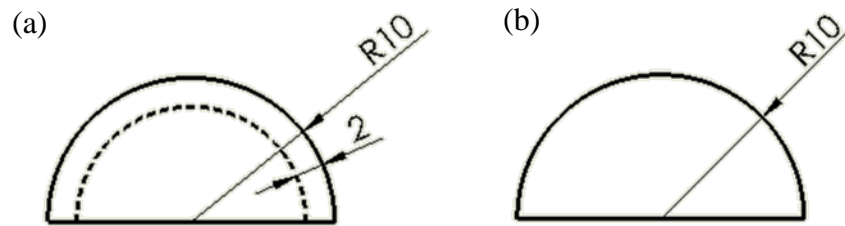


Figure 2.14 2D sketches and dimensions of hard objects used in this study; (a) hollow, (b) solid. Measurements in mm. R= radius.

2.2.2.3. *Manufacture of hard object*

The virtual dome models were 3D printed using a ZPrinter 350 (ZCorporation). 3D printing is a form of additive manufacturing where layers of powdered material are laid down one by one and fused together to construct a 3D physical object. The 3D print material used was composed of a combination of zp150 high performance composite powder and zb63 clear binding solution. The powder, which forms the bulk of the material, consists of plaster (<90% by weight) and vinyl polymer (<20% by weight). The binder that then acts to fuse the powder is formed from humectant (<10% by weight) and water (65-99% by weight). Prior to printing, the ratio of binder to powder was pre-programmed so that both the shell and the core of the 3D print were the same to produce a homogenous material. The position of the dome in the 3D printer build chamber was also considered as the direction of the layers may restrict crack propagation if orientated vertically. Therefore it was decided to place the domes upright in the XY plane so that the layers were deposited horizontally (Figure 2.15).

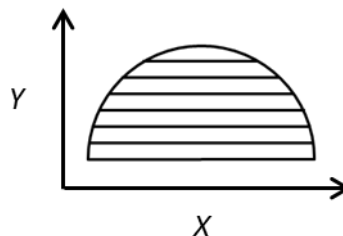


Figure 2.15 Orientation of the 3D printed layers, which measured 0.088mm in thickness. Image not to scale.

Once printed the hollow dome models were post-processed by lightly misting the models on both sides with an Epsom salt (7oz) and water (16oz) solution. Epsom salt (magnesium sulphate) and water is commonly used in 3D printing to cure and harden

models. However whether the solid models would fully absorb the solution was questionable. If, for instance, the solution was not fully saturated to the core it would impair the homogeneity of the model and potentially influence fracture behaviour. Therefore to gauge the permeability of the 3D print material a small experiment was conducted by soaking several solid 3D prints in a solution of water and blue dye. The models were placed in the solution and removed at 3 different time intervals (15 minutes, 30 minutes and 60 minutes). At each interval the models were then cut in half using a scalpel in order to visually observe the extent of absorption. It was found that despite differences in duration, the liquid did not permeate through the whole model (Figure 2.16). Further to this it was also observed by soaking the 3D prints appeared to disintegrate the material. Therefore it was decided to leave the solid models uncured.

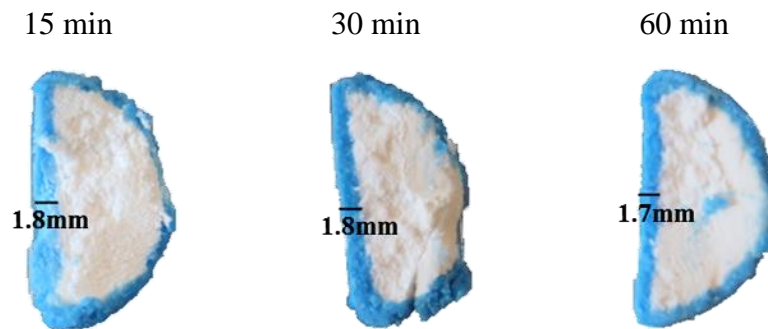


Figure 2.16 Images taken of the solid 3D printed domes after being soaked in dye solution for 3 different durations (15min, 30min, 60min). Regardless of time, the liquid only permeated approximately 2mm inwards.

To increase the brittleness of the domes the cured hollow models and uncured solid models were gently dried in a vacuum oven (Gallenkamp Vacuum Oven) at a temperature of 75°C and pressure of ~15 mbar for 24 hours. Throughout the duration of the experiments, the models were maintained in a desiccator containing silica gel in order to keep dry and avoid exposure to moisture in the air. A maximum lifetime of 7 days was assigned for the domes until new ones were made.

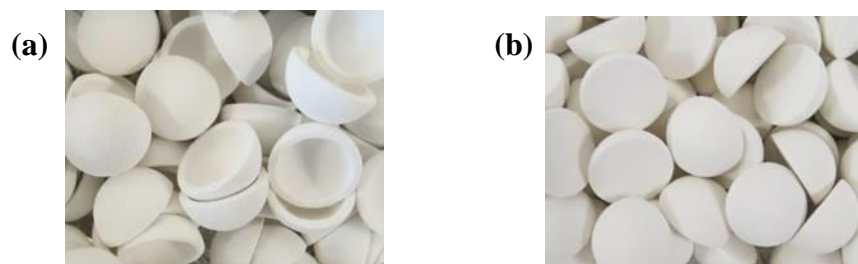


Figure 2.17 Photographs of the hollow (a) and solid (b) 3D printed domes which were used to quantify the mechanical performance of cusps.

In order to gauge the stiffness of the oven dried 3D print material the Young's modulus was calculated by compressing a sample of 15 cylinders ($\text{Ø}=20\text{mm}$, $\text{H}=30\text{mm}$) at a slow displacement rate (5mm/min). The Young's modulus value is presented in Table 2.4 along with a selection of different foods for comparison.

Table 2.4 Young's modulus of the 3D print material used in this study (zprint 150 vacuum dried, N=15) compared to a selection of food materials. Note: Young's modulus was calculated from 3D print material that was tested the same day that the domes were removed from the oven.

Material	E \pm SD (MPa)
3D print material	143.48 \pm 4.77
<i>Sacoglottis gabonensis</i> *	285.37 \pm 109.51
Almond nut*	30.74 \pm 3.50
Coconut husk*	1067.10 \pm 146.62
Carrot*	6.38 \pm 1.48
Gummy bear ⁺	0.07 \pm 0.03
Dried apricot ⁺	0.99 \pm 0.29
Apple flesh ⁺	3.41 \pm 0.10
Cherry pit ⁺	186.92 \pm 69.61
Prune pit ⁺	189.48 \pm 1.20
Popcorn kernel ⁺	325.40 \pm 218.83

*= From Pampush et al. (2011) ⁺ = From Williams (2005)

2.2.3. Experimental design and analysis

To test the mechanical performance of cusps for each optimality criterion, the cusp models were attached to the mobile element (crosshead) of a universal testing machine (Mecmesin MultiTest 2.5~i), which was fitted with a 2.5kN load cell. 3D printed domes were placed on a platform and positioned directly beneath the model so that the tip of the cusp was aligned to the centre of the dome. In order to prevent fragments from being lost, a plastic tube was placed around the dome. Data from the compression tests was collected using Emperor (version 1.18-408) software. Audio videos were taken during each test, and photographic and written descriptions were made after compression to record fracture and fragmentation behaviour. Figure 2.18 shows the basic experimental setup used for each compression test.

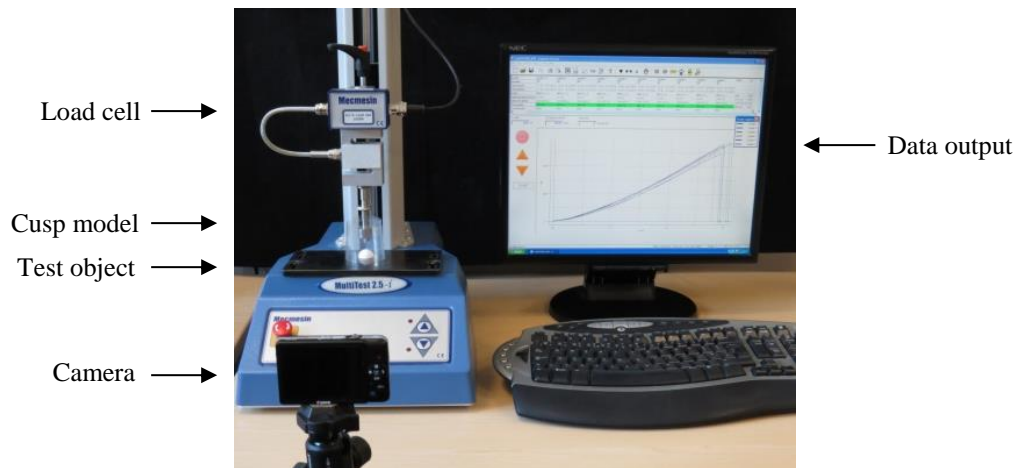


Figure 2.18 Experimental set up for compression tests. Cusp models were fixed to a universal testing machine with the test object situated beneath. Data during the tests was collected using computer software and videos were recorded throughout each test.

2.2.3.1. Alignment of domes

To improve the reliability between repeats and between the difference cusp models, an alignment process was devised to help place the dome in the same position for each test. In SolidWorks 2014 (Dassault Systèmes SolidWorks Corp.) a dome was created of the exact same dimensions as the ones used in this study but with the added design of a M6 internal thread at the centre (Figure 2.19).

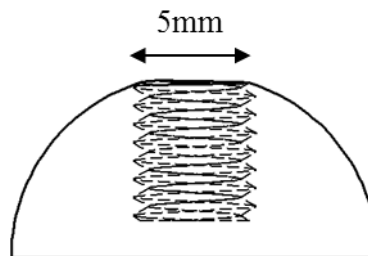


Figure 2.19 Design of alignment dome. A 5mm hole was extruded at the centre where a M6 internal thread was designed by cutting a 60° triangular ridge (height=0.87mm, pitch=1) along a spiral.

This alignment dome was then 3D printed and screwed directly onto the crosshead of the universal testing machine, and lowered until in contact with the platform. At this point a circle was drawn around the circumference of the dome in order to mark where the dome should be placed for each test (Figure 2.20).

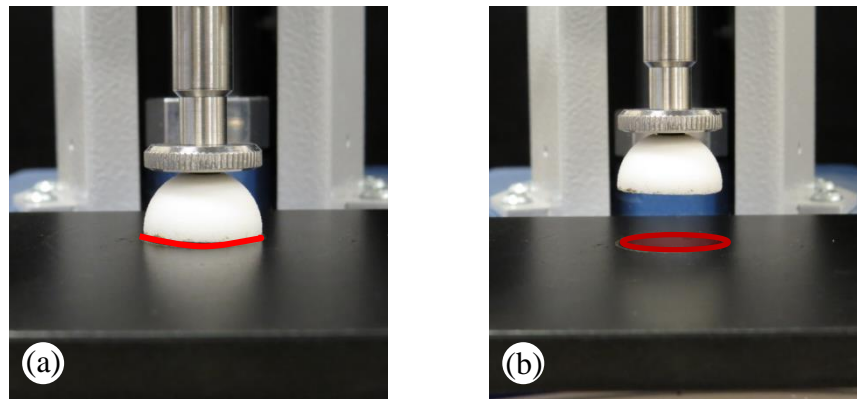


Figure 2.20 Alignment of test objects; a dome was attached to the universal testing machine and lowered until touching the platform (a) where an outline was then drawn to mark the position of the dome for each test (b).

2.2.3.2. Test program

The machine was controlled by a test program in the software Emperor (version 1.18-408). In the first stage of the program the dental models were lowered until touching the tip of the dome, which was indicated by a detection of 1N of force. At this point the displacement level was set to zero (home position) and the models were driven through the test object at a low displacement rate of 5 mm/min. This particular velocity was chosen as Lucas et al.(1994) observed that orangutans tend to apply static loading when biting hard food items, which has led to researchers using the low controlled speed of 5mm/min when physically testing the effect of tooth shape on hard food object breakdown (Lucas et al., 1994, Berthaume et al., 2010). Each test was terminated automatically after failure using a percentage break command where a percentage drop in force signalled the machine to stop compression and the cusp model was returned to the home position at the same slow displacement rate. The percentage used to stop the machine needed to be chosen carefully as a too low percentage may stop the machine prematurely due to small fluctuations in force, and if too high the machine may continue compressing after failure had occurred. Due to the differences in fracture behaviour between solid and hollow models it was necessary to compose two different programs that varied in percentage break. For the solid domes a percentage break of 10% was used. However this was found to be too low to capture fracture in hollow models. Therefore a 70% drop in force was used for the hollow models in order to filter through minor fractures prior to failure. Scripts of both test programs are included in appendix A p. 229.

2.2.3.3. Measurement of force, energy, duration and contact surface area

Data on force, displacement and time was automatically recorded throughout each test at a sampling rate of 500 Hz in the Emperor software (version 1.18-408). From this, estimates on force, energy and duration at various aspects of food breakdown can be made.

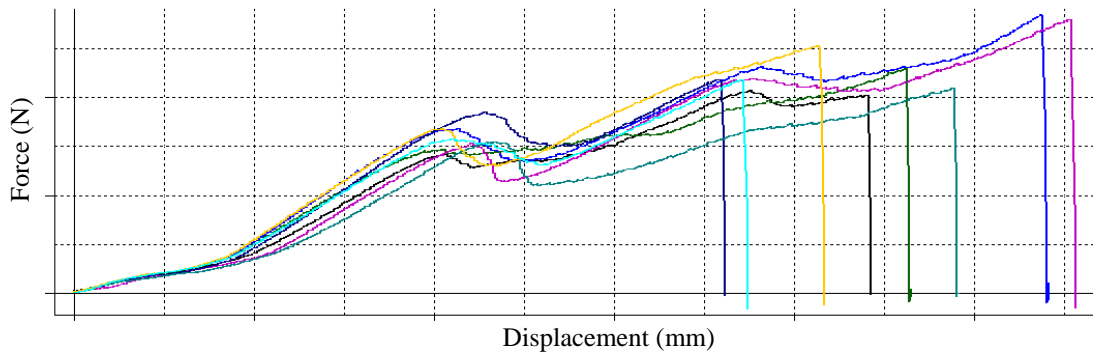


Figure 2.21 Pattern of hollow dome breakdown using model C120 as an example. 8 repeats displayed.

For the breakdown of hollow domes it was noticed that one or more fractures often occurred prior to failure (Figure 2.21). Therefore it was decided to take measurements from two places of the graph; the highest force to initiate fracture (first peak in graph) and the maximum force to break the object, which was often associated with the point at breakage (ultimate failure). At both of these points, data was recorded on force, displacement and time. Energy was then calculated in the software Emperor (version 1.18-408) as the area under the graph for both initial fracture and peak force based on the force and displacement values (Figure 2.22).

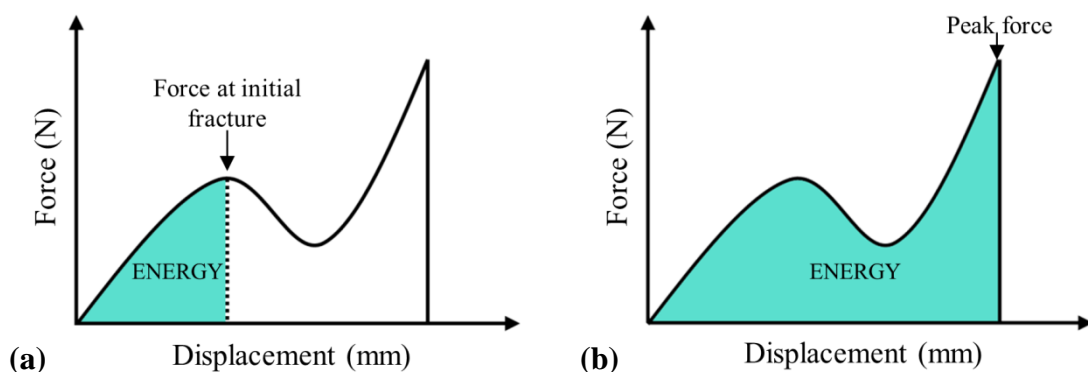


Figure 2.22 Energy measurements for hollow dome breakdown. Energy was calculated as the area under the graph at (a) maximum force at initial fracture and (b) peak force (maximum) recorded before complete failure (breaking point).

In contrast to the hollow domes, the solid domes produced force-deformation curves with single peaks, which corresponded with both initial fracture and the occurrence of mechanical failure of the object (Figure 2.23).

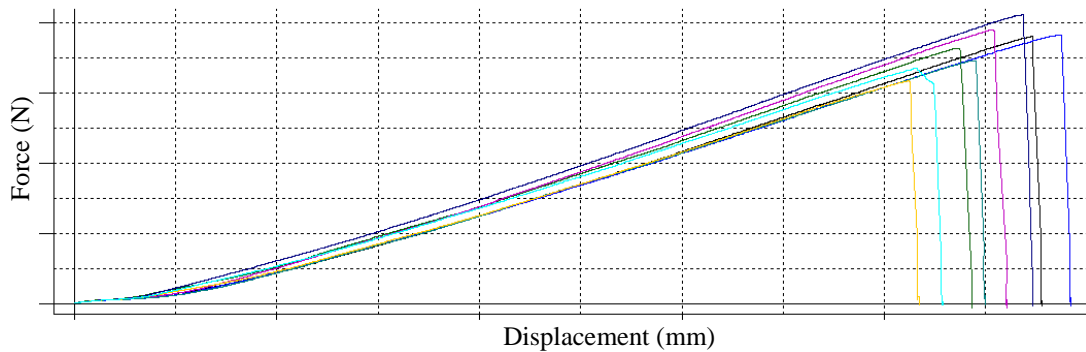


Figure 2.23 Pattern of solid dome breakdown using model C120 as an example. 8 repeats displayed.

Therefore for the solid hard objects measurements on force, displacement and time were taken at this single peak at the point of maximum force. Energy was therefore also calculated as the area under the force/displacement plot at peak force (Figure 2.24).

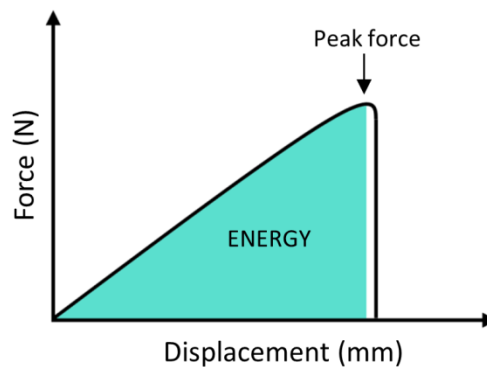


Figure 2.24 Energy measurement for solid food breakdown. Energy was calculated as the area under the graph at peak force.

For both hollow and solid hard objects the surface area of contact was also calculated at the point of initial fracture and/or peak force by using the displacement levels to crop the 3D dental models in SolidWorks 2014 (Dassault Systèmes SolidWorks Corp.) and re-estimating surface area.

2.2.3.4. Measurement of fragmentation

Ideally when relating food breakdown to digestive efficiency, the variable of most interest is surface area i.e. the amount of new surface area exposed after breakage. However in practise this is very difficult to measure due to the irregular geometries of the fragments. That being the case, an alternative solution is to infer the extent of new

surface area created for digestion by using a sieving method to measure the fragmentation. Previously, sieving methods have commonly been used in clinical dental research to quantify the masticatory performance of living human subjects (Edlund and Lamm, 1980, Olthoff et al., 1984, Lucas et al., 1986b, Olthoff et al., 1986, van der Bilt et al., 1987, Slagter et al., 1992, Peyron et al., 2004). Typically the participants are asked to chew a pre-weighed food item, which is then removed from the oral cavity and passed through a stack of sieves of decreasing aperture. The particles retained in each sieve fraction are then weighed individually to assess the degree of food breakdown. Based on this research, it was decided to take a similar sieving approach.

Each dome was weighed prior to compression using Ohaus balances, which had a readability of 0.001g. After each test, the platform of the universal testing machine was detached and the fragments removed and weighed to monitor any weight changes throughout the process. The fragments were then tipped into a stack of 10 Endacott sieves where the mesh diameters ranged from 14mm to 0.63mm (Figure 2.25). Any fragments less than 0.63mm were captured in the base container at the bottom of the sieve. The sieve stack was gently shaken manually to distribute the particles based on volume. Each sieve was then removed and the fragments (if present) were photographed and weighed. A final weigh of all the fragments was made to compare to the individual weights added up. This was carried out as it was noticed that some fragments were so small and few in number that the weight was beyond the sensitivity of the scales. Furthermore some fragments would unavoidably be lost due to the procedure. Therefore any change in weight was documented.

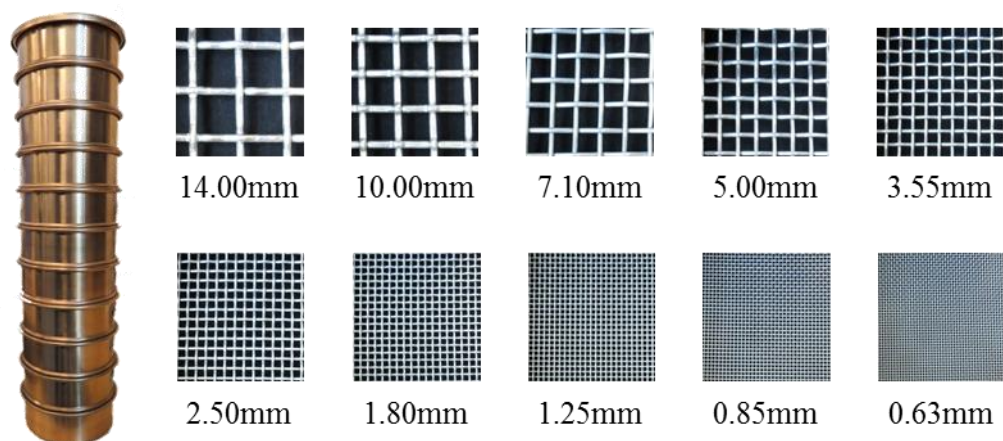


Figure 2.25 Sieve stack and meshes contained within. Mesh images taken at the same scale.

In order to compare overall fragmentation performance it was decided to reduce the data to a single value by using a Fragmentation Index (FI) developed by Edlund and Lamm

(1980). The data was divided into 3 categories based on mesh dimension. These followed as course (particles $\geq 10 \times 10 \text{mm}$), medium (particles $\geq 7.10 \times 7.10 \text{mm}$, $< 10 \times 10 \text{mm}$) and fine (particles $< 7.10 \text{mm}$), (See Figure 2.26).



Figure 2.26 Examples of fragments for each size category. Images from E120 test runs.

A formula was then used to calculate fragmentation index, which provided a single value to define the distribution of material across the three size categories based on weight. For this formula the following definitions were used:

x = weight (g) of material in coarsest category.

y = weight (g) of material in the medium category.

$T-x-y$ = weight (g) of material in the finest category, where T = total weight of sample.

Based on these variables, a Fragmentation Index was calculated using equation 2.4 where a number is produced between 0 and 1. Numbers close to or equal to 0 indicate poor fragmentation performance (low quantity, large pieces) whereas numbers equal to or close to 1 correspond to the best fragmentation performance (high quantity, small pieces).

$$\text{Fragmentation Index} = 1 - \frac{(x + y)}{(2T - X)}$$

(2.4)

The Fragmentation Index operates based on the following criteria:

1. FI=1 when $x=y=0$ (all particles are fine);
2. FI=0 when $x=T$ (no fragmentation);
3. FI decreases with y when x is constant;
4. FI decreases with x when y is constant;
5. FI decreases with x when $x+y$ is constant.

2.2.3.5. Repeatability of experimental design

Numerous factors are involved throughout the experimental procedure, which may compromise the repeatability of the results. These include factors such as the manufacture of the 3D printed domes, post processing of the domes in the vacuum oven and small deviations in the alignment of the domes. Although it is difficult to isolate all of these variables, a series of tests were made to gauge the reproducibility of the overall experimental design. To investigate inter- and intraobserver reliability, two batches of solid domes were made by two different researchers. Batch A was made by researcher 1 on day 1 and batch B was made by researcher 2 (the author, KS) on day 2. For each batch, both the observers independently fractured a sample of 10 domes using the C60 cusp model. Tests were conducted on the same day using the same experimental procedure presented in this chapter. Maximum force to break the domes was then used to assess reliability using a one-way ANOVA where significant differences were accepted when $p > 0.01$. For batch A, 10 repeats were useable for the study. However for batch B smaller sample sizes were used where 4 repeats was excluded for researcher 1 and 1 repeat for researcher 2. These repeats were excluded as a large amount of chipping occurred without brittle failure, which was generally associated with the cusp tip being maligned.

In terms of interobserver reliability we found no significant differences between the mean peak force at failure and different observers for batch A ($n=10,10$, $F_{1,18}=0.4585$, $p=0.5069$) and batch B ($n=6,9$, $F_{1,13}=4.921$, $p=0.04496$). In terms of intraobserver reliability we found no significant differences between the mean peak force at failure and the different batches for both researcher 1 ($n=10,6$, $F_{1,14}=5.911$, $p=0.02908$) and researcher 2 ($n=10,9$, $F_{1,17}=0.2468$, $p=0.6257$). A further test was made to see if the same batch of domes could be used over a period of a week. This was tested to see whether the time of the domes left in the desiccator since being dried in the vacuum oven affect the physical properties and thus the reliability of using them over several days. Therefore an extra set of repeats of batch B were made by researcher 2 but were conducted 7 days after being dried. We found no significant differences between the peak force at failure for the domes used on day 1 and for those used on day 7 ($n=9,10$, $F_{1,17}=1.329$, $p=0.2649$). It was therefore concluded that the methodology could be confidently reproduced by a different observer and also within an observer on different days. The results also indicate that the domes of the same batch could be used over a 7 day period. However, while no significant differences were found, the variation in

results were considerable between certain repeats, which should be kept in mind when examining the data collected to infer tooth performance.

Table 2.5 Results of peak force (N) recorded to break solid domes using C60 cusp tip to examine inter- and intraobserver reliability.

	Researcher 1		Researcher 2		
	Batch A	Batch B	Batch A	Batch B	Batch B (7 days)
1	657.9	850.9	724.7	808.3	683.2
2	782.2	781.1	596.3	576.1	576.5
3	807.9	800.9	905.4	821.0	545.5
4	766.1	746.7	688.8	724.7	743.0
5	642.5	892.3	608.2	631.3	539.5
6	647.4	703.0	687.4	744.1	727.7
7	779.2	-	781.4	645.5	598.9
8	561.9	-	648.1	740.0	715.0
9	620.1	-	851.3	646.3	704.9
10	709.0	-	763.1	-	759.4
Avg.	694.4	795.8	725.5	704.2	659.3
Std. dev.	83.2	68.7	101.1	83.9	85.2

2.2.3.6. Data analysis

For data collection, a total of 10 repeats were made for each cusp model. The results for each optimality criterion (force, energy, duration, fragmentation) and surface area were displayed in box plots where the dashes within the box indicate the median, the box itself bounds the second and third quartiles, the whiskers indicate the maximum quartile ranges and the circles indicate any outlying data points. Results were subjected to statistical analysis using one-way analysis of variance (ANOVA) in the statistical package Past 2.14 (Hammer et al., 2001). If significant differences were found ($p < 0.001$) then a post hoc Tukeys test was performed for pairwise comparison where relevant. For analyses where variances were unequal then an unequal variance version of ANOVA was used (Welch F test). To examine whether some cusps are better than others for optimising for multiple performance indicators, the averages for each optimality criterion were plotted against force.

2.3. Results

The following results are divided into two main sections; hollow hard object breakdown (section 2.3.1 p. 78) and solid hard object breakdown (section 2.3.2 p. 99). For each section, a brief description on the mode of fracture is presented followed by the results for each optimisation criterion; force, energy, duration and, in the case of solid domes, fragmentation. To facilitate the interpretation of the data, results on surface area and displacement diagrams are also included. Bivariate plots are provided to examine overall cusp optimality. Averages and standard deviations for all tests are included in appendix A along with written and photographic descriptions.

2.3.1. Hollow hard object breakdown: mechanical performance indicators

The following results examine the mechanical performance of cusps to fracture hollow hard objects in relation to food access, where a structure such as a shell or endocarp, must be broken to extract the food within. In terms of mode of fracture, overall differences were observed between the different cusp models. The sharpest model, B60 experienced the greatest amount of plastic deformation where the cusp was observed to puncture the shell without propagating cracks (Figure 2.27a). However, for the majority of cusp models the hollow domes broke into two or more pieces via indentation (Figure 2.27b). Cracks were typically observed to initiate at the point of contact with each cusp from the inside of the dome and propagate outwards dividing the object into 2 or more pieces. For the bluntest models, cracks were initiated on the inner surface of the model and propagated outwards. In this case the hollow domes were compressed and multiple cracks propagated at the sides of the dome (Figure 2.27c).

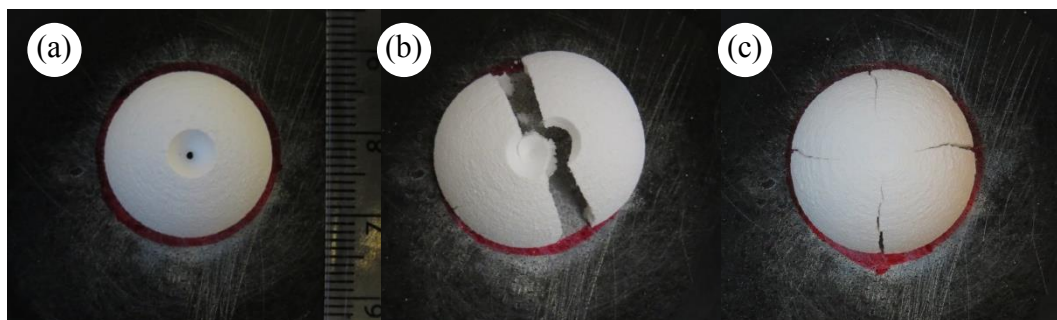


Figure 2.27 Examples of the fracture patterns observed during hollow hard object breakdown when compressed by a variety of different cusp forms; (a) B60, (b) B90, (c) E120.

As previously mentioned, the hollow domes exhibit multiple fractures prior to failure when indented by a cusp model. Therefore the results for the mechanical performance indicators were recorded at both the point of initial fracture (first peak in

force/displacement plot), which will be presented first, followed by the results at peak force (breakage). As the majority of the hollow domes did not break for the B60 cusp, this particular model has a smaller sample (N=3) for the results at peak force.

2.3.1.1. Force recorded at initial fracture (hollow object)

A clear relationship exists between cusp form and force required to initiate fracture in hollow hard food items. For cusps of the same blunting distance (B, C, D, E), those with larger angles were shown to increase the force required at initial fracture (Figure 2.28a). Significant differences were found between the angles for each of the groups ($p < 0.001$). However, the results between the 90° and 120° models of the E group were found to be very similar and based on pairwise comparison, were not significantly different to one another ($p = 0.7827$). When comparing cusps of the same angle (60° , 90° , 120°), increasing bluntness was shown to increase with the force required at initial fracture (Figure 2.28b). Significant differences were found between the bluntness values for all the groups ($p < 0.001$). However the 120° group diverged from the general trend of increasing force with increasing bluntness as E120 recorded a drop in the force required at initial fracture in comparison to the sharper model, D120, and is found to not be significantly different to C120 ($p = 0.9993$). However overall it can be concluded that independently, both an increase in angle and bluntness elevates the forces necessary to induce fracture.

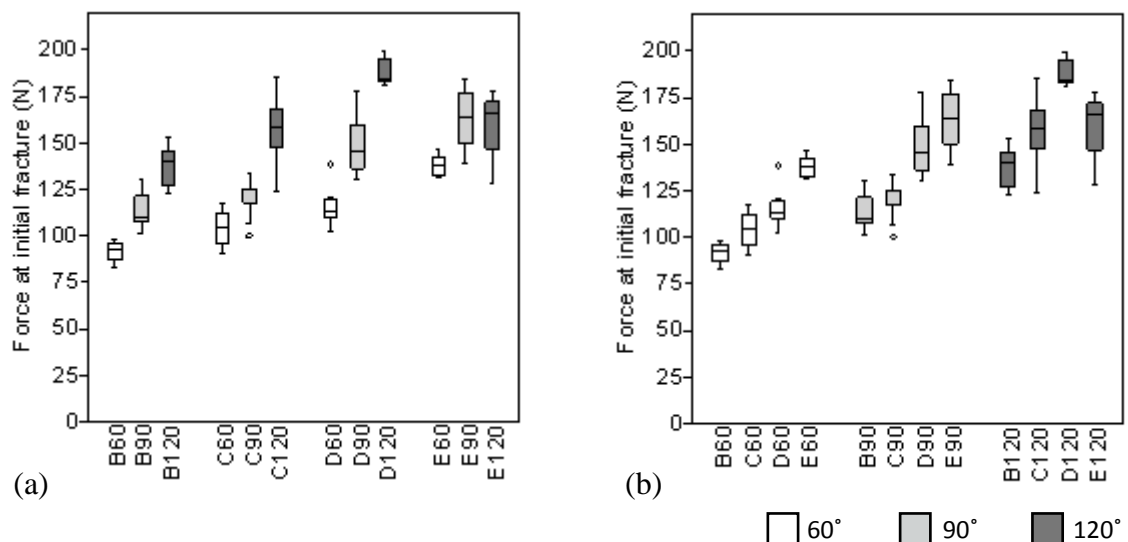


Figure 2.28 Boxplots illustrating the effect of angle (a) and bluntness (b) on the force required to initiate fracture in hollow hard objects.

When considering both angle and bluntness together in the form of radius of curvature, the values were also shown to be significantly different (Welch F test; $F_{42,3}=116.1$,

$p=6.615E-28$). There appears to be a curvilinear trend where the force at initial fracture increases with increasing radius of curvature (Figure 2.29). However E120 ($R=18$) is a clear exception to this pattern as it shows a notable decrease in force. The best performing cusp form for this criterion was B60, which was the sharpest and acutest model of the series. This model had the lowest force at initial fracture (average 91.8N), which was approximately half the value of force required by the least efficient cusp design, D120 (average 188.2N).

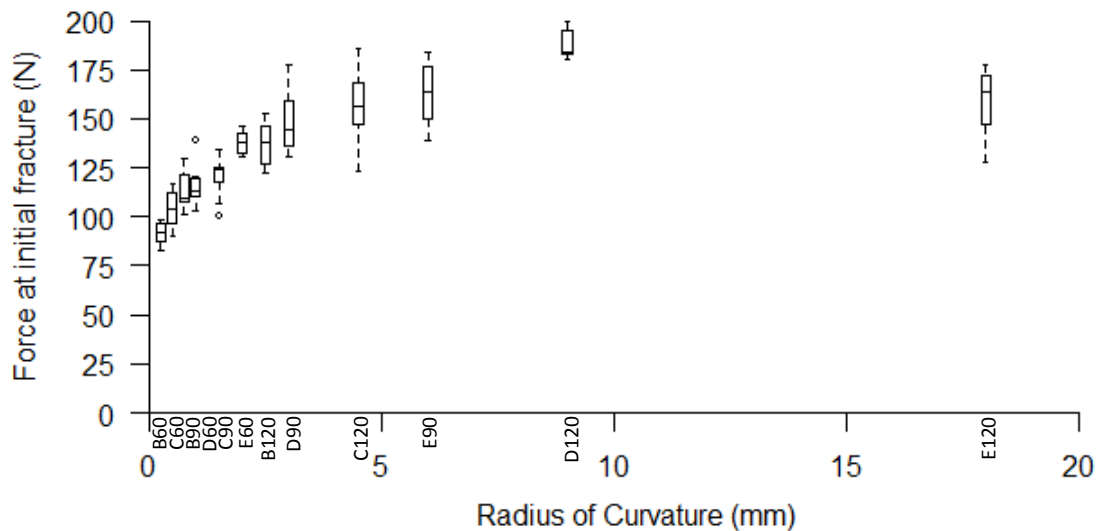


Figure 2.29 The force required to initiate fracture in hollow hard objects in relation to the radius of curvature of the cusp tips, a combination of both angle and bluntness values.

2.3.1.2. Energy recorded at initial fracture (hollow object)

In comparison to force, the relationship between cusp form and energy expended at initial fracture of hollow hard objects was less clear. For cusps of the same bluntness, energy expenditure did appear to increase with increasing angle for some of the groups (C, D, E). However a large amount of overlap was observed between the different angles and significant differences were only found in groups C ($F_{2, 27}=10.96$, $p=0.000328$) and D ($F_{2, 27}=37.48$, $p=1.621E-08$) (Figure 2.30a). For cusps of the same angle there was again no clear trend in energy values but significant differences were found in groups 90° and 120° cusps ($p<0.001$) (Figure 2.30b).

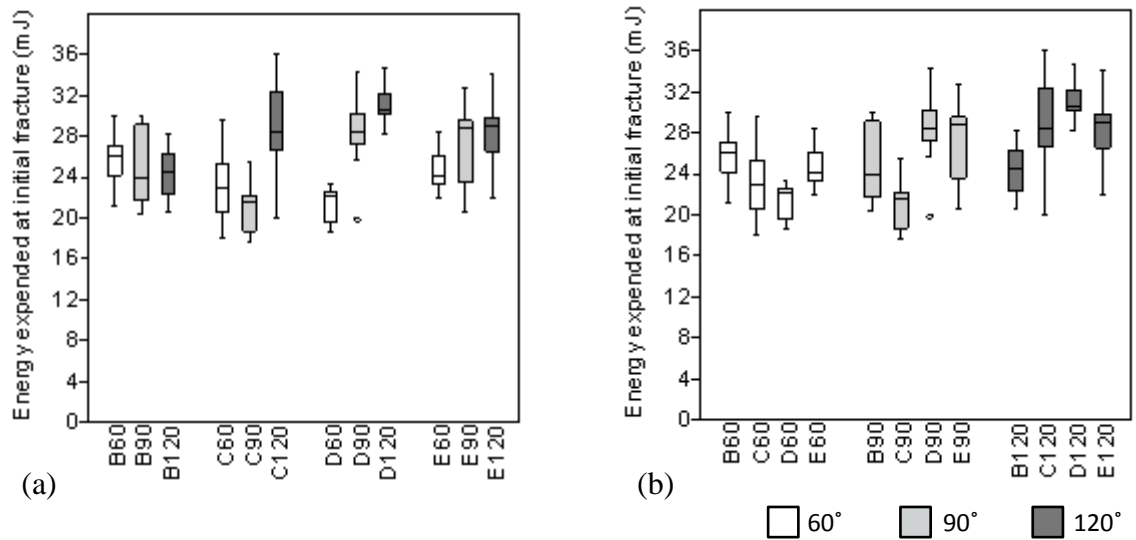


Figure 2.30 Boxplots illustrating the effect of angle (a) and bluntness (b) on the energy expended at initial fracture in hollow hard objects.

Significant differences were found between the cusps of varying radius of curvature based on energy at initial fracture ($F_{11,108}=9.368$, $p=1.256E-11$). Generally, the energy values were higher in the cusps with a greater R value although there does not appear to be a clear pattern of trend (Figure 2.31).

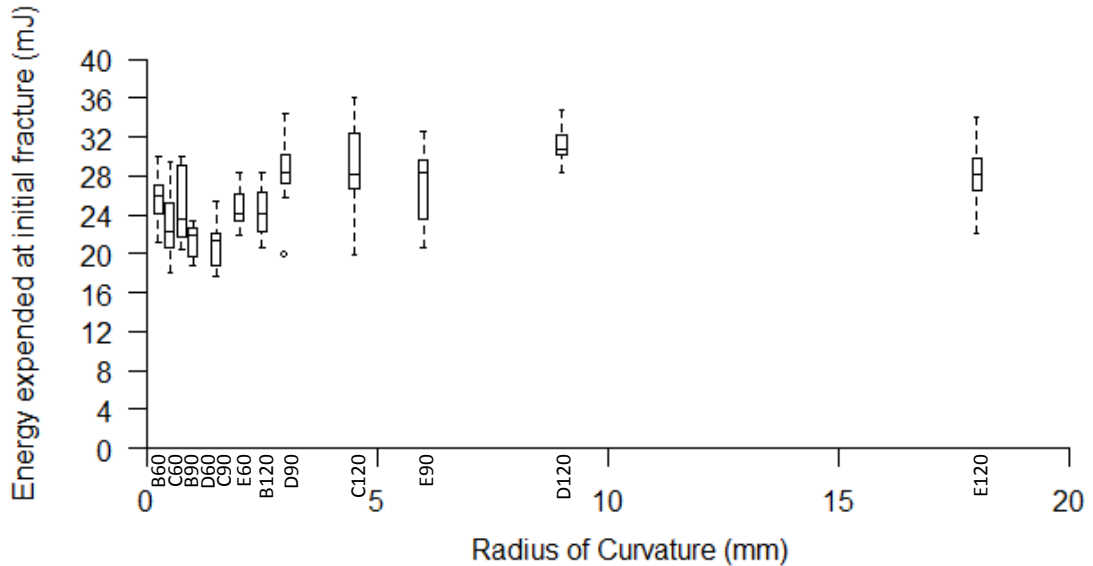


Figure 2.31 Energy expended at initial fracture of hollow hard objects in relation to the radius of curvature of the cusp tips, a combination of both angle and bluntness values.

2.3.1.3. Duration recorded at initial fracture (hollow object)

The results indicate that cusp form may have some effect on the duration of time before initial fracture of hollow domes occurs but it is not clear for all the groups. For cusps of the same bluntness, time at initial fracture was shown to clearly decrease with

increasing angle for group B and decrease in time between 60° and 120° cusps for group C (Figure 2.32a). Significant differences were found in group B ($F_{2,27}=53.17$, $p=4.329E-10$) but not in the remaining other groups ($p>0.001$) where a large amount of overlap in time values was observed, particularly for groups D and E. For cusps of the same angle, time at initial fracture was shown to decrease with increasing bluntness for 60° and 90° models (Figure 2.32b). Significant differences were found for both of these groups ($p>0.001$) but not in the 120° cusps ($F_{3,36}=0.219$, $p=0.8826$). For the 120° models a low time at initial fracture appeared to be maintained despite differences in bluntness.

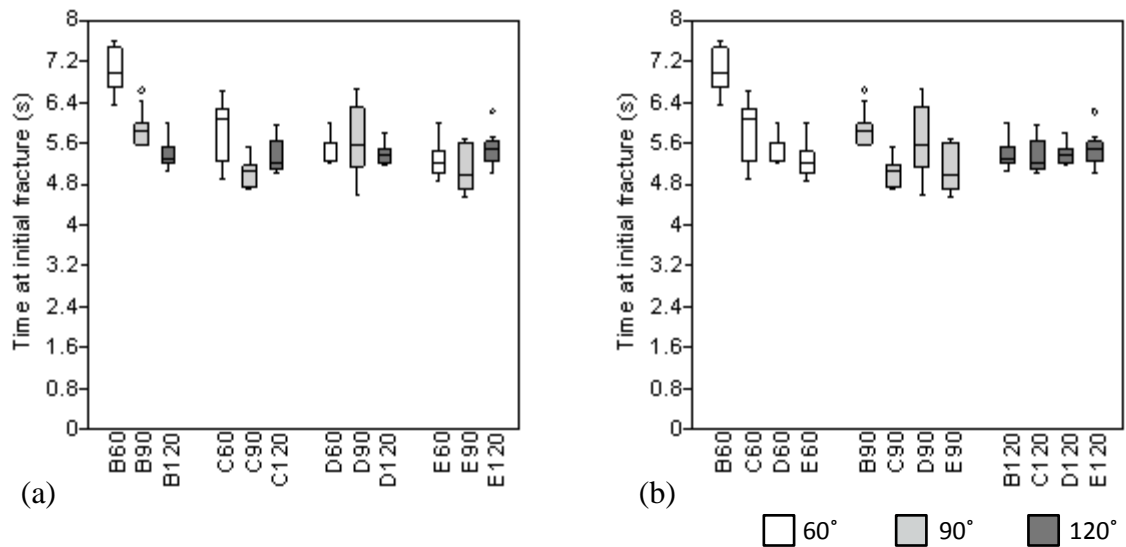


Figure 2.32 Boxplots illustrating the effect of angle (a) and bluntness (b) on time required to initiate fracture in hollow hard objects.

A clearer pattern becomes apparent when taking into account the radius of curvature (Figure 2.33). Significant differences were found between models of different radius of curvature (Welch F test: $F=16.11_{42,42}$, $p=8.781E-12$). Time at initial fracture rapidly decreased for the first 4 models with the smallest R values (B60, C60, B90, D60) and appeared to plateau for the remaining blunter models, which, based on Tukey's pairwise comparison were found not to be significantly different between one another ($p>0.001$). Overall the sharper cusps with the lowest radius of curvature were least efficient in terms of time to initiate fracture in hollow hard objects. In contrast blunter and wider models performed the best for this optimality criterion.

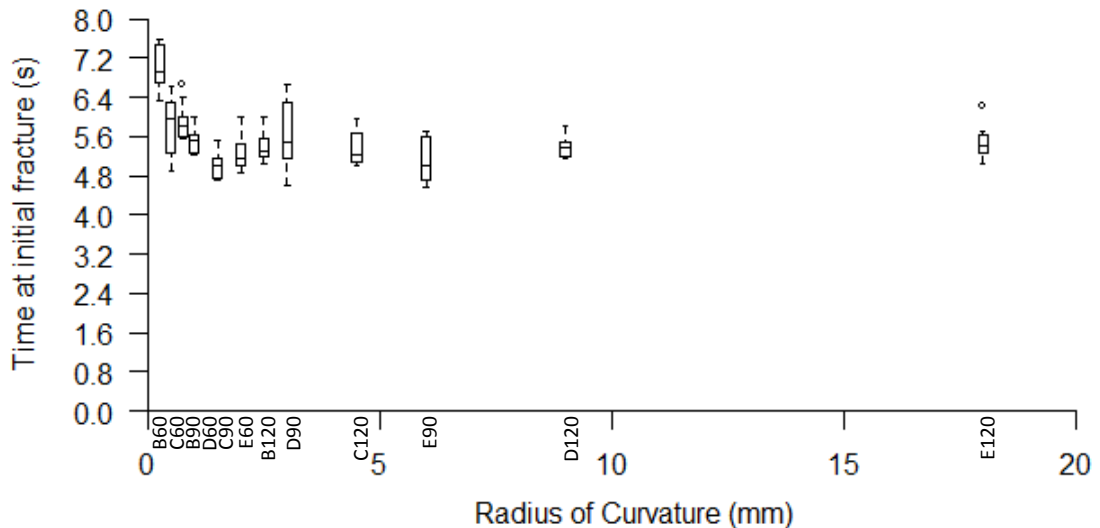


Figure 2.33 Time required to initiate fracture in hollow hard objects in relation to the radius of curvature of the cusp tips, a combination of both angle and bluntness values.

2.3.1.4. Surface area recorded at initial fracture (hollow object)

A clear relationship exists between cusp form and surface area of the tip in contact with the dome at initial fracture in hollow hard objects. For cusps of the same bluntness, surface area at initial fracture is shown to increase with increasing angle (Figure 2.34a). Significant differences were found within each group of blunting distances ($p > 0.001$), and a pairwise comparison indicates that results from each cusp model were significantly different from one another ($p > 0.001$). Furthermore, it was also observed that the variability between results appeared to increase with increasing angle. For cusps of the same angle, the surface area at initial fracture was also shown to increase with increasing blunting distance (Figure 2.34b). Significant differences were found within each group ($p > 0.001$) and for the 120° group, the results for each cusp model was significantly different to one another. The same was true for the 60° and 90° group but not between the B and C cusp models, the sharpest models in the blunting series. Similar to the effect of angle, it was also observed that the variability between the repeats increased with increasing bluntness.

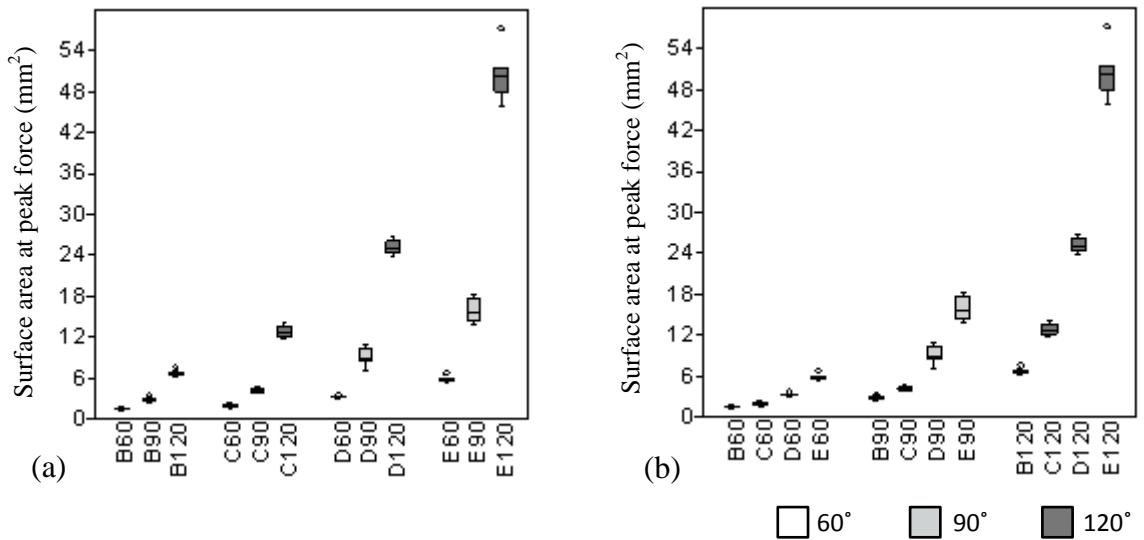


Figure 2.34 Boxplots illustrating the effect of angle (a) and bluntness (b) on the surface area of the cusp in contact with the dome at initial fracture of hollow hard objects.

When considering all the cusp models together in the form of radius of curvature, significant differences were also found between groups (Welch F test: $F_{41,96}=918.6$, $p=2.863E-46$). The results demonstrate that a positive linear relationship exists between surface area on contact with the dome at initial fracture and radius of curvature (Figure 2.35).

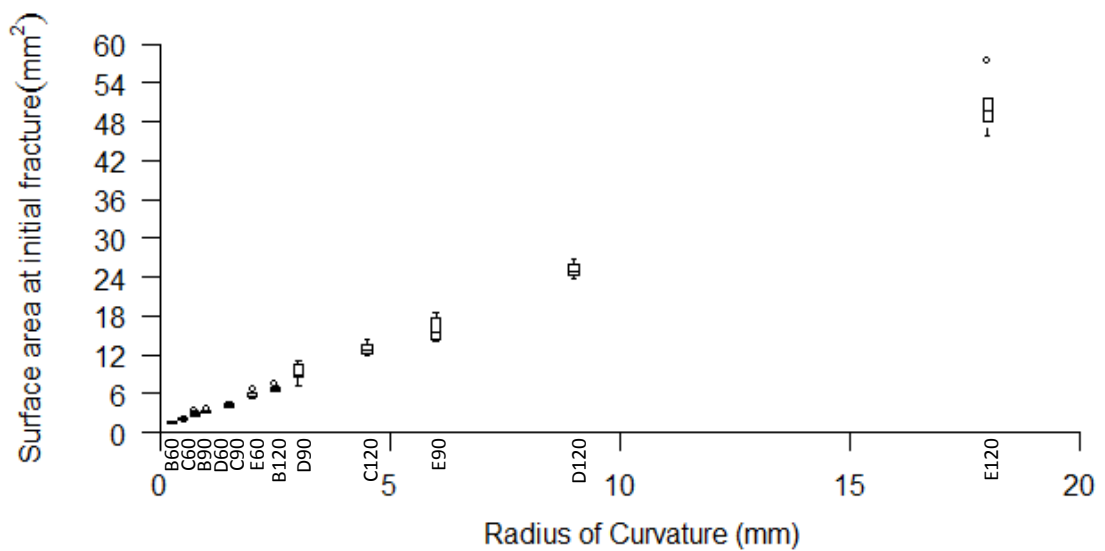


Figure 2.35 Surface area of the cusp tip at the initial fracture of hollow hard objects in relation to the radius of curvature of the cusp tips, a combination of both angle and bluntness values.

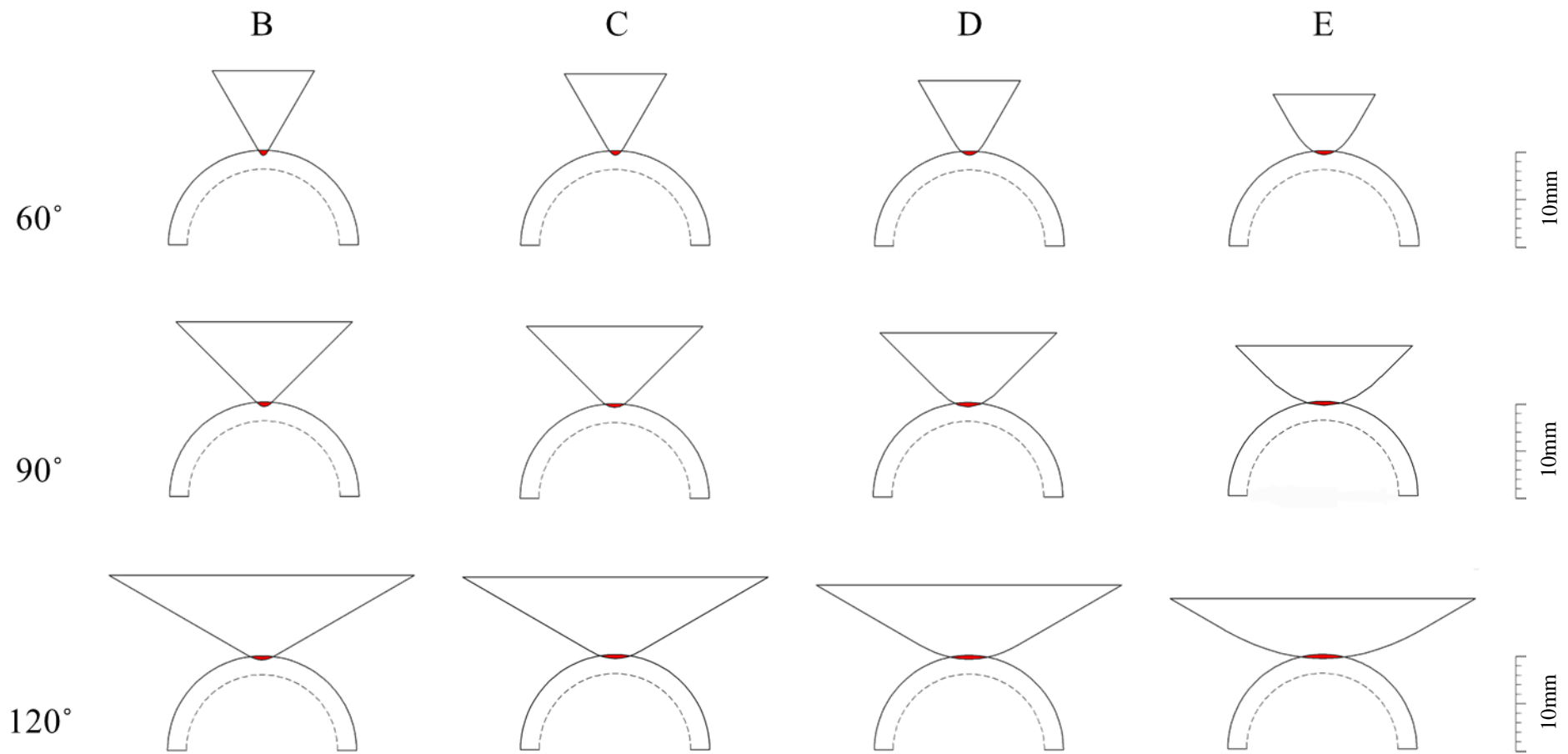


Figure 2.36 Schematic representation of the average level of displacement of each cusp model into the hollow dome at the point of initial fracture (the red area represents the surface area in contact with the dome).

2.3.1.5. Bivariate plots of mechanical indicators at initial fracture (hollow)

When initiating fracture in a hollow hard object, cusp models considered most optimal were those that required a low amount of time and energy relative to a low force. The best performers in terms of both energy and force were the cusp models with a low R values with models C60 and D60 performing especially well (Figure 2.37). It is difficult to distinguish which is the best as although C60 required a lower force, it was higher in energy than D60. The D120 model was singled out as the least optimal in the series which required the highest values for both energy and force.

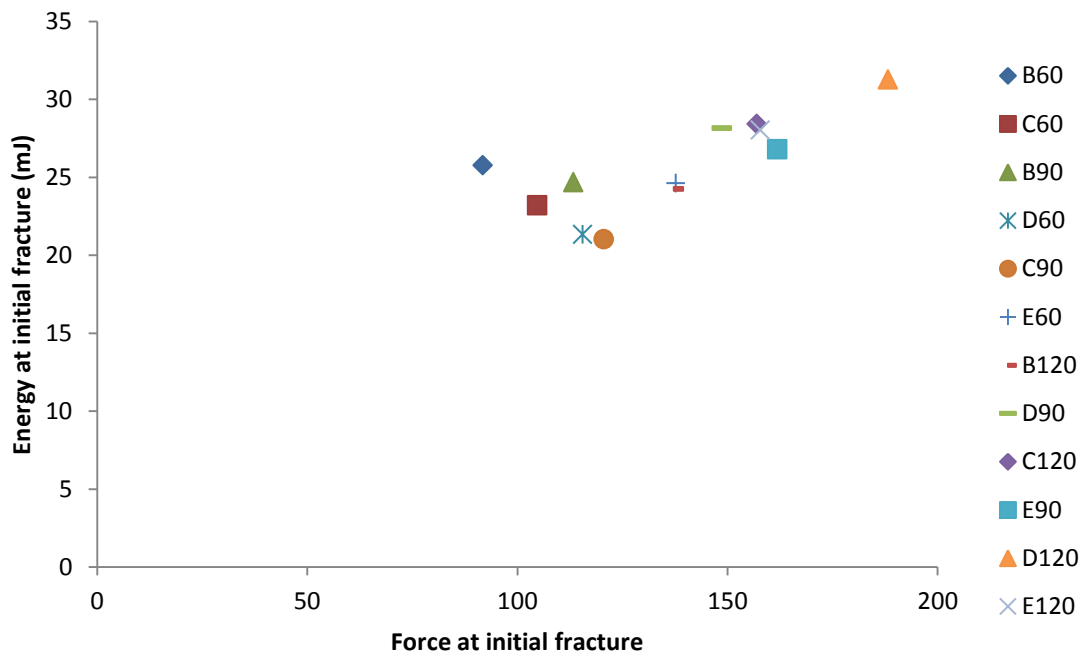


Figure 2.37 Bivariate plot of mean force and energy to initiate fracture in a hollow hard object for each cusp design. Note: cusp names in the legend are in order of increasing radius of curvature with B60 having the lowest R value and E120 the highest.

When optimising for both time and force to initiate fracture, the best performing models consisted of some of the sharper cusps, which were C60, D60 and C90 (Figure 2.38). However, a low radius of curvature value may not necessarily indicate optimality as the sharpest cusp in the series (B60), although was most optimal for force, took the longest time to initiate fracture. Once the degree of sharpness dropped to a certain level, the time values were observed to be very similar. It therefore appears that to optimise for both time and force to initiate fracture in hollow hard objects, a moderately sharp cusp would be most beneficial.

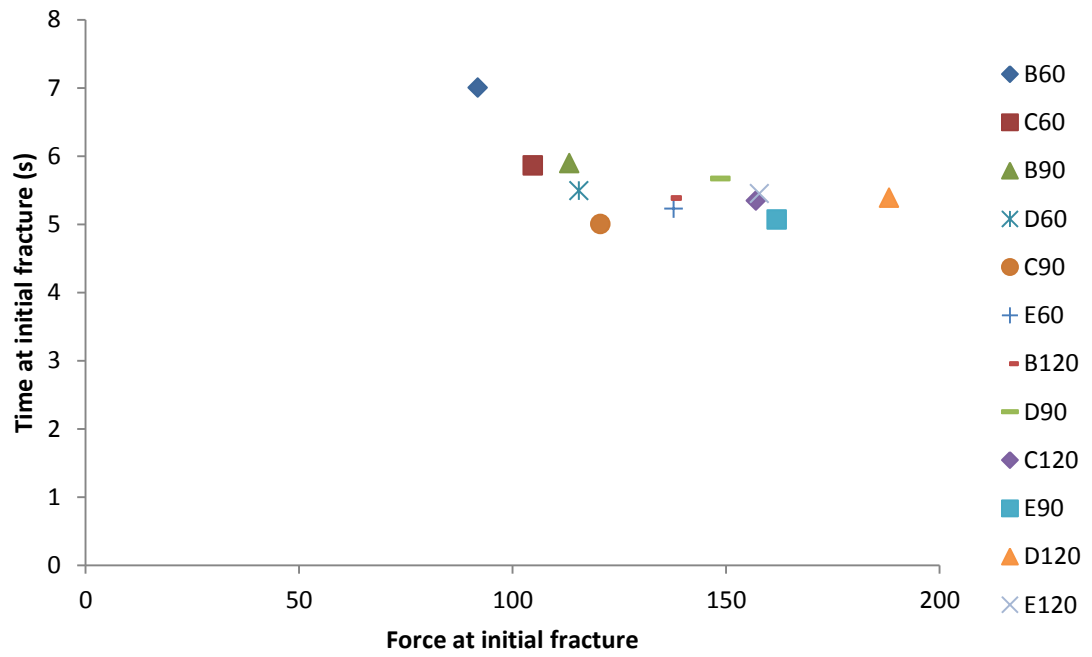


Figure 2.38 Bivariate plot of mean force and time to initiate fracture in a hollow hard object for each cusp design. Note: cusp names in the legend are in order of increasing radius of curvature with B60 having the lowest R value and E120 the highest.

2.3.1.6. Force recorded at breakage point (hollow)

In contrast to the force required to initiate fracture, the relationship between cusp morphology and maximum force at failure is less clear. For cusps of the same bluntness, there was no significant difference between angles for each group ($p < 0.001$) (Figure 2.39a). However in groups B and D the force appears to decrease with increasing angle. Furthermore the level of variance also appears to decrease with increasing angle suggesting that wider cusps are more consistent in fracture behaviour. For cusps of the same angle, there was no significant differences between blunting distances for each group ($p < 0.001$) (Figure 2.39b), although there does appear to be a decrease in peak force across levels of increasing bluntness for 60° and 90° cusps. For both cases of angle and bluntness, the model C60 seems to deviate from any potential pattern by displaying a much lower force than expected in comparison to the other cusp models.

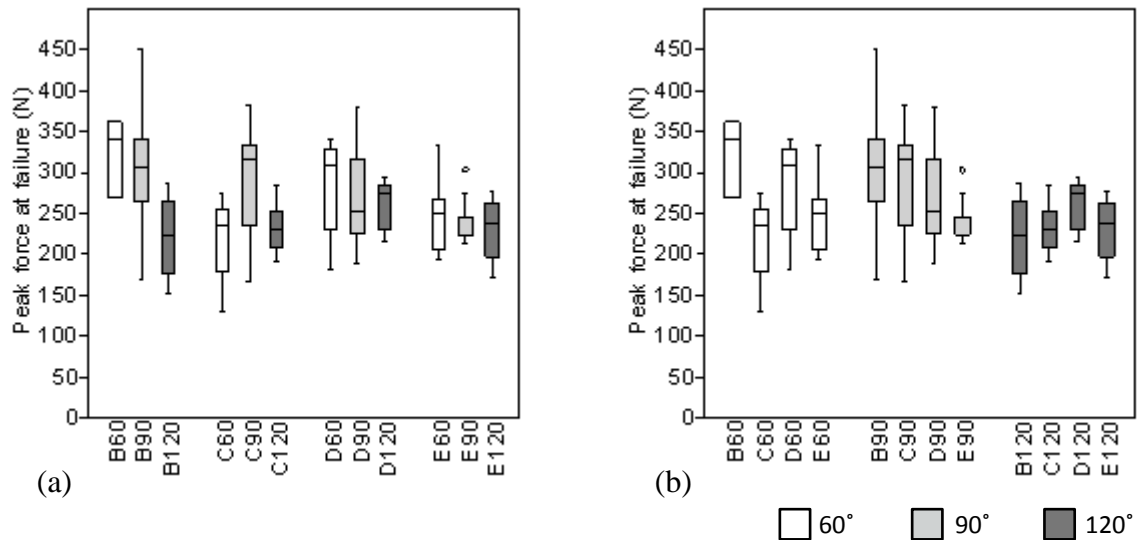


Figure 2.39 Boxplots illustrating the effect of angle (a) and bluntness (b) on the maximum force required to break the hollow hard objects.

A slightly clearer pattern is evident when accounting for radius of curvature (Figure 2.40). In this case, significant differences were not found between the groups (Welch F test; $F_{31,8}=2.661$, $p=0.01532$), however the results show a slight decrease in force with increasing radius of curvature. As radius of curvature increases, the force values appear more similar and also less variable between the repeats within each model. Again, C60 is shown to deviate from the other models. For this criterion, the blunter models appear to be more efficient as they are more likely to consistently produce a lower peak force at failure in comparison to the sharper cusps.

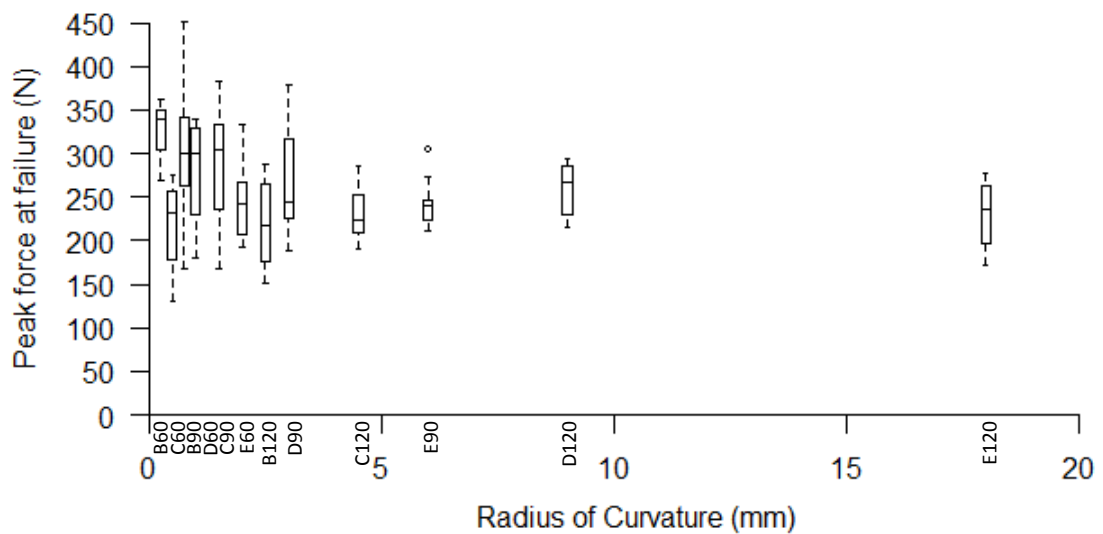


Figure 2.40 Maximum force required to break hollow hard objects in relation to the radius of curvature of the cusp tips, a combination of both angle and bluntness values.

2.3.1.7. Energy recorded at breakage point (hollow)

A clear relationship exists between cusp morphology and energy expended at peak force to break hollow hard objects. For cusps of the same bluntness, energy was shown to decrease with increasing angle (Figure 2.41). Significant differences were found between cusps of different angles for all of the bluntness groups except group E ($p<0.001$). A considerable amount of overlap was observed between C60 and C90, which was confirmed to be not significantly different in value ($p=0.9591$). Not only was energy decreasing with wider angles, it was also much more consistent. Energy at peak force was shown to decrease with increasing bluntness for cusps of the same angle (Figure 2.41b). Significant differences were found for each group of angles ($p<0.001$) except for the 120° group (Welch F test: $F_{19,41}=2.834$, $p=0.06513$). The variability was also observed to decrease with increasing bluntness, which was particularly noticeable

when comparing the first and last bluntness level in each group of angles. It was also noted that the model C60 deviated from the pattern in the 60° models by exhibiting a much lower average energy than expected in comparison to the other models.

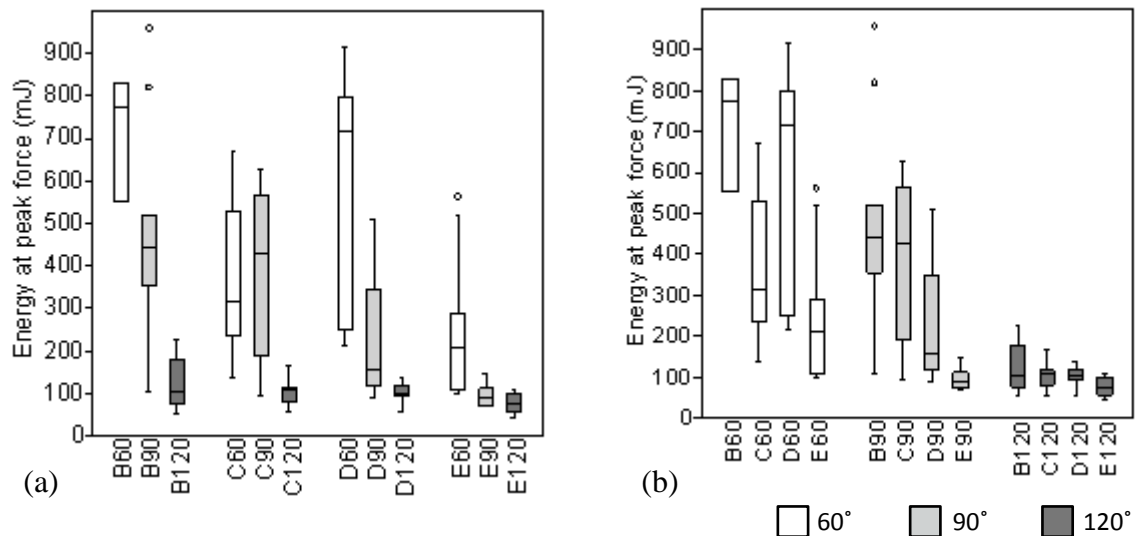


Figure 2.41 Boxplots illustrating the effect of angle (a) and bluntness (b) on the energy expended at peak force to break the hollow hard objects.

When considering all the models together in terms of radius of curvature, energy was shown to decrease with increasing radius of curvature (Figure 2.42). Models were found to be significantly different (Welch F test: $F_{31,29}=13$, $p=8.677E-09$). However two of the models (C60 and B90) deviate from the pattern by dropping in energy in comparison to the other models. Further analysis using a Tukey’s pairwise comparison also indicates that for the last 4 models (largest radius of curvature), were not significantly different ($p<0.001$) showing energy to plateau. Again the variance was also noticed to drastically narrow with increasing radius of curvature suggesting that models with a larger radius of curvature are much more consistent in terms of energy expenditure. For this optimality criterion, the least efficient cusp was the sharpest cusp B60, which used on average the greatest amount of energy to reach peak force to break hollow hard objects (717.67 mJ). In contrast the most efficient cusp was E120, which used the least amount of energy (average=76.98mJ) and was the most predictable in performance (SD=24.06).

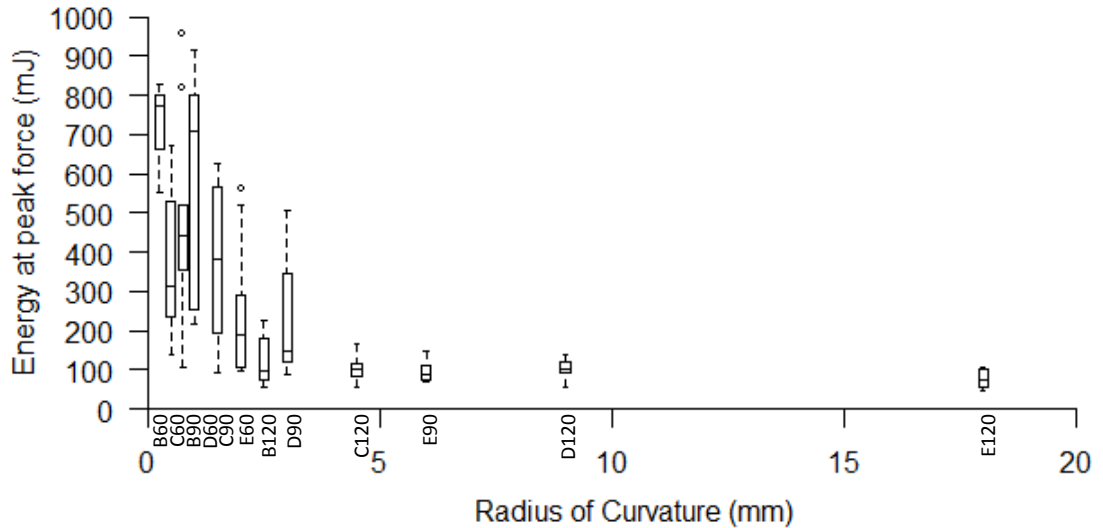


Figure 2.42 Energy expended at peak force to break hollow hard objects in relation to the radius of curvature of the cusp tips, a combination of both angle and bluntness values.

2.3.1.8. Duration recorded at breakage point (hollow)

A clear relationship exists between cusp morphology and the time it takes to reach peak force to break hollow hard objects. For cusps of the same bluntness, the time at peak force decreased with increasing angle (Figure 2.43a). Significant differences were found between the angles for each group of blunting distances ($p < 0.001$) except for group E (Welch F test: $F_{16,11} = 7.17$, $p = 0.00593$). Additionally the range within the repeats of each cusp also appears to narrow with increasing angle. For cusps of the same angle, the time at peak force was shown to decrease with increasing bluntness (Figure 2.43b). Significant differences were found between each blunting distance for all groups of angles except for the 120° models (Welch F test: $F_{19,48} = 4.623$, $p = 0.01331$). The model C60 was noted to fall out from the pattern of decreasing time with increasing bluntness and largely overlapped with D60, which were found to not be significantly different from one another ($p < 0.001$). The variance was also observed to narrow with increasing bluntness for each group of angles.

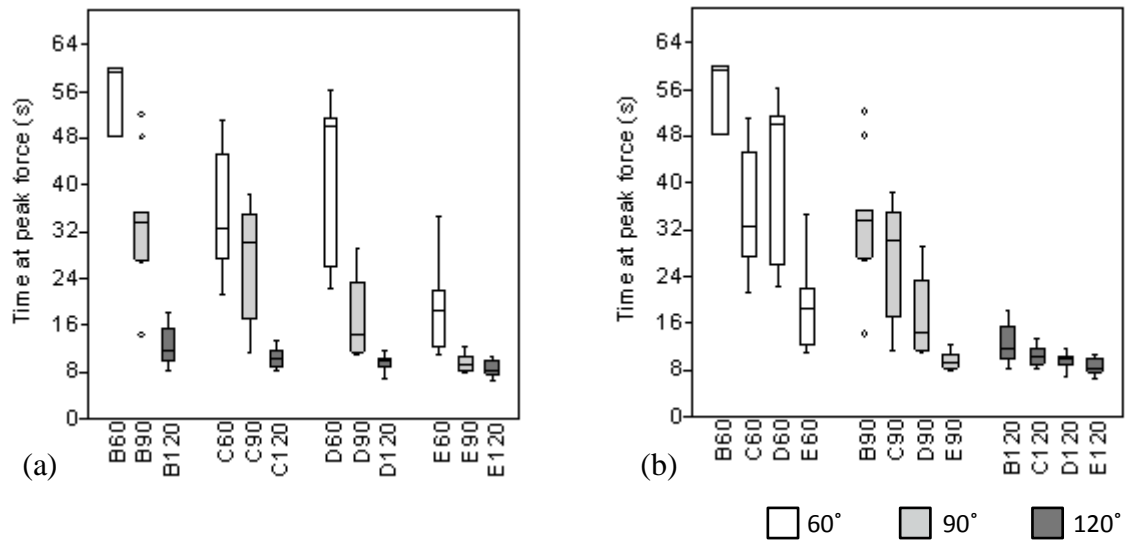


Figure 2.43 Boxplots illustrating the effect of angle (a) and bluntness (b) on the time it takes to reach peak force to break hollow hard objects.

A clear pattern existed in terms of radius of curvature where time at peak force was shown to decrease with increasing radius of curvature (Figure 2.44). Significant differences were found between the cusp radius of curvatures (Welch F test: $F_{31.33}=27.44$, $p=5.083E-13$). However C60 and B90 were found to both fall from the general pattern by showing a decrease in time in comparison to the other cusps in the sequence. The variability within repeats was also shown to narrow with increasing radius of curvature indicating that blunter cusps are much more consistent at reaching peak force in shorter period of time. The least efficient cusp was the sharpest cusp in the series B60, which took on average 55.91 seconds to reach peak force whereas the most optimal was the bluntest cusp E120, which on average took 8.64 seconds to reach peak force and was the most predictable in performance ($SD=1.40$).

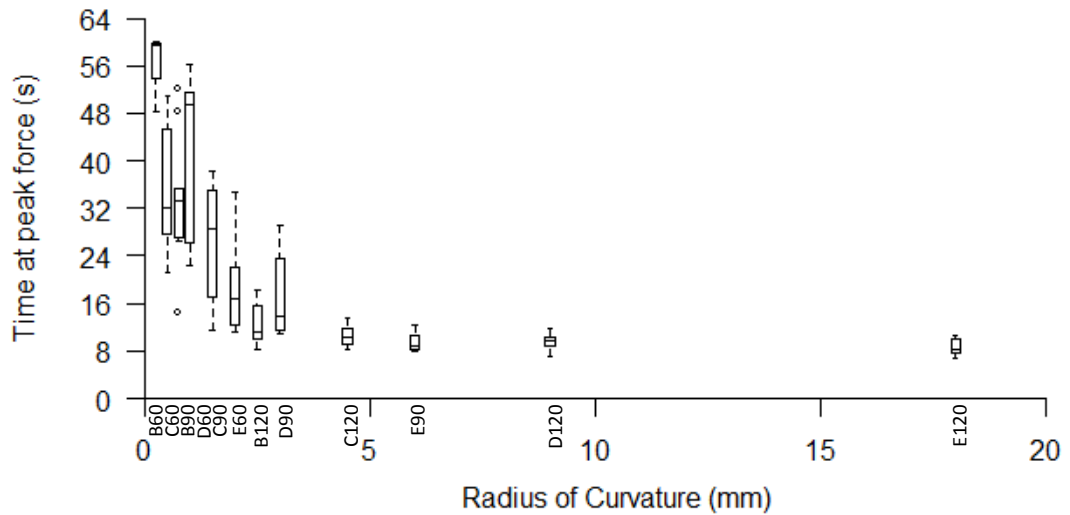


Figure 2.44 Time at peak force to break hollow hard objects in relation to the radius of curvature of the cusp tips, a combination of both angle and bluntness values.

2.3.1.9. Surface area recorded at breakage point (hollow)

Interestingly in comparison to the results at initial fracture, there does not appear to be a clear relationship between cusp form and the surface area of the cusp in contact with the dome at the point of the hollow hard objects breaking. For cusps of the same blunting distance there was not a consistent pattern between angle and surface area at peak force (Figure 2.45a). Furthermore, significant differences were only found between models in the E group (Welch F test; $F_{14.81}=58.09$, $p=9.79E-08$) where surface area appears to increase with angle. For cusps of the same angle, there again does not seem to be a consistent pattern or trend across the different levels of bluntness and the surface area at peak force (Figure 2.45b). Significant differences were only found for the 120° group (Welch F test; $F_{19.29}=56.26$, $p=1.001E-09$), where the surface area at peak force was shown to increase with bluntness.

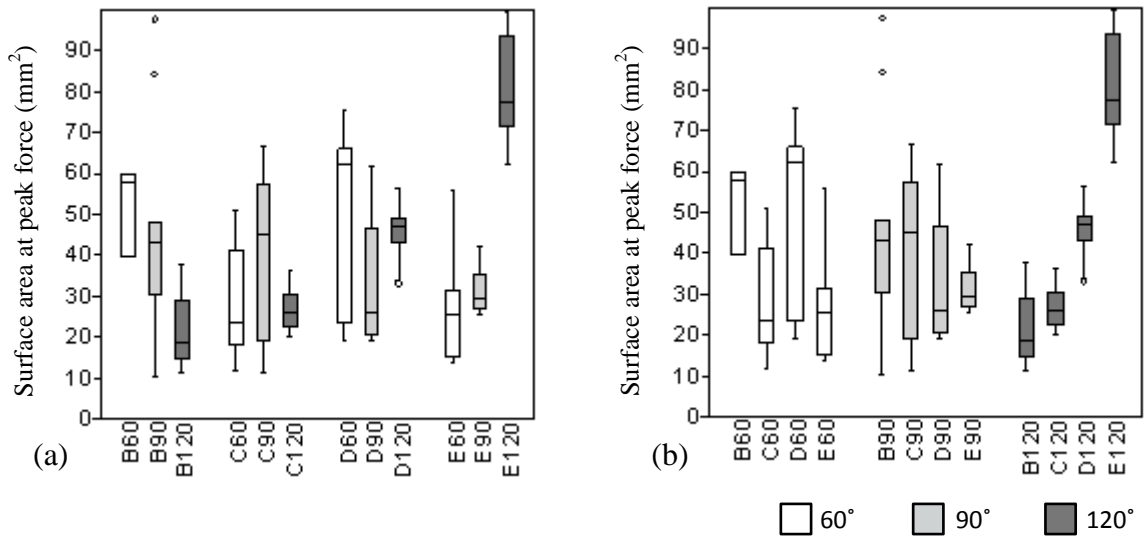


Figure 2.45 Boxplots illustrating the effect of angle (a) and bluntness (b) on the surface area of the cusp to break hollow hard objects.

Radius of curvature does not appear to be clearly related to surface area of the cusp in contact with the dome at peak force however significant differences were found between the different groups (Welch F test: $F_{31,67}=15.42$, $p=9.069E-10$) (Figure 2.46). Based on a pairwise comparison E120, the cusp with the largest radius of curvature ($R=18\text{mm}$) was significantly different to all the other models. Although a clear relationship cannot be observed, it seems that the cusps with a radius of curvature up to $\sim 5\text{mm}$ are largely overlapped in values. Beyond this R value, the surface area then appears to increase with radius of curvature.

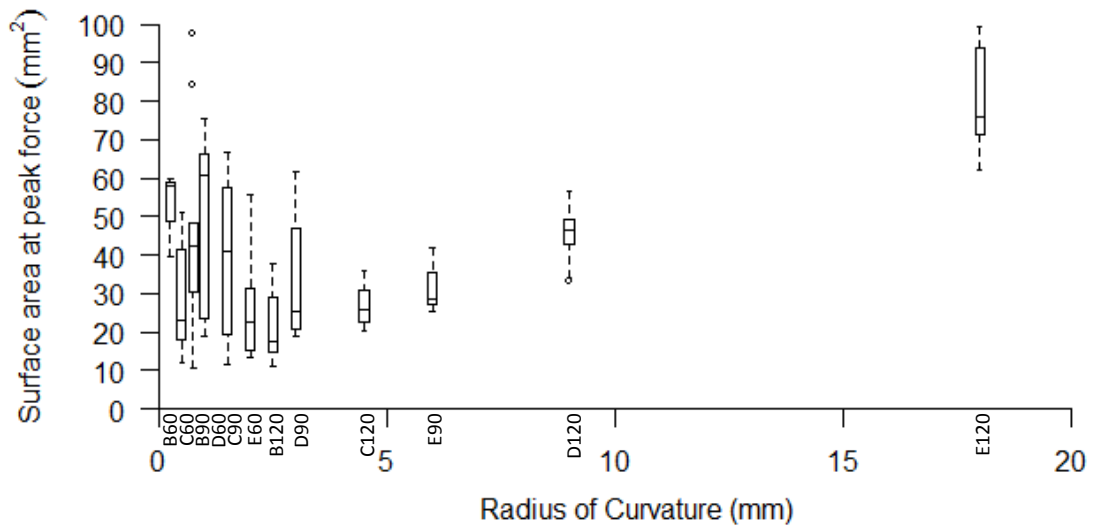


Figure 2.46 Surface area of cusp in contact with the dome at peak force to break hollow hard objects in relation to the radius of curvature of the cusp tips, a combination of both angle and bluntness values.

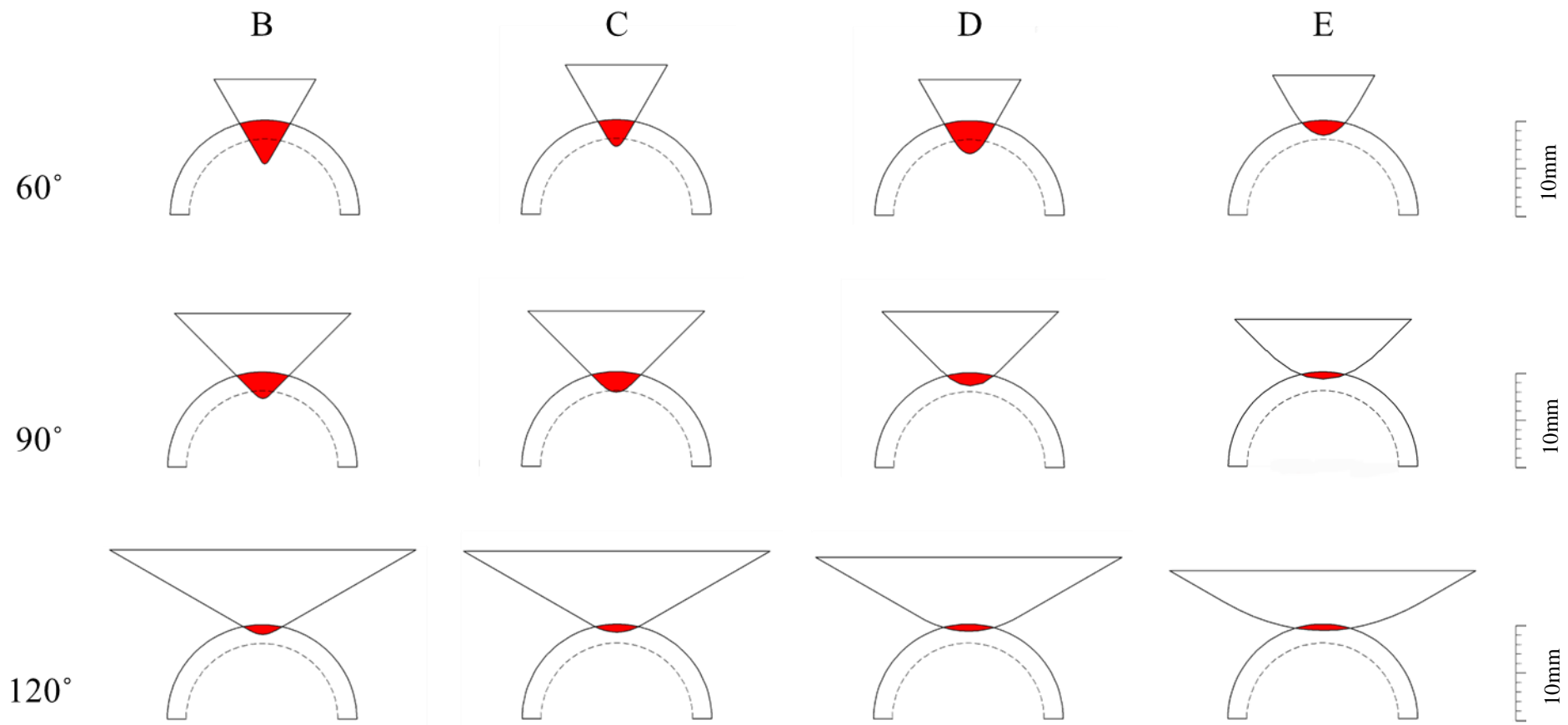


Figure 2.47 Schematic representation of the average level of displacement of each cusp model into the hollow dome at peak force (the red area represents the surface area in contact with the dome).

2.3.1.10. Bivariate plots of mechanical indicators at breakage point (hollow)

Same as initial fracture, to break a hollow hard object the models considered as most optimal were those that required the lowest amount of energy and time relative to force. To optimise for both energy and force, the most optimal designs had a larger radius of curvature where the E120 and B120 models performed the best out of the series (Figure 2.48). Interestingly, the C60 model was noted to deviate from the rest of the models requiring an unusually low level of force for the amount of energy expended. The least optimal was the sharpest model B60, which required the greatest amount of force and energy to break a hollow hard object.

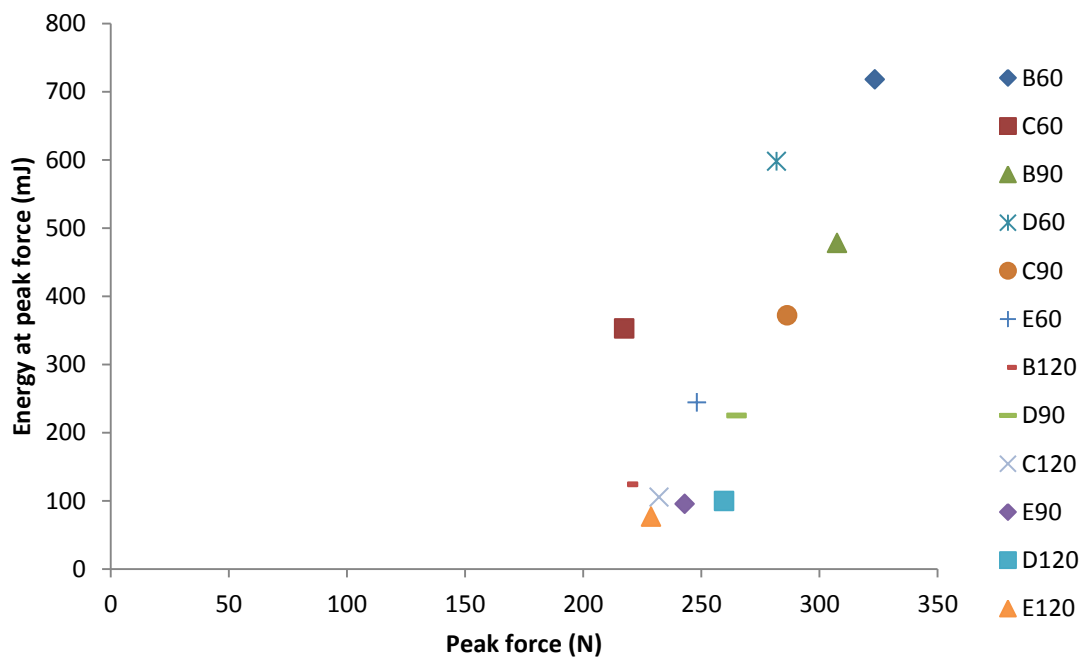


Figure 2.48 Bivariate plot of mean force and energy to break a hollow hard object for each cusp design. Note: cusp names in the legend are in order of increasing radius of curvature with B60 having the lowest R value and E120 the highest.

The exact same pattern was reflected in time where the most optimal designs were again the blunter models (Figure 2.49).

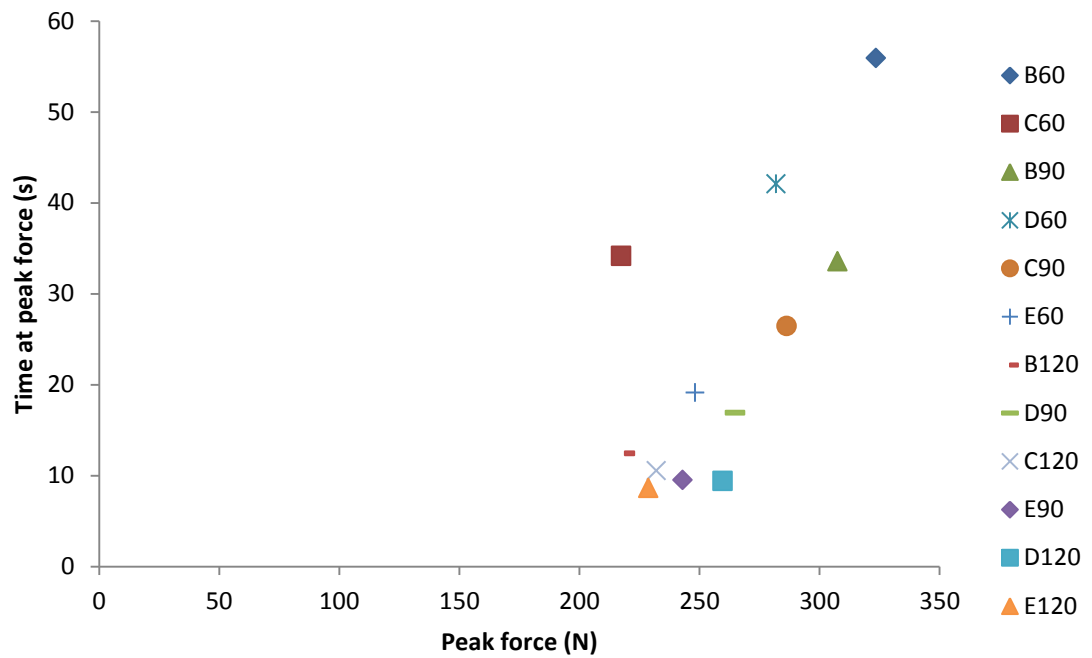


Figure 2.49 Bivariate plot of mean force and time to break a hollow hard object for each cusp design. Note: cusp names in the legend are in order of increasing radius of curvature with B60 having the lowest R value and E120 the highest.

2.3.2. Solid hard object breakdown: mechanical performance indicators

The following results examine the mechanical performance of cusps to fracture solid hard objects in relation to food consumption, where the food is broken down for digestion. As with the hollow domes, the mode of fracture was observed to vary across the different cusp morphologies. For the majority of cusp models the solid domes were subjected to indentation and split typically into 2-3 pieces (Figure 2.50a). Quite often the area of indentation would form a small piece as seen in Figure 2.50a. In contrast, the bluntest models of the series tended to “crush” the domes by compacting the 3D print material at the top (Figure 2.50b). Cracks were then observed to form at the sides of the dome as the material displaced outwards breaking the dome into 2-4 pieces. The area of compressed 3D print material at the central of the dome also regularly formed an isolated piece. As a result of the crushing effect, a large amount of fine particles were often generated by the blunter models once the pieces fell apart from handling post crush.

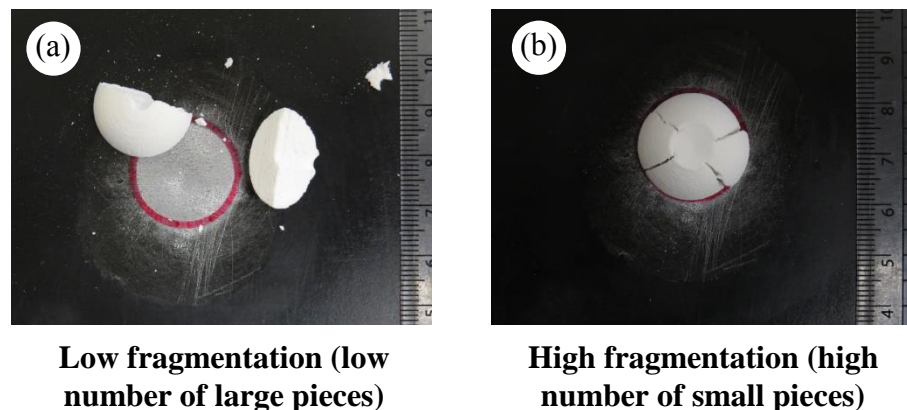


Figure 2.50 Examples of the two extremes in fragmentation observed during the breakdown of solid hard objects. Image (a) shows a solid dome fractured by C60 where the dome split into 2 pieces. Image (b) shows a solid dome fractured by E120 where the dome was highly compacted and split into 4 pieces.

2.3.2.1. Force recorded at breakage point (solid object)

A clear relationship was found to exist between cusp morphology and the maximum force required to break solid hard objects. For cusps of the same bluntness, peak force was shown to increase with increasing angle and significant differences were found within each blunting group ($p < 0.001$) (Figure 2.51a). For cusps of the same angle, peak force was also shown to increase with increasing bluntness and significant differences were found within each group ($p < 0.001$) (Figure 2.51b).

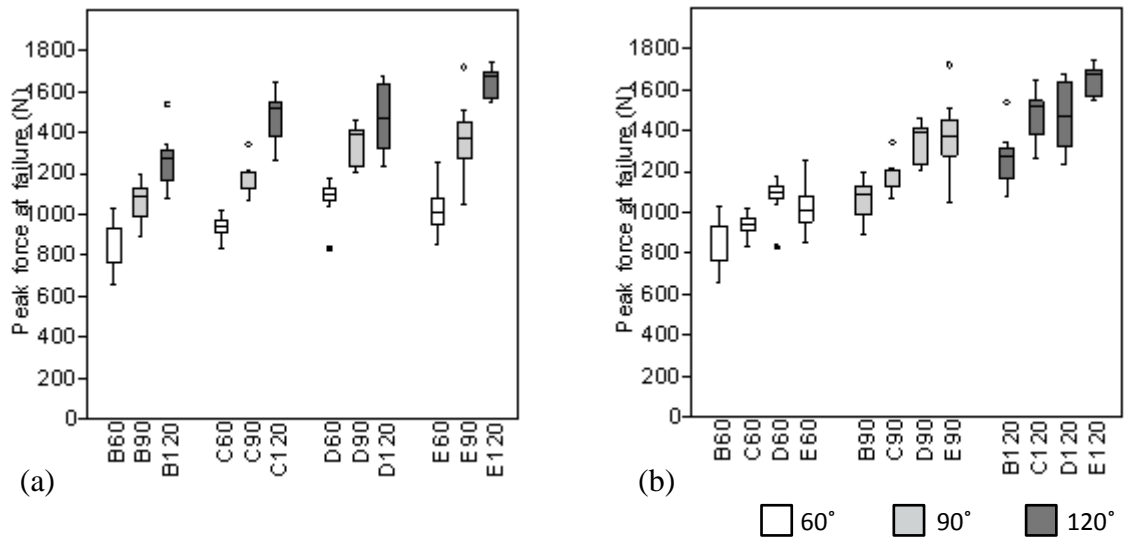


Figure 2.51 Boxplots illustrating the effect of angle (a) and bluntness (b) on the maximum force required to break the solid hard objects.

When considering all the cusps, peak force was shown to increase with increasing radius of curvature in a curvilinear pattern (Figure 2.52). Significant differences were found between the means of the different cusps (Welch F test; $F_{42,37}=64.31$, $p=8.731E-23$). However two models were noted to deviate from this pattern showing a drop in force (E60, E90). The most efficient cusp was the sharpest model B60, which required the lowest maximum force to break solid hard objects (average 878.40N) whereas the least optimal was E120, which required the highest maximum force (average 1639.26N).

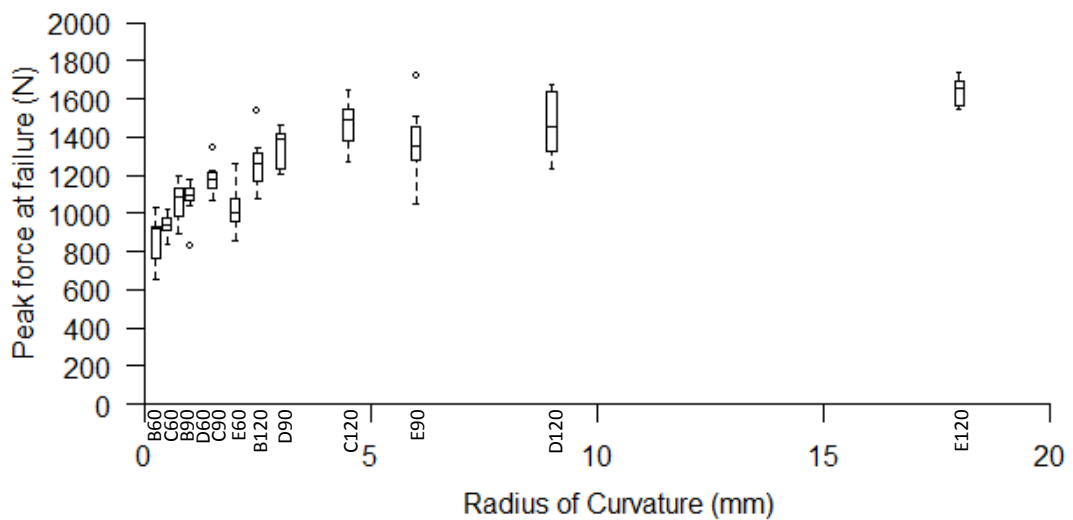


Figure 2.52 Maximum force required to break solid hard objects in relation to the radius of curvature of the cusp tips, a combination of both angle and bluntness values.

2.3.2.2. Energy recorded at breakage point (solid object)

There was no obvious pattern or trend found between energy expended at peak force and cusp morphology. For cusps of the same bluntness, there were no significant differences found between angles in each group with the exception of the E models where energy appeared to increase with increasing angle ($F_{2,27}=13.49$, $p=8.677E-05$) (Figure 2.53a). For the majority of models energy values were quite variable and overlapped across different angles. For cusps of the same angle, there were no significant differences found between level of bluntness in each group of angles ($p>0.001$) (Figure 2.53b). Energy values were again highly variable and overlapped across each group. However for both graphs (Figure 2.53a, Figure 2.53b) E60 was noticed to expend an unusually low amount of energy in comparison to the other models.

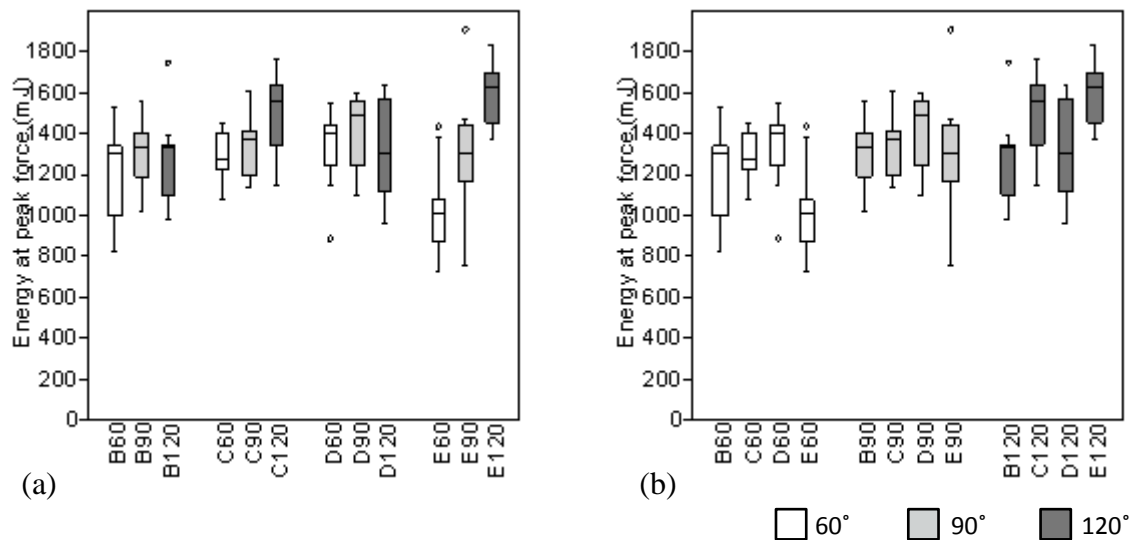


Figure 2.53 Boxplots illustrating the effect of angle (a) and bluntness (b) on the energy expended at peak force to break the solid hard objects.

For radius of curvature, significant differences in energy were found between the different cusps ($F_{11,108}=4.343$, $p=2.281E-05$). However there did not appear to be an obvious pattern between the two variables, which were found to be largely overlapping due to wide ranges (Figure 2.54). Despite this, the least efficient cusp was evidently E120, which required on average the highest amount of energy (average= 1591.8mJ).

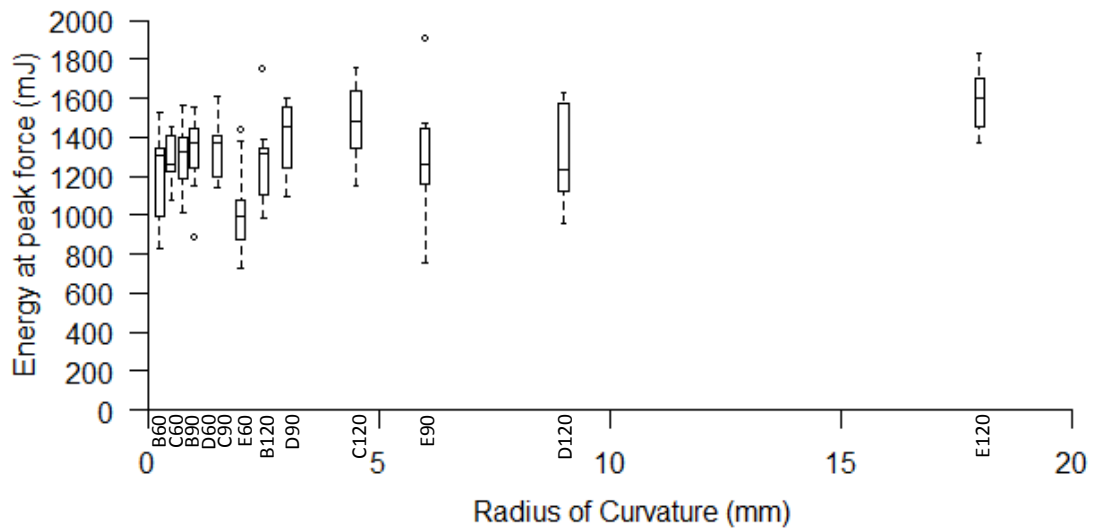


Figure 2.54 Energy expended at maximum force required to break solid hard objects in relation to the radius of curvature of the cusp tips, a combination of both angle and bluntness values.

2.3.2.3. Duration recorded at breakage point (solid object)

A clear relationship was found between cusp morphology and the time it took to reach maximum force to break solid hard objects. For cusps of the same bluntness, time was shown to decrease with increasing angle (Figure 2.55a). Significant differences were found in groups B, C, and D; furthermore angles were also shown to be significantly different from one other within each group ($p < 0.001$). The E models were an exception to this pattern where no significant differences were found between the angles ($F_{2,27} = 3.457$, $p = 0.04604$). However it was noticed that the E models start to show the same pattern of decreasing time with angle as the other groups but then increase in time with the widest angle, E120. For groups of the same angle, time was shown to decrease with increasing bluntness (Figure 2.55). Significant differences were found in all the groups ($p < 0.001$). However only the 60° and 90° groups displayed a consistent trend where time decreases with increasing bluntness. In contrast, the models in the 120° group largely overlapped in values despite differences in bluntness. The bluntest model E120 was also shown to display the opposite trend from the other groups by increasing in time from the previous model D120.

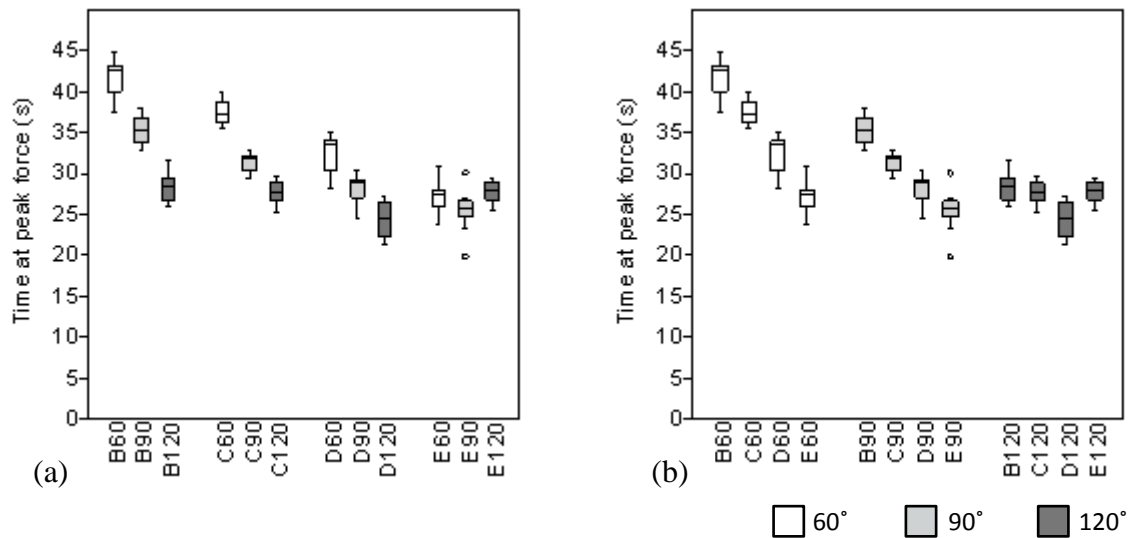


Figure 2.55 Boxplots illustrating the effect of angle (a) and bluntness (b) on the time it takes to reach maximum force to break solid hard objects.

When considering all the cusp models, time was clearly shown to decrease with increasing radius of curvature (Figure 2.56). Significant differences were found between the cusps ($F_{11,108}=73.75$, $p=5.179E-45$). Although time decreased with increasing radius of curvature it was also shown to plateau with the blunter models and then rise slightly at the bluntest model, E120. The duration results therefore suggest that sharper, acuter cusps are less efficient by taking the longest time to reach maximum force to break solid hard objects. D120 was found to be the best performing cusp by taking on average 24.34 seconds to reach peak force. In comparison the least efficient cusp model was B60, which on average required 41.75 seconds.

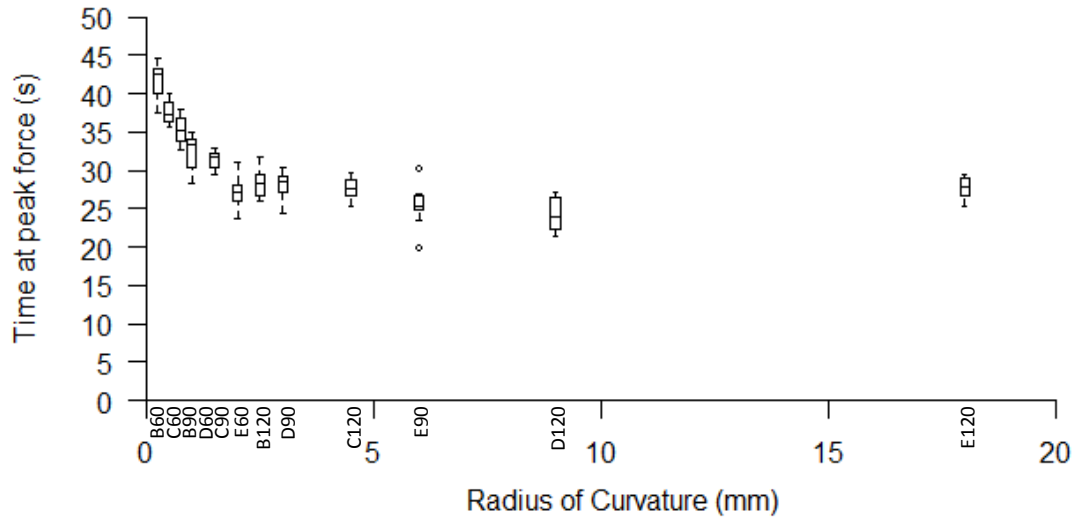


Figure 2.56 Time taken to reach the maximum force required to break solid hard objects in relation to the radius of curvature of the cusp tips, a combination of both angle and bluntness values.

2.3.2.4. Fragmentation (solid object)

Differences in cusp morphology were found to have an effect on the fragmentation of solid hard objects. For cusps of the same bluntness, fragmentation was generally shown to increase with increasing angle (Figure 2.57a). However significant differences were only found in group D ($F_{16,06}=11.73$, $p=0.0007233$). It was also observed that the variability within the repeats appeared to narrow with increasing angle, particularly in the groups C, D and E. For cusps of the same angle (Figure 2.57b), fragmentation was shown to generally increase with bluntness for 90° and 120° degree cusps; however the 60° cusps were very similar in fragmentation performance despite differences in bluntness. No significant differences were found between the different bluntness values for all of the angle groups ($p>0.001$).

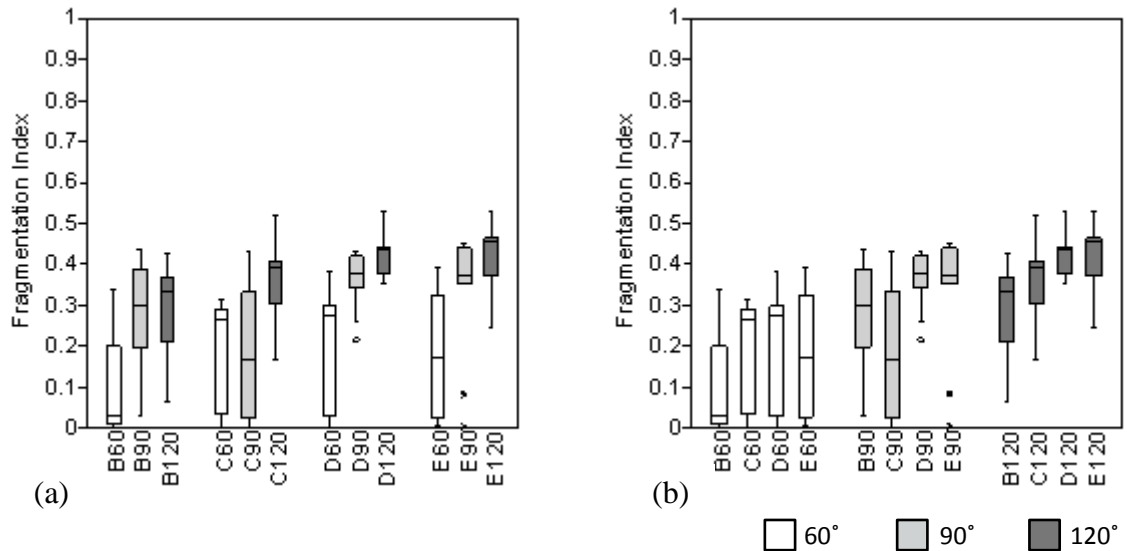


Figure 2.57 Boxplots illustrating the effect of angle (a) and bluntness (b) on the fragmentation of solid hard objects.

When considering both variables of angle and bluntness in the form of radius of curvature, a clearer trend is apparent where fragmentation generally increases and becomes much more consistent with increasing radius of curvature (Figure 2.58). It seems that although some of the sharper cusps were able to promote the same level of fragmentation, the blunter cusps were able to achieve this far more frequently. For this analysis, significant differences were found between the different cusps ($p < 0.001$). The most efficient fragmentation (high number of small pieces) was achieved by the blunter models where the best performing cusp was D120 (average FI=0.4221) closely followed by E120 (average FI=0.41258). In comparison, the poorest performer was B60 (average FI= 0.09038), which mostly broke the domes into 2 pieces.

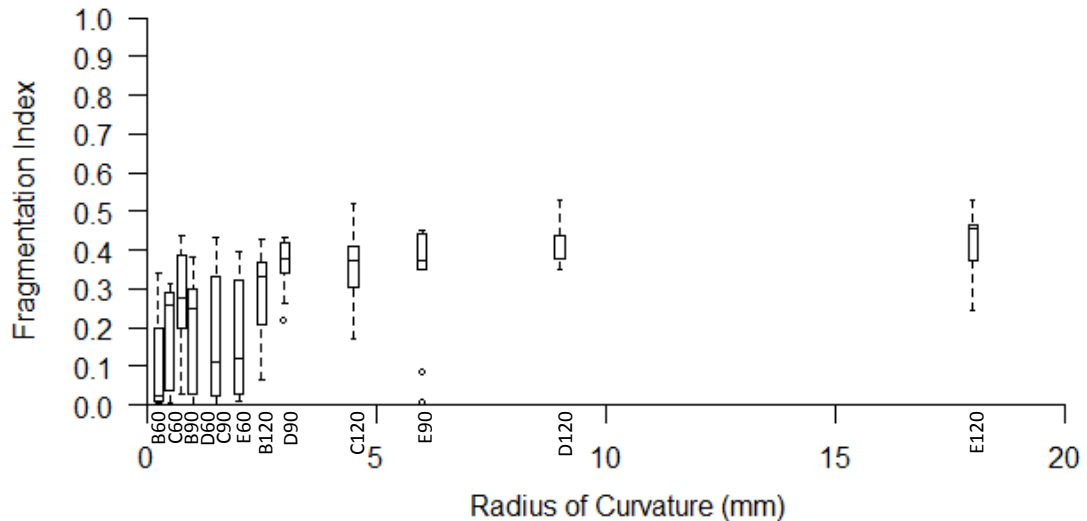


Figure 2.58 Fragmentation of solid hard objects in relation to the radius of curvature of the cusp tips, a combination of both angle and bluntness values.

2.3.2.5. *Surface area recorded at breakage point (solid object)*

A clear relationship exists between cusp form and the surface area of the cusp in contact with the dome at peak force to break solid hard objects. For cusps of the same blunting distance, surface area at peak force was shown to increase with increasing angle (Figure 2.59a). Significant differences were found within each group and a pairwise comparison indicated that the results were also significantly different between each cusp model ($p > 0.001$). It was also observed that the variability between the repeats for each cusp model appeared to increase with increasing angle. For cusps of the same angle, surface area at peak force was shown to increase with increasing blunting distance and significant differences were found between the cusp models within each angle group ($p > 0.001$) (Figure 2.59b).

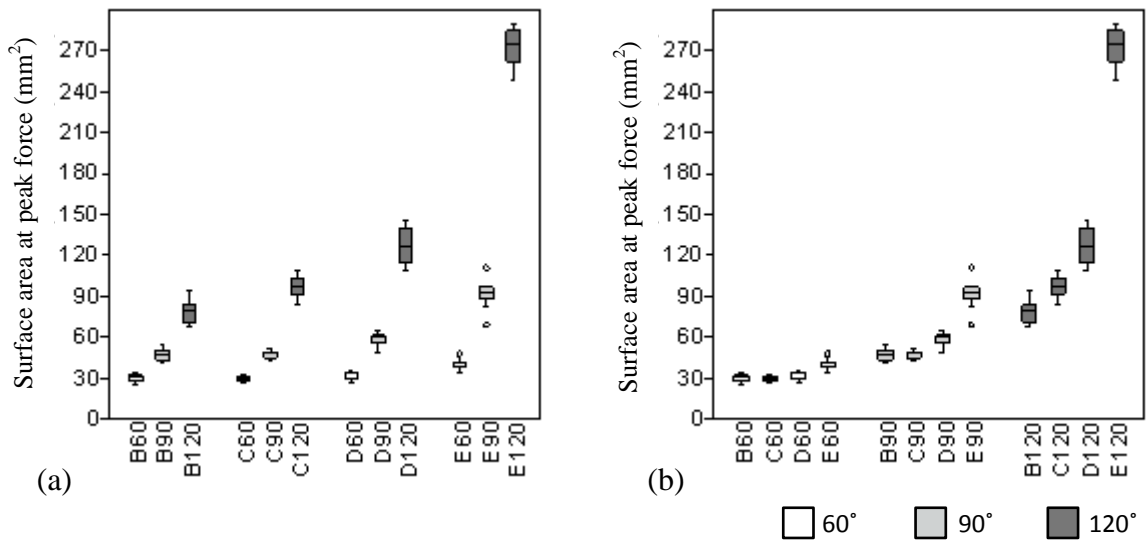


Figure 2.59 Boxplots illustrating the effect of angle (a) and bluntness (b) on the surface area of the cusp to break the solid hard objects.

Surface area in contact with the dome at peak force was shown to increase with increasing radius of curvature and significant differences were found between groups (Welch F test: $F_{42,17}=389.7$, $p=1.125E-38$) (Figure 2.60). The variability between the results was also observed to increase with increasing radius of curvature. Interestingly any deviations from the linear trend seemed to follow the individual patterns for angle.

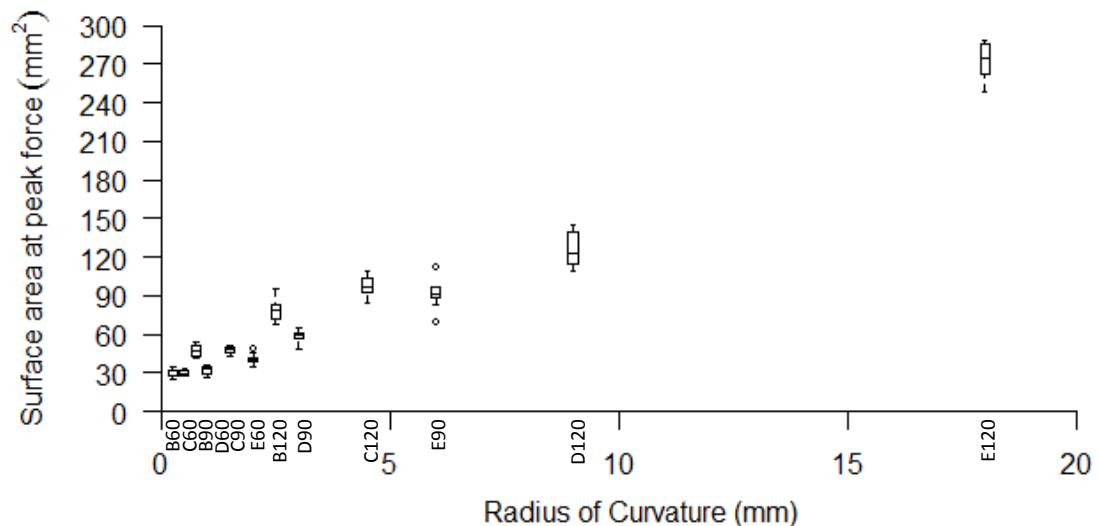


Figure 2.60 Surface area in contact with the dome at peak force to break solid hard objects in relation to the radius of curvature of the cusp tips, a combination of both angle and bluntness values.

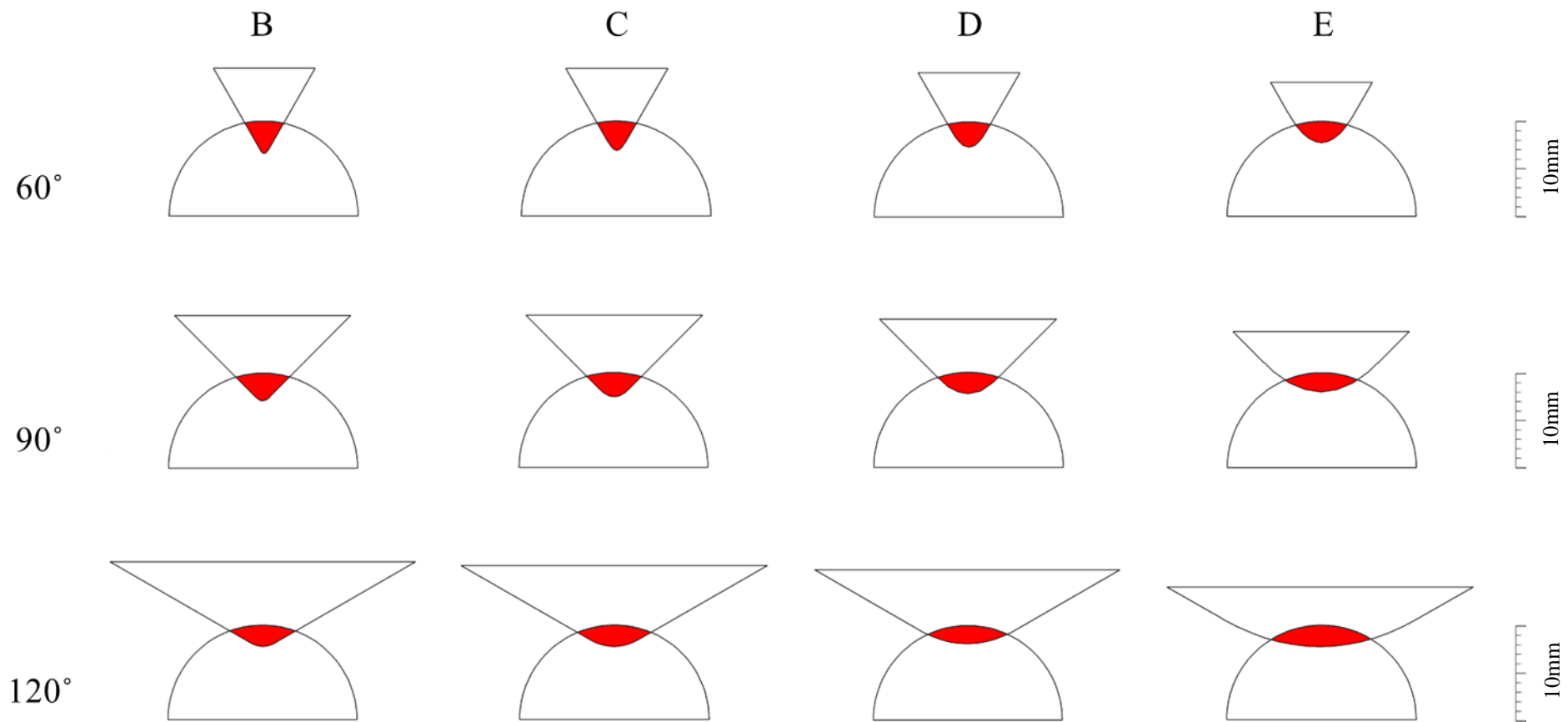


Figure 2.61 Schematic representation of the average level of displacement of each cusp model into the solid dome contact at peak force (the red area represents the surface area in contact with the dome).

2.3.2.6. Bivariate plots of mechanical indicators at breakage point (solid)

To break a solid hard object, the models considered most optimal were those that required the least amount of force, energy and time yet produced the greatest amount of fragmentation. In terms of energy and force, the general observed trend was that efficiency decreased with increasing radius of curvature (Figure 2.62). The E60 model of somewhat intermediate radius of curvature was shown to perform particularly well by requiring a surprisingly low amount of force and energy for its design. Along with B60 and C60 these were considered the best performing models. In contrast the least optimal was the bluntest cusp in the series, E120.

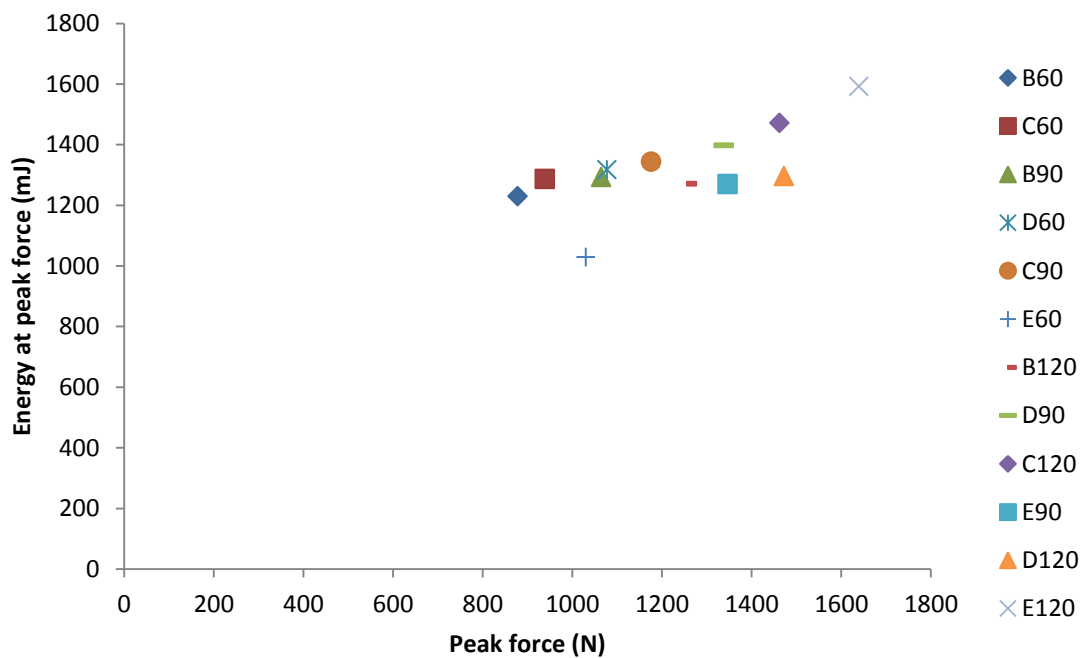


Figure 2.62 Bivariate plot of mean force and energy to break a solid hard object for each cusp design. Note: cusp names in the legend are in order of increasing radius of curvature with B60 having the lowest R value and E120 the highest.

For the optimisation of both time and force the E60 model was clearly the most efficient cusp morphology requiring a low amount of force and the lowest amount of time (Figure 2.63). Neither extremes in sharpness and bluntness could optimise for both variables although individually were best in one (i.e. sharpest models were best at reducing force but were worst in terms of energy, whereas the bluntest models were best at reducing energy but worst in terms of force).

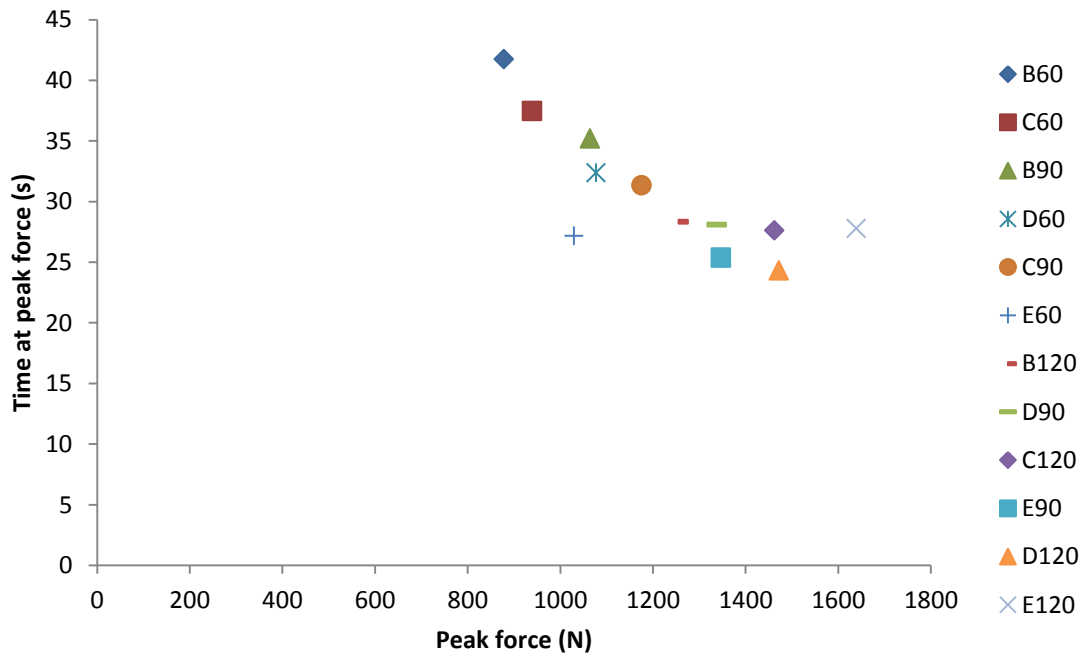


Figure 2.63 Bivariate plot of mean force and time to break a solid hard object for each cusp design. Note: cusp names in the legend are in order of increasing radius of curvature with B60 having the lowest R value and E120 the highest.

For the optimisation of both fragmentation and force the best performing cusps were C60 and B90, which were relatively sharp (Figure 2.64). The extremes in radius of curvature could only be optimised for one of the variables.

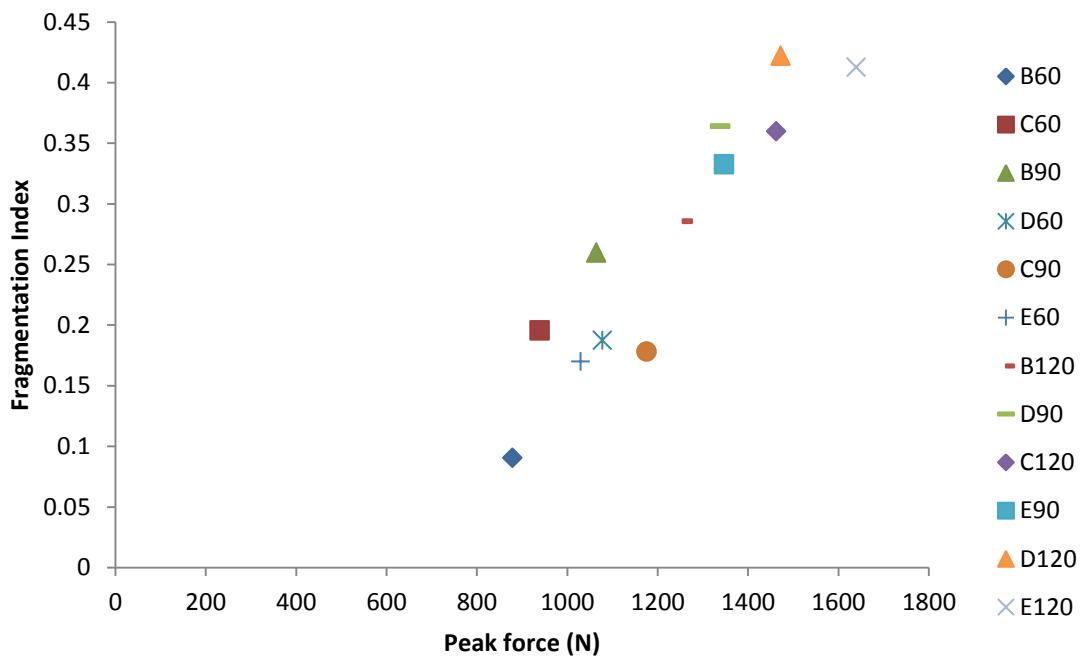


Figure 2.64 Bivariate plot of mean force and fragmentation index to break a solid hard object for each cusp design. Note: cusp names in the legend are in order of increasing radius of curvature with B60 having the lowest R value and E120 the highest.

2.4. Discussion

Mammalian hard object feeders present a wide diversity of tooth forms. However it is unclear why such variation exists and whether certain tooth shapes perform better than others during the processing of hard foods. In order to shed light on the matter, this study has varied the shape parameters of a single cusp to examine the effect on mechanical performance. By controlling for the physical properties of both the cusp and the food item has created an ideal means to examine the relationship between cusp morphology and function in hard object feeding. The findings from this chapter will now be discussed in relation to specific research questions and in the broader context of dental functional morphology.

2.4.1. Does cusp morphology affect the mechanical performance of hollow hard object breakdown?

The following section will discuss the results of hollow hard object breakdown in relation to food access, where a structure such as a shell or endocarp, must be broken to extract the food within. One cusp model, C60, will not be considered in discussion as it was found to greatly deviate in behaviour from the rest of the series. As this particular model was repeatedly used in several sensitivity studies prior to use, it is speculated whether damage may have occurred to the cusp tip thus affecting fracture performance.

In terms of the fracture behaviour, the hollow domes were observed to vary depending on the cusp used to break it. Previous research by Lawn and Lee (2009) and Lee et al. (2009) suggest that when teeth bite onto a hollow structure such as a seed casing, both median and radial cracks can be generated. Median cracks initiate at the area of contact between the shell and the indenter, whereas radial cracks initiate from the inner surface of the shell as a result of a high concentration of tensile stress. Evidence of both forms of crack initiation was found in this study. For the majority of tests, medial cracks were initiated at the area of indentation causing the dome to break into 2 or more pieces (Figure 2.65a). In contrast, radial cracking was the typical method of crack initiation by the bluntest cusp models where fracture lines were often observed to be longer and more prominent on the inner surface of the dome (Figure 2.65b).

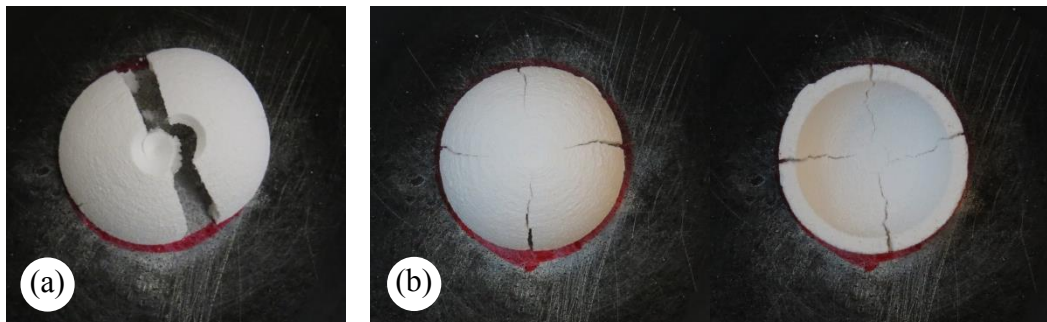


Figure 2.65 Examples of both modes of fracture exhibited during hollow hard object breakdown. Image (a) shows a hollow dome fractured by one of the sharpest cusp designs, B90 where medial cracks initiated from the area of indentation. Image (b) shows a hollow dome (superior and inferior) fractured by one of the bluntest cusp designs, E120 where radial cracks initiated from the inner surface due to tensile stress.

However, not all of the cusp models were successful in fracturing the hollow domes. The sharpest cusp, B60, was recorded to fracture only 3 of the domes out of 10 repeats. For the remaining test runs the domes were pierced by the cusp causing plastic deformation without fracture (Figure 2.66). This finding is consistent with predictions made by Lucas (2004), which suggest that sharper cusps suppress cracking once stress is confined to a small enough volume. However, whether this is a disadvantage for all hard object feeders is questionable. For example, in sooty mangabeys, McGraw et al (2011) notes that the canines are sometimes used to puncture the food item *S. gabonensis* prior to processing using their posterior dentition. It may therefore be the case that a sharp point can be used to puncture the food item and create a weak spot in which cracks can be later propagated once processed by a blunter tooth shape.

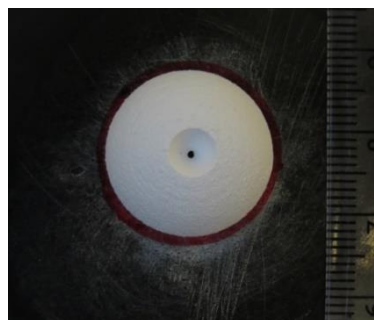


Figure 2.66 Example of one of the hollow domes compressed by B60 where plastic deformation occurred without fracture.

In relation to the mechanical performance indicators, both the results at initial fracture and peak force at failure will be drawn upon. At the point of initial fracture of the hollow hard object, force was shown to increase with increasing angle, bluntness and thus radius of curvature. As surface area at initial fracture was also found to increase with each shape variable, the results support theoretical predictions by Lucas (1982,

2004) where an increase in surface area reduces localised stresses on the food item thereby increasing the amount of force required. Interestingly the E120 model, which had by far the largest contact surface area at initial fracture, deviated from this pattern where the force value was shown to decrease with bluntness and radius of curvature. The drop in force observed for this particular model may be due to the way in which the hollow dome is fractured. Based on a Finite Element Analysis (FEA) simulating the contact of a dental row onto a hemispheric shell, Berthaume et al. (2010) found that a high amount of tensile stress is generated on the inner surface of the hemisphere (Figure 2.67). A high stress distribution associated with a large contact surface area may actually help build up tensile stress in the inner layer of the hollow dome, thus warranting a lower degree of force.

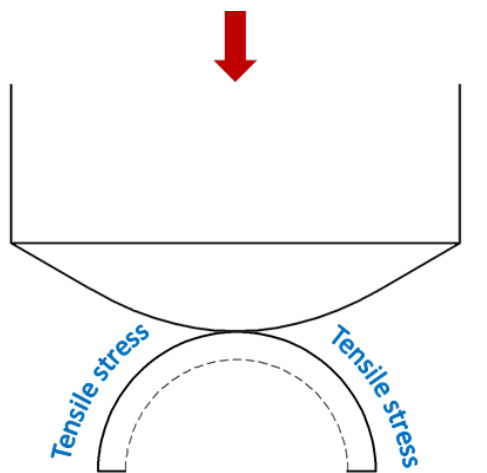


Figure 2.67 Diagram illustrating the contact between the E120 model and a hollow hemisphere. Red arrow indicates the direction of force. Scaled 2:1.

Contrary to initial expectations, energy did not follow the same pattern as force in relation to increasing surface area. Although energy increased with increasing angle for some of the groups, when considering radius of curvature the values decreased within the first few models of the series and then increased as the models increased in bluntness. An explanation for this pattern may be found in the displacement values, which along with force, determines the amount of energy used at initial fracture. The graph displayed in Figure 2.68 indicates that the displacement value is highest in the sharpest cusp (B60) and then drastically decreases to a plateau. As the sharpest cusps displaced the most, this is likely to have elevated the amount of energy expended despite a low force value. It also suggests a potential trade-off between force and displacement with increasing radius of curvature where sharper cusps have a low force and high displacement, and blunter cusps have a high force but low displacement. As

such, a linear relationship as observed between force and cusp form cannot be established with energy. Furthermore, these results suggest that force should not be used to infer energy as has been used previously (Crofts and Summers, 2014).

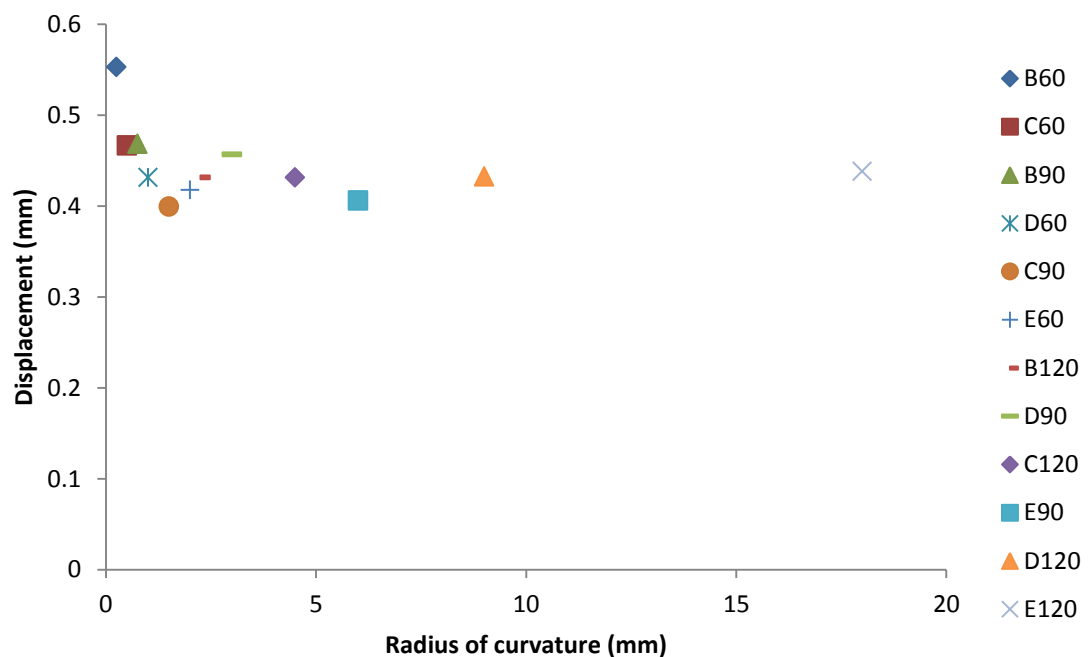


Figure 2.68 Bivariate plot showing the displacement at the initial fracture of a hollow hard object against the radius of curvature value of each cusp design.

In terms of duration, time at initial fracture was shown to clearly decrease with increasing angle in the B group and with increasing bluntness in the 60° group but not for the other remaining groups. These observations were reflected in the radius of curvature results where time drastically decreased in value for the first four models (the sharpest cusps of the series) and then plateaued for the remaining models. The observed pattern is mirrored in the displacement values suggesting that a higher displacement warrants a longer duration for initial fracture to occur thus supports initial predictions.

The results at maximum force to break a hollow hard object were considerably different to those at initial fracture. The relationship between cusp form and force was notably less clear. Although there was some decrease in force observed with increasing angle and bluntness, there were no significant differences found for any of the groups and many of the results were greatly overlapped. In terms of radius of curvature, the sharper cusps were generally shown to reach higher peak forces but were extremely variable in comparison to the blunter cusps. Furthermore, as a clear pattern could not be detected between peak force and surface area it seems that cusp form is less important for breaking hollow hard food items. The relationship between cusp form and energy

however was much clearer where energy was shown to consistently decrease with increasing angle, bluntness and radius of curvature. The wider and blunter models were also found to be much more consistent in behaviour exhibiting a smaller amount of variability in the repeats in comparison to the sharper models. A clear relationship also existed between cusp form and duration at peak force where time decreased with increasing curvature showing a pattern similar to that seen with energy. Both the patterns for energy and duration were reflected in the displacement (Figure 2.69).

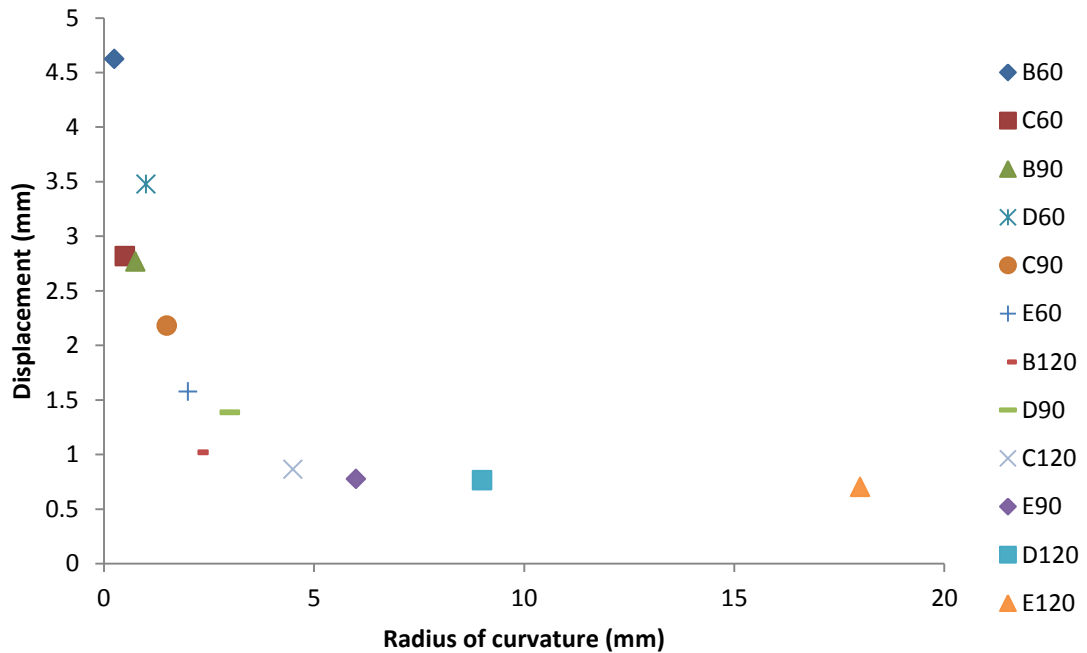


Figure 2.69 Bivariate showing the displacement at peak force to break a hollow hard object against the radius of curvature value of each cusp design.

2.4.2. Which cusp morphology is most optimal for hollow hard object breakdown?

For the breakdown of a hollow hard object, the cusps considered most optimal were those that required the least amount of energy and time relative to a low force. To initiate fracture, the most optimal cusp was the D60 model, which had a radius of curvature of 1mm. Although this was one of the sharpest cusps of the series, sharpness itself could not be used as an indicator of efficiency as the sharpest cusp B60 ($R=0.25$) took the longest time to initiate fracture and was comparatively higher in energy.

In contrast to the initiation of fracture, the cusps that were most optimal to break a hollow hard object were E120 and B120, which had a wider angle and higher radius of curvature. Both of these models were shown to require the least amount of time and energy relative to a low force. In comparison, the sharpest cusp (B60) was undoubtedly

the least optimal as it took the highest energy, longest duration and highest force. It was also more likely to puncture the hollow dome rather than induce fracture.

Therefore, the most optimal cusp shape for hollow food breakdown depends on whether initial fracture or breakage is being optimised for. It may be the case that some species use their teeth to initiate fracture in order to weaken the structure. Although it may take more processing, a lower force would be required at initial fracture in comparison to at breakage and as the item is damaged, the force required to propagate cracks using alternative dentition is also reduced. Furthermore, some feeders use other parts of their anatomy to process foods. For example, McGraw et al. (2011) acknowledges that while teeth are used to fracture hard food items, sooty mangabeys also use their hands to manipulate foods during food processing.

2.4.3. Does cusp morphology affect the mechanical performance of solid hard object breakdown?

The following section will discuss the results of solid hard object breakdown in relation to food consumption, where a structure must be broken down into a high number of small pieces for digestion. As with the hollow domes, the mode of fracture was observed to vary across the different cusp morphologies where the sharper models tended to initiate fracture via indentation (Figure 2.70a) and the blunter models tended to compact and crush the solid domes (Figure 2.70b).

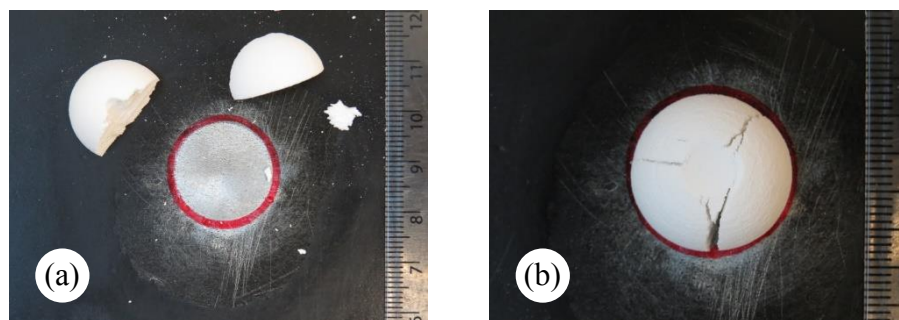


Figure 2.70 Examples of the two different modes of fracture exhibited during solid hard food breakdown. Image (a) shows a solid dome that was fractured via indentation by D60 where the dome typically split apart at fracture. In contrast, image (b) shows a dome that was crushed by D120 where the 3D print material was slowly compacted under compression.

Similar to the initial fracture of hollow hard objects, the maximum force required to break solid hard objects was shown to clearly increase with increasing angle, bluntness and thus radius of curvature. As surface area was also shown to increase with increasing angle, bluntness and radius of curvature, the results support the prediction that force increases as a result of increasing contact surface area. In contrast, the relationship

between cusp form and energy was more ambiguous. Although energy appeared to increase with increasing angle for some of the groups, the results were mostly overlapped obscuring any clear trend for angle, bluntness and radius of curvature. However, the cusp with the greatest radius of curvature (E120) was observed to expend the largest amount of energy out of the series. A clear relationship was found between cusp form and duration to reach peak force where time was shown to decrease with increasing angle for groups B, C, D and bluntness for group 60° and 90°. For the E group and 120° group the values were similar therefore in terms of overall radius of curvature, duration decreased and then reached a plateau with the blunter models. The same pattern was reflected in the displacement where sharper cusps had the largest displacement; therefore supporting initial predictions (Figure 2.71).

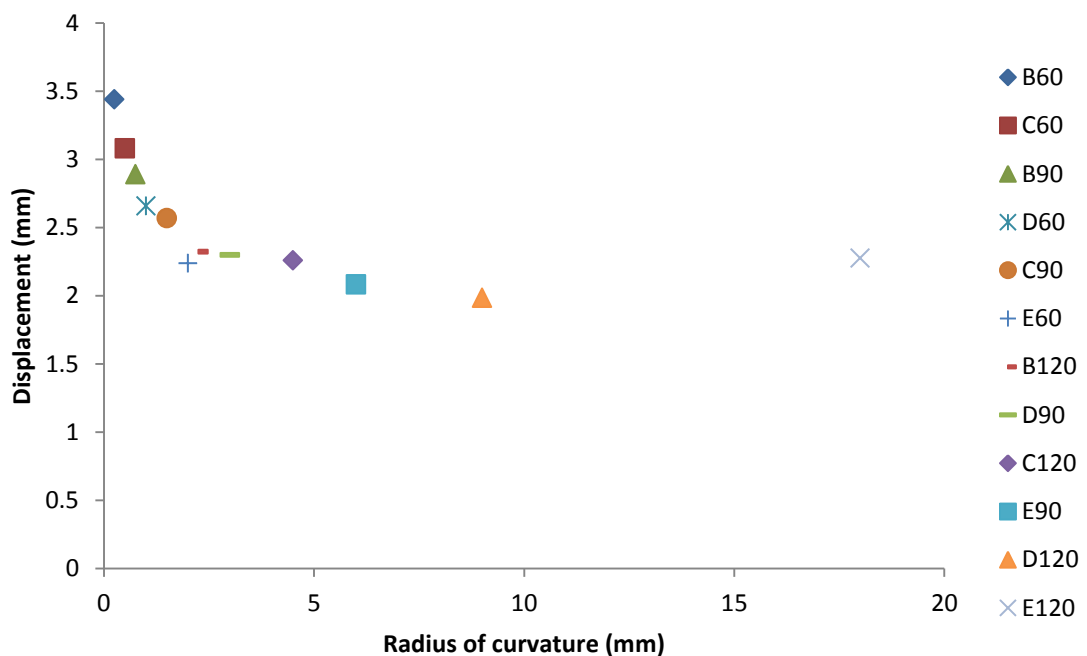


Figure 2.71 Bivariate plot showing the displacement at peak force to break a solid hard object against the radius of curvature value of each cusp design.

Cusp form was also shown to have an effect on the fragmentation of solid hard objects. The degree of fragmentation generally increased with increasing angle, bluntness and radius of curvature, except for the 60° models, which were noticed to produce a similar level of fragmentation. Although there was a considerable amount of overlap in fragmentation index between most of the models, the blunter cusps were the most consistent at producing a high amount of fragmentation.

2.4.4. Which cusp morphology is most optimal for solid hard object breakdown?

For the breakdown of a solid hard object, the most optimal cusps were those that required the least amount of energy and time yet produced the greatest amount of fragmentation relative to a low force. For both energy and time the most optimal cusp was E60 ($R=2\text{mm}$). The reason why this design in particular might have been the most optimal for these variables is that it was reasonably sharp warranting a lower force, yet it was blunt enough to have a low level of displacement. Although the bluntest cusps produced consistently the greatest amount of fragmentation they were least optimal in terms of force. When considering the optimisation of both fragmentation and force the C60 and B90 models performed the best, which were considerably sharper than models that were most efficient for fragmentation alone.

2.4.5. Summary of findings

The results from this study have demonstrated that cusp morphology can greatly influence the mechanical performance required to break down hard food items. Generally, sharper cusps required the least amount of force to initiate fracture in hollow hard objects. However this came at the cost of a larger displacement causing a higher than expected energy and a longer duration. Interestingly, the results at peak force to break a hollow dome did not follow the same patterns as initial fracture. As there was no clear relationship between cusp form and force, efficiency was largely driven by displacement where blunter cusps required the least amount of energy and time to reach point of failure. The findings at peak force to break a solid dome, however, were very similar to those found with initial fracture of the hollow domes. This could be due to the fact the peak force and initial fracture occurred simultaneously during solid food break down. In terms of fragmenting the solid domes, the blunter, wider cusps were most efficient. Furthermore, the sharpest cusp of the series (B60) was observed to be the least effective at promoting crack growth as it had the lowest fragmentation index for the solid domes and was also noted to frequently puncture the hollow shells without fracturing them into pieces.

To optimise for several different parameters at the same time it is clear that a compromise must be made. To initiate fracture in both hollow and solid domes, a cusp with a relatively small radius of curvature is most optimal; however it cannot be too sharp as this decreases optimality by warranting a larger displacement and suppresses crack propagation. This is consistent with previous research (Lucas, 1979, Luke and Lucas, 1983) that suggest a blunt cone is most suitable for a hard diet as it maintains a

point contact yet promotes crack propagation ensuing the shatter of the food item into pieces. However, as cusp form does not appear to be related to force when breaking hollow hard objects, the wider and blunter models were most optimal for this aspect of hard object feeding. Figure 2.72 summarises the key cusp morphologies that were most optimal during hard object breakdown.








Hollow	Initial fracture	 D60 ($R=1$)	 C90 ($R=1.5$)	
	Complete failure (peak force)	 B120 ($R=2.25$)	 E120 ($R=18$)	
Solid	Initial fracture and complete failure (peak force)	 C60 ($R=0.5$)	 E60 ($R=2$)	 B90 ($R=0.75$)

Figure 2.72 Cusp designs that were most optimal to initiate fracture and break hollow and solid hard food items.

2.4.6. General discussion and application of results for further study

Based on the results recorded for this study on hard dome models, it is clear there are several different cusps forms that could be advantageous for hard object food breakdown. While the tooth cusp designs used in this study were very much stylised, and were not based directly on existing morphologies found in nature, this approach has increased understanding on the mechanical relationship between cusp form and food breakdown. Whether the teeth of actual hard object feeders are indeed optimised for such a diet, still needs to be examined. In order to do this, cusp shape of hard object feeders would need to be quantified. To date, radius of curvature has frequently been used to quantify cusp tip morphology (Yamashita, 1998a, Hartstone-Rose and Wahl, 2008, Berthaume et al., 2010), yet only a small sample of data has been collected for living hard object feeders and extinct (predicted) hard object feeders (Table 2.6). Although some of the R values are quite similar to the proposed optimal cusp designs in this study, they are also quite variable between species and lack any indication of angle. In order to examine this further, more data ultimately needs to be collected on both radius of curvature and angle in hard object feeders.

Table 2.6 Examples of radius of curvature values recorded from the postcanine teeth of extant and extinct hard object feeders.

	P3	P4	M1	M2	Reference
<i>Pongo pygmaeus</i> (N=8)	-	-	-	0.75-2.42	Berthaume (2014)
Modern Hyaenidae (3 species, N= 33)	2.63	2.22	0.58 (ant.), 1.23 (pos.)	-	Hartstone-Rose and Stynder (2013)
<i>Paranthropus boisei</i> (N=1)	7.41	6.98	8.08	10.5	Berthaume et al. (2010)
<i>Paranthropus robustus</i> (N=1)	2.45	2.06	3.14	3.75	Berthaume et al. (2010)

What is interesting, however, is that cusp radius of curvature does appear to vary across the dental row and also within a single tooth (Table 2.6) (Berthaume, 2014). This strongly suggests that a combination of cusps of varying shapes and sizes are utilized during feeding that may have different roles throughout the process. For example, sharper cusps may be used to initiate fracture whereas wider, blunter cusps are used to facilitate the propagation of fracture within the food item. Additionally, changes in tooth shape along the dental row may be particularly relevant when considering bite force production. Previous research suggests that the positioning of muscles on the skull and the location where force is transferred onto a food along the dental row (bite point) can greatly affect bite force (Dechow and Carlson, 1990, Dumont and Herrel, 2003). Therefore the shapes of cusps may be influenced on where they are positioned on the dental row in relation to how much force can efficiently be transferred from the masticatory muscles.

An important factor of tooth optimisation that has not been considered in this study is the tooth's own resistance to fracture. Unlike many other vertebrate species that replace their teeth when they break, mammals are generally restricted to a maximum of two generations of dentition (Ungar, 2015). As dental failure can greatly affect an individual's survival, it is vital that teeth are able to break foods sufficiently without damaging the tooth itself. Several studies have indicated that the composition and structure of dental tissues can play an important role in tooth preservation among hard object feeders (Dumont, 1995, Lucas et al., 2008, Ungar, 2008, McGraw et al., 2012). For example, thick enamel helps prevent fracture from radial cracks forming at the enamel-dentine junction in mammals that consume large hard objects (Lucas et al., 2008). In addition to the internal dental architecture, the shapes of the teeth can also

have an effect on fracture resistance. Using Finite Element Analysis (FEA), Crofts (2015) were able to demonstrate that taller and thinner cusps had an increased level of in-model strain when loaded by a food item. This is consistent with research by Rudas et al. (2005), where an increase in radius of curvature of a curved brittle glass layer was shown to decrease the critical load required for it to break. Indeed in this study, some of the original sharpest cusp designs were purposely excluded from analysis as they were found to be particularly liable to deformation (Figure 2.73). Therefore, it seems likely that there is a functional trade-off between reducing the force to initiate fracture in foods and self-preservation of the tooth itself (Berthaume et al., 2010, Crofts and Summers, 2014, Crofts, 2015).



Figure 2.73 Image of a stainless steel B30 cusp with a deformed tip.

Extending on the idea of optimising for both food breakdown and tooth preservation, Berthaume et al. (2013) considers the importance of multiple cusps on a single tooth crown. Using FE modelling, 4 cusped bunodont molars were loaded by a brittle hemisphere representing a food object. By varying the combination of cusp radii of curvature on the tooth crown, they found that a mixture of dull and sharp cusp morphologies were the most optimal by creating high stress in the food object whilst minimising the stress in the tooth enamel. In contrast, the least optimal crown design comprised of entirely sharp cusps where stresses were higher in the enamel than in the food item.

2.5. Conclusions

The results from this study demonstrate that cusp morphology, determined by bluntness, angle and radius of curvature; greatly affect the mechanical performance to break down hard brittle food items. By using multiple mechanical performance indicators, this study extends on previous research (Crofts and Summers, 2014) by showing that there are several factors that may be optimised during food breakdown, each requiring different tooth forms. Therefore, trade-offs may have to occur in order to optimise for a particular factor, or alternatively a level of intermediate efficiency is required to achieve optimality of multiple different factors simultaneously. This may in part explain the diversity of tooth form observed in hard object feeders. However, other factors such as the structural integrity of the tooth may also need to be accounted for when considering tooth optimality.

Chapter 3: Quantification of dental wear in a developmental sample of a hard object feeding primate (*Cercocebus atys*)

3.1. Introduction

The shapes of teeth vary considerably among primates, which have largely been associated with various dietary adaptations (e.g. Kay, 1973, 1975, Kay and Hylander, 1978, Yamashita, 1998a). However tooth morphology varies not just interspecifically but also within an individual's lifetime as a result of dental wear (Figure 3.1) (Dennis et al., 2004). Previous research by Galbany et al. (2014) suggests that the mechanical properties associated with hard foods accelerate wear in hard object feeders. As the shapes of teeth are highly related to function (see chapter 2), this chapter aims to examine how a tooth wears across development in the hard object feeding sooty mangabey (*Cercocebus atys*) and how this may in turn affect tooth shape, and potentially functionality.

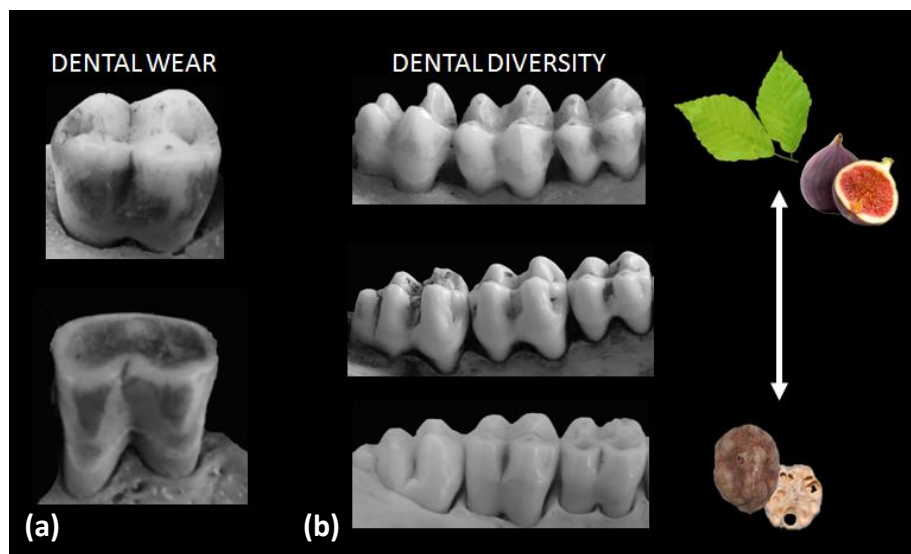


Figure 3.1 An unworn and worn *C.atys* first molar (a) and examples of adult molar cusp diversity in primates with different diets (a). From top: *Allenopithecus*, *Papio*, *Cercocebus*. Photographs: Karen Swan.

3.1.1. Dental wear and masticatory efficiency

Dental wear is essentially the gradual loss of dental tissue from the tooth crown (Lucas, 2004, Lucas and Omar, 2012). There are several different causes of wear, which include attrition (tooth-tooth contact), abrasion (food-tooth contact), and chemical dissolution (erosion) (Lucas, 2004). The mechanical imprints, particularly from the abrasion of food and extraneous grit can be detected on the surface of the tooth using microscopic analysis, where the pattern and orientation of fine scratches and pits have been shown to be related to diet (Teaford et al., 2013, Ungar, 2015). However it is macroscopic wear, the gross changes of the tooth topography that is of interest in this thesis as this ultimately effects masticatory performance (Lucas et al., 2013).

As enamel is non-regenerative, the effects of wear are irreversible and can have detrimental repercussions on the digestive efficiency, reproductive success, and ultimately survival of an individual (Gipps and Sanson, 1984, Lanyon and Sanson, 1986, Pahl, 1987, Pérez-Barbería and Gordon, 1998, King et al., 2005, Cuzzo and Sauter, 2006, Venkataraman et al., 2014). For example, mammals such as koalas and red deer that exhibit high amounts of dental wear have been observed to increase food intake and time spent chewing in order to compensate for a decrease in dental efficiency (Pérez-Barbería and Gordon, 1998, Logan and Sanson, 2002). Furthermore, in cases of extreme tooth wear in koalas, the size and number of large food particles in the small intestine have been found to be greater than those with less worn teeth indicating a decrease in digestive efficiency (Lanyon and Sanson, 1986). This is also reflected in the graminivorous primate *Theropithecus gelada* where older individuals with the greatest magnitude of wear have been found to have a higher mean faecal particle size, particularly during the dry seasons when fallback feeding of tougher vegetation occurs (Venkataraman et al., 2014).

However, several studies have indicated that dental wear can be advantageous and actually promote digestive efficiency. It is well known that many herbivorous mammals require their teeth to be worn into a 'secondary morphology' in order to improve and maintain shearing potential (Fortelius, 1985, Evans et al., 2005, Ungar, 2015). This appears to also hold true for some primates. For instance, using dental topographic techniques, several authors have found that although the slope and relief of the occlusal surface decreases with wear (i.e. becomes flatter), the surface angularity remains fairly consistent (Ungar and M'Kirera, 2003, Dennis et al., 2004, King et al., 2005, Bunn and Ungar, 2009, Cuzzo et al., 2014). A high degree of surface angularity or 'jaggedness'

created by the exposed dentine is considered to be particularly beneficial for the breakdown of tough, pliant foods. Much like a serrated blade, this surface trait dramatically changes the direction of the forces acting on the food thereby increasing damage potential (Frazzetta, 1988, Ungar and M'Kirera, 2003). These findings heavily imply that although the crown has decreased in volume, the tooth is wearing in such a way that mechanical efficiency is maintained by encouraging the formation of cutting edges. However, as is also the case with koalas (Lanyon and Sanson, 1986), several studies have indicated that once the teeth have worn beyond a certain point, advantageous shape aspects such as surface angularity and crest sharpness also decline and so does the normal tooth function (Dennis et al., 2004, King et al., 2005, Venkataraman et al., 2014).

To date, the study of tooth functionality and wear in primates has predominately focussed on folivorous or generalist feeders including; the ring tailed lemur (Cuozzo et al., 2014), howling monkey (Dennis et al., 2004), sifakas (King et al., 2005), chimpanzees, and gorillas (Ungar and M'Kirera, 2003). Yet the effects of dental wear on the feeding efficiency of hard object feeders have remained relatively unknown. Similar to many herbivorous primates, hard object feeding is a mechanically demanding diet that has frequently been associated with high amounts of dental wear (Fleagle and McGraw, 1999, Fleagle and McGraw, 2002). Galbany et al. (2014) have already shown that proportionally, the hard object feeding mandrill (*Mandrillus sphinx*) has a significantly higher degree of wear than the yellow baboon (*Papio cynocephalus*) that predominately feeds on underground storage organs. From their findings they hypothesise that the accelerated dental wear in mandrills may represent an adaptation to process hard food items and propose that a flatter worn tooth may increase efficiency to process hard foods due to a uniform distribution of high occlusal force onto the food item (Kay, 1981). Additionally, sharp cusps may not be selected for as they are likely to produce higher stress in the enamel than in the food item therefore compromising the preservation of the tooth (Berthaume et al., 2013). However to date, dental wear and its associated shape changes has not been quantified across development in a hard object feeding primate. This chapter will attempt to expand on research by Galbany et al. (2014) by examining dental wear and associated shape changes in a developmental sample of the hard object feeding sooty mangabey (*Cercocebus atys*).

3.1.2. Quantification of gross occlusal wear

There are two main ways in which gross occlusal wear (macrowear) of a tooth can be quantified. The first is by measuring the amount of wear (i.e. how much dental tissue has been lost from the occlusal surface), which is typically inferred by measuring the amount of exposed dentine on the occlusal surface. The second approach is to quantify the shape changes that occur as a result of wear using current techniques in dental metrics. Both of these different avenues will be reviewed in the following two subsections.

3.1.2.1. Percentage of dentine exposure

Traditionally, the quantification of dental macrowear has relied on scoring methods, which involve a visual assessment of the tooth in order to rate the degree of wear based on a list of descriptions (Molnar, 1971, Scott, 1979a, Smith, 1984, Cuzzo et al., 2010). Although straightforward to use in practise, there is an element of subjectivity in this method. This has therefore prompted several researchers to use photographic images of teeth to calculate the percentage of dentine exposure (PDE) on the occlusal surface to improve objectivity and precision (Richards, 1984, Phillips-Conroy et al., 2000, Elgart, 2010, Galbany et al., 2011a, Clement and Hillson, 2013, Morse et al., 2013, Galbany et al., 2014). PDE is estimated by tracing dentine pools and dividing the total surface area of exposed dentine by the surface area of the occlusal surface. However, as discussed by Mayhall and Kageyama (1997) this method is limited in that it fails to capture the initial stages of tooth wear of the enamel prior to the exposure of dentine. Furthermore it does not record the loss of tissue mass or volume, or the loss of crown height. Nevertheless, PDE provides a relatively quick and intuitive method to indicate how much a tooth has worn since eruption. Furthermore, if recording the amount of wear on two adjacent molar teeth, the rate of wear can be calculated (Smith, 1972). To quote Scott (1979b: 203) “teeth have a “built in” rate indicator in that not all teeth erupt at the same time”. Therefore the differences in wear between the teeth can be used to indicate rate of wear (ratio of PDE). Assuming an individual’s wear rate remains constant throughout life, the rate of wear can be used as a comparison between different species regardless of age variation (Scott, 1979b).

Previously, Morse et al. (2013) quantified the PDE in *Cercocebus atys* to examine the pattern of wear across the postcanine row. In this study, the wear along the postcanine row was compared between three sympatric primate species that reside in the Taï forest in western Africa, which in addition to *C.atys*, included the western red colobus

(*Procolobus badius*) and the black and white colobus (*Colobus polykomos*). The results found that the distribution of wear varied across the rows indicating differences in tooth use across the species. Regarding *C.atys* the majority of wear occurred on the P4-M1 teeth thus implying the area most used in hard object feeding. However the level of wear was not documented across development. Furthermore, although PDE is important when measuring the magnitude of wear, it does not account for the associated morphological changes that ultimately affect the nature, magnitude and distribution of stress on the food item (Spears and Crompton, 1996a, Ungar, 1998). Therefore methods in quantifying dental morphology must also be sought.

3.1.2.2. Dental morphology

As discussed in chapter 1, there are a variety of different methods that can be used to quantify tooth morphology (see also Evans, 2013). However, many of these metrics are restricted to unworn teeth (e.g. Kay, 1978, Kay and Covert, 1984), or they have no meaningful output that can be directly related to functionality (e.g. Ungar and M'Kirera, 2003, Evans et al., 2007, Bunn et al., 2011).

In terms of tooth function, cusp form has been of great interest to previous researchers (Yamashita, 1998a, Hartstone-Rose and Wahl, 2008, Berthaume et al., 2010, 2013, 2014, Crofts and Summers, 2014). As cusps provide the first point of contact with the food item, they are highly involved in the process of crack initiation and propagation, which is essential for food breakdown. In accordance with this, the results from chapter 2 suggest that the angle, bluntness, and associated radius of curvature of a single cusp can greatly affect the mechanical performance to fracture brittle food items. However, throughout development, these features of the cusp are liable change as the enamel is worn away. For example, Evans (2005) found that in a sample of microchiropterans, the cusp tips classed with the least amount of wear had a significantly higher sharpness than worn specimens, which was indicated by a smaller radius of curvature. As demonstrated in chapter 2, the radius of curvature is a product of both angle and bluntness; therefore both of these may potentially be affected by the wear process.

However, the quantification of cusp morphology is necessarily restricted to specimens that have cusps. In the cases of extreme wear in primates, the cusps have commonly been shown to be entirely removed from the surface (Dennis et al., 2004, King et al., 2005). Therefore an alternative must be used to investigate other shape changes that may affect tooth functionality. Dental wear is often accompanied by a change in

convexity and concavity across the occlusal surface as a result of sharpening certain features or the formation of concavities where the enamel has worn away. In terms of dental topography, the quantification of mean curvature (ϕ) of the surface offers a way to encapsulate these changes by profiling the degree of concavity and convexity across the surface (Guy et al., 2013). Similar to other topographic techniques (e.g. Bunn et al., 2011), this method works using a polygon surface mesh where mean curvature is calculated for each polygon. A colour map can then be used to indicate the area and degree of concavity and convexity for the entire occlusal surface. Although this method has not previously been used to examine dental wear it could yield an interesting perspective on how dental topography may change throughout development.

3.1.3. Aims and objectives

The current literature suggests that in some primates the effects of dental wear are not always detrimental to an individual's survival, in contrast, wear may actually help to maintain masticatory efficiency throughout the majority of an individual's life (Ungar and M'Kirera, 2003, Dennis et al., 2004, King et al., 2005, Cuzzo et al., 2014, Venkataraman et al., 2014). However, the potential for wear to maintain functional aspects of tooth form across development has yet to be explored in specialist hard object feeders. The overall aim of this chapter is therefore to examine how the teeth wear across development in the hard object feeding primate *C. atys*. This species presents an interesting study group in terms of dental wear, as the diet appears to be highly specialised as soon as the permanent M1 is functional, where the teeth are used to fracture highly resistant endocarps (McGraw et al., 2011, Morse et al., 2013). Using a combination of different quantification methods, dental wear of the lower M1 will be examined in a developmental sample of *C. atys* to address the following research questions:

1. *What is the pattern of wear on the M₁ over the lifetime of C. atys?*

To answer the above question, the pattern of wear will be documented in *C. atys* based on a visual assessment of the occlusal surface. This will be accompanied by a quantification of the amount of wear on the tooth based on the percentage of exposed dentine (PDE).

2. *Does the functional shape of the M₁ change as the tooth wears in C. atys?*

The functional shape of the M₁ tooth of *C. atys* will be quantified throughout different stages of development based on cusp morphology (angle and radius of curvature) and the degree of concavity and convexity of the occlusal surface.

Given that the tooth is used for hard object feeding throughout development, it is predicted that once the tooth has worn to a certain level, the shape of the tooth will remain the same in order to maintain functionality.

3. *How does the rate of wear in a M₁ tooth of C. atys compare to other primate species?*

Using the data gathered on PDE, the rate of wear will be calculated by comparing the amount of wear on M1 when the M2 comes into occlusion. To gauge how quickly the teeth are wearing in relation to other primates, the results will be compared to the wear rates recorded by Elgart (2010) for species of *Pan* and *Gorilla*. Based on previous research (Galbany et al., 2014) it is expected that the rate of wear will be higher in *C. atys* due to its stress-resistant diet.

3.2. Materials and method

The following section outlines the materials and methods used to quantify dental wear and its associated morphological changes in a developmental sample of *C. atys*.

3.2.1. Sample

A total of 26 *Cercocebus atys* mandibles housed at the Hull York Medical School (HYMS) were used to form a developmental sample ranging from individuals with unerupted M1s through to adults with fully erupted M3 teeth (O'Higgins and Jones, 1998, O'Higgins and Collard, 2002). These individuals were previously wild shot in Sierra Leone, West Africa over a time span of 4 years during the 1950's. As these specimens were all located in the same region it is reasonable to assume they would have a similar dietary ecology. The mandibular first molar was singularly selected for analysis as it is the first permanent tooth to erupt thus presenting the broadest range of observable wear across development. Furthermore, this tooth is also known to be involved in hard object feeding behaviours (Morse et al., 2013). The M₁ was selected from the right quadrant of the mandible, which presented the best preserved teeth across the sample. Depending on the quantification method used, the sample size varied accordingly to suit the necessary prerequisites of the method (See Table 3.2).

3.2.1.1. Preparation of teeth for virtual analyses

For two of the morphological analyses (cusp radius of curvature and angle, and concavity/convexity profiling) it was necessary to create virtual 3D models of the teeth. A selection of the specimens was previously scanned using a microCT scanner (X-Tek Metris) at the University of Hull (Medical and Biological Engineering Research Group), where voxel size ranged between 0.099-0.153mm in the XY coordinates across the sample. Full details on the resolution for each scan are provided in Table B.1 in appendix B (p. 257). The microCT scans were then exported as stacks of TIFFS (image files) and then converted into 3D models using Avizo 8.0 commercial software (FEI). The production of a 3D model required a semi-automated segmentation to separate the dental crowns from surrounding bone, tissue and air based on a predefined grey scale. As this chapter is solely interested in dental morphology, the threshold was set to maximum density to capture the enamel. The segmentation for the entire sample was undertaken collaboratively by the author and Edwin Dickinson. Once segmentation was complete, surfaces were generated from the isolated teeth, which were smoothed and converted into a .ply surface file format for the analyses.

3.2.1.2. *Developmental categories*

In order to assess dental wear across ontogeny, it was first necessary to allocate each specimen to a developmental category. This was achieved using the eruption sequence of teeth; a technique that has commonly been used to provide information on life history and construct age estimations (Smith, 1994, Swindler, 2002). Apart from the M1, which is the first permanent tooth to erupt, the order of eruption naturally varies between different primate species (Swindler, 2002). As far as the author is aware the full order of eruption for living sooty mangabeys has yet to be published, therefore the deciduous and permanent teeth present in the mandible and cranium were documented for each specimen of this particular sample of *C.atys* to provide a rough estimate of eruption sequence (see Table B.2 appendix B, pp. 258-260). Although a larger sample size encompassing every state of eruption would be more ideal, the present sample suggests the order of dental eruption of the permanent teeth to follow a similar pattern seen in several other Old World primates; M1-I1-I2-M2-P3-P4-C-M3 (Swindler, 2002). This estimate is complimented by Morse et al. (2013), which presents the eruption sequence for the posterior teeth of *Cercocebus* as M₁, M₂, P₄, M₃, with the M₂ and P₄ erupting near simultaneously. Based on this eruption sequence, the specimens were allocated to one of five different stages from Stage 0 with an unerupted M1 (still developing in the crypt) to Stage 4 with M3 fully erupted and as such possessing a full permanent dentition (Table 3.1, Figure 3.2).

Table 3.1 Developmental stages used in study based on the eruption sequence in *Cercocebus atys*.

	Developmental stage	Description
0	Pre M1 eruption	All deciduous dentition are present to the M1 in the process of eruption.
1	M1 eruption	Any single M1 is fully erupted and appears in line with the occlusal plane to M2 partially erupted.
2	M2 eruption	Any single M2 is fully erupted and appears in line with the occlusal plane.
3	Partial M3 eruption	The presence of any single M3 in the process in erupting. This is indicated by the tooth protruding above the alveolar margin.
4	M3 eruption	Full eruption of all the M3 teeth where the M3 appears in line with the occlusal plane.

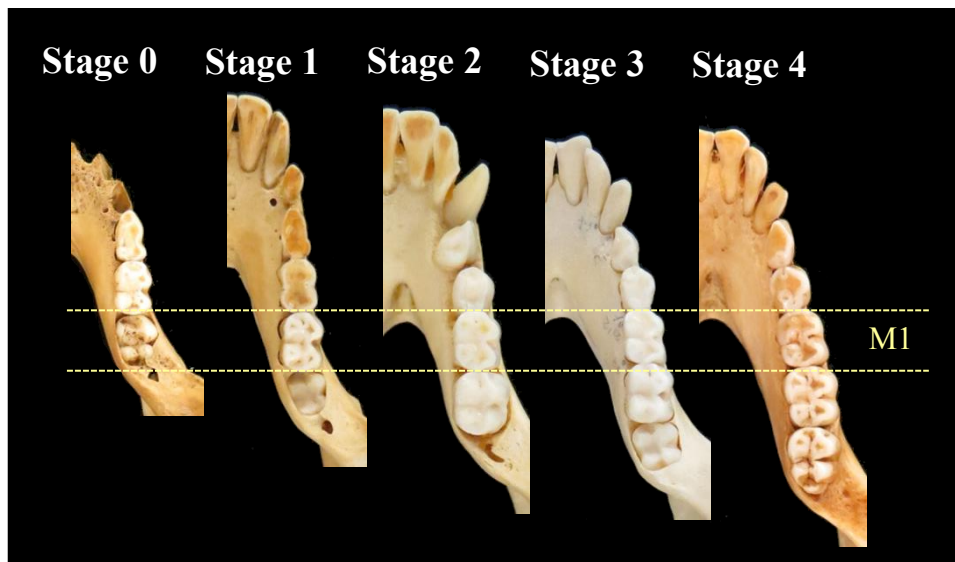


Figure 3.2 Mandibles of *C.atys* showing examples of the state of dental eruption for each developmental stage used in the study. Specimens used in figure (left to right) are C13.41, C13.33, C13.17, C13.11 and C13.29.

3.2.1.3. Dental chronology

Although the eruption sequence provides an estimate for developmental stage, it does not provide a precise indicator for absolute chronological age. Rather opportunely, the ages for some of the specimens in the sample have independently been estimated by Donald Reid (Newcastle Dental School) and have been made available by O’Higgins (per. comm.). Data was previously collected using the short-period and long-period incremental lines of the enamel and dentine tissues, the timings for crown formation and dental development were reconstructed in the sooty mangabey. Information on the daily secretion rates, periodicity, prism lengths and enamel thickness of upper and lower teeth of two *C.atys* specimens were then extrapolated to provide an age category of 3-6 month intervals for each specimen. These estimated ages provided by O’Higgins are included in Table 3.2 where available.

Table 3.2 Table displaying information for each *C. atys* specimen in the sample. Specimens used for each quantification study is indicated with an ‘X’.

Specimen	Sex	Estimated age	Eruption stage	Eruption details		PDE	Radius of curvature	Concavity/convexity profiling
				Cranium	Mandible			
C13.41	?	1.0-1.5	0	M1 unerupted	M1 unerupted (right M1 partially erupted)	X	X	X
C13.33	Female	3.5-4.0	1	M1 erupted -M2 partially erupted	M1 erupted-M2 partially erupted	X	X	X
C13.36 [†]	Female	NR	1	M1 erupted	M1 erupted	X	-	-
C13.42 [†]	Female	3.0-3.5	1	M1 erupted -M2 partially erupted	M1 erupted-M2 partially erupted	X	-	-
C13.43•	Female?	2.0-2.5	1	M1 erupted	M1 erupted	-	X	X
C13.17	Male	NR	2	M3 unerupted	M3 unerupted	X	X	X
C13.28	Female	5.0-5.5	2	M3 unerupted	M3 unerupted	X	X	X
C13.31	Male?	3.5-4.0	2	M3 unerupted	M3 unerupted	X	-	X
C13.35	Female	NR	2	M3 unerupted	M3 unerupted	X	-	X
Unknown 1 [†]	?	NR	2	-	M3 unerupted, P4 partially erupted	X	-	-
C13.1	Female	NR	3	M3 unerupted	Fully erupted	X	-	X
C13.3	Female	NR	3	M3 partially erupted	Fully erupted	X	-	X
C13.11 [†]	Female	5.0-5.5	3	M3 unerupted	M3 partially erupted	X	-	-
C13.12	Female	NR	3	M3 partially erupted	Fully erupted	X	-	X
C13.13*	Male	NR	3	M3 unerupted	M3 partially erupted	-	-	X
C13.20	Male	5.5+	3	M3 partially erupted	M3 near fully erupted	X	X	X
C13.26	Male	5.5+	3	M3 near fully erupted	Fully erupted	X	-	- (Damaged)
C13.27	Female	5.5+?	3	M3 partially erupted	Fully erupted	X	-	- (Damaged)
C13.2	Female	NR	4	Fully erupted	Fully erupted	X	-	X
C13.18 [†]	Male	NR	4	Fully erupted	Fully erupted	X	-	-
C13.19	Male	NR	4	Fully erupted	Fully erupted	X	-	X
C13.21	Male	5.5+	4	Fully erupted	Fully erupted	X	-	X
C13.22	Male	5.5+	4	Fully erupted	Fully erupted	X	-	X
C13.29	Female	5.5+	4	Fully erupted	Fully erupted	X	-	X
Unknown 2 [†]	Male	NR	4	-	Fully erupted	X	-	-
TOTAL						23	6	17

• Missing specimen, [†]No CT scan, *Occluded by soft tissue, NR=not recorded.

3.2.2. Percentage dentine exposure

Dental macrowear was assessed by calculating the percentage of dentine exposed (PDE) on the tooth surface. High resolution photographs were taken from each specimen using a Zeiss Stemi 2000-C stereo microscope fitted with a Moticam 2.0MP camera which produced images with a 1600-1200 pixel resolution. A section of the tooth row from M₁ to M₃ was positioned directly underneath the microscope so that the occlusal surface was parallel to the lens and the mesial-distal aspect of the tooth was aligned by eye to a flat plane. A millimetre scale was placed in line with the occlusal surface to allow for subsequent measurements to be taken. Following previous methods (Phillips-Conroy et al., 2000, Elgart, 2010, Galbany et al., 2011a, Clement and Hillson, 2013, Morse et al., 2013, Galbany et al., 2014), dentine pools and the occlusal surface of the M₁ and M₂ teeth were outlined using the image processing software ImageJ 1.46r (Abràmoff et al., 2004), and wear estimated by dividing the surface area of exposed dentine by the surface area of the occlusal surface (Figure 3.3).

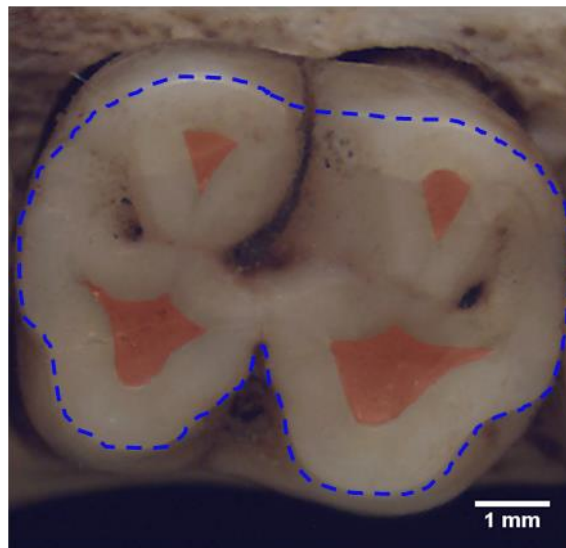


Figure 3.3 Illustration of the measurements used to estimate percentage of dentine exposure. The blue dashed outline indicates the perimeter of the occlusal surface where the occlusal area was taken, while the red shaded areas highlight regions of dentine exposure. Image is of a M₁ tooth of *C. atys* (specimen C13.31).

All measurements were taken by the author (KRS). A small study on intraobserver error, conducted by repeating measurements of a single specimen (C13.3) over 5 separate days, found the error to be low (Range= 0.242-0.251, \bar{X} = 0.247, SD=0.003). In the case of the specimen C13.41 that had an unerupted M1, wear was automatically classed as 0. None of the specimens in the sample exhibited any signs of ante-mortem tooth loss in both sets of dentition. For a small number of the individuals there was evidence of post-mortem enamel chipping but as the coloration was clear where the

enamel band was, the outline of exposed dentine could still be traced, therefore these specimens were included in the study. Specimen C13.13 was excluded from analysis because the upper and lower jaws were fully occluded due to the presence of soft tissue, thus the occlusal surfaces could not be observed. This analysis could also not be performed on specimen C13.43 because although the CT scan was present, the physical specimen was missing from the collection. Therefore the sample size for this analysis was restricted to 23. For a breakdown of the sample sizes for each eruption stage for the M1 and M2 teeth see Table 3.3.

Table 3.3 Sample size for each eruption stage for both M1 and M2 teeth that were used to estimate PDE and dental wear rate.

Eruption stage	Sample size (N)	
	M1	M2
0	1 (unerupted)	-
1	3	2 (unerupted)
2	5	5
3	7	5
4	7	6
TOTAL	23	18

3.2.3. Dental wear rate

Based on the percentage of dentine exposure of the M₁ and M₂, an estimate of dental wear rate was calculated. This was achieved using the principal axis technique (Scott, 1979b, Richards, 1984, Benfer and Edwards, 1991, Elgart, 2010). Scott (1979b) first advocated the use of this statistical technique over previously used methods including the correlation coefficient and regression analysis, as it does not assume a causal relationship between M1 and M2 wear variables nor that the X variable is measured without error. Therefore this method has been regarded as most suitable for expressing trends between the two molar variables (Scott, 1979b). A model II or major axis regression was performed in PAST using the measurements of wear on the M₁ and the M₂ once in occlusion. Based on the equation of the major axis, the slope was used to indicate how much the rate of wear in one tooth compares to the other and the y-intercept was used to indicate how much the first tooth (M₁) was worn down when the second tooth (M₂) is fully erupted. This analysis was performed on a subset of the sample that had both M₁ and M₂ at occlusion and was compared. In order to gauge how high the wear rate is in *C. atys*, the results are compared to the wear rate of *Gorilla* and *Pan* species that was collected using the same method by Elgart (2010). An additional

two analyses were also performed on males and females separately to investigate any potential sex differences in wear rate.

3.2.4. Quantification of cusp radius of curvature and angle

Cusp morphology was examined on the M₁ teeth using radius of curvature and angle measurements. Although mathematically quite simple, these measurements can be problematic when applied to tooth cusps, which are conical and naturally irregular in their geometry. This being the case, the angle and *R* values are likely to vary depending on where they are taken on the cusp point. In response to this, several previous studies have opted to taking measurements from predefined planes such as the buccolingual and mesiodistal directions based on 2D profile outlines or cross sections (Yamashita, 1998a, Berthaume et al., 2010, Frunza and Suci, 2013, Berthaume, 2014). However for this study, it was decided to take measurements from cross sections at the major and minor axes to allow for an approximate range of values to be taken from each cusp, which included the metaconid, protoconid, entoconid and hypoconid (Figure 3.4).

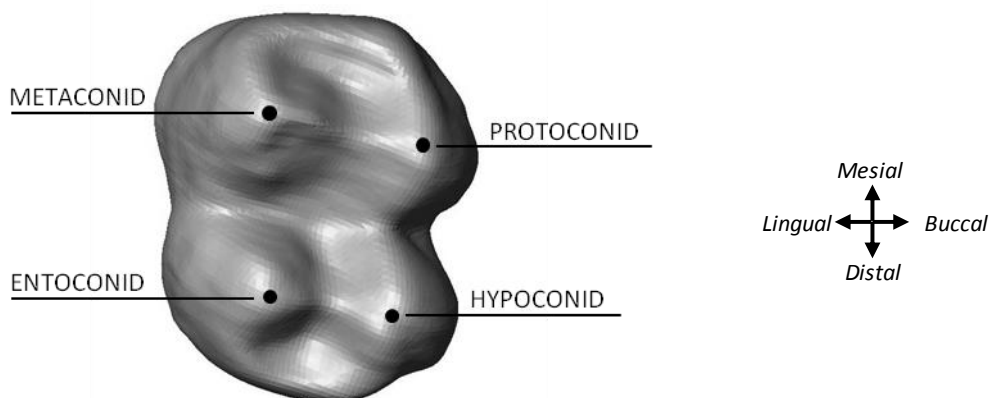


Figure 3.4 The cusps of a lower *C.atys* M1 that were quantified in this study using radius of curvature and angle measurements.

Prior to analysis the 3D surfaces of the teeth were first orientated to the same plane of reference. There are many different ways in which the lower teeth may be orientated in relation to the food item during mastication as the mandible rotates to open and close the jaw. This, as a result, determines the topography of the tooth in contact and the direction of force transmitted onto the food object. As the direction of the tooth when *C.atys* applies a bite is unknown, this study will assume that the bite direction is perpendicular to the occlusal surface.

Each specimen was aligned to a flat plane using three landmarks in the software Geomagic (2013). As this research focuses on the shape of the M1 tooth in relation to

function, it was decided to use a landmark configuration that best reflects this. According to previous research by Morse et al. (2013), there are two main teeth that form a functional complex during hard object feeding in sooty mangabeys. This complex comprises of P4/M1 teeth in adults, and DP4/M1 teeth in juveniles. With this in mind the first landmark was placed on the right M₁ at the most superior point of the distal-buccal aspect of the tooth and the second landmark was placed on the most superior point on the buccal side of the right DP₄/P₄. Assuming that the M1 teeth wear bilaterally at similar rate, the final landmark was placed on the most superior point of the distal-lingual part of the left M₁. Figure 3.5 shows how the teeth are positioned in relation to the flat plane where the lingual side of the teeth forms the first point of contact. Once oriented the P₄/DP₄ and left M₁ were deleted to isolate the right M₁ for analysis.

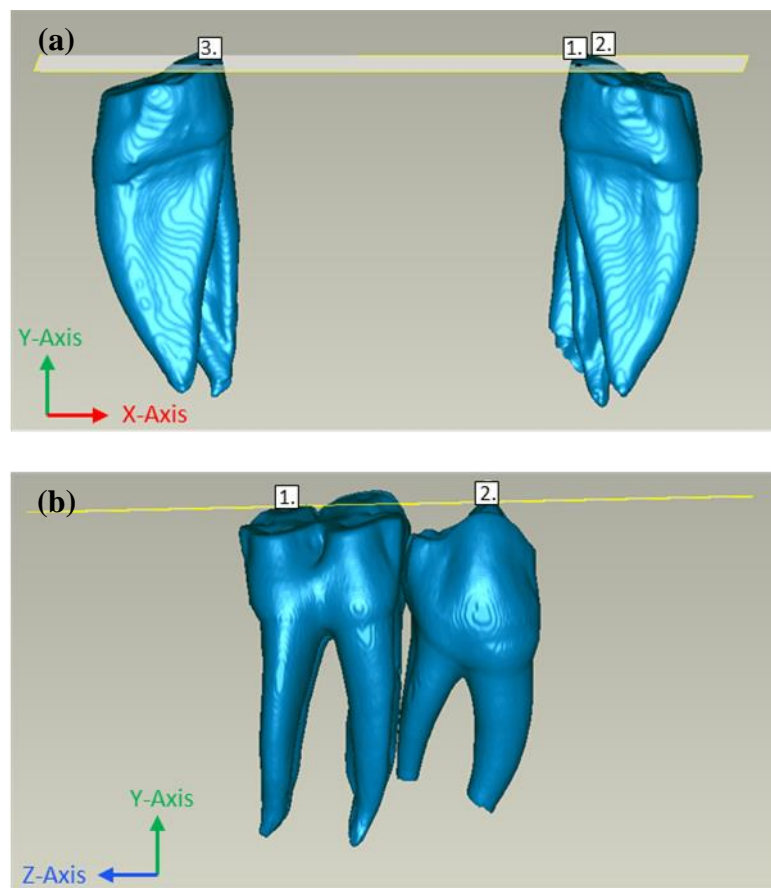


Figure 3.5 Demonstration of the process used to orientate the M₁ tooth to a flat plane using 3 landmarks situated on the functional complex; (a) distal view, (b) buccal view.

To estimate the major and minor axis, a flat plane was lowered on top of the occlusal surface of the M₁ tooth until it reached the base of each cusp, which was approximately just before the cusp starts to merge with the bucco-lingual bridge. A screenshot of the exposed cusp silhouette was then imported into imageJ 1.46r (Abràmoff et al., 2004)

and modified to expose the minor and major axes of the cusp base. This image was then superimposed over the cusp to direct the line of cropping in Geomagic (2013) and re-orientated so that the cross section was parallel to the viewer (Figure 3.6).

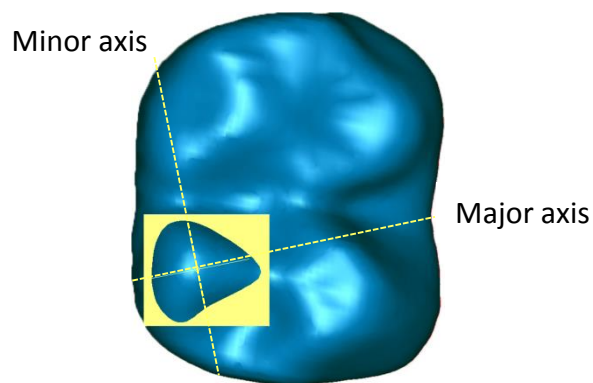


Figure 3.6 Image displaying the outline of the cusp base that was used to take major and minor cross sections of the cusp.

Radius of curvature was then calculated by fitting a circle to the cross sections using a circle fitting tool in Geomagic (2013). This involved placing two points lateral to the apex of a 2D curve so that the circle and curve osculate and the circle intersects the apex of the cusp. The subtended angle was then calculated by orientating lines at the sides of the cusp cross section starting from the base (Figure 3.7).

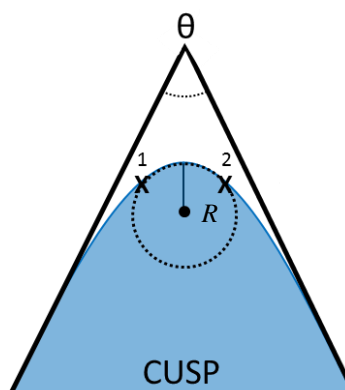


Figure 3.7 Image illustrating the analysis of cusp morphology. Measurements were taken from all or a selection of the cusps of the M_1 molar where radius of curvature and angle were calculated based on the major and minor cross sections of each cusp.

3.2.5. Concavity/convexity profiling

Naturally, the cusp radius of curvature and angle measurements outlined above can only be used on a small subsample as the cusps are not present on all of the specimens of different developmental stages. However, the use of concavity/convexity profiling will allow for an examination of the topographic shape changes across the entire sample.

An assessment of the degree of concavity and convexity of the M_1 was made by calculating the mean curvature (ϕ) for each polygon in the mesh. Mean curvature is derived from the mean value of the two principal curvatures, i.e. the maximum (k_1) and minimum (k_2) curvatures (equation 3.1), and essentially measures how much the surface deviates from flatness (Guy et al., 2013). The ϕ value can therefore be used to examine concavity and convexity, where negative values indicate concave regions and positive values indicate convex regions. In cases where the positive and negative principal curvatures cancel each other out, the ϕ value is close to or equal to 0, thus signalling flat areas. The greater the number deviates from 0 (flatness), the more extreme the degree of concavity or convexity (Guy et al., 2013).

$$\frac{(k_1 + k_2)}{2}$$

(3.1)

Mean curvature was calculated in the software Avizo 8.0 (FEI), which estimates the principal curvatures at each point by approximating the surface locally with a quadric form, where the eigenvalues of the quadric form are the curvature values and the eigenvectors are the directions of the principal curvatures. The ϕ values for each triangle can then be extracted in ASCII format and visually assessed by generating a colour map on the surface. Prior to analysis a small pilot study was conducted to examine the effects of orientation and simplification (reduction of triangles) of the surface on the mean curvature values. A basic dome was first created in SolidWorks 2014 (Dassault Systèmes SolidWorks Corp.) which was deformed in Geomagic (2013) by pulling the centre of the dome downwards, thus creating a shape that had both concave and convex aspects (Figure 3.8). Mean curvature was then calculated and the value for each triangle of the mesh recorded.

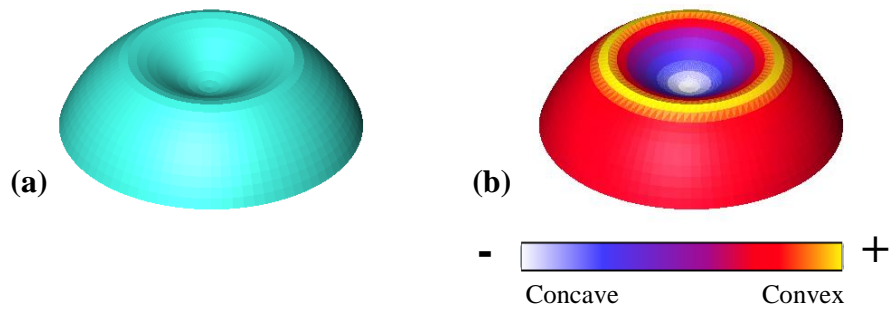


Figure 3.8 Basic bowl shape used in pilot study to investigate the effects of orientation and simplification on mean curvature values that varied in both concavity and convexity; (a) shows the original surface and (b) shows the surface with a colour map indicating mean curvature value.

To explore the effects of orientation, the same model was rotated by 45° (Figure 3.9) and ϕ re-estimated. It was expected that this action should not have an effect on the curvature calculations as the polygons themselves have not been altered; they have only moved within the global reference system.

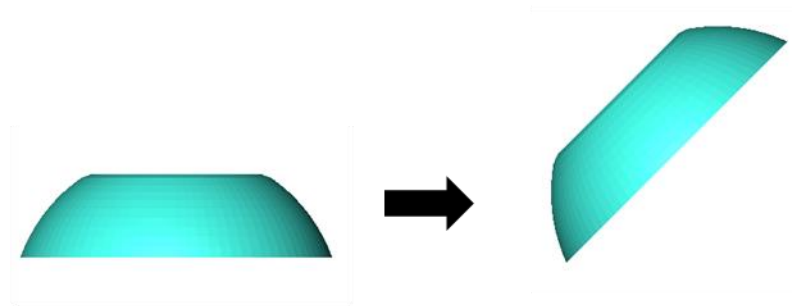


Figure 3.9 The rotation of the model by 45° to examine the effect of orientation on mean curvature.

The effect of surface simplification (also known as decimation) on mean curvature was then examined by reducing the number of triangles of the original model. This was achieved in Avizo 8.0 (FEI) using an edge collapsing algorithm where triangles are lost by converting edges into points (Figure 3.10a). The surface was reduced by 50% and 75% of the original triangle count (Figure 3.10b). Unlike orientation, the ϕ value is expected to be sensitive to surface simplification as the triangles are re-tessellated to approximate the original surface. Although generally the overall shape is maintained, this process can obfuscate certain geometries and alter the resolution of the tooth.

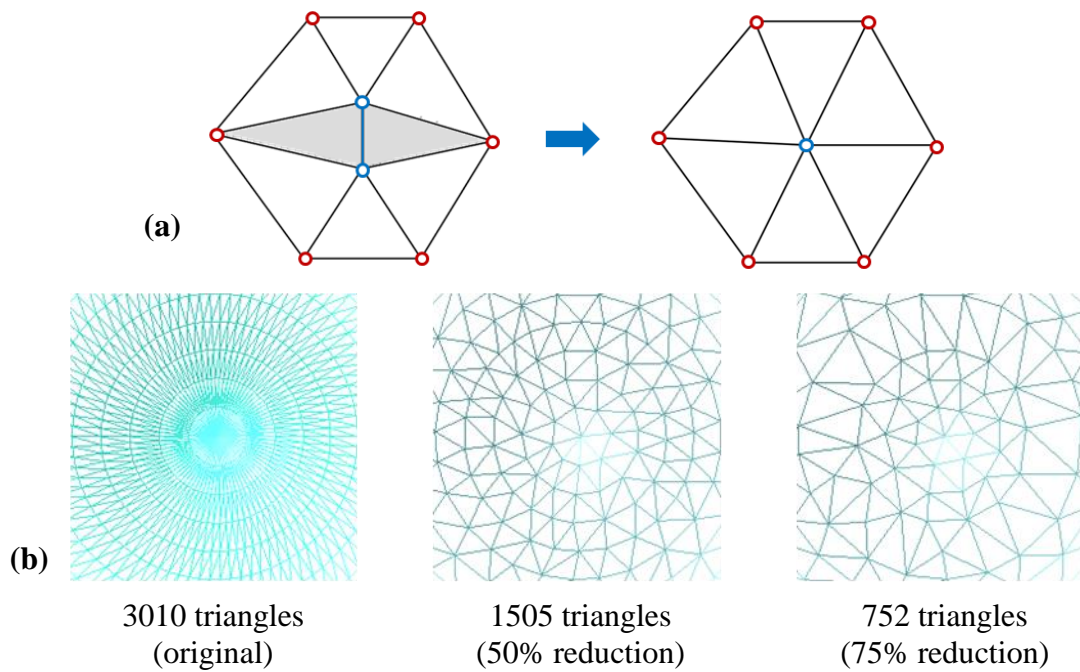


Figure 3.10 An illustration of the simplification process used in Avizo 8.0 (FEI). Surfaces were simplified using an edge collapsing algorithm where an edge (blue) was collapsed into a single point and the grey triangles removed from the mesh (a). Following simplification from the original, two further simplified models with a reduction in triangle count were produced (b).

As expected the act of rotating the model had no effect on the mean curvature values, therefore it can be concluded that this method is orientation independent (Table 3.4). However the simplification of the surface was shown to affect the mean curvature values where the surfaces with fewer triangles had a higher average ϕ value and a greater proportion of convex regions (Table 3.4).

Table 3.4 Results of pilot study examining the effects of orientation and simplification of a simple curved dome model on mean curvature values.

Surface	Triangle #	Mean curvature values (ϕ)							
		Mean	Median	Max	Min	# neg	#pos	% neg	% pos
Shape 1	3010	0.036	0.085	0.232	-0.286	860	2150	28.571	71.429
Rotated 45°	3010	0.036	0.085	0.232	-0.286	860	2150	28.571	71.429
Simplified 50%	1505	0.084	0.090	0.309	-0.274	186	1319	12.359	87.641
Simplified 75%	752	0.087	0.096	0.283	-0.282	113	639	15.027	84.973
Shape 2	3010	0.008	0.085	0.311	-0.541	946	2064	31.429	68.571
Simplified 50%	1505	0.070	0.091	0.442	-0.535	283	1222	18.804	81.196

To investigate whether two different shapes maintain the same proportion of convex and concave triangles once simplified a second model was made by increasing the concavity of the original shape (Figure 3.11). Interestingly when comparing the shapes with the original number of triangles, the second shape has an expected higher proportion of negative ϕ values. However, to compare a simplified version of shape 2

with the original shape 1, the proportion is lower (Table 3.4). Therefore, despite an attempt being made to generate the same shape, the number of triangles clearly has an effect on how the ϕ values are calculated.

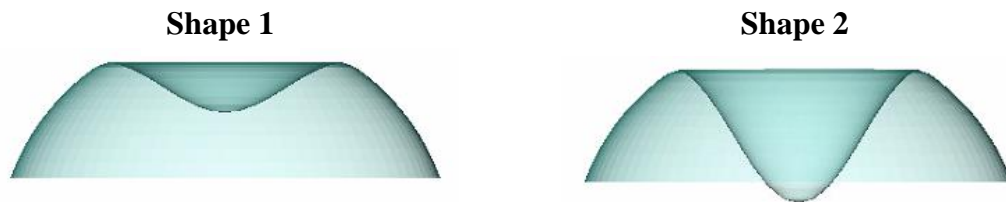


Figure 3.11 A comparison of the two shapes used to investigate sensitivity to mesh simplification, where shape 2 was created by extending the centre of shape 1 so as to increase concavity.

This presents an interesting finding as several studies that use polygon based dental metrics often simplify the surfaces to the same number of triangles prior to analysis (e.g. Bunn et al., 2011, Guy et al., 2013). This raises concern when applying this technique to different sized teeth where larger teeth naturally have a higher number of triangles than smaller teeth (if using the same scan resolution). Therefore by simplifying all of the surfaces to the same number of triangles could be detrimental when comparing shape differences between specimens. In contrast to Guy (2013), it was therefore decided against simplifying the surface in order to retain the gross morphological differences among the teeth.

For the mean curvature analysis of the *C.atys* sample, each tooth was first aligned in Geomagic (2013) so that the occlusal surface was parallel to a flat plane. The teeth were then cropped at approximately the cementoenamel junction to isolate the crown. Other dental topographic analyses have been known to use the lowest point of the talonid basin as a cropping reference (Ungar and M'Kirera, 2003), however this was not feasible in this study as many of the teeth had worn beyond this point. As orientation was not shown to influence mean curvature, a rigid translation was performed in Avizo 8.0 (FEI) so that all the teeth were in the same position for the purpose of the colour map images. The base was then removed as an artificial sharp edge was created where the base and the side of the tooth connect, which is likely to elevate the overall convexity values. Mean curvature values were then calculated for each polygon in Avizo 8.0 (FEI), which was displayed on the tooth using a colour map where cold shades indicate concave regions and warm colours indicate convex regions. Histograms were also made in order to display the percent frequency of mean curvature for each

specimen therefore providing an indication of the incidence of concavity and convexity on the occlusal surface.

3.3. Results

3.3.1. What is the pattern of wear on the M₁ over the lifetime of *C. atys*?

In order to examine the pattern of wear in *C. atys* a visual assessment was made of the occlusal surface at different developmental stages. This was accompanied by a quantification of the amount of wear on the tooth based on the percentage of exposed dentine (PDE). As the individual at stage 0 contains an unerupted M₁, this stage will not be discussed in relation to PDE.

3.3.1.1. Description of wear

The occlusal morphology of M₁ was shown to undergo several important changes throughout development. At stage 1 where the M₁ has just come into occlusion, the individuals have clear signs of dental wear on the cusp tips where small dentine windows have started to form (Figure 3.12). The least worn tooth in stage 1, based on the percentage of dentine exposure, was specimen C13.36, which exhibited a small amount of wear on the protoconid. This particular cusp was noticed to be the most worn in all of the specimens for this group suggesting it is the first cusp to wear.

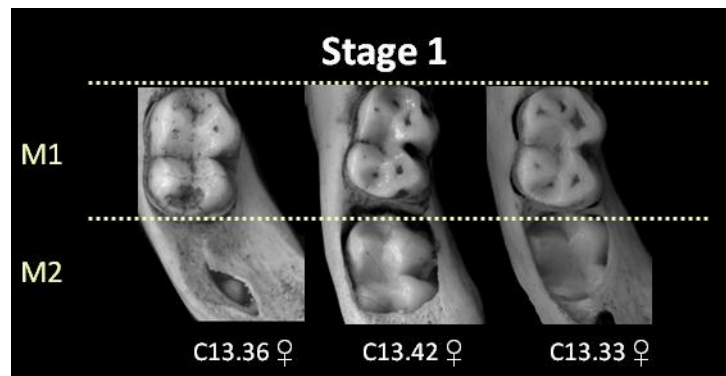


Figure 3.12 Images of dental wear in stage 1 individuals. Specimens are ordered based on increasing dentine exposure from left to right. Known sex is indicated where ♀=female and ♂=male.

At stage 2 where the M₂ has fully erupted, the dentine windows have widened and the cusps have started to become obfuscated (Figure 3.13). The cusp tips, which were previously rounded, have become flattened with an enamel ridge surrounding each dentine window. When considering both stages 1 and 2 of the present sample, the cusps

were observed to wear differentially with the buccal cusps experiencing the most amount of wear throughout development.

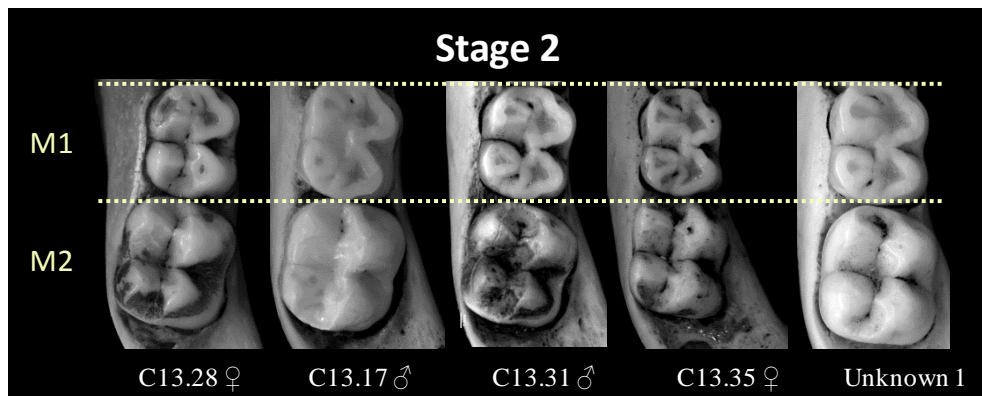


Figure 3.13 Images of dental wear in stage 2 individuals. Specimens are ordered based on increasing dentine exposure from left to right. Known sex is indicated where ♀=female and ♂=male.

Taking the results of wear stages 1 and 2 into account, the cusps appeared to wear in a sequence with the protoconid wearing first followed by the hypoconid, metaconid and finally the entoconid (Figure 3.14). This last cusp, which resisted wear for the longest amount of time, was shown to remain intact for one of the specimens in stage 2 (C13.28). This indicates that all cusps are lost very early on in development and occurs during the first 2 developmental stages.

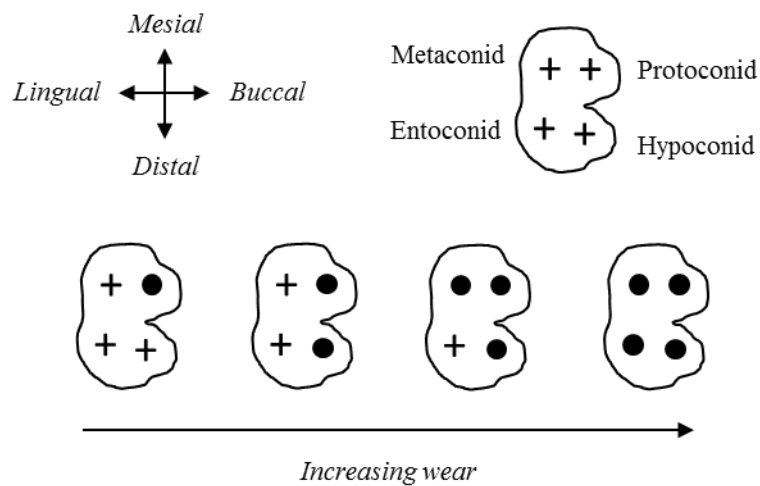


Figure 3.14 Schematic demonstrating the order of cusp elimination in a *C. atys* M₁ where cusps were observed to wear the most on the buccal side of the tooth. Crosses indicate cusps present, circles indicate cusp elimination.

Once the M3 is in the process of eruption (stage 3), the effects of wear on the M₁ were observed to further progress (Figure 3.15). The dentine windows where the cusps were situated continued to widen and in some specimens such as C13.27, have started to

merge buccolingually at each loph thus forming two dentine lakes. During stage 3 the outline of the tooth starts to take the appearance of a figure of 8 where two grooves have developed in the middle of the buccal and lingual sides of the tooth giving a waisted appearance (e.g. specimen C13.12, Figure 3.15). The mesial and distal aspects of the tooth were also noticed to form a flat edge where they meet the adjacent teeth.

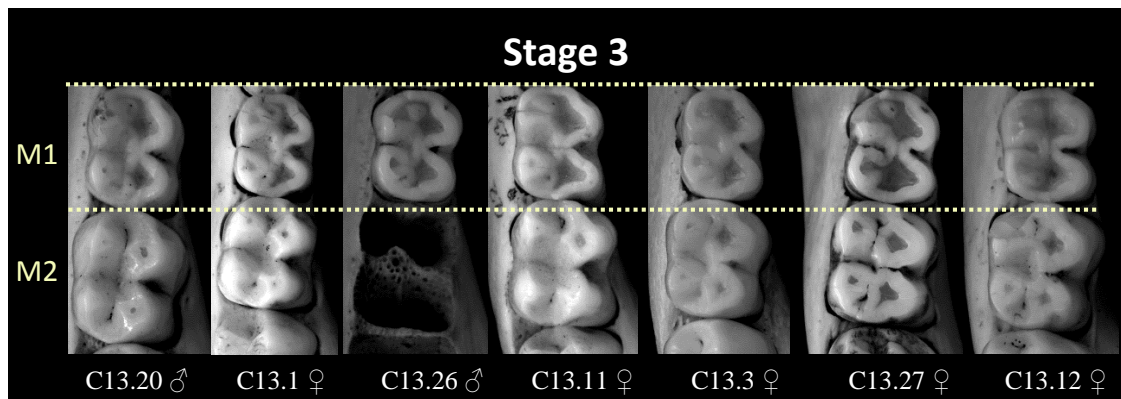


Figure 3.15 Images of dental wear in stage 3 individuals. Specimens are ordered based on increasing dentine exposure from left to right. Known sex is indicated where ♀=female and ♂=male.

By stage 4, when all permanent teeth are fully erupted, any remnants of the cusps have been entirely obliterated from the occlusal surface in the majority of specimens (Figure 3.16). In the least worn teeth of this group the two dentine lakes have started to merge in the centre and an enamel band is visible at the perimeter of the occlusal surface. There is also considerably less enamel present in the inner area of the occlusal surface in comparison to the preceding stages. In the later phases of stage 4, the enamel is solely confined to the outer periphery of the tooth enclosing a single pool of dentine in the centre. The shape of the occlusal outline as a figure of 8 is also much more distinctive in the more worn teeth.

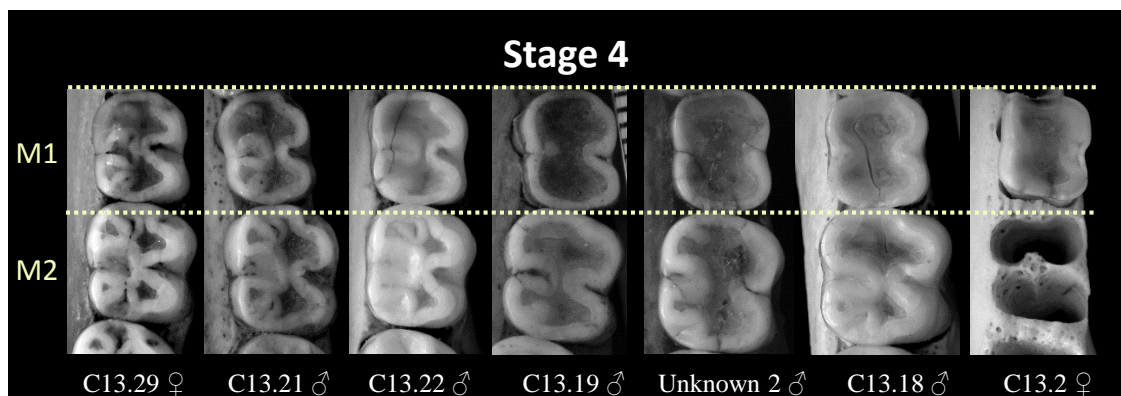


Figure 3.16 Images of dental wear in stage 4 individuals. Specimens are ordered based on increasing dentine exposure from left to right. Known sex is indicated where ♀=female and ♂=male.

3.3.1.2. Percentage of dentine exposure

The results of the analysis of dentine exposure clearly demonstrate that dental wear of the M_1 starts early once the tooth has fully erupted (Figure 3.17). While stage 0 has no level of dentine exposure, by stage 1 dentine was recorded in all the specimens of this group. Of this stage the smallest amount of wear was found in specimen C13.36, which had a PDE value of 0.3%. From this point onwards the M_1 was shown to steadily increase in wear throughout development with significant differences detected between the group means as determined by a Welch F test ($F=25.25_{9,771}$, $p=6.36E-05$) (Figure 3.17).

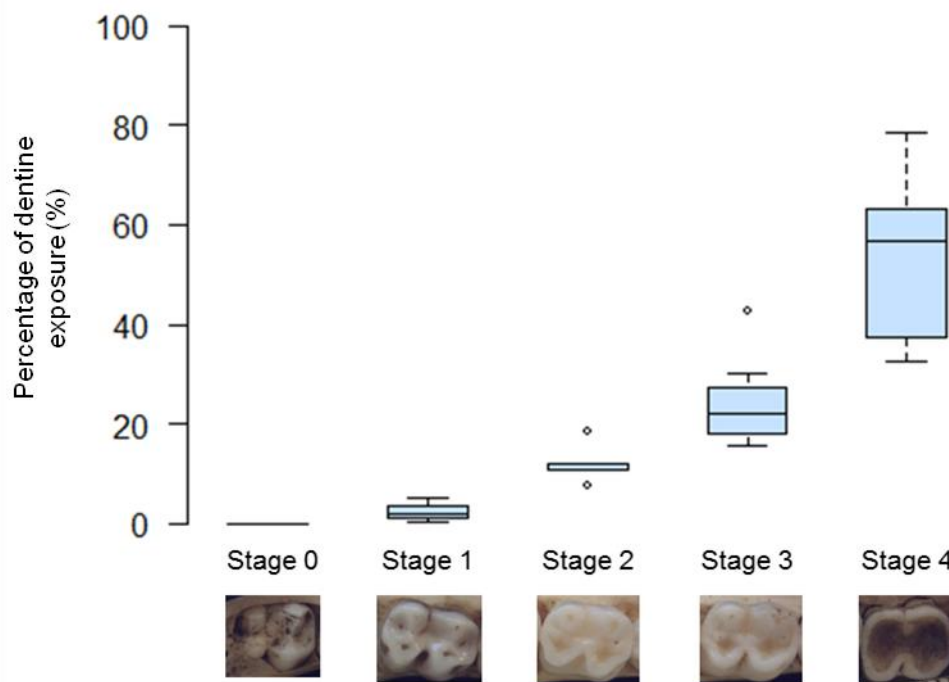


Figure 3.17 Percentage of dentine exposure of the M_1 for each developmental stage. Images display an example of a M_1 for each stage.

By stage two, the average PDE value had increased by over 9% from stage 1, however no significant differences were found between the two stages ($p<0.001$) (Table 3.5). A further difference in averages was found between stage 2 and 3 where PDE had increased by 12.5%. Again no significant differences were found between these two groups however an outlier (unknown 1) of stage 2 was shown to overlap with stage 3. By stage 3 the PDE values were much more variable ranging between 15.5% and 42.6%. Compared to the average, the upper value measured from C13.12 was extremely high showing a great deal of overlap with stage 4. The final group, stage 4 was found to be significantly different to both stages 1 and 2 ($p<0.001$) and exhibited the greatest amount of within-group variability ($SD=17.27$). The PDE values ranged from 32.7% in

specimen C13.29 to 78.7% found in specimen C13.2. Based on the average PDE the amount of wear was shown to drastically increase by 28.4% from stage 3.

Table 3.5 Averages and standard deviations of the percentage of dentine exposure on the M₁ for each developmental stage.

Stage	N	Percentage dentine exposure (%)	
		Avg.	St. Dev.
0	1	n/a	n/a
1	3	2.53	2.54
2	5	11.95	3.95
3	7	24.44	9.43
4	7	52.79	17.27

Percentage of dentine exposure was also examined in the M₂ (Figure 3.18), which has not been associated with hard object feeding behaviours in the sooty mangabey. For this tooth, the amount of wear could not be assessed until stage 2 when the M₂ teeth had fully erupted. At this stage there were no signs of wear in 3 of the 5 specimens. In the ones that did exhibit wear; the PDE value was extremely low measuring 0.7% and 0.1%. Wear was shown to increase across the 3 developmental stages however no significant differences were found between the group means (Welch F test: $F=13.63_{5,973}$, $p=0.005942$).

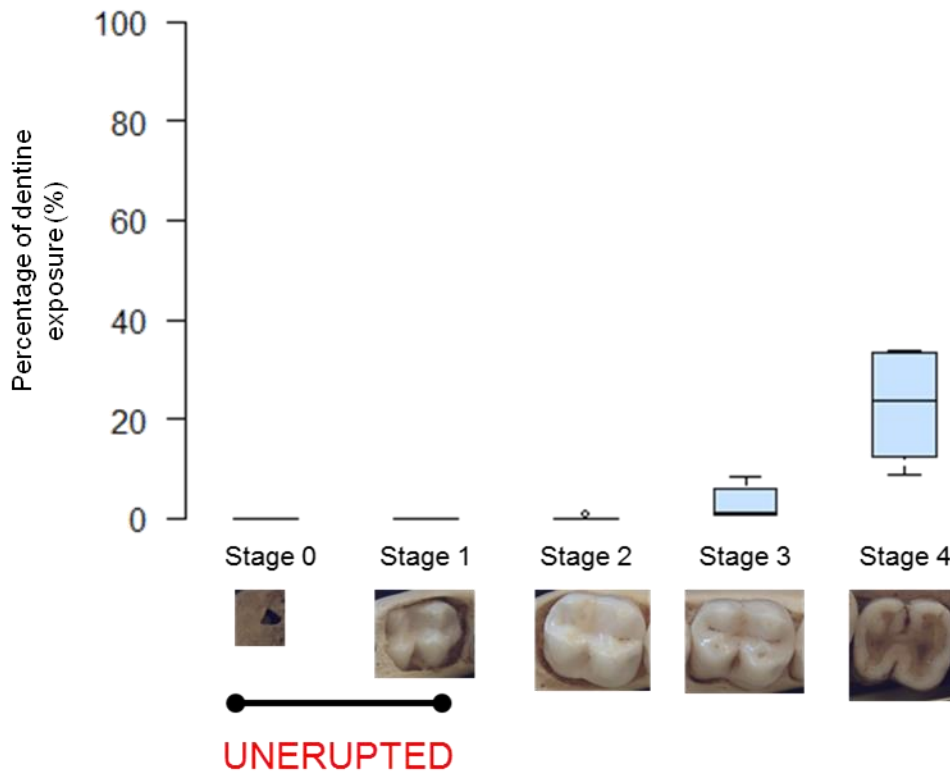


Figure 3.18 Percentage of dentine exposure of the M₂ for each developmental stage. Images display an example of a M₂ for each stage.

Based on the averages (Table 3.6) the PDE values increased slightly (3.3%) from stages 2 to 3. In stage 3 the amount of wear was quite varied ranging between 0.92% in specimen C13.1 to 8.34% in specimen C13.27. From stage 3 to stage 4, the average PDE value drastically increased by 19.2%. The results for this stage were even more varied ranging between 9% in specimen C13.22 to 33.9% in C13.19.

Table 3.6 Averages and standard deviations of the percentage of dentine exposure on the M₂ for each developmental stage.

Stage	N	Percentage dentine exposure (%)	
		Avg.	St. Dev.
0	1	n/a	n/a
1	2	n/a	n/a
2	5	0.15	0.29
3	5	3.46	3.54
4	6	22.70	10.82

Does the functional shape of the M₁ changes as the tooth wears in *C.atys*?

In order to assess any shape changes or maintenance in functional dental morphology, the M₁ tooth of *C. atys* was quantified throughout different stages of development based on cusp morphology (angle and radius of curvature) and the degree of concavity and convexity of the occlusal surface, results are presented below.

3.3.1.3. Quantification of cusp morphology

In terms of cusp morphology, it is clear that the unworn cusp shape is not retained throughout development. In the case of *C.atys*, the initial bilophodont tooth form is quickly worn down, causing the tips of the cusps to flatten (Figure 3.19). For many of the specimens small indents were also observed to appear at the centre of the cusps as a result of the formation of dentine windows. As a consequence of this cusp flattening, only 6 out of the 19 specimens available with CT scans possessed cusp tips that could be used to record measurements of radius of curvature and angle. Furthermore, as the cusps individually experience different levels of wear, not all the cusps of the same molar could be analysed in some of the specimens.

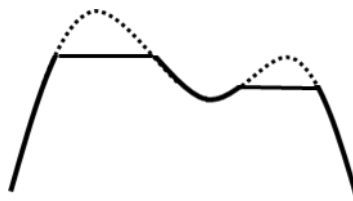


Figure 3.19 Diagram of a M1 tooth in lateral view displaying how the unworn state of the cusps (dashed line) are flattened (solid line) as a result of dental wear.

Only two specimens from stages 0 and 1 (C13.41 and C13.43 respectively) presented teeth in which measurements could be taken from every single cusp (Table 3.7). For the remaining individuals values were taken where possible. The highest number of measurements for both *R* and angle were recorded from the entoconid cusp. In contrast, the protoconid and hypoconid provided the lowest number of measurements. This finding was not surprising when considering the observed order of cusp wear (Figure 3.14 p. 144). Due to the small sample size it was difficult to detect any clear patterns and trends between the different developmental stages, or apply any statistical analysis. However several observations were made from the data collected.

Table 3.7 Radius of curvature values for the cross sections of the minor and major axis of each cusp. Highest and lowest values recorded are shown in bold. Dashes indicate where measurements could not be taken due to wear.

Specimen	Eruption stage	Metaconid		Protoconid		Entoconid		Hypoconid	
		Minor	Major	Minor	Major	Minor	Major	Minor	Major
C13.41	0	0.70	0.68	0.71	1.28	0.77	0.91	0.87	1.42
C13.43	1	0.64	0.65	0.79	1.22	0.71	0.75	0.70	1.45
C13.33	1	0.57	-	-	-	-	0.76	-	-
C13.28	2	-	-	-	-	0.89	0.72	-	-
C13.17	2	0.68	-	-	-	0.87	0.98	-	-
C13.20	3	-	1.19	-	-	0.69	-	-	-

The radius of curvature values varied considerably between the different cusps and between the minor and major axis of each cusp. Based on the two unworn specimens the sharper cusps were generally the metaconid and entoconid located on the lingual side of the tooth whereas the blunter cusps, particularly on the major axis, were the protoconid and hypoconid on the buccal side of the tooth. Out of the values recorded the smallest radius of curvature was 0.57mm, which was taken from the minor axis of the metaconid of specimen C13.33 whereas the largest value measuring 1.45mm was taken from the major axis of the hypoconid of specimen C13.43 (Figure 3.20).

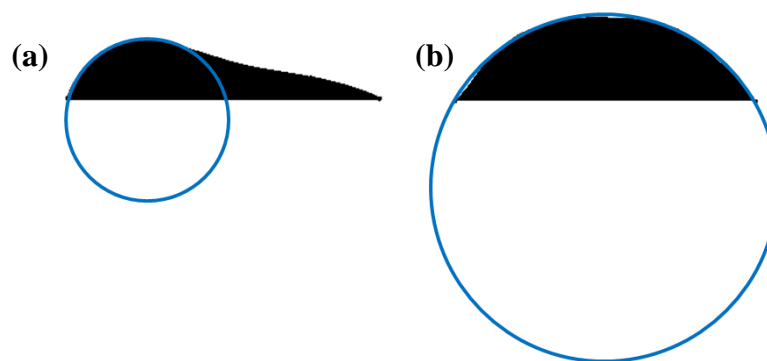


Figure 3.20 Diagrams displaying the two extremes of radius of curvature values recorded from the cusp cross sections of the sample; (a) shows the smallest radius of curvature taken from the minor axis of the metaconid of specimen C13.33 and (b) shows the largest radius of curvature taken from the major axis of the hypoconid of specimen C13.43.

In terms of angle, the number of measurements recorded was slightly higher than for radius of curvature as this did not rely on the shape of the cusp tips (Table 3.8). The measurements were again observed to vary between the different cusps and between the minor and major axes. Based on the stage 0 tooth (C13.41) the protoconid presented the widest angle measurements followed by the hypoconid, which are both located on the buccal side of the tooth. Specimen C13.43 of stage 1 development again showed the protoconid to be the widest in angle but the remaining cusp measurements were much

more similar in value. However how much the difference between the specimen from stage 0 and the specimen from stage 1 is due to wear or by individual variation is unknown. Overall the smallest angle measurement was taken from the minor axis of the metaconid of specimen C13.20, which was 52.36°, whereas the widest angle was over double the size of this measuring 148.05° based on the major axis of the protoconid of specimen C13.41.

Table 3.8 Angle values for the cross sections of the minor and major axis of each cusp. Highest and lowest values recorded are shown in bold. Dashes indicate where measurements could not be taken due to wear.

Specimen	Eruption stage	Metaconid		Protoconid		Entoconid		Hypoconid	
		Minor	Major	Minor	Major	Minor	Major	Minor	Major
C13.41	0	63.11	70.92	135.45	148.05	67.17	71.74	115.80	102.43
C13.43	1	97.93	87.02	113.34	101.54	91.65	102.61	90.63	81.58
C13.33	1	92.63	100.60	-	-	82.84	87.18	-	-
C13.28	2	-	-	-	-	66.52	82.94	-	-
C13.17	2	75.77	115.77	-	-	118.52	115.72	-	-
C13.20	3	52.36	101.16	-	-	73.77	87.41	-	-

3.3.1.4. Quantification of concavity and convexity of the occlusal surface

In order to investigate any changes in the magnitude and distribution of concavity and convexity on the occlusal surface throughout development, the mean curvature was calculated for each triangle of the M₁ for a subset of the original sample. Several of the specimens were not included in this analysis due to the lack of an available CT scan or the M₁ was damaged in such a way that may affect the mean curvature values. Concavity and convexity results are presented below.

At stage 0, the unworn M₁ represented by specimen C13.41 exhibits a high contrast in mean curvature values showing both extremely convex (yellow) and concave (white) regions (Figure 3.21). The most convex or “hottest” features of the tooth are located at the tips of the cusps, the crests joining the buccal and lingual cusps and the edge of the tooth in both mesial and distal aspects. This is contrasted with highly concave or “cold” regions found in the occlusal basins and grooves. Interestingly the overall morphology appears to emphasise both concavity and convexity with little indication of flatness across the surface.

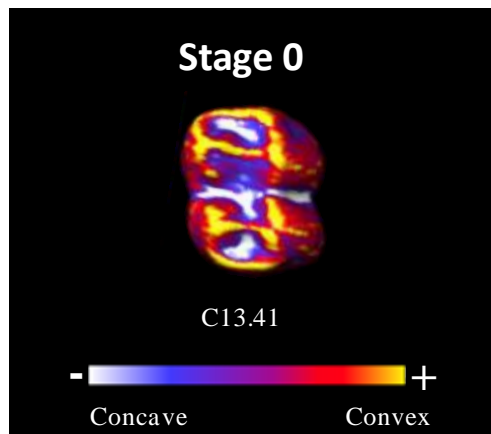


Figure 3.21 Stage 0 mean curvature colour map where cold colours indicate concave regions and warm colours indicate convex regions.

For stage 1, the newly erupted M_1 was represented by two specimens, which exhibited two very different morphologies (Figure 3.22). Specimen C13.43 appeared to more closely resemble C13.41 of stage 0 where the extremes of concavity and convexity were evident on the basins and cusps. However the convexity of the crest joining the cusps in the buccal-lingual direction was much less prominent in this specimen. In contrast, specimen C13.33 showed a much more drastic change in morphology from stage 0. The cusps, which were previously four highly convex points, were now shown to flatten with a small concave pit developing at the centre surrounded by a convex outer band. Of the four cusps of this specimen, the protoconid had the highest degree of concavity.

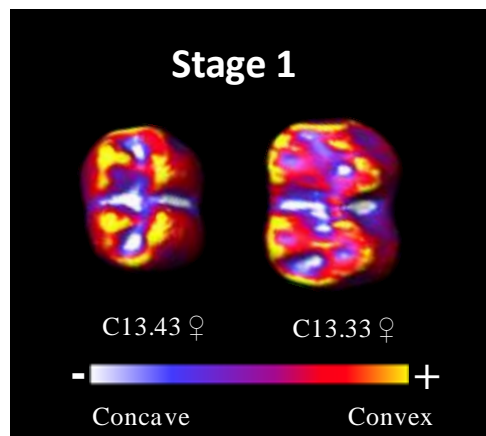


Figure 3.22 Stage 1 mean curvature colour maps where cold colours indicate concave regions and warm colours indicate convex regions. Specimens are ordered based on increasing dentine exposure from left to right. Known sex is indicated where ♀=female and ♂=male.

The specimens of stage 2 (Figure 3.23) continued to exhibit an overall morphology similar to that of C13.33 of stage 1 (Figure 3.22). Only one of the specimens (C13.28) had retained a cusp which resembled the unworn state of stage 0. The remaining cusps of the sample showed small concavities at the top or were completely flattened. In one

of the specimens (C13.35) the protoconid appeared to be completely obliterated from the surface. Generally, the entire occlusal surface increased in flatter regions indicated by purple colouring, which was particularly prominent in specimens C13.17 and C13.35. Any convex regions were largely restricted to the outer perimeter of the tooth and varied in magnitude between high (yellow) and moderate (red). These regions generally gave the appearance of a ridge which enclosed a mixture of flat and concave morphologies within.

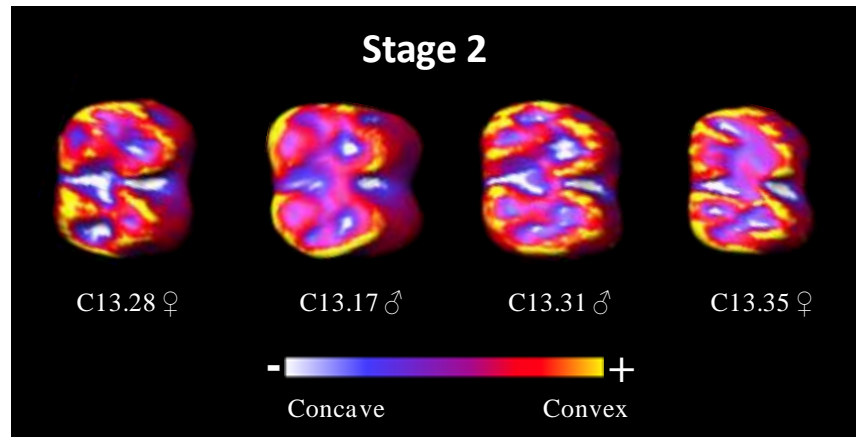


Figure 3.23 Stage 2 mean curvature colour maps where cold colours indicate concave regions and warm colours indicate convex regions. Specimens are ordered based on increasing dentine exposure from left to right. Known sex is indicated where ♀=female and ♂=male.

In stage 3 (Figure 3.24), the M₁ teeth mostly showed characteristics similar to that described in stage 2 (Figure 3.23). However there were some changes observed in the occlusal morphology. The most notable of these was the further development of a ridge at the periphery of the tooth, which generally appeared higher in convexity than stage 2. Some of the highly concave pits where the buccal cusps were previously situated also appeared to increase in size.

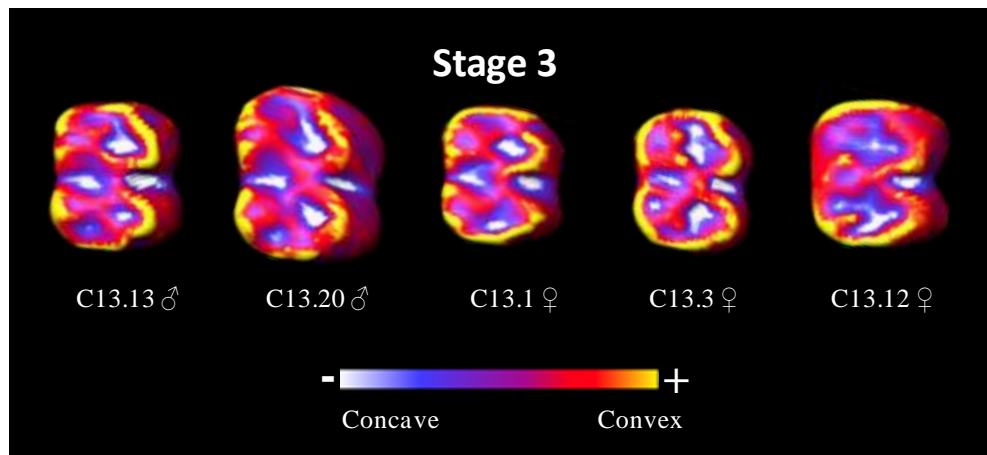


Figure 3.24 Stage 3 mean curvature colour maps where cold colours indicate concave regions and warm colours indicate convex regions. Specimens are ordered based on increasing dentine exposure from left to right. Known sex is indicated where ♀=female and ♂=male.

By stage 4 (Figure 3.25), when all permanent teeth are fully erupted, the specimens with low amounts of wear presented a similar pattern of convexity and concavity to stages 2 and 3 (Figure 3.23, Figure 3.24). However it was noted that any traces of the cusps were near completely gone and the concavities on the surface were larger and less extreme in magnitude. The more worn M_1 teeth of this category, on the other hand, showed signs of diverging in morphology from the previous stages. These specimens exhibited a distinctive morphology where the highly convex ridge at the perimeter had further developed and surrounded a single, concave pool of dentine. The overall appearance was less complex than the other M_1 morphologies and greatly contrasted with the initial unworn state (Figure 3.21).

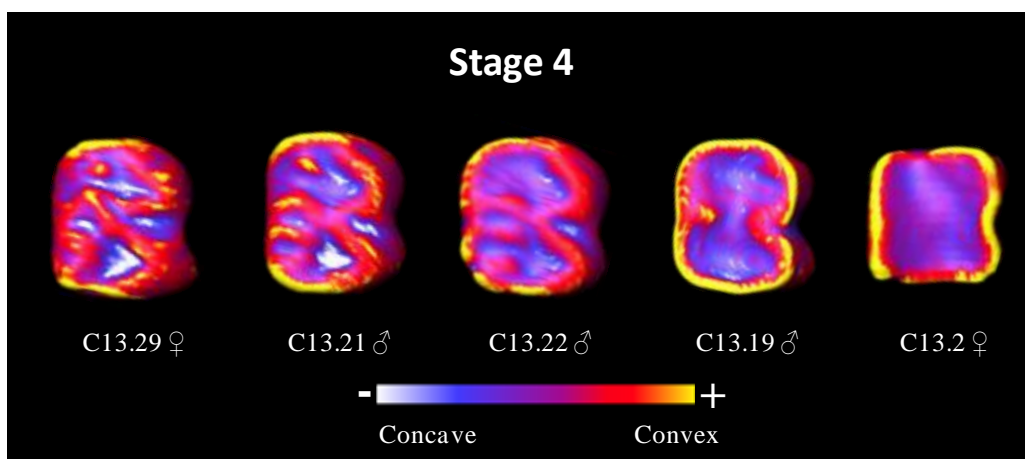


Figure 3.25 Stage 4 mean curvature colour maps where cold colours indicate concave regions and warm colours indicate convex regions. Specimens are ordered based on increasing dentine exposure from left to right. Known sex is indicated where ♀=female and ♂=male.

Examples of the histograms of the percentage frequency of mean curvature are provided for each developmental stage in Figure 3.26 (for each individual specimen see appendix B pp. 262-265). For the majority of individuals the ϕ values ranged between -5 to 5 for the entire occlusal surface. There were some exceptions to this where extremely high or low numbers were produced, which was likely the result of minute pits or cracks on the surface. These triangles were therefore omitted from the study. The highest frequency of mean curvature value for all of the specimens was between 0.4-0.6, with the exception of C13.2, which had a highest frequency ϕ value between 0-0.2. Regardless of developmental stage, the majority of specimens showed a similar distribution pattern of frequency for ϕ values (Figure 3.26). However in some of the specimens in stage 4 that were highly worn were noted to deviate from this pattern and were less evenly distributed around the peak value (Figure 3.26: stage 4).

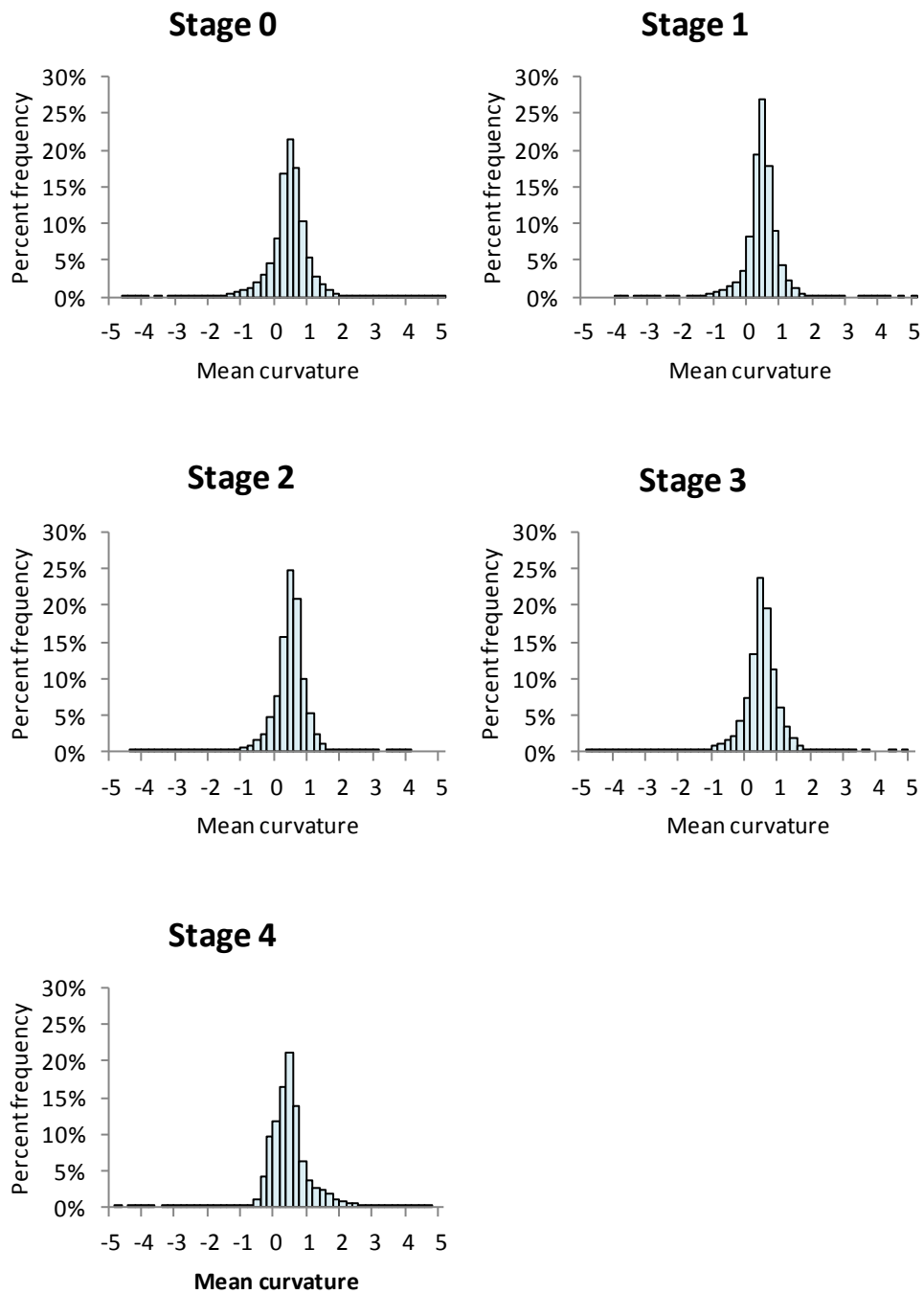


Figure 3.26 Examples of the histograms showing the percent frequency of mean curvature values from each developmental stage; Stage 0= C13.41, Stage 1= C13.33, Stage 2= C13.28, Stage 3 = C13.13, Stage 4= C13.19.

3.3.2. How does the rate of wear in a M₁ tooth of *C. atys* compare to other primate species?

To examine the rate of wear in *C.atys* a Model II regression was performed of the wear on the M₁ and M₂ by calculating the line using a major axis equation. Given that M₂ was unerupted, missing or damaged in several of the specimens, this analysis was restricted to a sample size of 16 and naturally excluded specimens from stages 0 and 1. Figure 3.27 shows the major axis regression where the specimens of each stage are indicated by colour. Three of the specimens (C13.18, C13.19, unknown2) from stage 4 (shown in red) were observed to stand out in the graph as being particularly worn in both M₁ and M₂ teeth.

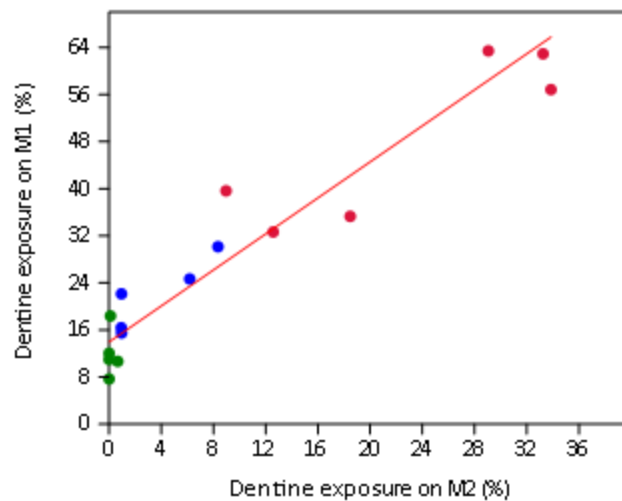


Figure 3.27 Major axis regression of the wear on M₂ and M₁ where stage 2= green, stage 3=blue and stage 4=red. Equation of the line provided in Table 3.9.

In comparison to species of *Gorilla* and *Pan* (Figure 3.28, Table 3.9), the wear rate indicated by the slope of the line, was found to be highest in *C.atys*, which was closely followed by *Pan paniscus*. In contrast the lowest wear rates were found in *P.t. schweinfurthii* and *Gorilla g. graueri*. Based on the regression's intercept, the amount of wear on M₁ when M₂ comes into occlusion was also shown to be highest in *C.atys*, which was followed by *Gorilla g. graueri*.

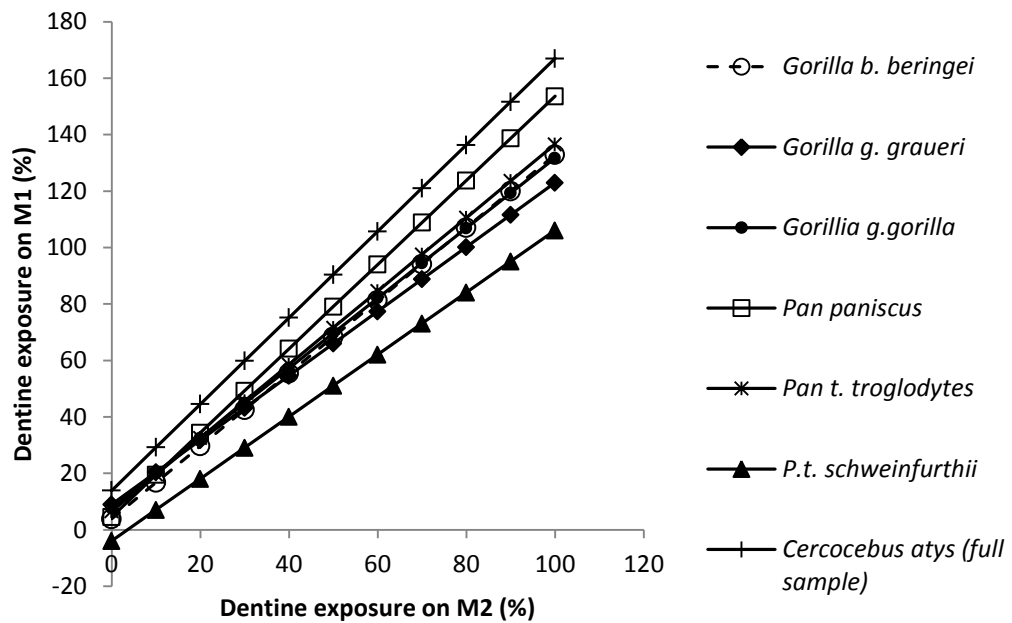


Figure 3.28 An interspecific comparison of the major axis lines for dental wear rate. Data for *Gorilla* and *Pan* were obtained from Elgart (2010). Equations of the lines are provided in Table 3.9.

The major axis equation was also compared between males and females in *C.atys* (Table 3.9). Based on the present sample the rate of wear was found to be higher in the females than the males. However in terms of the amount of wear on M1 when M2 comes into occlusion the values were extremely similar.

Table 3.9 Equations of the Major Axis from Model II regression for each species. For *C.atys* the MA equation was also calculated for males and females separately. 95% confidence intervals for the slopes are also provided for each equation.

Group	N	Equation of major axis	95% confidence interval of slope
<i>Gorilla b. beringei</i> *	16	$y = 1.29x + 3.9$	1.2-1.5
<i>Gorilla g. graueri</i> *	28	$y = 1.14x + 9.0$	1.0-1.5
<i>Gorilla g. gorilla</i> *	68	$y = 1.24x + 7.7$	1.1-1.4
<i>Pan paniscus</i> *	16	$y = 1.49x + 4.6$	1.0-2.0
<i>Pan t. troglodytes</i> *	52	$y = 1.30x + 6.6$	1.2-1.5
<i>P.t. schweinfurthii</i> *	7	$y = 1.10x - 3.9$	0.8-1.1
<i>Cercocebus atys</i> (full sample)	16	$y = 1.53x + 13.97$	1.1-1.8
Males	7	$y = 1.55x + 12.67$	1.2-1.8
Females	6	$y = 1.98x + 12.63$	-0.6-2.7

* Data obtained from Elgart (2010).

3.4. Discussion

How teeth wear during the lifespan of an individual can provide a wealth of information regarding the dietary ecology of a species. The rate of wear, and the ways in which teeth change or maintain their shape has previously been linked to dietary adaptations in primates (Ungar and M'Kirera, 2003, Dennis et al., 2004, King et al., 2005, Elgart, 2010, Cuzzo et al., 2014, Venkataraman et al., 2014), however, little is known about the ontogeny of dental form and function. *Cercocebus atys*, being a specialist hard object feeder, provides an excellent opportunity to investigate this where adults and juveniles feed on the same stress resistant food items throughout life (McGraw et al., 2011), yet the adults have been observed to exhibit high amounts of dental wear (Morse et al., 2013). The results of this study have described and quantified how the M₁ tooth wears in this hard object feeding primate, *C. atys*. By quantifying both the amount of dentine exposure and morphological changes (cusp radius of curvature and angle, and the concavity and convexity of the occlusal surface) of the M₁ throughout development has provided an in depth assessment on the pattern of wear in *C. atys*. These findings will now be summarised and discussed in relation to specific research questions and in the context of the feeding ecology, phylogeny and life history of *C. atys*.

3.4.1. What is the pattern of wear on the M₁ over the lifetime of *C. atys*?

The results indicate that the M₁ in *C. atys* undergoes several transformations throughout an individual's life. At stage 0, the unworn molar presents a bilophodont arrangement where four cusps are joined by two parallel ridges (lophs), which is a characteristic trait of cercopithecoïd (old world) primates in general (Happel, 1988, Benefit, 2000, Phillips-Conroy et al., 2000, Swindler, 2002). Within the first two developmental stages the cusps were eliminated in a sequence where the protoconid showed the first signs of wear, followed by the hypoconid, metaconid and entoconid. Initially established as a small pinpoint, the dentine exposure on the cusp tips progressed to form triangular lakes surrounded by an enamel band. Eventually, these areas of exposed dentine start to merge across each loph and form a single dentine pool that is narrower in the middle of the central basin (i.e. figure of 8 shape), and is outlined by a distinctive enamel ridge.

Interestingly, this pattern of wear does not appear to be unique to *C. atys* in comparison to closely related species. According to Phillips-Conroy et al. (2000), the bilophodont molars in cercopithecoïds wear in a predictable manner, which closely follow the description provided in this chapter. This is evident in Figure 3.29 where the dental

wear in yellow baboons (*Papio cynocephalus*) recorded by Galbany et al. (2011b) exhibit a very similar pattern of wear across ontogeny to *C. atys*.

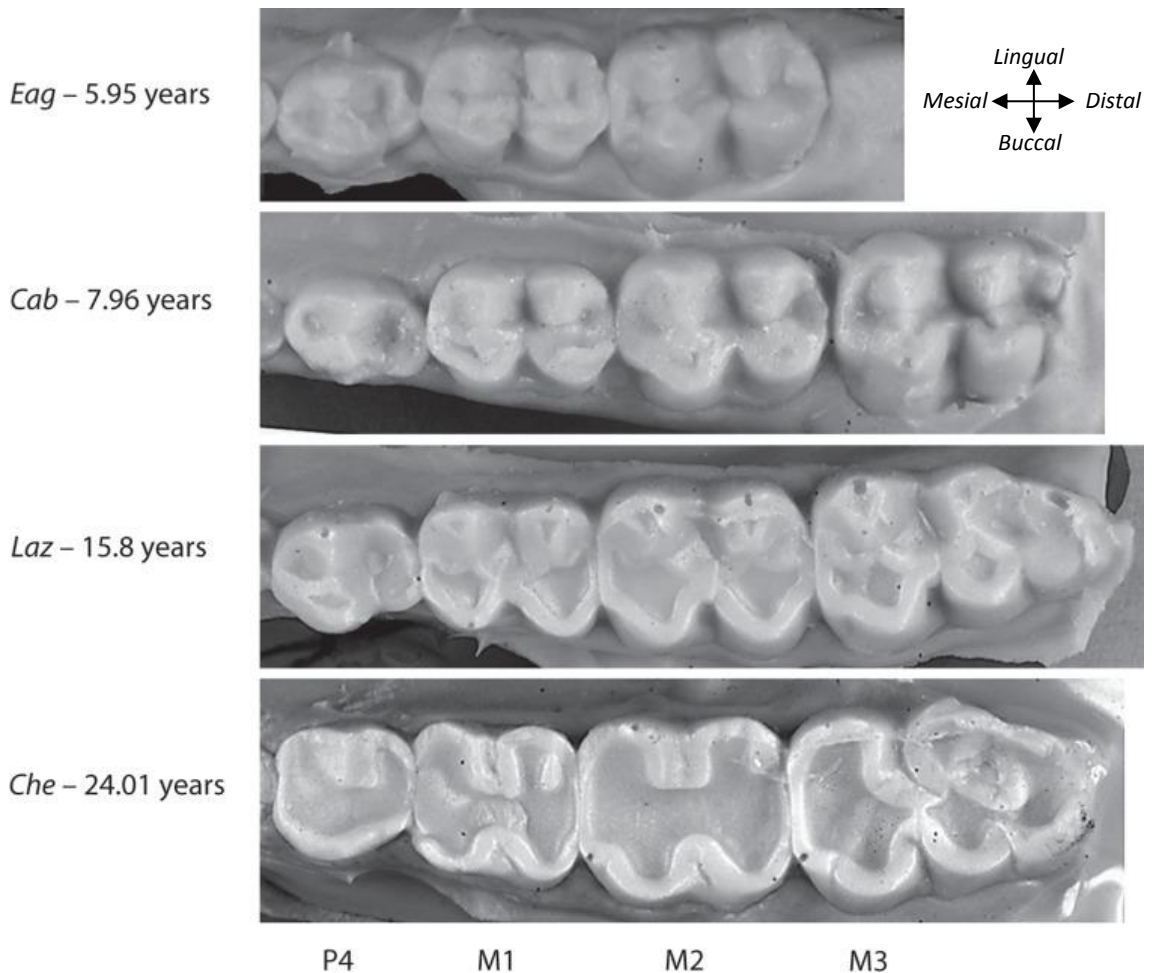


Figure 3.29 Casts of the postcanine dental row (lower, left) of four different female yellow baboon (*Papio cynocephalus*) individuals from the Amboseli basin that represent different age groups. From Galbany et al. (2011b).

Furthermore, Benefit (2000) states that uneven wear occurs on the occlusal surface of cercopithecine molars where the lingual cusps of the upper molars and the buccal cusps of the lower molars wear more rapidly. Although data on upper molars was not collected in this study, the wear pattern of the lower *C. atys* molar is consistent with this trend. Given the differences in craniofacial and masticatory form between large bodied Papionini (e.g. *Papio*) and small bodied Panionini (e.g. *Cercocebus*) (Singleton, 2002, Fitton, 2008), it seems unlikely that the similar patterns of wear are caused by jaw kinematics (Ross and Iriarte-Diaz, 2014). One explanation for the similarity in wear between cercopithecine species may be related to phylogeny where a common initial tooth form (bilophodonty) is being worn in a similar way as the teeth move in and out of occlusion during tooth-food-tooth contact.

3.4.2. Does the functional shape of the M₁ change as the tooth wears in *C. atys*?

As dentine exposure increased throughout development in *C. atys*, so did the functional morphology of the tooth. The cusps, which provide the main point of contact with foods, were shown to rapidly wear down within the first two developmental stages. The tips of the cusps was observed to flatten rather than taper, therefore the process of wear is not directly comparable to the blunting series created in chapter 2, and the cusp morphology could only be measured in a select few individuals. However, the removal of cusps in itself is likely to increase the surface area of initial contact, therefore based on the findings in chapter 2, it is hypothesised that the loss of cusps will increase the force required at fracture. To investigate this further, the measurements taken of the unworn cusps of specimen C13.41 (stage 0), will be used to inform part of the next chapter (4), which will investigate the function of cusp form in *C. atys*.

In terms of the topography of the tooth, the occlusal surface was shown to increase in concavity throughout development in *C. atys*, where the cusp tips were replaced by shallow concavities that increased in expansion with increasing wear. In the specimens exhibiting extreme amounts of wear in stage 4, the crown was reduced to a single concavity surrounded by a highly convex enamel ridge. Interestingly, previous studies on dental wear in folivorous primates have associated this dentine pool with decreased functionality (Dennis et al., 2004, King et al., 2005). For example, King (2005) found that the Milne-Edwards' sifakas (*Propithecus edwardsi*) wear their teeth throughout life to maintain compensatory blades for shearing leaves. However they suggest that “when the occlusal surface has been reduced to a shallow dentine bowl surrounded by a low-relief enamel band” marks the point of dental senescence at approximately 18 years old (King et al., 2005: p.16581).

Unfortunately, the exact ages in the sample presented in this study are unknown. Although developmental stages were indicated by eruption sequence, these stages are naturally capped to the point when all the teeth are erupted, which occurs between 6 to 10 years of age in sooty mangabeys where peak likelihood is 7.5 years in males and 7.75 years in females (McGraw et al., 2011). The dental chronology data, although useful, is nevertheless also restricted to the developmental timeline of the teeth where the maximum estimated age is 5.5 years. However in the wild, *C.atys* has been documented to live up to 18 years (Rowe, 1996). This means that the specimens of the final stage (stage 4) that have fully erupted permanent teeth are derived from an extremely large time frame in comparison to the other eruption categories. It is therefore

unclear when the extremely worn, ridged morphology of stage 4 occurs during the *C.atys* lifetime. It may be the case that this tooth form only exists in extremely old individuals, or occurs relatively soon after the M3 has erupted. Assuming that adults are classed based on the presence of fully erupted teeth, this may partially explain why such a large amount of variation in PDE scores in *C.atys* were previously found by Morse et al. (2013).

In relation to the functional implications of wear, one of the most astounding findings from this study was the sheer amount of exposed dentine on the occlusal surface in adult *C. atys* particularly in stage 4 of development where exposed dentine comprised up to 79% of the entire occlusal surface. Research in clinical dentistry suggests that the exposure of dentine can lead to dentine hypersensitivity where external stimuli such as temperature or pressure on the tooth can trigger pulpal nerves, which in turn can lead to a pain response (Addy, 2002). Further to this, the recession of enamel can also leave the tooth vulnerable to infection. If exposed, bacteria can diffuse through the dentinal tubules towards the pulp thus causing inflammation in the pulpo-dentine complex (Love and Jenkinson, 2002). This in itself may compromise feeding efficiency in individuals with high amounts of wear. However, further research is required to find out when in time the extremes in dental wear occurs in *C.atys* and also how this morphology with increasing concavity may affect mechanical performance. The latter of these, will be addressed in chapter 4.

3.4.3. How does the rate of wear in a M₁ tooth of *C. atys* compare to other primate species?

Using the data published in Elgart (2010), the rate of wear in *C. atys* was found to be higher in comparison to *Pan* and *Gorilla* species. Furthermore, the amount of wear on M1 when M2 comes into occlusion was also shown to be highest in *C. atys*. As *C. atys* has relatively thicker enamel (McGraw et al., 2012), there are two main explanations for the observed differences in wear when compared to the great ape species. Firstly, given that the great ape sample is composed entirely of folivorous and frugivorous primates (e.g. Yamagiwa et al., 1994, Yamagiwa et al., 1996, Wrangham et al., 1998, Conklin-Brittain et al., 2001, Elgart-Berry, 2004, Rogers et al., 2004), a higher rate and magnitude of wear could be related to the physical properties of foods in the sooty mangabey diet that warrant high occlusal forces. This would appear to corroborate findings by Galbany et al. (2014) where hard object feeding mandrills had a higher degree of wear to yellow baboons that feed on underground storage organs. An

alternative explanation is that the proportion of extraneous particles such as grit, quartz dust and phytoliths covering the food items foraged by *C. atys* from the forest floor are accelerating the amount of dental wear. However, Daegling (2011) suggests that grit is unlikely to be the leading cause of wear in the posterior teeth of sooty mangabeys due to the way they process their foods. During hard object feeding behaviours, *C. atys* are known to frequently bite or scrape the seed casing using their incisors prior to placing the food item onto the postcanine row where only 3.7% of postcanine crushing behaviours involve no incisal preparation.

3.5. Conclusions

The results from this study demonstrate that the M1 tooth in *C. atys* drastically changes in morphology throughout development as a result of dental wear. The cusps of the initial unworn bilophodont form were shown to rapidly wear within the first 2 stages of development, which represented ages up to 5 years old. For the remaining developmental stages, the occlusal surface became progressively flatter and increased in concavities as a result of dentine exposure, which eventually led to the formation of a single concave dentine pool surrounded by an enamel ridge. When comparing the pattern of wear to closely related species, suggests that the shape formations created during the wear process are likely to be a result of phylogeny. Regardless of this, the differences in tooth shape between juveniles and adults may potentially cause functional implications in processing hard food items, which form the main dietary resource in sooty mangabeys.

Chapter 4: The effect of dental wear on the mechanical performance of a hard object feeder (*Cercocebus atys*)

4.1. Introduction

The sooty mangabey (*Cercocebus atys*) is a specialised hard object feeder that is well known for accessing seeds from large and highly stress resistant endocarps using their premolar and molar dentition (Fleagle and McGraw, 1999, Daegling et al., 2011, McGraw et al., 2011). In order to break open such mechanically protected foods, members of *Cercocebus* have been associated with a suite of anatomical specializations in adults including; large incisors, enlarged premolars, thick enamel and powerful jaws (Hylander, 1975, 1979, Kay, 1981, Daegling et al., 2011, McGraw et al., 2012). These traits suggest that *Cercocebus* species in general are adapted for their mechanically demanding diet. However, one of the most intriguing observations of *C. atys*, is that all individuals appear to partake in hard object feeding behaviours as soon as weaning commences and that these foods form the major dietary component of this species (McGraw et al., 2011, Morse et al., 2013). How juveniles are able to cope with the mechanical demand of such a diet is particularly puzzling given the ontogenetic changes in craniofacial form (O'Higgins and Jones, 1998) and the fact that juveniles have absolutely smaller muscles than adults (Fitton et al., 2015). Research from chapter 3 has already shown that in addition to the skull and masticatory muscles, the dental morphology of a *C.atys* molar also undergoes several important shape changes as a result of dental wear, which could affect the mechanical performance of food breakdown. This raises the important question of how these changes in tooth form impact the mechanical capability to breakdown hard food items. In order to further investigate this, the present chapter will examine how changes in crown topography, as a result of dental wear, affect the mechanical efficiency of hard food breakdown.

4.1.1. Feeding and development in *C. atys*

Previous research suggests that *Sacoglottis gabonensis* is the major food source of sooty mangabeys as soon as they have been weaned (McGraw et al., 2011, Morse et al., 2013). At what ages this occurs in mangabeys (*Cercocebus spp.*) is unclear as the lactation period has been indicated to last until 4-5 months in *Cercocebus albigena johnstonii* (Rowell and Chalmers, 1970); 6-10 months in *C.galeritus* (Groves, 1978),

and 12-18 months in *C. atys* (Fruteau et al., 2010). However, as noted by Fruteau et al. (2010), estimations on time of weaning are likely to vary as it is difficult to define the point at which the lactation period ends. For instance, in *C. atys*, infants have been observed to start eating a variety of foods at approximately 5-6 months old whilst still suckling on a regular basis. This apparent mixture of solid and milk based subsistence then continues until 12-18 months (Fruteau et al., 2010). Despite of this, it appears that with the onset of M1 eruption, all individuals are likely to have started feeding on *Sacoglottis gabonensis* based on the age estimates provided by the dental chronology data in section 3.2.1.3 p. 133 where individuals are estimated to be aged between 2-4 years old.

4.1.2. Ontogenetic changes of the masticatory apparatus in *Cercocebus atys*

The craniofacial form of *C. atys* has previously been shown to change in form during ontogeny (O'Higgins and Jones, 1998). Using the same sample of *C. atys* used in this thesis, O'Higgins and Jones (1998), found that the adults (larger individuals) compared to juveniles (small individuals) possessed a relatively longer rostrum with an increased degree of klinorhynch (muzzles being relatively rotated under the upper face) (Figure 4.1). These alternations in craniofacial form during development are likely to impact the masticatory system.

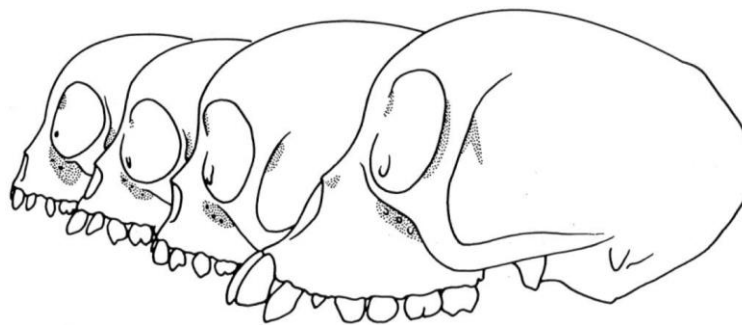


Figure 4.1 Diagram illustrating the changes in craniofacial form in *C. atys* during development. From O'Higgins and Jones (1998).

Indeed, a recent study by Fitton et al. (2015) measured the masticatory lever arm lengths across this same *C. atys* developmental sample (Figure 4.2). Their results suggest that the mechanical advantage (MA) of muscles may be more advantageous in juvenile *C. atys*, compared to adults. Fitton et al. (2015) propose that this increase in MA may compensate for the possible reduced muscle force available to younger individuals, a consequence for their absolutely smaller muscles. The study also measured a smaller tooth-food contact surface area during a bite in the juveniles (due to minimal dental wear) compared to a large contact surface area on the heavily worn *C. atys* teeth in the

adults. Consequently, the study proposed that the teeth of juveniles would be more advantageous than the adults; reducing the force required to break a *S. gabonensis* endocarp due to differences in stress concentration.

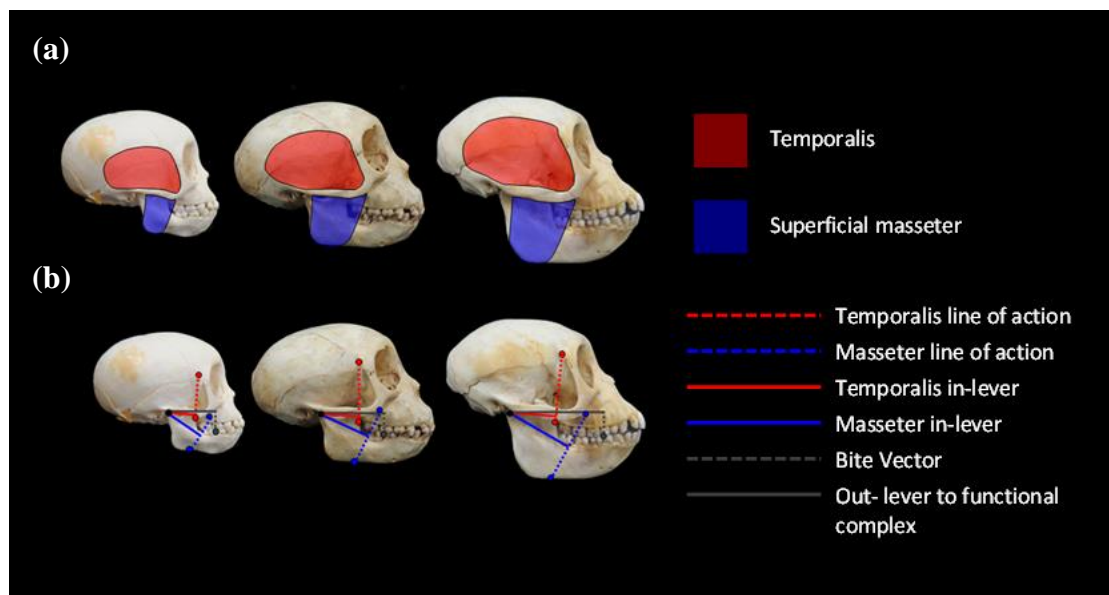


Figure 4.2 Developmental changes in the masticatory apparatus in *C. atys*. During development changes occur in (a) muscle cross sectional area (CSA), and (b) mechanical advantage (MA) (muscle in-lever/out-lever). Adapted from Fitton et al. (2015).

4.1.3. Dental wear, form and function in *C. atys*

In chapter 3, one of the main observations from the developmental *C. atys* sample is the progressive obliteration of cusps from the occlusal surface with increasing wear. As discussed in chapter 2, cusps are extremely important in food breakdown as they form the first point of contact where forces generated by the masticatory muscles are transmitted onto the food item. It has already been shown that by altering the shape of a single cusp can have profound effects on the force and energy required to break down foods (Chapter 2, Evans and Sanson 1998). Shape aspects that minimise surface area such as acute angles and high tip sharpness, increase pressure on the food object therefore require lower forces to initiate fracture. In addition to this, the results from chapter 2 also suggest that the surface area of contact can also affect the duration of fracture and the degree of fragmentation where cusps with a larger surface area require less time to fracture whilst producing a higher amount of fragmentation.

As well as the shape of an individual cusp, the surface area in contact with the food item can also be altered based on the number of cusps. In theory, by increasing the number of contact points increases the overall contact surface area and therefore leads to the reduction of localised stresses in food object for a given force (Evans and Sanson,

2005b, Berthaume et al., 2010). Evans and Sanson (2005b) therefore suggest that for some feeders it may be beneficial to have a reduced number of cusps in order to minimise contact surface area and reduce the force required to initiate fracture. This could be achieved by either reducing the overall number of cusps or by increasing the spacing between them so that fewer cusps are in contact with the food item at the same time. Conversely, they also argue that a greater number of cusps may also be advantageous for some species as this distributes force over a larger area of the food object. By maximising the number of indentation points at contact increases the number of locations at which cracks can be initiated. Therefore crowns with a high number of cusps are likely to promote physical food breakdown by aiding the initiation and propagation of cracks.

An additional observation from chapter 3 was the formation of a distinctive enamel band on the outer perimeter of the crown in *C.atys* specimens with extreme wear. Typically, this occurred after the cusps were obliterated from the surface and concave dentine lakes start to form in their place. Eventually the lakes start to merge to form a single concavity surrounded by an enamel ridge. One study by Croft and Summers (2014) notes that not only do the teeth of durophagous organisms take on a range of different primary morphologies but they can also be worn to the point of concavity. Along with cusp height and base, they explored the effects of concavity and convexity on the mechanical performance to fracture 3D printed snail shells. Based on a series of 5 different models that varied in degree of concavity and convexity (Figure 4.3) they found that the concave teeth required a much higher force to break the shells in comparison to flat or convex teeth. They concluded that as the body of the whorl of the snails fitted within the concavity of the tooth this increased the contact surface area with the shell, thus warranting a higher force at fracture.



Figure 4.3 Series of 5 cusps used by Crofts and Summers (2014) to investigate the effects of concavity and convexity to fracture brittle snail shells.

4.1.4. Aims and objectives

The results from chapters 2 and 3 provide an excellent platform in which to further examine the relationship between dental morphology and function in *Cercocebus atys*. From chapter 2, it was shown that by altering the shape of a single cusp can hold implications on mechanical efficiency suggesting that some cusps are better than others

at breaking down certain foods. The first aim of this study, therefore, is to examine whether the unworn cusp morphology of the hard object specialist *C.atys* is optimised for the breakdown of hard foods. In order to investigate this, a cusp model will be created based on the radius of curvature and angle measurements of the cusps of an unworn M₁ *C.atys* tooth. The mechanical performance to break hollow and solid hard foods will then be tested using physical compression and the results compared to the cusp morphospace created in chapter 2.

However what is apparent from chapter 3 is that the M₁ crown of *C. atys* undergoes several shape changes from its initial unworn state as a result of dental wear throughout development. Whether these changes confer a functional disadvantage or advantage in the adult sooty mangabey is of yet unknown. Therefore the second aim of this chapter is to examine how the changes in dental form in a *C.atys* tooth affect the mechanical performance to process hard food objects. Based on the findings in chapter 3, a series of hypothetical crowns will be created that mimic the features of dental wear observed in a *C.atys* molar. The mechanical performance to break hollow and solid hard foods will then be tested using physical compression.

Research questions:

1. *Is the unworn morphology of a C.atys cusp optimised for the breakdown of hard foods in comparison to other cusp morphologies?*

Given that hard foods are consumed as soon as the M1 erupts (McGraw et al., 2011, Morse et al., 2013), it is expected that the unworn cusp morphology will adequately perform in all of the optimisation criteria for both hollow and solid hard object breakdown in comparison to other potential cusp morphologies. This will involve minimising the force, energy and duration to initiate fracture/break a hollow and solid hard object, and to maximise fragmentation in a solid hard object.

2. *Are there any differences in mechanical performance between different crown wear morphologies when used to break hard food items?*

It is expected that there will be no significant differences found between the different wear states. This is based on the premise that once the M1 has erupted, all members have been observed to feed on the seeds of *Sacoglottis gabonensis* regardless of age (McGraw et al., 2011); therefore the effects of dental wear should be minimal in the breakdown of such foods.

4.2. Materials and methods

The procedure used to examine the mechanical efficiency of teeth will closely follow that used in chapter 2. This will involve creating stainless steel tooth models that will be used to fracture 3D printed brittle food replicas under physical compression.

4.2.1. Design and manufacture of dental models

4.2.1.1. *C.atys cusp*

A single cusp was created based on the average radius of curvature and angle measurements of the cusps of an unworn M_1 *C.atys* tooth ($R=0.94\text{mm}$, $\text{angle}=97^\circ$). These measurements were taken from the unerupted M_1 of specimen C13.41. Information on how the angle and radius of curvature were measured from this specimen is included in chapter 3. To make a cusp with the R and angle dimensions of a *C.atys* molar but comparable to the hypothetical series, the drawing had to be reversed engineered. In other words, rather than predefining the angle and blunting distance that produces a resultant R value, the angle and R were used to calculate the blunting distance (y_o) (equation 4.1).

$$y_o = \frac{R}{\tan^2 \frac{1}{2} \theta} \quad (4.1)$$

In order to achieve this, a template triangle was first constructed with a height of 10mm in the CAD software SolidWorks 2014 (Dassault Systèmes SolidWorks Corp.). To set the angle of the acting point of the triangle to 97° , the base was estimated using the following equation 4.2:

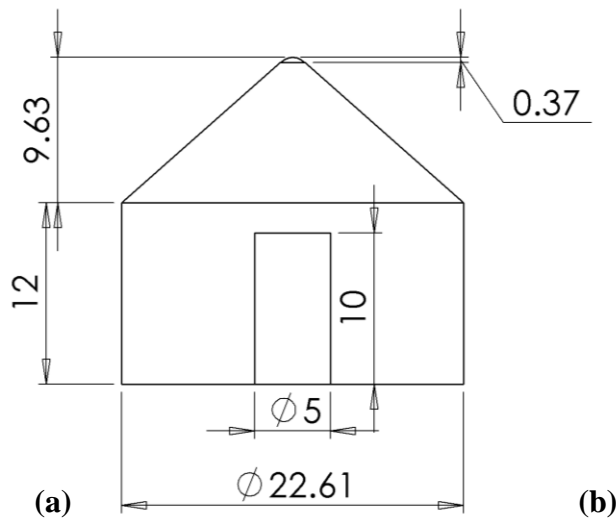
$$\text{Base} = 2 \times \text{height} \times \tan \frac{1}{2} \theta \quad (4.2)$$

A parabolic curve was then fitted to the tip of the triangle to create a point with a radius of 0.94mm. The blunting distance calculated from equation 4.1 (0.74mm) could then be used to calculate the point at which the parabola and the template triangle merge to form a cone (x_o) (equation 4.3).

$$x_o = \tan\left(\frac{1}{2}\theta\right) \times y_o$$

(4.3)

A base was added to the cone, which included an M6 internal thread at the bottom so that the model could be attached and detached to the universal testing machine. Full details of the design of the model with dimensions are presented in Figure 4.4.



Cusp measurements	
Height (mm)	9.63
Base (mm)	22.61
Y_o (mm)	0.74
Apex	0.37
R (mm)	0.94
Angle (°)	97

Figure 4.4 Design and dimensions of *C.atys* cusp model where (a) shows a sketch of the model with dimensions (scaled at 2:1) and (b) lists the measurements used to design the *C.atys* cusp.

Using the same procedure used to make the hypothetical series, this model was then manufactured in stainless steel (SS304) from a STEP file using CNC machining provided by Star Prototype Manufacturing Co.,Ltd (Figure 4.5).

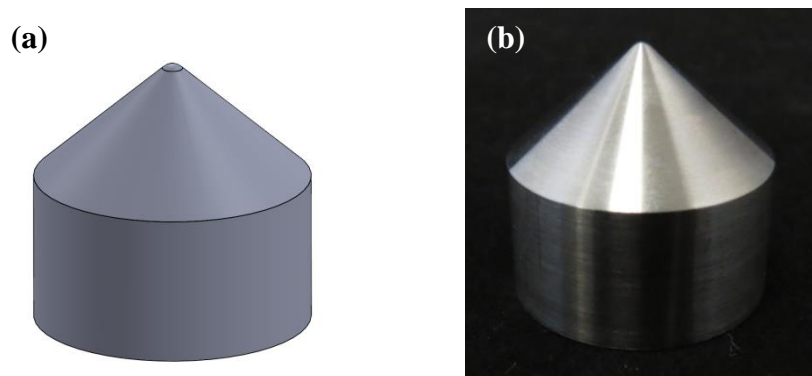
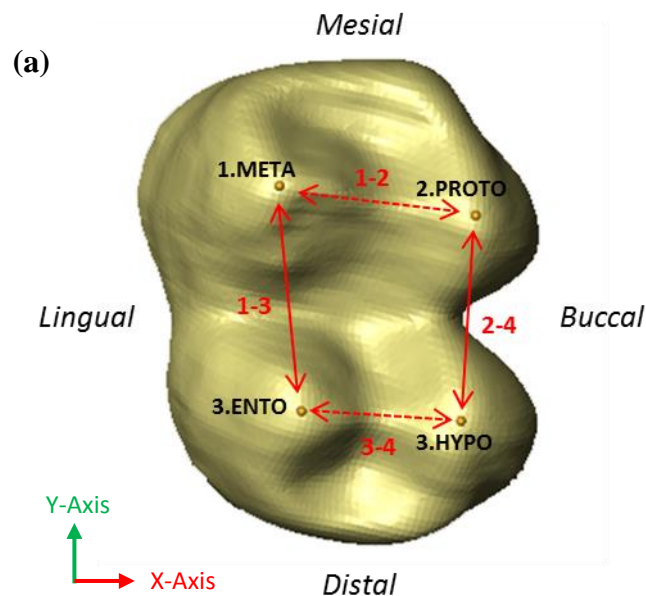


Figure 4.5 *C.atys* cusp model where a CAD file (a) was CNC machined in stainless steel (b).

4.2.1.2. Dental wear series

To investigate the effects of dental wear a 4 cusped crown was first created, which represented the unworn state of a *C.atys* M₁. The individual cusps were designed using the dimensions of the *C.atys* cusp made in the previous section (4.2.1.1). As the original design was far too large in comparison to a real *Cercocebus* cusp, it was modified by reducing the height to 2mm based on the height of the tallest cusp (metaconid) of C13.41. This design was duplicated to make a 4 cusp model in which cusps could be placed on a crown and removed sequentially until there were no cusps present. However prior to this it was first important to consider how far apart the cusps should be positioned as this is likely in itself to have an effect on food breakdown (Evans and Sanson 2005). To make the models comparable to a *Cercocebus* tooth, it was decided to use the intercuspal distances of the unworn M₁ of C13.41. In Avizo 8 (FEI), landmarks were placed on the tip of each cusp and the 3D coordinates exported to estimate the inter-landmark distances (Figure 4.6a). As the cusps were all different heights, the Z coordinate was altered to the same value and 2D linear measurements taken in the XY plane.



(b)

Direction	Cusp distances	Landmarks	Length (mm)	Average (mm)
Mesial-distal	Meta-ento	1-3	3.90	3.73
	Proto-hypo	2-4	3.55	
Buccal-lingual	Meta-proto	1-2	3.43	3.09
	Ento-hypo	3-4	2.76	

Figure 4.6 Intercuspal measurements from an unworn *C.atys* M₁. Landmarks were placed on each cusp of specimen C13.41 (a) that were used to calculate the intercuspal distances (b).

On average, the measurements were found to be longer in the mesial-distal direction than the buccal-lingual direction, thus presenting a rectangular arrangement of cusps (Figure 4.6b). However this arrangement may complicate the process of cusp removal as the results may vary depending on which side the cusp (s) are removed. As this study is primarily interested in the loss of cusps rather than replicating the exact measurements of a *Cercocebus* tooth, it was decided to place the cusps at equal distance using the average maximum length of 3.70mm (1 dp), which was taken from the mesial–distal distances. However an extra 4 cusp model was made based on the average distances in both the mesial-distal and buccal-lingual directions to examine what the effect would be of a rectangular cusp arrangement, but this was not used to examine the effect of cusp number on mechanical performance.

To create the crown, each cusp was attached to a cylinder with the same diameter as the base of the cusp (5.35mm) and a height of 5mm. This formed one component of the crown (Figure 4.7a). Four of these components were then overlapped to construct both the crown of the four cusp model, which maintained an equal distance of 3.70mm between each adjacent cusp, and the crown of an intercuspal 4 cusp model, which was overlapped using the average dimensions in the mesial-distal and buccal-lingual directions (Figure 4.7b,c,d).

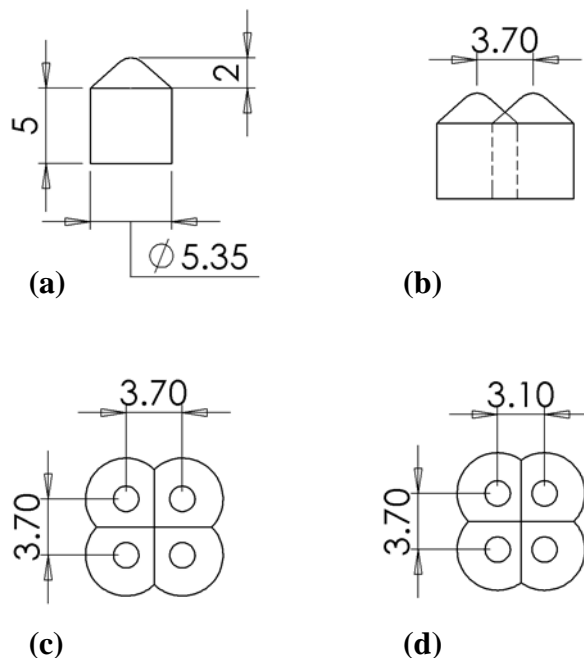


Figure 4.7 The creation of a hypothetical crown with 4 cusps: (a) the design and dimensions of an individual cusp, positioned on the top of a cylinder, (b) 4 of the individual cusp components were then overlapped at certain distances apart to form a crown, (c) the top view of the cusps positioned at equal distances apart, (d) the top view of the cusps positioned at unequal distances apart. Measurements in mm. Drawings are scaled 2:1.

To simulate the effects of cusp loss due to wear, the cusps of the equal distance 4 cusp model were then effectively ‘knocked out’ one by one to form a 3 cusp, 2 cusp, 1 cusp and 0 cusp crown (Figure 4.8).

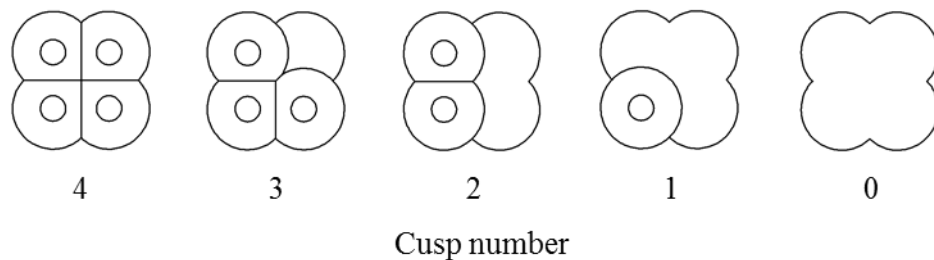


Figure 4.8 Simulation of cusp loss due to dental wear. Cusps were removed one by one from a 4 cusp (unworn) model to create a 3 cusp, 2 cusp, 1 cusp and 0 cusp crown. Drawings are in top view and scaled 2:1.

It was acknowledged that the position of the cusps could have an additional impact on the mechanical performance. Previous experiments in chapter 2 have shown that when the dome has been misaligned underneath a single cusp, the fracture and fragmentation pattern deviates from the rest of the sample. It is quite possible in reality that the food is deliberately placed underneath the tooth in such a way to maximise performance. It was therefore decided to make an extra one cusp model with the cusp orientated in the centre to compare to the original 1 cusp model in order to examine this effect in isolation (Figure 4.9).

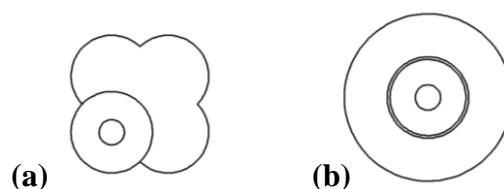


Figure 4.9 Single cusped models used to investigate the effect of cusp position on food breakdown; (a) shows the cusp placed laterally in comparison to (b) where the cusp is positioned at the centre. Drawings are in top view and scaled 2:1.

To investigate the morphology observed in later wear states, a hypothetical dental model was created with a ridge at the perimeter that enclosed a single concavity. The dimensions of the ridge and the depth of the concavity were based on the measurements of a worn adult M_1 (specimen C13.22).

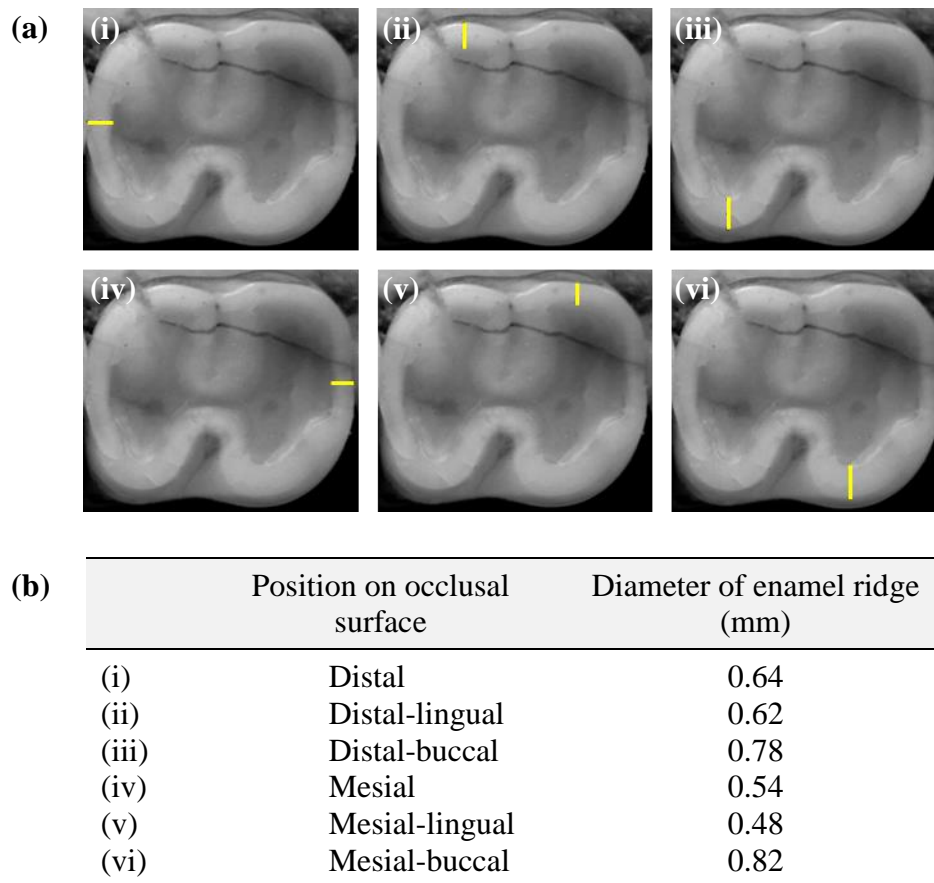


Figure 4.10 Measurements of the enamel ridge taken from an image of specimen C13.22. Linear measurements were taken of the outer enamel ridge at 6 different locations: (i), distal-lingual (ii), distal-buccal (iii), mid-mesial (iv), mesial-lingual (v) and mesial-buccal (vi). Locations are shown in (a) and the corresponding diameters in (b).

Using the image taken for chapter 3, the diameter of the enamel band was measured at 6 different locations (Figure 4.10) in ImageJ 1.46r (Abràmoff et al., 2004). The widest diameter, which was taken from the mesial-buccal side of the tooth, was then used to define the diameter of the ridge in the hypothetical model.

The depth of the concavity was then estimated from a 3D virtual model of the M₁ of specimen C13.22 in the software Geomagic (2013). The tooth was first positioned so that the occlusal surface was parallel to a flat plane and the depth measured from the tip of the enamel ridge to the lowest point of the dentine pools. From this, the maximum depth was estimated as 1.85mm. These measurements of the ridge and concavity of a real *Cercocebus* molar were then used to construct a hollowed out cylinder (Figure 4.11a,b) that would replace each of the four cusps in the unworn model. The cylinders were overlapped at equal distances from the centre using the same measurements used to construct the cusped models (Figure 4.11c).

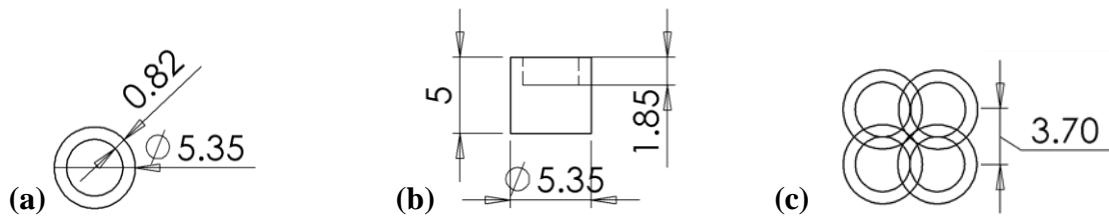


Figure 4.11 Hollowed out cylinder used to construct the ridged model. Dimensions are provided in (a) top view and (b) front view. Four of these cylinders were then overlapped to form a crown (c). Measurements in mm. Drawings are scaled 2:1.

To create the concavity, the centre of the model was cut using a circle with a 5.35mm diameter. It was noticed that in the worn M_1 , the edges that met the adjacent teeth in the mesial and distal directions were typically straight. To replicate this, a rectangle was merged on both the mesial and distal sides and the groove on the inside cropped to create a straight edge (Figure 4.12ab).

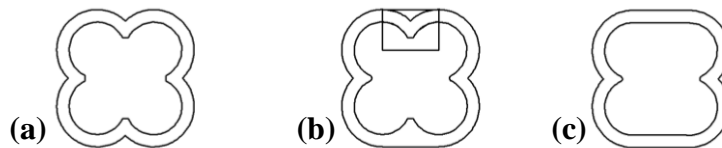


Figure 4.12 Construction of the ridge model. A central concavity was created (a) and the mesial and distal sides were flattened using a rectangle and the buccal and lingual grooves rounded (b) to produce the final model (c). Measurements in mm. Drawings are scaled 2:1.

To finalise the model the buccal and lingual grooves were rounded by fitting a small circle at the end (Figure 4.12c). The final design and dimensions of the ridged model are presented in Figure 4.13.

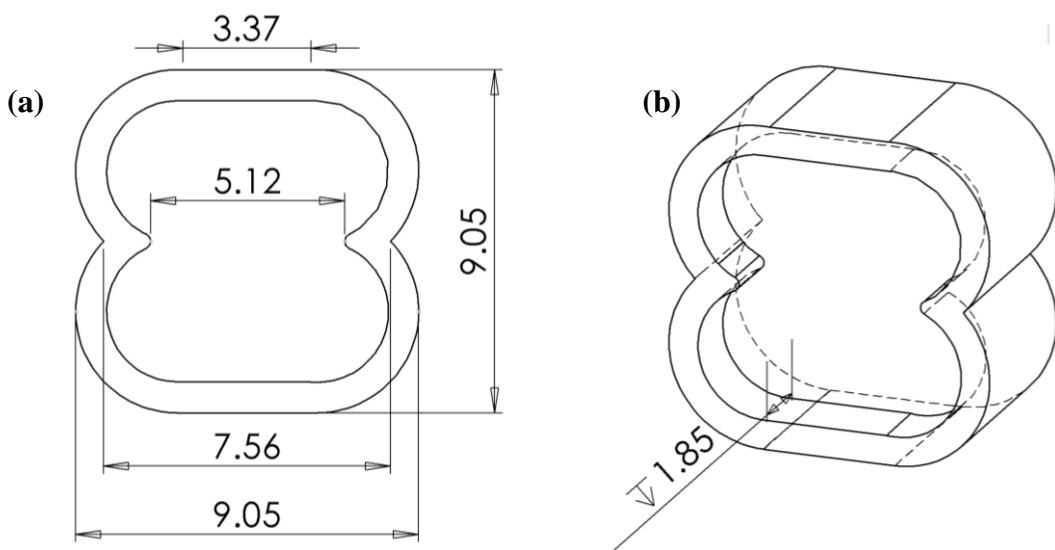


Figure 4.13 Design and dimensions of the ridged model in (a) top view and (b) dimetric view. Measurements in mm. Drawings are scaled 5:1.

An additional model was created that had the same occlusal outline as the ridged model but without the concavity and ridge (Figure 4.14). Therefore two flat models were included in the series that varied in shape.

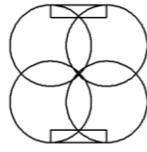


Figure 4.14 Flat version of the ridged model. Drawing scaled 2:1.

Same as with the cusp models, a base was designed in order to attach and detach the dental models to the universal testing machine (dimensions provided in Figure 4.15a). Each crown was merged to the centre of a cylinder, which incorporated a hole for a M6 internal thread to be tapped (Figure 4.15b).

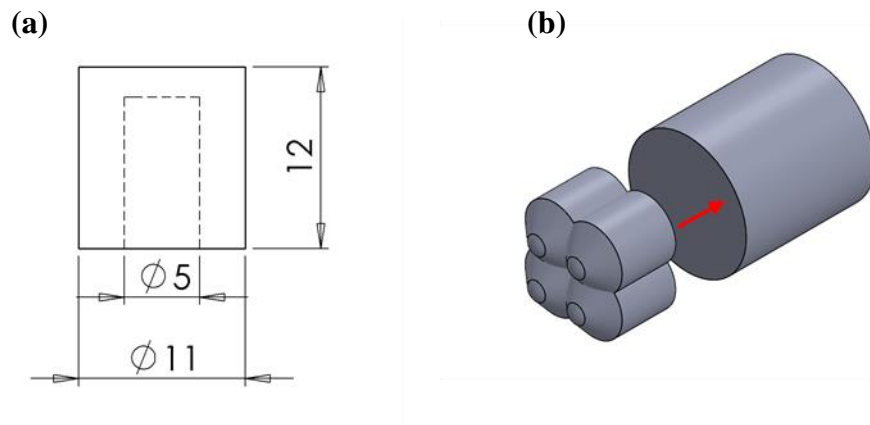


Figure 4.15 Base used to attach the crowns to the universal testing machine. A base was sketched, which included a hole at the bottom in which a M6 internal thread could be tapped (a). This was then merged with each crown to create an assembled model (b). Measurements in mm. Diagram scaled 2:1.

The models were again manufactured in stainless steel (SS304) using CNC machining (Star Prototype Manufacturing Co.,Ltd) (Figure 4.16).



Figure 4.16 Stainless steel crown models used to investigate the effects of dental wear on mechanical performance in *C.atys*. Images from left to right; 4 cusp, 3 cusp, 2 cusp, 1 cusp, 0 cusp, 0 ridge, ridge.

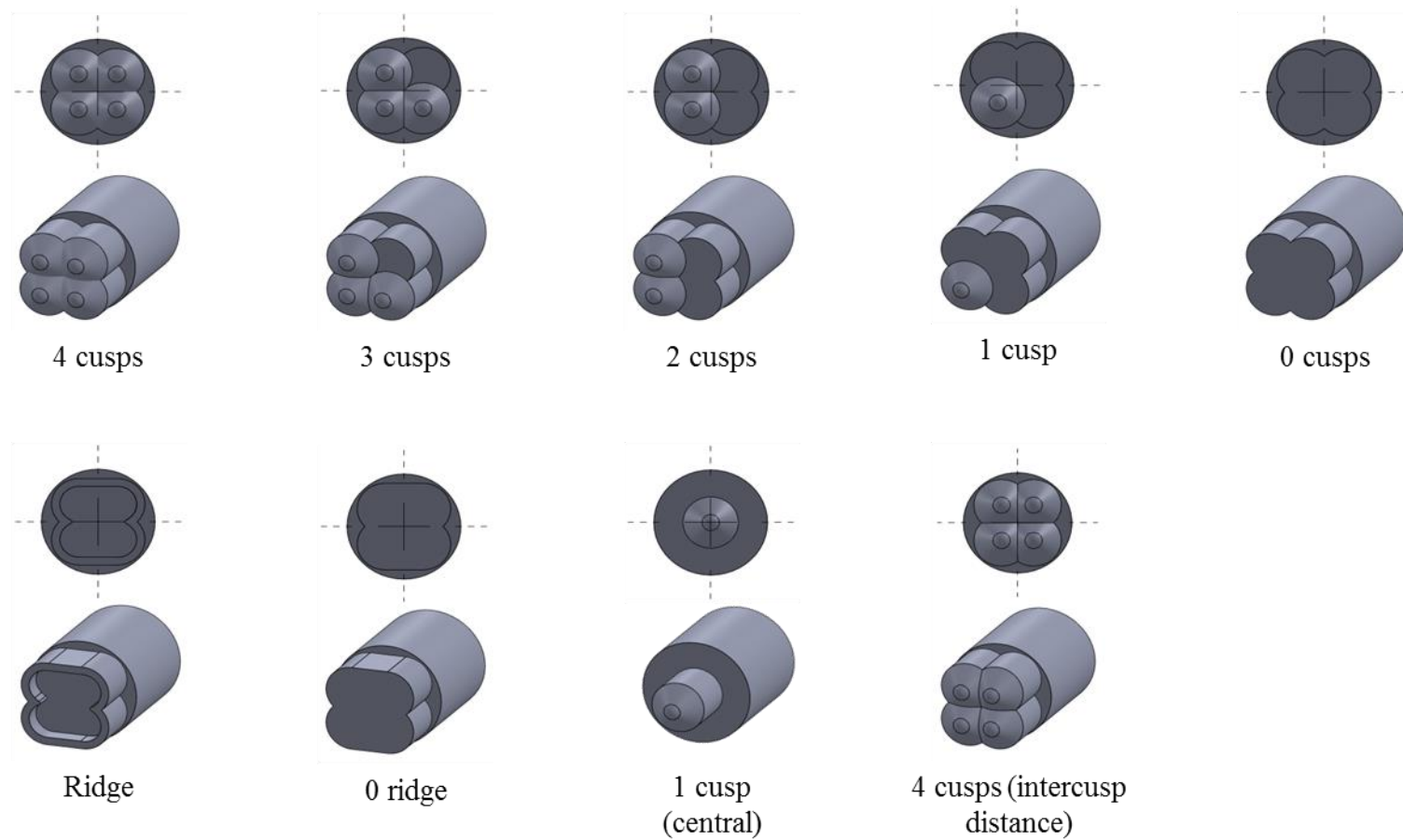


Figure 4.17 The final designs of the dental models used to investigate the effects of dental wear in *C. atys*. Additional models 1 cusp (central) and 4 cusps (intercusp distance) were also included to examine any potential influences of cusp placement. Models are shown in top and dimetric views.

4.2.2. Design and manufacture of hard food objects

Following chapter 2, hard brittle objects were designed in SolidWorks 2014 (Dassault Systèmes SolidWorks Corp.) and 3D printed (Zprinter 350, ZCorporation), which enabled for size, shape and mechanical properties to be controlled for. The same two forms of hemispheres were made, which included both a hollow and solid version. For further details on dimensions and procedure see chapter 2 (pp. 66-68).

4.2.3. Experimental procedure to test mechanical performance of dental models

All mechanical tests followed the exact same experimental procedure outlined in chapter 2. Each dental model was individually attached to a universal testing machine (Mecmesin MultiTest 2.5~i) with the hard food object positioned centrally underneath. Compression tests were then performed using the same test programs (see appendix A p. 229) in order to extract data on the peak force and corresponding energy and duration values for both hollow and solid hard objects. For the solid hard objects, the additional performance indicator of fragmentation was also recorded using a sieving technique (see section 2.2.3.4). Based on the weights of particles captured in 3 different mesh sizes, the fragmentation index was calculated where a score closer to 1 indicates a high amount of fragmentation, i.e. a high number of small particles (see section 2.2.3.4 pp. 73-75). To aid the interpretation of the results, the displacement level at peak force was also recorded and was used to calculate the corresponding amount of contact surface of the model using the software SolidWorks 2014 (Dassault Systèmes SolidWorks Corp.).

4.2.4. Data analysis

A total of 10 repeats were made for each dental model. To investigate whether the *C.atys* cusp is optimal for the breakdown of hard food items, the results were compared to the hypothetical series in chapter 2. This involved individually plotting force against each of the other performance indicators to evaluate how well the cusp performed when considering more than one variable.

The results for the crown morphologies were displayed using boxplots where the dashes within the box indicate the median, the box itself bounds the second and third quartiles, the whiskers indicate the maximum quartile ranges and the circles indicate any outlying data points. Any statistical differences between the group means were determined using a one-way analysis of variance (ANOVA) in the statistical package Past 2.14 (Hammer et al., 2001). In the case of unequal variances than the Welch F test was used as an

alternative. When significant differences were found ($p < 0.001$) then a post hoc Tukeys test was used to make pairwise comparisons.

4.3. Results

The results will now be presented on:

1. *Cusp optimality in C. atys*

To investigate the optimality of an unworn *C.atys* cusp to breakdown hollow and solid hard foods the mechanical performance was compared to the hypothetical cusp series created in chapter 2, where cusp tip radius of curvature varied between 0.25mm-18mm.

2. *Mechanical implications of dental wear in C. atys*

Crown models representing wear states in *C.atys* were compared in mechanical performance to break down hollow and solid hard food items.

3. *The effect of cusp arrangement on mechanical performance*

Two extra sets of results were included in order to examine the potential effects of cusp placement on the breakdown of both hollow and solid hard foods. The first of these compared the results in mechanical performance between the 1 cusp model used in the wear series, and a one cusp model where the cusp was positioned so it was aligned to the centre of the dome during compression. The second set of additional analyses considered the impact of the positioning of multiple cusps in contact with the food surface. To compare to the 4 cusp model, an extra dental model was made that placed the 4 cusps in a rectangular configuration similar to that seen in *C.atys*.

Written and photographic descriptions of the results for each dental model are provided in appendix C along with averages and standard deviations for all data collected in this chapter.

4.3.1. Cusp optimality in *C. atys*: Hollow hard object breakdown

As with chapter 2, the results for the breakdown of hollow hard objects will include performance data from both initial fracture (first peak in the force/displacement plot) and peak force.

4.3.1.1. Bivariate plots of mechanical indicators at initial fracture (hollow)

When initiating fracture in a hollow hard object, cusp models considered most optimal were those that required a low amount of time and energy relative to a low force. In terms of duration, the *C. atys* cusp model performed reasonably well and falls out with some of the better performing models (C60, B90, D60, C90) (Figure 4.18). However, it does not appear to be as optimal as the D60 and C90 models, which required a similar force at fracture but at a faster time; although it is worth noting that asides from the B60 model that took 7 seconds, all of the models reached overall a similar time, which varied between 5-6 seconds.

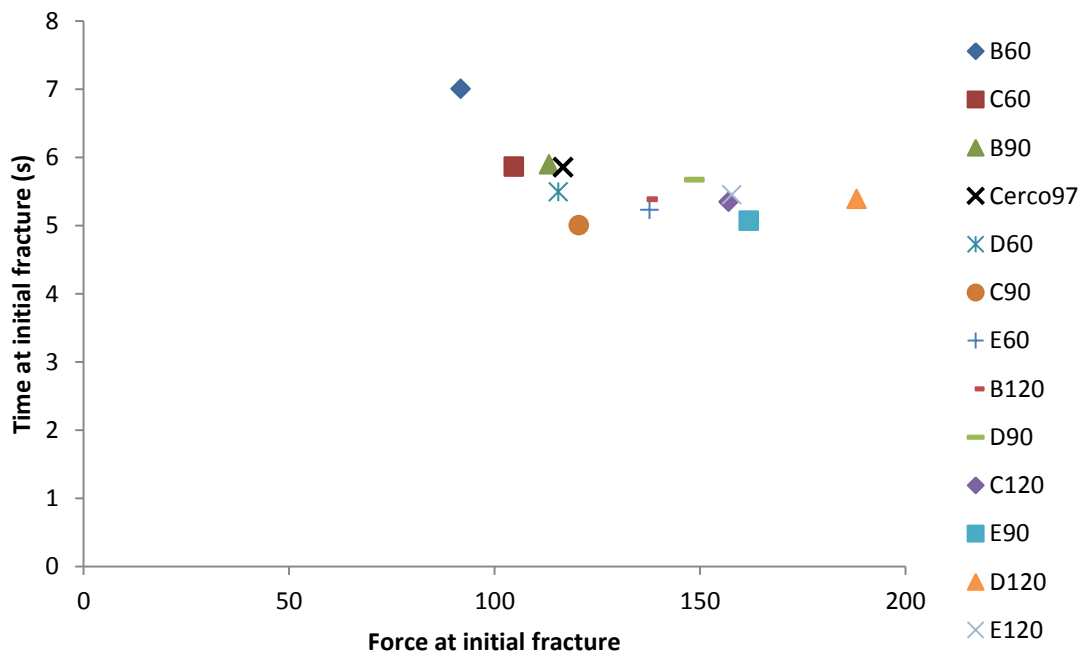


Figure 4.18 Bivariate plot of mean force and time to initiate fracture in a hollow hard object for each cusp design. Note: cusp names in the legend are in order of increasing radius of curvature.

When accounting for energy at initial fracture, the *C.atys* cusp model clustered with the better performing models (C60, B90, D60, C90), which were low in both force and energy values (Figure 4.19). Similar to time, the *C.atys* cusp was not the best of this group as some of the other models reached a similar force yet required a lower energy (e.g. D60, C90).

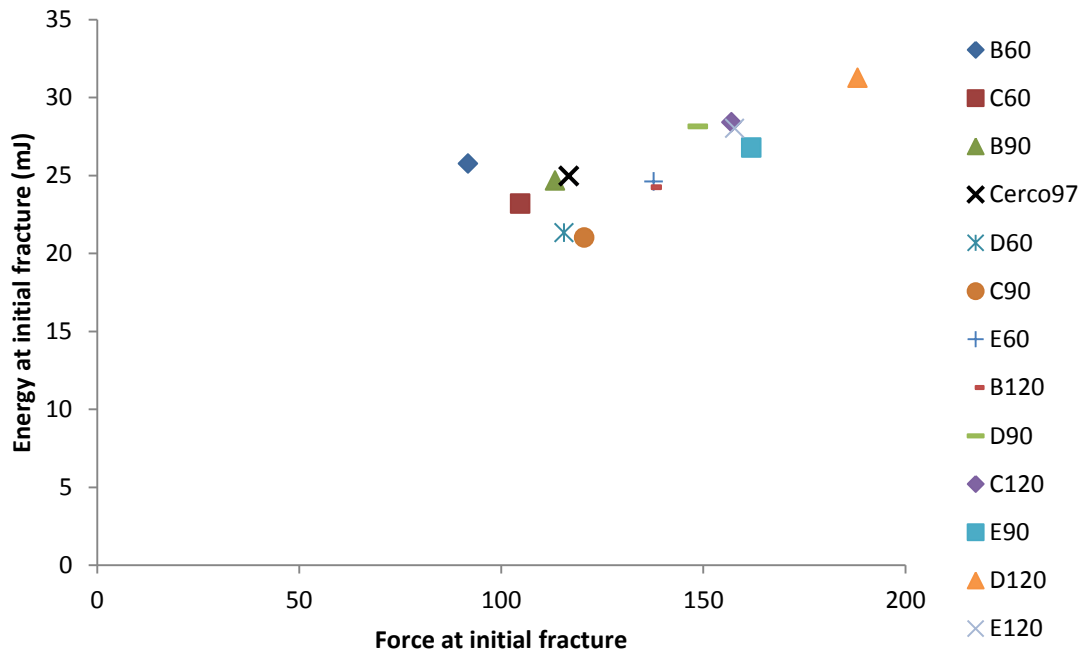


Figure 4.19 Bivariate plot of mean force and energy to initiate fracture in a hollow hard object for each cusp design. Note: cusp names in the legend are in order of increasing radius of curvature.

4.3.1.2. Bivariate plots of mechanical indicators at breakage point (hollow)

At peak force to break a hollow hard object, the models considered as most optimal were those that required a low amount of time and energy relative to force (same as initial fracture). In this case however, the *C.atys* cusp performance was moderate (Figure 4.20). For time and force, the *C.atys* model was mid-range for both of these variables. Although it does not appear to be particularly optimised for this criterion, it was not the worst performer out of the sample.

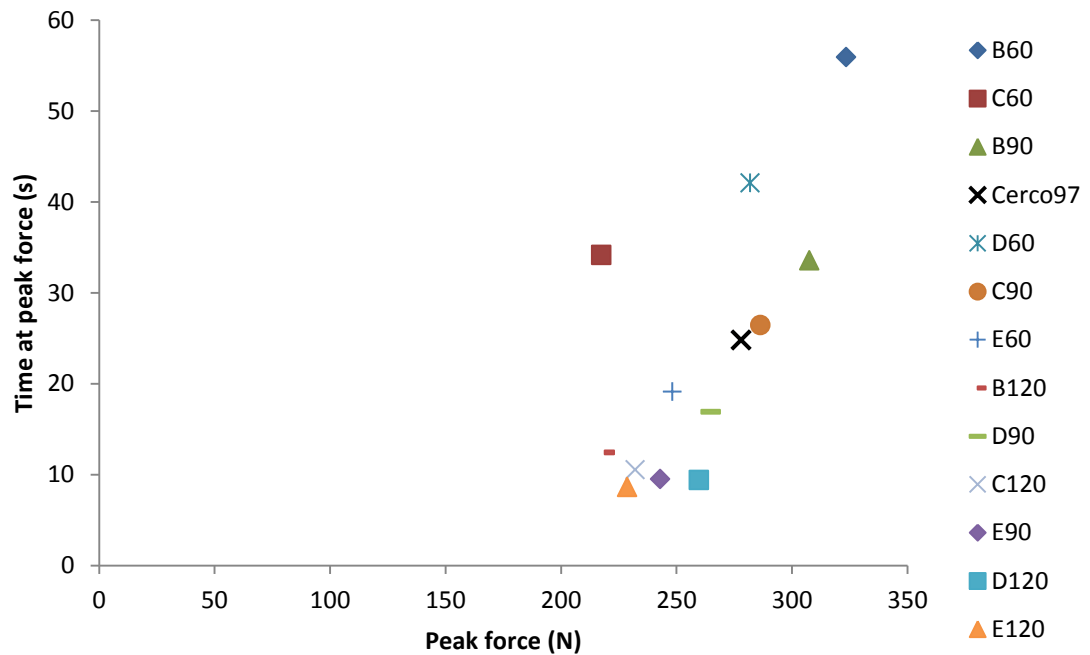


Figure 4.20 Bivariate plot of mean force and time to break a hollow hard object for each cusp design. Note: cusp names in the legend are in order of increasing radius of curvature.

The results for energy show an extremely similar pattern to that seen with time relative to force (Figure 4.21). The *C.atys* cusp was again very much mid-range in performance, neither appearing advantageous or disadvantageous in performance in comparison to the other models.

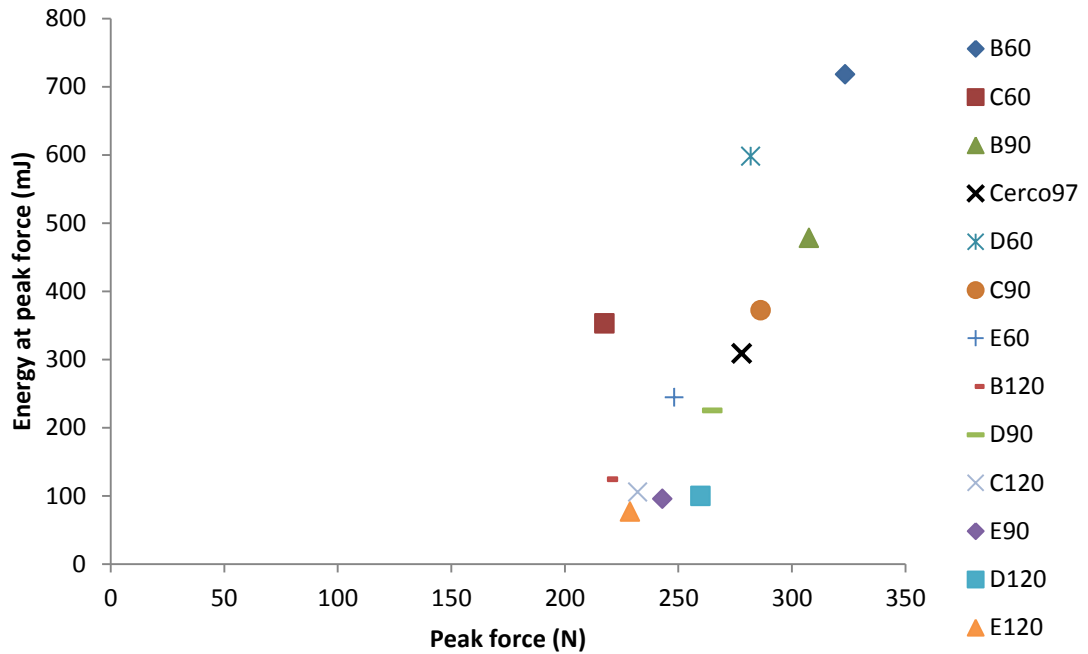


Figure 4.21 Bivariate plot of mean force and energy to break a hollow hard object for each cusp design. Note: cusp names in the legend are in order of increasing radius of curvature.

4.3.2. Cusp optimality in *C. atys*: Solid hard object breakdown

4.3.2.1. Bivariate plots of mechanical indicators at breakage point (solid)

To break a solid hard object, the cusps that required the lowest force, time and energy yet produced the highest amount of fragmentation were considered as most optimal. In terms of time relative to force, the *C. atys* cusp was one of the better performing cusps, requiring one of the lowest values for both variables (Figure 4.22). Of this grouping the E60 model appeared to be the most optimised model, falling out from the rest of the models.

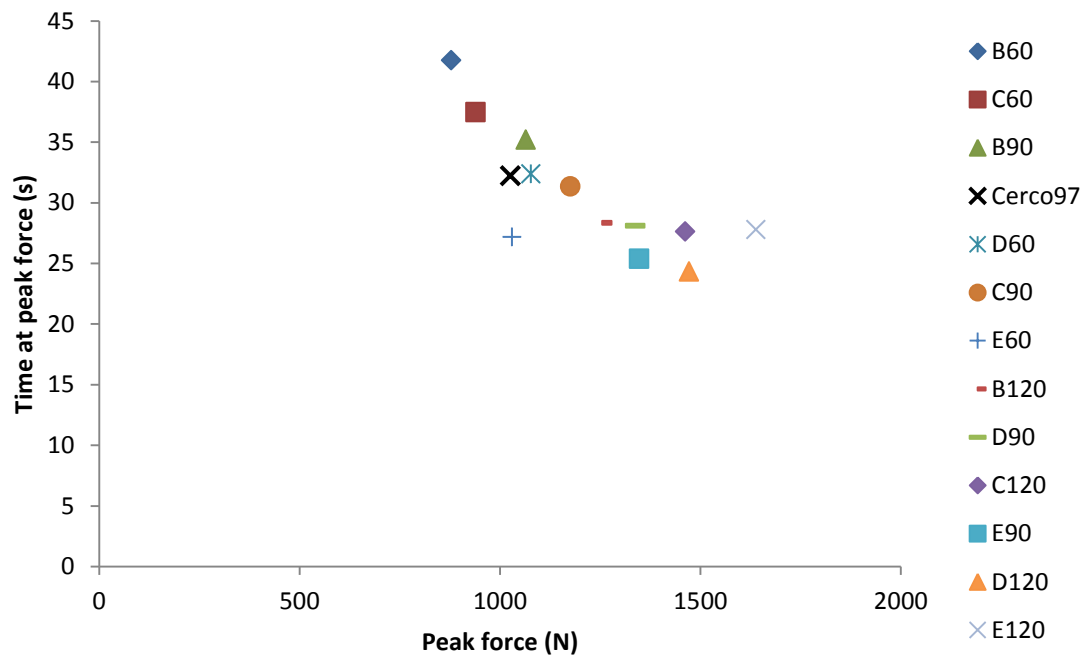


Figure 4.22 Bivariate plot of mean force and time to break a solid hard object for each cusp design. Note: cusp names in the legend are in order of increasing radius of curvature.

For the optimisation of both force and energy, the *C.atys* cusp, along with the E60 model, was found to be the most optimised out of the sample (Figure 4.23). Both of these models used considerably less energy than expected for the amount of force used to break the solid hard object. This is demonstrated in Figure 4.23, which shows the two models diverging from the rest of the models on the y axis.

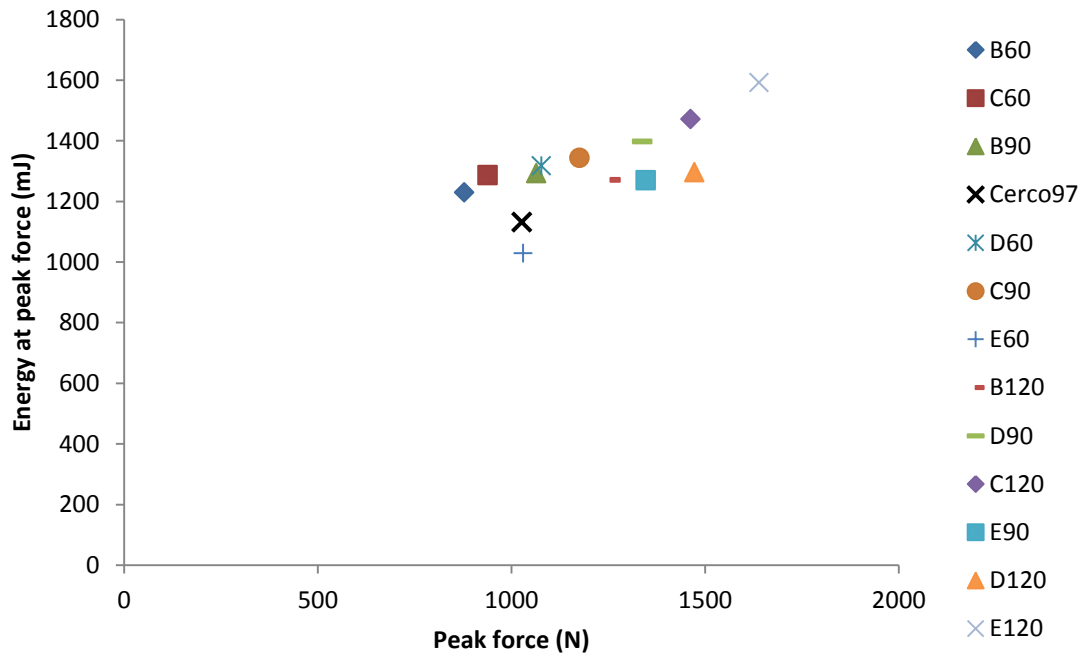


Figure 4.23 Bivariate plot of mean force and energy to break a solid hard object for each cusp design. Note: cusp names in the legend are in order of increasing radius of curvature.

In terms of fragmentation and force, the *C.atys* was found to be the most optimised out of all the cusp models as it produced the highest amount of fragmentation relative to the amount of force produced. This is clearly shown in Figure 4.24 where the *C.atys* cusp is shown to strongly diverge on the y axis, thus deviating in fragmentation index from the models with the most similar radius of curvature.

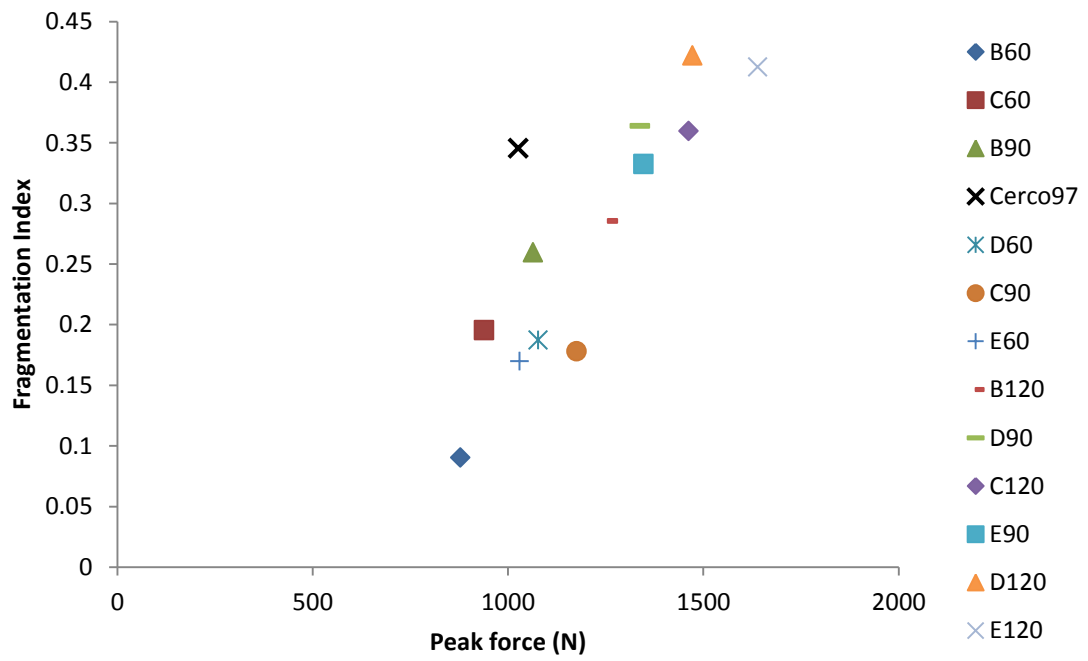


Figure 4.24 Bivariate plot of mean force and fragmentation index to break a solid hard object for each cusp design. Note: cusp names in the legend are in order of increasing radius of curvature.

4.3.3. Mechanical implications of dental wear in *C. atys*: Hollow hard object breakdown

Across the wear series, the way the hollow domes fractured was observed to vary. For the cusped models, the typical mode of fracture was via indentation where stress was concentrated at the point(s) of contact. In contrast, the flat and ridged models created a greater distribution of stress, which encouraged a build-up of tensile stress within the inner surface of the dome. As a result of this, the domes were observed to break almost instantaneously by bending outwards and collapsing in on themselves. The number of pieces that the hollow dome broke into was also noted to vary between different crown models. For the majority of models, the domes fractured and broke apart into several pieces (Figure 4.25a). However, for some, including the 2 cusp, 1 cusp and ridge model, several of the domes fractured but did not break apart (Figure 4.25b).

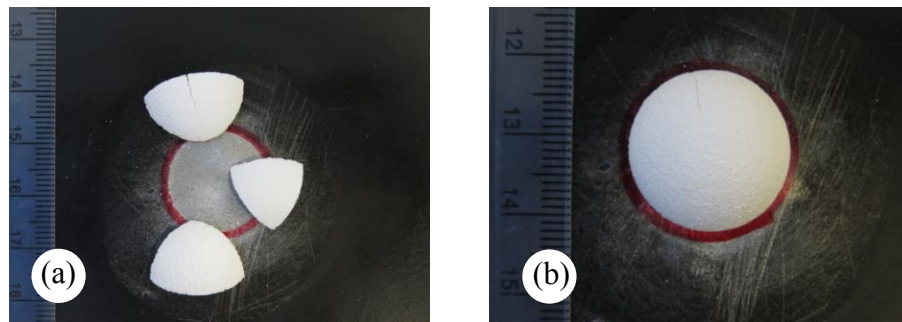


Figure 4.25 Comparison of fragmentation behaviour of hollow domes. The majority of models fractured and fragmented the domes into pieces (a), however some of the models only managed to fracture the dome (b).

Similar to the single cusp morphologies in chapter 2, the 1 cusp model exhibited multiple peaks in the force displacement plot. Therefore for each performance indicator for hollow hard object breakdown, both peak force and initial fracture are displayed in the results for the 1 cusp model (purple box plot).

4.3.3.1. Force recorded at breakage point (hollow object)

In terms of the peak force to break a hollow hard object, no significant differences were found between the different tooth morphologies as determined by a one-way ANOVA ($F_{6,61}=4.298$, $p=0.00112$). A lot of overlap in force values was observed between all of the models (Figure 4.26). Of these, the highest average force was found in the 0 cusp model (191.2N) followed by the 4 cusp (188.25N) and 3 cusp (187.2N) models. In comparison, the 1 cusp model had the lowest average force of 141.02N. A second test was run using the initial force at fracture for the 1 cusp model. In this case significant differences were found between the group means (Welch F test: $F_{25,51}=35.04$, $p=3.953E-11$) where the 1 cusp model was significantly different to all the other morphologies ($p<0.001$). This suggests that the force required to initiate fracture decreases with loss of cusps until the crown is modelled as flat where the force increases to a similar level as the 4 cusp (unworn) model.

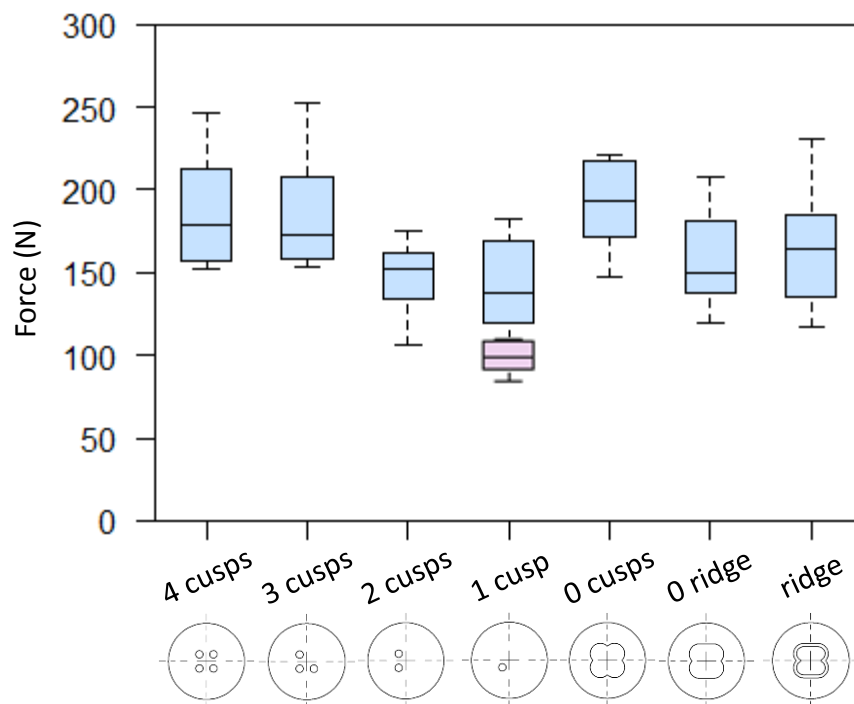


Figure 4.26 Boxplot displaying the peak force required to break a hollow hard object for each wear state shown in blue. The force required to initiate fracture for the 1 cusp model is shown in purple.

4.3.3.2. Energy recorded at breakage point (hollow object)

In terms of the energy required at peak force to break a hollow hard object, no significant differences were found between the tooth wear morphologies (Welch F test: $F_{27,01}=5.015$, $p=0.001437$). However the single cusp model was noted to require on average the highest amount of energy (79.89mJ), whereas the remaining models were quite similar in value and showed a great deal of overlap (Figure 4.27). The single cusp model was also noticed to be highly variable with values ranging between 22.6 mJ-126.7 mJ. When using the energy data at initial fracture for the 1 cusp model, significant differences were found between the group means ($F_{6,61}=5.733$, $p=8.879E-05$). Using a pairwise comparison, the ridge model was found to be significantly different to the 1 cusp model at initial fracture ($p<0.001$) and had the highest energy value (44.82mJ). However, no significant differences were found among the other models ($p>0.001$). The energy at initial fracture for the 1 cusp model was also found to be much more consistent in behaviour than at peak force.

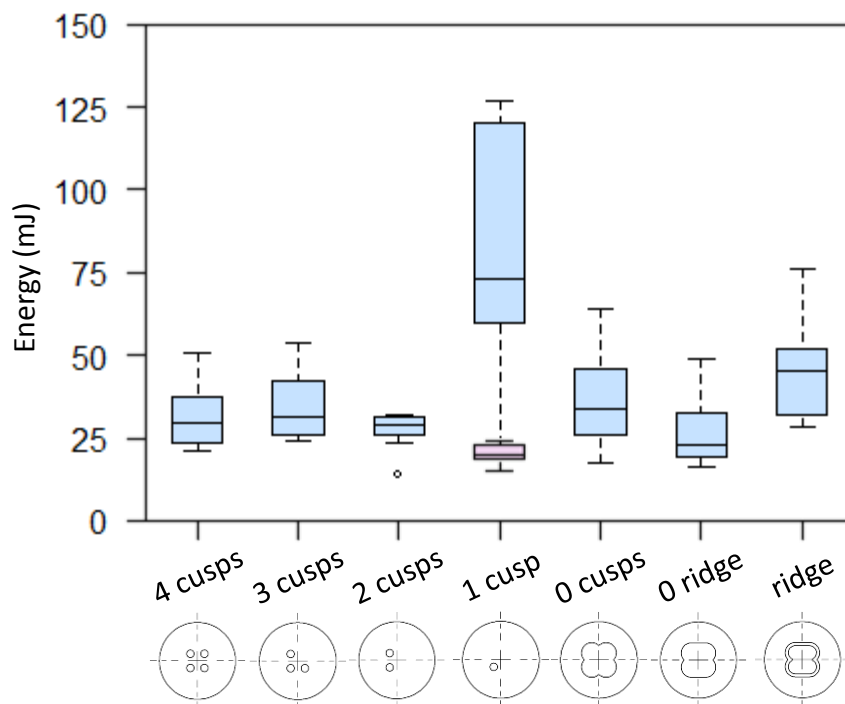


Figure 4.27 Boxplot displaying the energy required at peak force to break a hollow hard object for each wear state shown in blue. The force required to initiate fracture for the 1 cusp model is shown in purple.

4.3.3.3. Duration recorded at breakage point (hollow object)

The time taken to break a hollow hard object at peak force was significantly different between the tooth wear morphologies (Welch F test: $F_{26,78}=18.22$, $p=2.606E-08$). The single cusp model took the longest time to reach peak force (12.41s) and was significantly different to all the other models ($p<0.001$) (Figure 4.28). The ridge model had the second highest average time (8.48s) but was only found to be significantly different to the 1 cusp model and the 0 ridged model ($p>0.001$). The remaining models were quite similar in time and overlapped in values. When using the time data at initial fracture for the 1 cusp model, significant differences were again found between the group means ($F_{6,61}=16.81$, $p=2.439E-11$). Using a pairwise comparison, the ridge model was found to be significantly different to all the other models ($p<0.001$) and had the highest average time value (8.48s). However, no significant differences were found among the other models ($p>0.001$). Similar to force and energy, the time at initial fracture for the 1 cusp model was also found to be much more consistent in behaviour than at peak force.

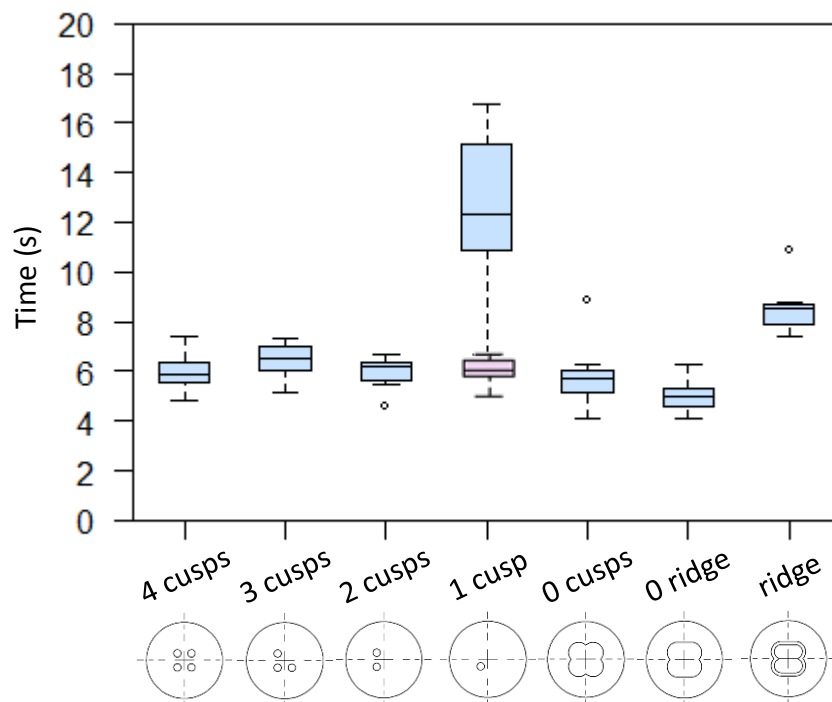


Figure 4.28 Boxplot displaying the time required at peak force to break a hollow hard object for each wear state shown in blue. The force required to initiate fracture for the 1 cusp model is shown in purple.

4.3.3.4. Surface area recorded at breakage point (hollow object)

From Figure 4.29, it is clear that the surface area at peak force is closely related to the crown wear morphology. Significant differences in surface area were found between the group means ($F_{6,61}=1504$, $p=2.683E-64$). The greatest surface area values at peak force were in the flat models; 0 cusps and 0 ridge, which were 87.7mm^2 and 87.3mm^2 respectively. These flat morphologies were not significantly different from one another ($p>0.001$) but were significantly different to all the other models in the series ($p<0.001$). The ridged model also had a high surface area value and was significantly different to all of the models ($p<0.001$). In contrast, the cusped models had the lowest surface area values and were shown to decrease in surface area with decreasing cusp number with the 2 cusp model having the lowest surface area (7.09mm^2). However at the 1 cusp wear state the surface area was shown to increase and was relatively variable. A second statistical test was run but using the surface area at initial fracture for the one cusp model. Significant differences were again found between the group means (Welch F test: $F_{24,45}=3815$, $p=4.415E-35$). In this case, the surface area to initiate fracture is shown to decrease across all the cusped morphologies with the 1 cusp model being significantly different to both the 4 cusp and 3 models ($p>0.001$). As soon as the tooth is flat, the surface area drastically increases but is reduced significantly with the ridged model.

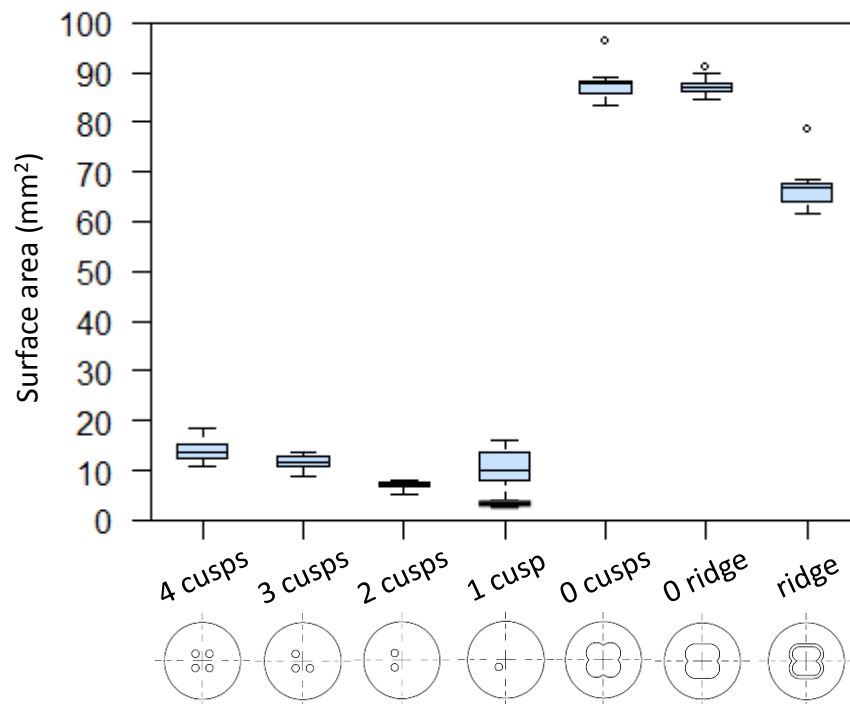


Figure 4.29 Boxplot displaying the contact surface area of each crown at peak force to break (blue) and initiate fracture (purple) in a hollow hard food object.

4.3.4. Mechanical implications of dental wear in *C. atys*: Solid hard object breakdown

As with hollow breakdown, the mode of fracture of the solid hard objects was observed to vary with crown morphology. For the cusped models, the domes were typically fractured via indentation breaking the domes into 2 or more pieces (Figure 4.30a). In contrast, the flat models (0 cusps, 0 ridge) tended to compact the 3D print material of the dome where the tops were flattened and the sides expanded giving an overall crushed appearance (Figure 4.30b).

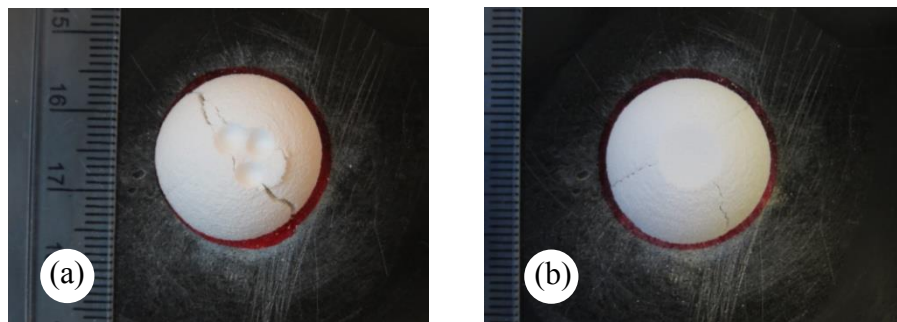


Figure 4.30 Comparison of fragmentation behaviour of solid domes. The majority of models fractured and fragmented the domes into pieces (a); however some of the models only managed to fracture the dome (b).

4.3.4.1. Force recorded at breakage point (solid object)

A clear pattern was observed between tooth wear morphology and the peak force required to break a solid hard object; where the force was shown to decrease with loss of cusps and then increase to an even higher degree in the extreme wear states (Figure 4.31). Significant differences were found between the group means (Welch F test: $F_{27.62}=15.96$, $p=7.713E-08$) therefore permitted a post hoc analysis of the data. Based on this, the ridge model was found to be significantly different to all the other models ($p<0.001$) and reached the highest forces (average= 1925.3N). The lowest average force was reached by the 1 cusp model (1018.4N), however it should be noted that the repeats were quite variable and overlapped greatly with the other cusped models and the flat models (0 cusps and 0 ridge). No significant differences in force were found between the 0 cusp and 0 ridge models nor between the different cusped models ($p>0.001$).

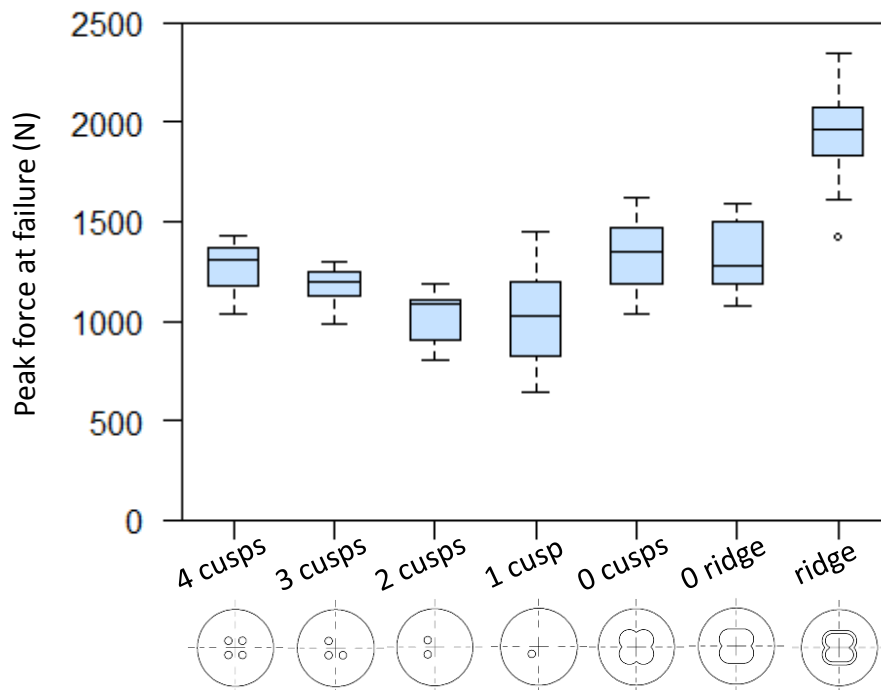


Figure 4.31 Boxplot displaying the maximum force required to break a solid hard object for each wear state.

4.3.4.2. Energy recorded at breakage point (solid object)

In terms of energy at peak force to break the solid hard object, significant differences were found between the different tooth wear morphologies (Welch F test: $F_{27.36}=9.352$, $p=1.311E-05$) (Figure 4.32). The ridged model was found to be significantly different to all the other models ($p<0.001$) and required on average the highest amount of energy (2697.32mJ). The lowest average energy value was recorded in the 0 ridge model (975.43mJ), which required less than half the energy of the ridge model. However, if excluding the ridge model, a clear pattern could not be detected among the models due to a large amount of overlap in energy values. None were found to be statistically different based on a pairwise comparison; therefore a single morphology could not confidently be classed as the best performer as there potentially appears to be several. However it was noted that the consistency between the repeats was variable across the sample with the 4 cusp, 3 cusp, 2 cusp and 0 ridge models being much more consistent in recorded energy than the other models.

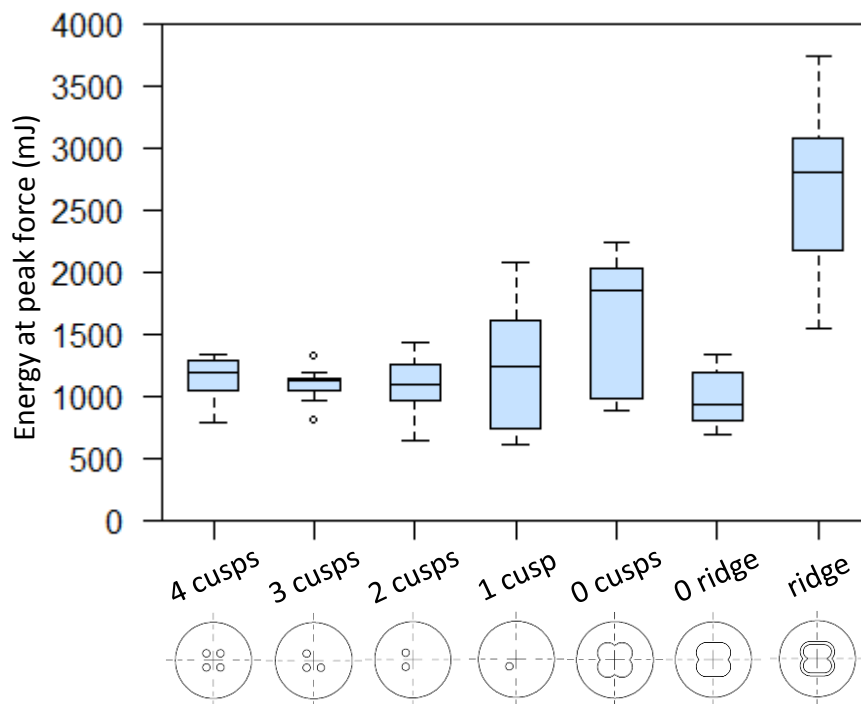


Figure 4.32 Boxplot displaying the energy required at peak force to break a solid hard object for each wear state.

4.3.4.3. Duration recorded at breakage point (solid object)

Significant differences were found between the crown morphologies based on the time taken at peak force to break a solid hard object (Welch F test: $F_{27,35}=33.64$, $p=2.152E-11$) (Figure 4.33). The single cusp and the ridged model took on average the longest time (36.3 and 38.4 s respectively) and were not significantly different from one another ($p>0.001$) and were both found to be significantly different to the others in the series ($p<0.001$). In contrast, the 0 ridge model took the quickest time averaging 20.6 seconds to reach peak force at failure. For the remaining models (4 cusps, 3 cusps, 2 cusps, 0 cusps) the average values were similar and were not significantly different ($p<0.001$). However there does appear to be a slight increase with time with loss of cusps. Again, variation was observed regarding the consistency between the repeats for each of the models. The 4 cusps, 3 cusps, 2 cusps and 0 ridge models were found to be the most consistent in duration in comparison to the other models where the 1 cusp crown was the most variable.

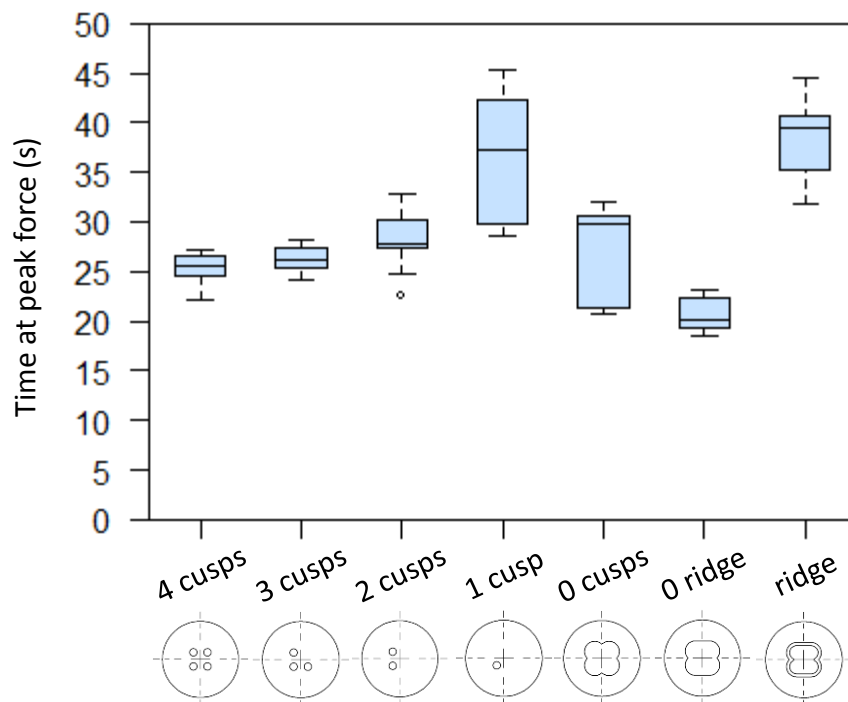


Figure 4.33 Boxplot displaying the time required at peak force to break a solid hard object for each wear state.

4.3.4.4. Fragmentation (solid object)

Significant differences were found between the crown morphologies in relation to how they fragment a solid hard food object (Welch F test: $F_{27,18}=39.26$, $p=3.786E-12$). However the fragmentation index was quite variable between the models rendering it difficult to detect a clear pattern or trend. This was largely due to the fact that the results were highly variable between the repeats in the more worn models, which included the 1 cusp, 0 cusp, 0 ridge and ridge models. For example, in the ridged model some of the domes were deformed with very little fragmentation (Figure 4.34a) whereas in others the dome was highly fragmented (Figure 4.34b).

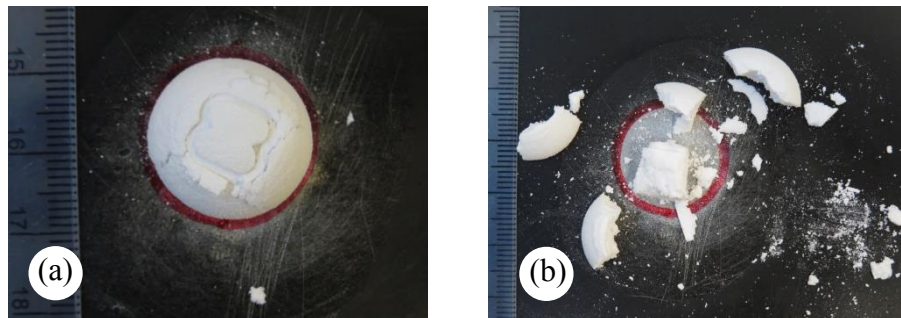


Figure 4.34 Examples of the extremes in fragmentation produced by the ridge model where in some of the repeats the dome was deformed with little fragmentation (a) and in others the dome was completely pulverised (b).

Overall, the results indicate that the most efficient crown for this criterion was the 3 cusp model, which had on average a fragmentation index of 0.64 where the dome was typically broken into 3 pieces (Figure 4.35). The poorest performers were the 1 cusp and flat models (0 cusps and 0 ridge) where in some of the repeats, fragmentation did not occur at all. Of these, the lowest average fragmentation index was found in the 1cusp model, which was 0.16.

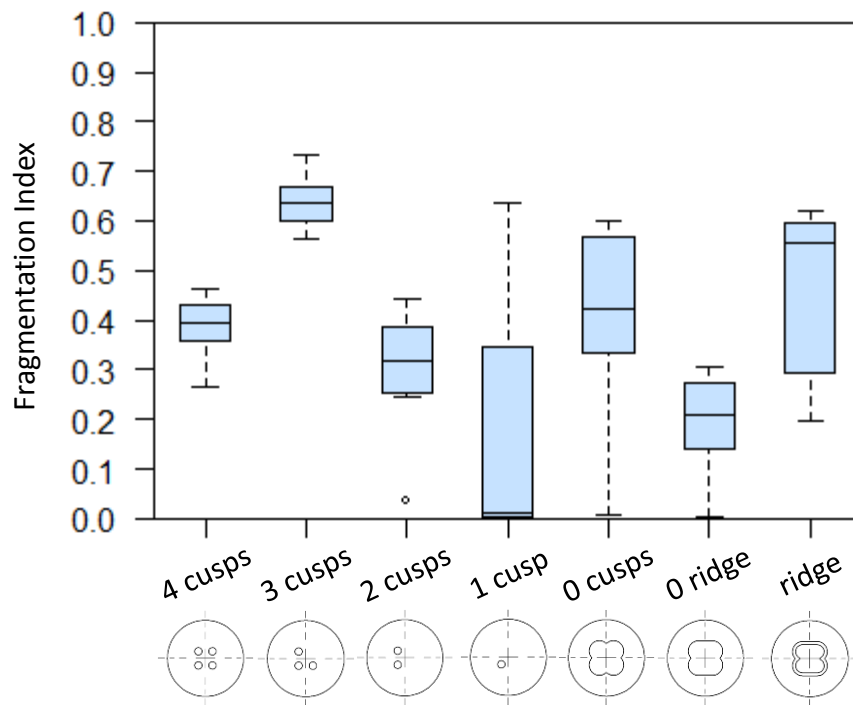


Figure 4.35 Boxplot displaying the degree of fragmentation of a solid hard object for each wear state where a high fragmentation index indicates a greater number of smaller particles.

4.3.4.5. Surface area recorded at breakage point (solid object)

In terms of the contact surface area at peak force, significant differences were found between the different crown morphologies (Welch F test: $F_{27,31}=219.8$, $p=8.455E-22$). Generally, a high contact surface area was associated with models representing the more worn tooth morphologies (Figure 4.36). The ridge model had the highest average surface area (228.6mm^2) and was significantly different to the other models ($p<0.001$). This was followed by the flat models 0 cusps and 0 ridge, which were not significantly different from one another ($p>0.001$). The lowest average value of these was found in the 2 cusp model, which was 92.1mm^2 . Despite differences in cusp number the 4 cusp, 3 cusp and 2 cusp models were similar in surface area values and were not significantly different from each other ($p>0.001$). These models along with the 0 ridge model were also found to be the most consistent in surface area at peak force.

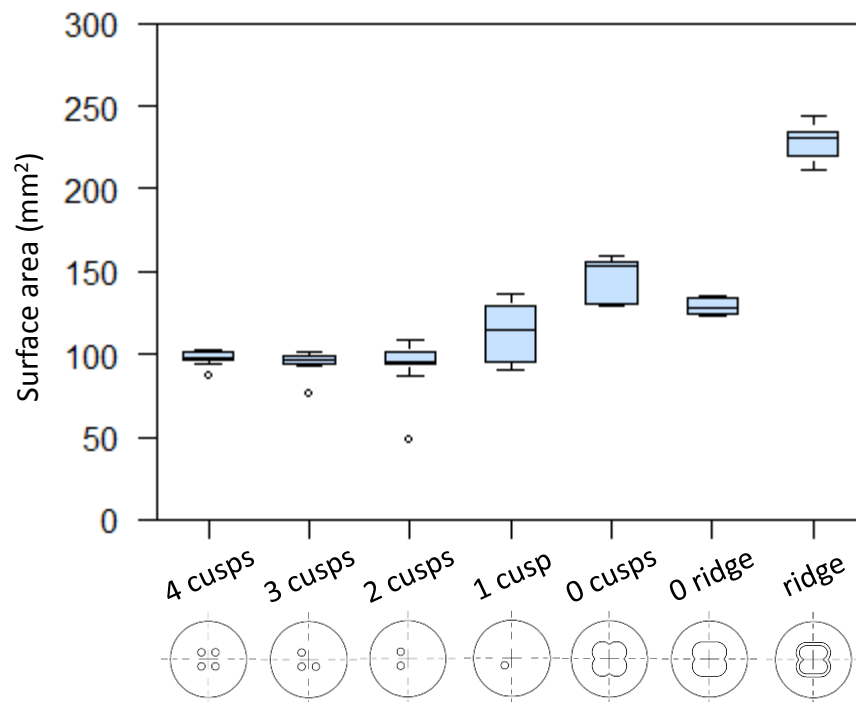


Figure 4.36 Boxplot displaying the contact surface area of each crown at peak force to break a solid hard food object.

4.3.5. The effect of 1 cusp arrangement on mechanical performance: Hollow hard object breakdown

In terms of hollow hard object breakdown, the centralised one cusp model was more able to consistently break the hollow dome apart in comparison to the lateral cusp model where fracture often occurred without fragmentation (Figure 4.37).

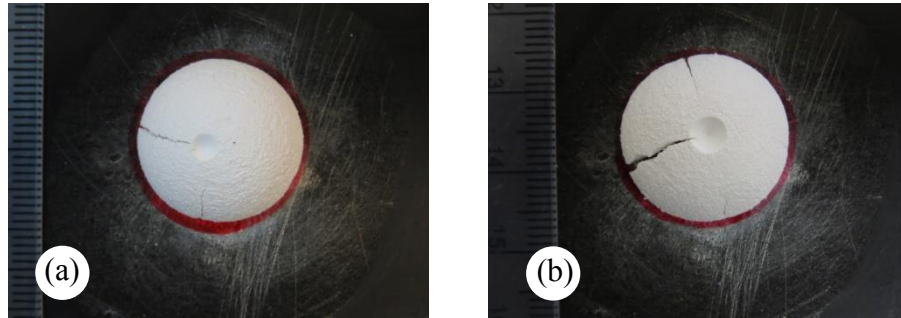


Figure 4.37 Examples of the hollow domes fractured by the (a) 1 cusp model (lateral) where in some of the repeats fracture occurred without fragmentation and (b) 1 cusp (central) model where all the hollow domes broke into 2-3 pieces.

At the peak force to break a hollow hard object (blue box plots), the centralised one cusp model tended to produce slightly higher values in force, time, energy and surface area in comparison to the laterally placed cusp (Figure 4.38). The increase in these values can largely be attributed to a greater displacement of the model, which was over 3 times greater for the central cusp than the laterally placed cusp. However, these differences were not supported statistically ($p > 0.001$ for all tests). An additional observation at peak force was that the central cusp was also more variable among repeats for time, energy and surface area. For the initial fracture of a hollow hard object (purple boxplots) the values for force, time, energy and surface were much lower in comparison to peak force at failure and were also much more consistent in behaviour. In this instance, the results appeared almost identical where no significant differences were found between the different single cusp models for each of the performance variables or for surface area.

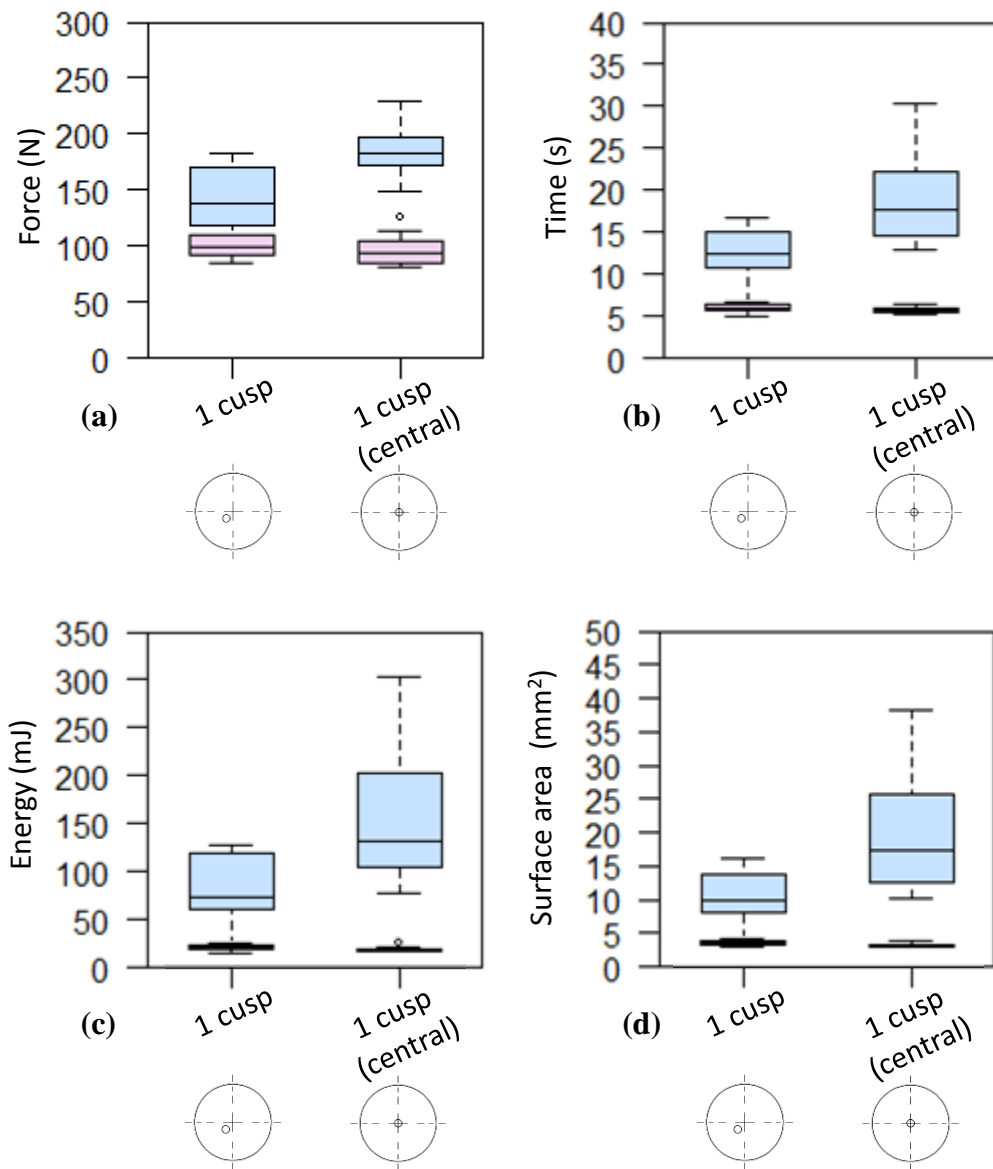


Figure 4.38 A comparison of the results between the single cusp models for each of the mechanical performance criteria and surface area. Results are shown at peak force (blue) and initial fracture (purple) to break a hollow hard object.

4.3.6. The effect of 1 cusp arrangement on mechanical performance: Solid hard object breakdown

Similar to the hollow domes, the 1 cusp model was also much poorer in fragmentation performance where some of the domes fractured and deformed considerably but were not fragmented at all (Figure 4.39a). Instead, chipping fracture was observed to occur as a result of off-axis loading. In contrast, the 1 cusp central model was able to fragment the domes into 2-4 pieces (Figure 4.39b).

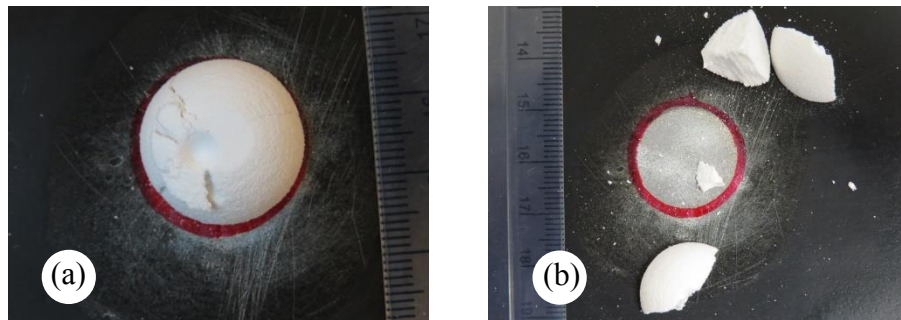


Figure 4.39 Examples of the solid domes fractured by the (a) 1 cusp model (lateral) where in some of the repeats fracture occurred without fragmentation and (b) 1 cusp (central) model where all the solid domes broke into 2-4 pieces.

The 1 cusp central model was shown to have a significantly higher amount of contact surface area at failure than the laterally placed cusp (Welch F test: $F_{9,55}=182.6$, $p=1.53E-07$). Despite of this, there were no significant differences found for any of the performance criteria, although, the 1 cusp model was noted to be much more variable in behaviour (Figure 4.40). In light of these results, it seems that the movement of a single cusp has the greatest impact on the physical breakdown of both hollow and solid hard objects where the centrally placed cusp performs the best.

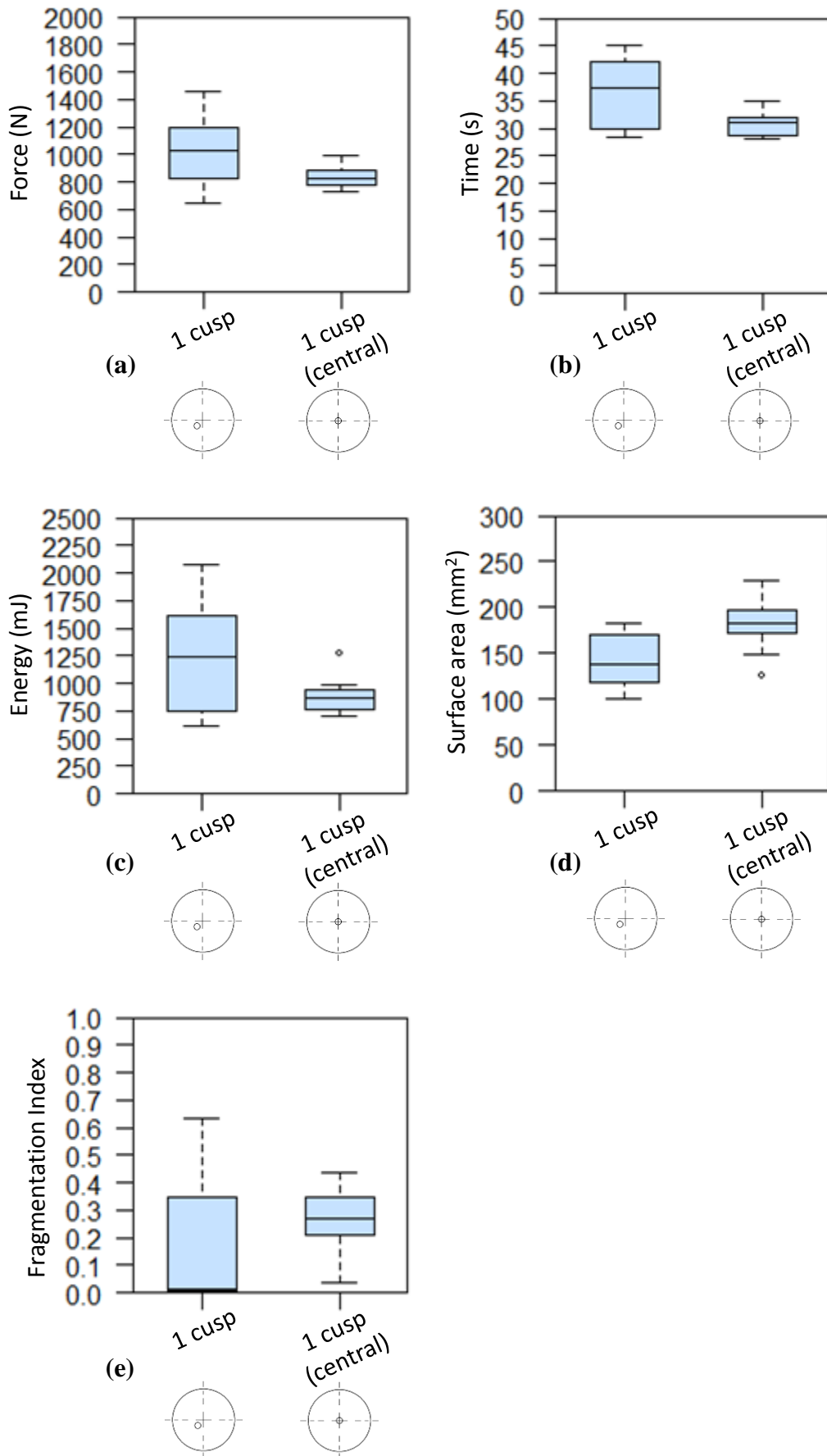


Figure 4.40 A comparison of the results between the single cusp models for each of the mechanical performance criteria and surface area to break a solid hard object.

4.3.7. The effect of 4 cusp arrangement on mechanical performance: Hollow hard object breakdown

The mechanical breakdown of a hollow hard object was very similar between the two different cuspal arrangements of the 4 cusp model (Figure 4.41). No significant differences were found between the 4 cusp and 4 cusp (intercuspal) crown morphologies for each of the performance indicators and for surface area ($p>0.001$).

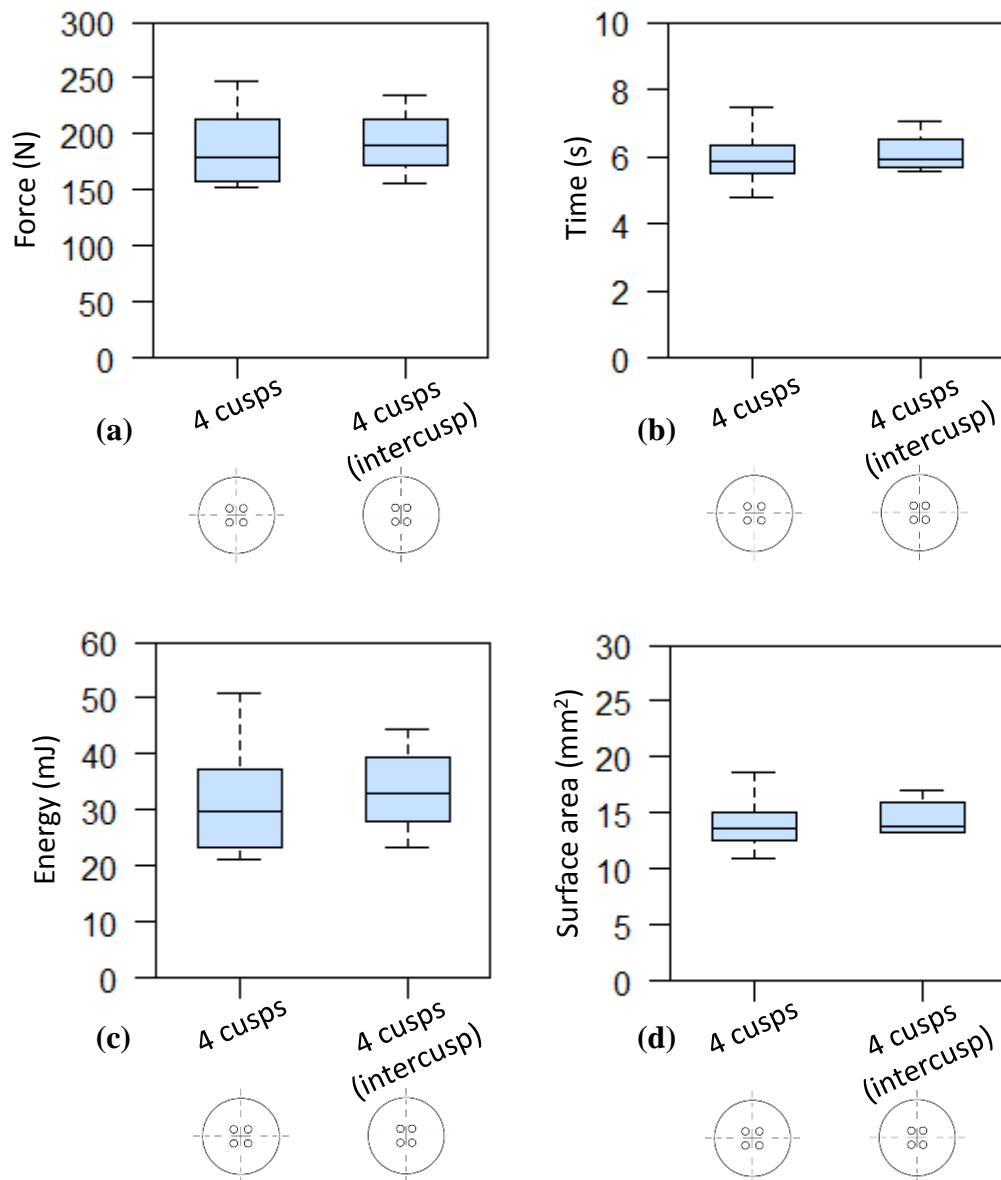


Figure 4.41 A comparison of the results between the 4 cusp models of different cuspal positions to break a hollow hard object for each of the mechanical performance criteria and surface area.

4.3.8. The effect of 4 cusp arrangement on mechanical performance: Solid hard object breakdown

Significant differences were found between the different 4 cusp models in terms of the contact surface area at peak force to break a solid hard object ($F_{1,18}=19.96$, $p=0.0002974$). However similar to the results of the one cusp models, no significant differences found between the two models for any of the performance criteria; force, time, energy and fragmentation (Figure 4.42).

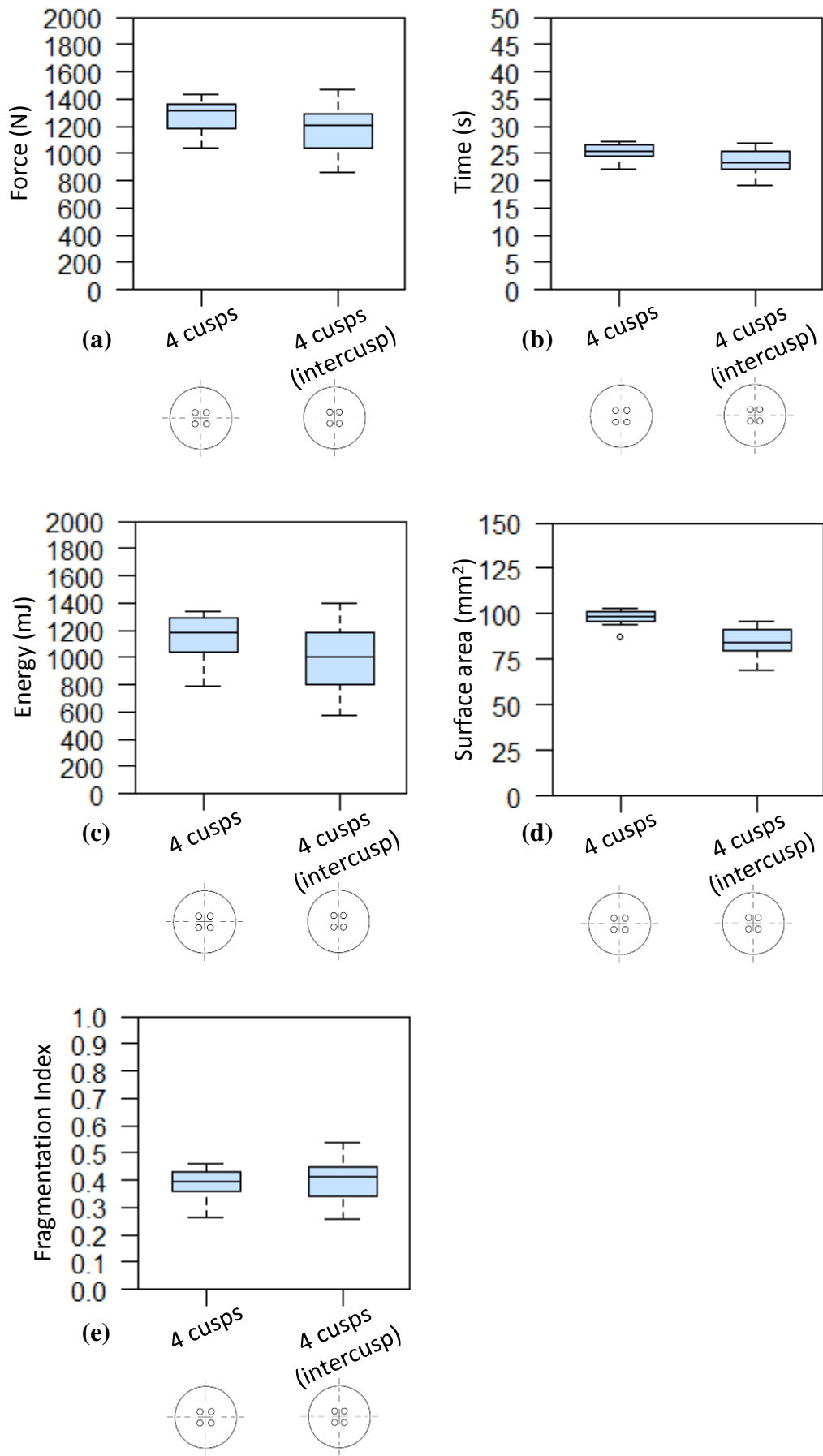


Figure 4.42 A comparison of the results between the 4 cusp models of different cuspal positions to break a solid hard object for each of the mechanical performance criteria and surface area.

4.4. Discussion

The aim of this chapter was to investigate how some of the key changes in *C.atys* dental morphology due to wear effect the breakdown of hard food items. Using mechanical testing, the optimality of a single unworn *C.atys* cusp was first examined in comparison to a large functional morphospace of hypothetical cusp morphologies (previously presented in chapter 2). Secondly, the main features of dental wear observed in a developmental sample of *C.atys* (see chapter 3) were also physically modelled and tested to examine how these changes in form may alter function. Several questions were originally outlined and are discussed below.

4.4.1. Is a single unworn cusp of *C. atys* optimised for hard object feeding?

Previously, several studies have made attempts to associate cusp radius of curvature with diet yet have produced conflicting results (Yamashita, 1998a, Hartstone-Rose and Wahl, 2008, Berthaume, 2014). Difficulties arise in that several cusp forms could exist to solve the same function, or alternatively, the same cusp morphology could be used for the breakdown of several different foods (Lucas and Teaford, 1994, Yamashita, 1998b). Therefore it is extremely difficult to distinguish species with different diets based on cusp shape alone. However, by using mechanical testing to quantify and compare the performance of cusps for a single food item, this study has allowed for a more direct means to examine whether a cusp shape seen in nature is functionally optimal for its diet.

Based on the functional optimality criteria examined in this chapter, the results suggest that the unworn *C.atys* cusp is optimised for the breakdown of hard foods. Although the *C.atys* cusp did not perform the best in any one of the individual criterion of force, energy, duration or fragmentation, it did adequately perform when considering all of the optimisation criteria for both hollow and solid hard object breakdown. In the cases of initial fracture of the hollow and peak force of the solid, which is coincidentally also initial fracture, the *C.atys* cusp morphology performed exceptionally well, where both time and energy were low relative to a low force. For the fragmentation of the solid dome, the *C.atys* cusp particularly stood out as being the most efficient, producing the highest amount of fragmentation for the amount of force produced. These findings therefore support the expectation that the unworn *C.atys* cusp is optimised for the mechanical breakdown of hard foods, which is vital given that the unworn M1 cusp form must be fully functional for hard object feeding as soon as it has erupted (McGraw et al., 2011, Morse et al., 2013).

However, as discussed in chapter 2, tooth optimality not only involves maximising the efficiency of food breakdown, but also to resist failure under high loads (Berthaume et al., 2013, Crofts, 2015). Generally, sharper cusps with a smaller radius of curvature are more susceptible to breakage (Rudas et al., 2005, Lawn and Lee, 2009, Crofts, 2015). How the dimensions of an unworn *C.atys* cusp implicate the risk of fracture are at present unknown and would require further research. Whilst acknowledging the unworn cusp is comparatively sharper than adult teeth in *C.atys*, it is predicted that the extent of fracture susceptibility is reasonably low seeing that (1) the unworn M1 is used for hard object feeding as soon as it is erupted (McGraw et al., 2011, Morse et al., 2013), and (2) although highly worn, it is not notably damaged in older specimens. Furthermore, research by Berthaume et al. (2013) suggests that a combination of different cusp morphologies on the crown allow for the optimisation of both food breakdown and resistance to fracture. Therefore when investigating the balance between these two different functions; the topography of the whole occlusal surface should be accounted for.

An additional factor that should be taken into consideration is that the unworn *C.atys* cusp design used in this study was based on the average radius of curvature and angle of four cusps from a single tooth. As shown in chapter 3, these measurements do vary between cusps of the same crown where lingual cusp tips were generally sharper and acuter in comparison to the buccal cusps. By taking an average may potentially mask the individual mechanical performance of each cusp. With this in mind, it may prove beneficial to test the performance of several cusp designs that exist on a single crown in future studies.

Finally, the results from chapter 3 indicate that the cusps on a *C.atys* M₁ are lost rapidly early on in development as the crown becomes progressively blunter and flatter as a result of dental wear. As adults also require the dentition to fracture the same hard foods (McGraw et al., 2011) raises the question of whether the changes in tooth shape from the unworn state affect the mechanical efficiency of hard object breakdown. Naturally, there is also more than one cusp on the crown, which form multiple points of contact with the food item. These factors were addressed as part of this chapter and will now be discussed in the following section.

4.4.2. Are there any differences in mechanical performance between different crown morphologies produced through wear when used to break hard food items?

During development, *C. atys* experiences not only changes in the skull and masticatory muscles (O'Higgins and Jones, 1998, Fitton et al., 2015) but also in the shapes of teeth as a result of dental wear (see chapter 3). Despite these anatomical changes, all members of *C. atys* partake in hard object feeding regardless of age group (McGraw et al., 2011). The aim of this study therefore was to investigate whether the shape changes associated with dental wear in *C. atys* affect the ability to process hard food items. The results will now be discussed in relation to the ontogeny and feeding ecology of *C. atys*.

In terms of hollow hard object breakdown, no significant differences were found in force and energy between the different crown morphologies associated with different stages of dental wear (4 sharp cusps through to flat with an enamel ridge). Despite drastic differences in contact surface area, the level of force was fairly similar between the different wear states. An explanation for this apparent equivalence in performance could be rooted in the interaction of the surface area of contact from the model and the fracture behaviour of the hollow dome. For the cusped models, the typical mode of fracture was via indentation where stress was concentrated at the point(s) of contact thereby maximising pressure (Figure 4.43a). In contrast, the flat and ridged models created a greater distribution of stress, which encouraged a build-up of tensile stress within the inner surface of the dome (Figure 4.43b). As a result of this, the domes were observed to break almost instantaneously by bending outwards and collapsing in on themselves. Both of these methods of fracture therefore appear equally able at generating stress within the food item thereby compensating for differences in surface area.

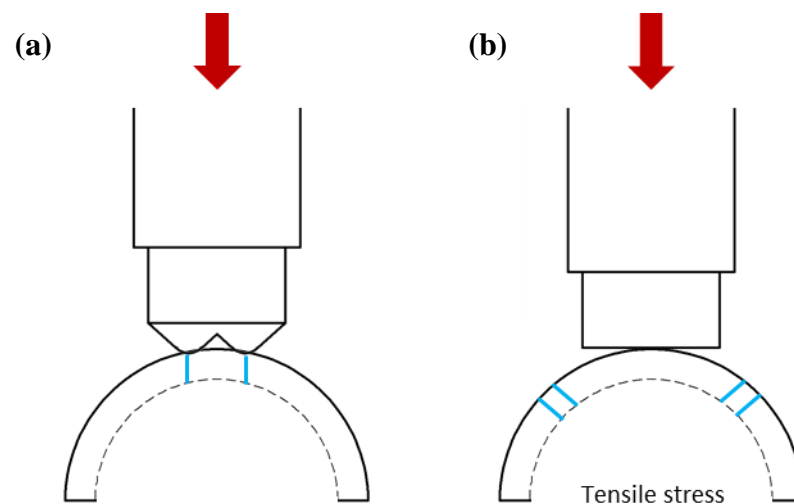


Figure 4.43 Diagram predicting two different ways the hollow dome could fracture depending on the crown model used for compression. For the cusped models (a), the force is localised at the points of contact onto the hollow dome causing fracture via indentation. In contrast, for the flat models (b), fracture is encouraged by a build-up of stress on the inside of the dome as a result of tensile stress. Red arrows indicate the direction of force applied to the dental models and blue lines indicate the areas of stress concentration in the hollow object. Scaled 2:1.

While no significant differences were found between groups, some interesting patterns were found between the different wear states. As the 4 cusps were eliminated to form the 2 cusp and 1cusp dental models, a slight reduction in force required to break the hollow hard objects was observed. Drawing upon previous research, a decrease in force is likely to occur as a result of a reduction in contact surface area which elevates the amount of localised stress in the food item (Evans and Sanson, 2005b). This is particularly interesting given that in *C.atys* and indeed in other cercopithecoid primates (Benefit, 2000), the tooth is positioned in the jaw with the cusps higher on one side thus forming 2 points at initial contact. Assuming a vertical bite, this would form only 2 points at initial contact (Figure 4.44). On the lower dentition in *C.atys*, the lingual cusps are not only much higher but are also less worn and retain their shape longer in the early stages of development in comparison to the buccal cusps (see chapter 3). Therefore within the first 5 years of life in *C. atys* the presence of 2 cusps could play an important role in lowering the amount of force required at fracture thus compensating for smaller absolute muscle size previously recorded (Fitton et al., 2015). This may therefore allow for a type of functional equivalence across the age groups.

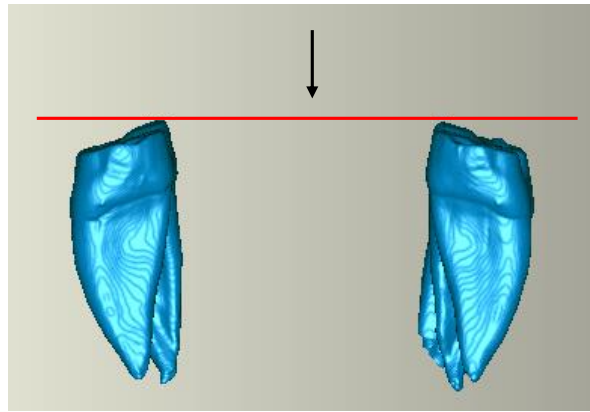


Figure 4.44 The orientation of *C. atys* molar teeth in centric occlusion where the lingual cusps form the first point of contact. C13.17 used as example. Image viewed in distal perspective.

Once reduced to 1 cusp, despite requiring a low force, this model expended the highest amount of energy and the longest duration to break the hollow object. The 1 cusp model was also highly variable in performance. It is worth keeping in mind however that if the M1 starts to become suboptimal in performance, an alternative tooth may be used during hard object feeding instead. For example, around the time the crown is reduced to a single cusp at stage 2 development, the permanent P4 starts to come through, which is also used during postcanine crushing behaviours in *C. atys* (Morse et al., 2013) (Figure 4.45).

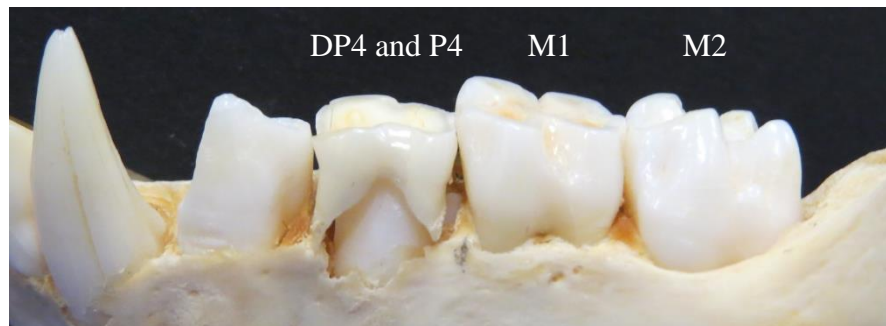


Figure 4.45 The eruption of the permanent mandibular P4 during stage 2 development (specimen C13.17). Photograph: Karen Swan.

However, what was most interesting about the 1 cusp model was that when used to fracture hollow domes, a drop in force occurred prior to breakage, which indicated initial fracture. When taking this into account, the point of initial fracture (first peak in graph) of the hollow dome for the 1 cusp model showed the force, energy and duration to be much lower and more consistent in behaviour than at peak force. In relation to *C. atys*, the act of initiating fractures could potentially play a vital role in weakening the structure in order to later induce complete failure of the stress resistant endocarps. For example, Daegling et al. (2011) suggests that the incisal activities undertaken by sooty

mangabeys prior to postcanine crushing are used to initiate cracks in the food item in which cracks can grow quickly once processed by the P4 and M1 teeth. This is based on the fact that in the wild, *C.atys* has been observed to discard over 50.4% of *Sacoglottis* endocarps after initial incision. They go on to suggest that prior to wear, the cusps of the postcanine teeth may also be used to do this. Therefore the role of the 1 cusp model and potentially the 2 cusp model may be to initiate fracture at a low force rather than to break the object in one go.

A further factor to consider is the degree of breakdown, as the number of pieces the hollow dome broke into was noted to vary between the different crown models. For the majority of models, the domes fractured and broke apart into several pieces (see section 4.3.3). However for some, such as the 2 cusp, 1 cusp and ridge model, several of the domes fractured but did not break apart. The significance of this finding in relation to *C. atys* is unclear as in reality a series of bites, or alternatively the hands might be used to break the food item apart subsequent to fracture (McGraw et al., 2011).

Interestingly, the worn states represented by the flat and ridge models were not shown to be particularly disadvantageous or advantageous. Previous research on folivorous primates has typically associated the extreme wear state of the enamel ridge with a single dentine pool with the onset of dental senescence (Dennis et al., 2004, King et al., 2005). However, this does not appear to be the case for the breakdown of hollow hard food items as there was little difference in performance between these models and the lesser worn crown morphologies.

In contrast to hollow object breakdown, the differences in mechanical performance were much more obvious between the different wear states when used to break solid hard objects. The same pattern of decreasing force was observed as the number of cusps decreased in number. Therefore the 2 cusp and 1 cusp models performed the best at minimising force, which as discussed previously could be potentially advantageous for juveniles that have a much smaller absolute muscle size. However, with the loss of cusps, a greater amount of time was required to reach the point of breakage. Interestingly, the peak force values between the flat models and the unworn 4 cusp model were very similar. The least efficient crown morphology to break down solid hard objects was undoubtedly the most worn state represented by the ridge model, which took on average nearly 2000N to reach peak force (~1000N more than the 1 cusp model). The ridge model also expended the greatest amount of energy and took the

longest time to break the object. As this morphology is limited to adults it may be the case that a greater absolute muscle size may help compensate for this poor level of dental efficiency. However, it is also worth noting that the ridge model was loaded centrally onto the solid object. In reality the food may be placed with the ridge positioned at the centre. This action may actually help lower the force, energy and time to break the object by concentrating a high level of stress in the centre of the food item (Figure 4.46).

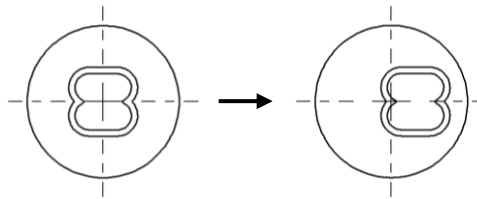


Figure 4.46 Diagram displaying a comparison of the placement of the ridge model on the dome.

Of great importance for digestion, the most efficient crown for fragmenting the solid food was the 3 cusp model, which was followed by the ridge model. Why the 3 cusp model performed the best is unclear but the displacement values indicate that both the cusps and the flat area where a cusp was eliminated were in contact with the dome at failure. The proportion and combination of both these morphologies could potentially aid the initiation and propagation of fracture. The poorest performers were the 1 cusp and flat models where in some of the repeats, fragmentation did not occur at all. Instead, the domes were compacted where the tops were flattened and the sides expanded giving an overall crushed appearance. It therefore may be the case that for the flatter teeth, a greater number of chews would be required to fragment the food sufficiently for digestion. Although not entirely consistent, the effect of a ridge shown in the later wear states may actually be more beneficial by generating a high amount of stress in the food object yet providing a means to wedge the item apart causing catastrophic failure. By producing a higher amount of fragmentation for digestion, the ridge model may therefore potentially compensate for high energy expenditure.

From these results, it is clear that cusp wear has a much greater effect on solid hard object breakdown than hollow. However, poor performance for breaking down solid hard objects may be less relevant for *C.atys* that fractures the endocarp of *S.gabonensis* for food access. It therefore seems that dental wear does not have a detrimental effect on mechanical performance throughout development in *C.atys*. However, the hemispheres used in this study to represent hard food items were highly simplistic in terms of both

geometry and structure. In reality, the endocarp of *S.gabonensis* is not strictly hollow; the interior in which the seeds are situated are surrounded by a complex honeycomb structure (See Figure 1.17e p. 45). Furthermore, the size and shape of the endocarp alone could also influence mechanical performance. For example, Crofts and Summers (2014) found that the shape of 3D printed snail shells that were compressed by the same dental models can highly effect the force required at fracture. Therefore future study may benefit by CT scanning and 3D printing the entire structure of the *S.gabonensis* endocarp when used to test the functional performance of *C. atys* teeth.

4.4.3. The effect of cusp placement

In addition to the analyses on wear morphology, two additional sets of results were included to investigate the effect of cusp positioning on the breakdown of hollow and solid hard food items. The 1 cusp model created for the wear series had a cusp orientated laterally to the centre of the dome. However, in reality, the food item may potentially be moved to increase masticatory efficiency. To examine whether this is the case, the mechanical performance of the 1 cusp model was compared to an additional 1 cusp model with the cusp orientated centrally to the dome. For both hollow and solid hard object breakdown, no significant differences were found in mechanical performance between the different cuspal positions. However the mode of fracture was notably different between the two different models. This was partially evident in the solid domes where the off-axis loading from the laterally placed cusp caused chipping fractures to occur where scallop shaped segments spalled off the side of the dome (Figure 4.47) (Constantino et al., 2010, Chai et al., 2011, Lawn et al., 2013). As the laterally placed cusp was also much more variable in relation to the fragmentation index, it does seem that this mode of fracture is less efficient. Although statistically insignificant, the results from this section definitely highlight the need for further research in this area.

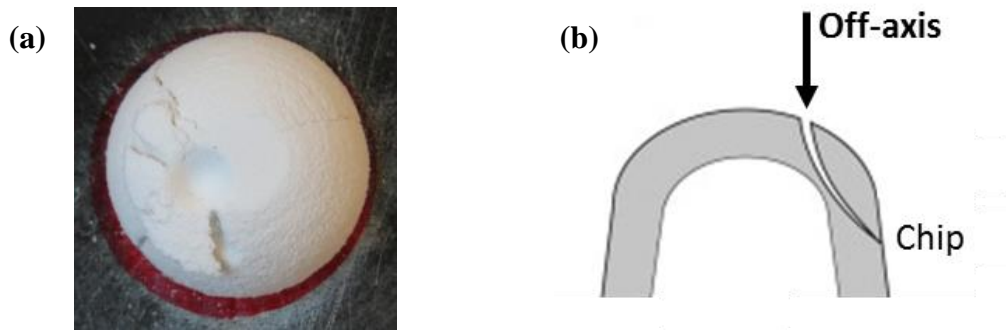


Figure 4.47 Chipping fracture that occurred when a single cusp was positioned laterally to the centre of the dome (a). This was the result of off-axis loading (b) – Adapted from Lawn et al. (2013).

The effect of the position of 4 cusps on mechanical performance was also examined. To simplify the simulation of wear, the 4 cusps of the unworn model were placed equally apart. However in the real *C.atys* tooth, the cusps exhibit a rectangular configuration. No significant differences were found between these two cuspal arrangements for each performance indicator. The changes in cusp positioning in this analysis may have been too subtle to detect any potential changes in mechanical performance. Further study in this area may benefit by simulating more drastic changes in cusp positioning and perhaps testing a selection of different arrangements.

4.5. Conclusions

During ontogeny, the M1 tooth of *C.atys* undergoes several different shape changes as a result of dental wear, which include the loss of cusps and the development of a distinctive enamel ridge containing a single concave pool of dentine. At the same time, the craniofacial and masticatory muscles also undergo significant changes in form (O'Higgins and Jones, 1998, Fitton et al., 2015). However both juveniles and adults have been observed in the wild to feed on the highly stress resistant endocarp of *Sacoglottis gabonensis* (McGraw et al., 2011). The results indicate that the unworn cusp of *C. atys* is optimised for both the breakdown of hollow and solid foods by providing a compromising form that is optimised for several different mechanical parameters. In terms of dental wear the mechanical performance to fracture hollow hard items was fairly similar between different wear morphologies suggesting a functional equivalence in dental form across development in *C. atys*. However this was not found with solid hard food breakdown where the extremely worn morphology required a much higher level of force and energy. In this case a greater absolute muscle size in older individuals may play a role by helping compensate for this apparent decrease in dental efficiency.

Chapter 5: Concluding remarks

By combining dental metrics with physical testing, this thesis offers a fascinating insight into the form and function of teeth in relation to hard object feeding. There were several key findings that will now be outlined and discussed below.

In chapter 2, the shape of a single cusp was shown to greatly affect the mechanical performance to breakdown hard food items. The combined results for multiple mechanical performance indicators suggest that different shaped cusps may be optimised for different roles during food breakdown. Therefore variation in cusp form along the dental row may represent a potential tool kit where sharper cusps are utilised to initiate fracture in food items, which are then transferred to blunter cusps to propagate fracture for food access and/or fragmentation. This may partly explain why such a diversity of tooth forms exists among hard object feeders, particularly when considering some are using their teeth for food access such as sooty mangabeys (McGraw et al., 2011) and pitheciine primates (Kinzey and Norconk, 1990, Norconk and Veres, 2011b), whereas others are using their teeth for food consumption such as hyenas (Kruuk, 1972, Van Valkenburgh, 2007).

However the results in chapter 3 demonstrate that the shapes of teeth within a species can drastically change throughout ontogeny. In the hard object feeding sooty mangabey, the unworn molar presents a high cusped bilophodont morphology that is reduced to a single dentine pool surrounded by an enamel ridge as a result of dental wear. Despite potential differences in diet, *C. atys* was found to follow a pattern of wear that is characteristic of cercopithecine primates in general (Phillips-Conroy et al., 2000, Benefit, 2000). This strongly suggests that phylogeny may play a prominent role in sculpting the tooth as it wears and that the unworn bilophodont form is an initial dental template shared among all cercopithecines.

The functional implications of dental wear in *C. atys* were then investigated in chapter 4 using physical compression. Interestingly, the effect of dental wear on mechanical performance was greatly influenced by whether the food object was hollow or solid. In terms of hollow hard object breakdown, functional equivalence appeared to occur despite differences in the surface area at initial contact. In contrast, crown morphology had a greater effect on the breakdown of solid hard objects where the ridge model was the least efficient morphology.

The ability of *C. atys* to consume a hard brittle diet in a comparably efficient way, despite significant changes in crown morphology, raises questions as to whether tooth morphology is as related to hard object feeding as previously thought. Possibly the most important factor in relation to hard object feeding is whether the individual can fit the item between the teeth in the first place i.e. gape. Also when loaded it is vital that the tooth is able to resist the loads applied to it without failing. This need to reduce tooth fracture during hard object feeding may explain some findings in this study and would be an interesting avenue to explore further.

5.1. Implications and directions for future research

The methodology used throughout this thesis to measure dental functional performance offers a firm foundation in which further research can build on. The use of CAD design and 3D printing to create a hypothetical food item opens many avenues for further study. For instance, variables such as size, shape, and shell thickness can be manipulated virtually and 3D printed to examine the effect on food breakdown. Furthermore, CT scanning could be used to recreate the exact structure of naturally occurring food items such as the *Sacoglottis gabonensis* endocarp.

As the geometry of the occlusal surface of teeth is highly complex, the dental models used in this study to simulate food breakdown were stylised in order to grasp a basic understanding between tooth form and function. The natural progression would therefore be to CT scan and manufacture the real teeth of *C. atys* and compare the mechanical performance of molars from different developmental categories. Extending on this, future experiments may include both upper and lower dental rows in contact with the food item during food breakdown.

References

- ABLER, W. L. 1992. The Serrated Teeth of Tyrannosaurid Dinosaurs, and Biting Structures in Other Animals. *Paleobiology*, 18, 161-183.
- ABRÀMOFF, M. D., MAGALHÃES, P. J. & RAM, S. J. 2004. Image processing with ImageJ. *Biophotonics international*, 11, 36-42.
- ADDY, M. 2002. Dentine hypersensitivity: New perspectives on an old problem. *International Dental Journal*, 52, 367-375.
- AGRAWAL, K. R., LUCAS, P. W., PRINZ, J. F. & BRUCE, I. C. 1997. Mechanical properties of foods responsible for resisting food breakdown in the human mouth. *Archives of Oral Biology*, 42, 1-9.
- ANDERSON, P. S. L. 2009. The effects of trapping and blade angle of notched dentitions on fracture of biological tissues. *Journal of Experimental Biology*, 212, 3627-3632.
- ANDERSON, P. S. L. & LABARBERA, M. 2008. Functional consequences of tooth design: effects of blade shape on energetics of cutting. *Journal of Experimental Biology*, 211, 3619-3626.
- ANTHONY, M. R. & KAY, R. F. 1993. Tooth form and diet in ateline and alouattine primates: reflections on the comparative method. *American Journal of Science*, 293, 356.
- ATKINS, A. & MAI, Y. 1979. On the guillotining of materials. *Journal of Materials Science*, 14, 2747-2754.
- ATKINS, A. G. & MAI, Y. W. 1985. *Elastic and plastic fracture: metals, polymers, ceramics, composites, biological materials*, Ellis Horwood.
- BENEFIT, B. R. 2000. *Old World monkey origins and diversification: an evolutionary study of diet and dentition*, Cambridge University Press.
- BENFER, R. A. & EDWARDS, D. S. 1991. The principal axis method for measuring rate and amount of dental attrition. In: KELLEY, M. A. & LARSEN, C. S. (eds.) *Advances in Dental Anthropology*. New York: Wiley-Liss.
- BERTHAUME, M., GROSSE, I. R., PATEL, N. D., STRAIT, D. S., WOOD, S. & RICHMOND, B. G. 2010. The Effect of Early Hominin Occlusal Morphology on the Fracturing of Hard Food Items. *The Anatomical Record: Advances in Integrative Anatomy and Evolutionary Biology*, 293, 594-606.
- BERTHAUME, M. A. 2014. Tooth cusp sharpness as a dietary correlate in great apes. *American Journal of Physical Anthropology*, 153, 226-235.
- BERTHAUME, M. A. 2016. Food mechanical properties and dietary ecology. *American Journal of Physical Anthropology*, 159, 79-104.
- BERTHAUME, M. A., DUMONT, E. R., GODFREY, L. R. & GROSSE, I. R. 2013. How does tooth cusp radius of curvature affect brittle food item processing? *Journal of The Royal Society Interface*, 10.
- BOESCH, C. & HEDWIGE, B. 1982. Optimisation of Nut-Cracking with Natural Hammers by Wild Chimpanzees. *Behaviour*, 83, 265-286.
- BOYER, D. M. 2008. Relief index of second mandibular molars is a correlate of diet among prosimian primates and other euarchontan mammals. *Journal of Human Evolution*, 55, 1118-1137.
- BUNN, J. M., BOYER, D. M., LIPMAN, Y., ST. CLAIR, E. M., JERNVALL, J. & DAUBECHIES, I. 2011. Comparing Dirichlet normal surface energy of tooth crowns, a new technique of molar shape quantification for dietary inference, with previous methods in isolation and in combination. *American Journal of Physical Anthropology*, 145, 247-261.

- BUNN, J. M. & UNGAR, P. S. 2009. Dental topography and diets of four old world monkey species. *American Journal of Primatology*, 71, 466-477.
- BUTLER, P. M. 1952. The milk-molars of Perissodactyla, with remarks on molar occlusion. *Proceedings of the Zoological Society of London*, 121, 777-817.
- CALKINS, D. G. 1978. Feeding behavior and major prey species of the sea otter, *Enhydra lutris*, in Montague Strait, Prince William Sound, Alaska. *Fishery Bulletin*, 76, 125-131.
- CHAI, H., LEE, J. J. W. & LAWN, B. R. 2011. On the chipping and splitting of teeth. *Journal of the Mechanical Behavior of Biomedical Materials*, 4, 315-321.
- CHOONG, M. F., LUCAS, P. W., ONG, J. S. Y., PEREIRA, B., TAN, H. T. W. & TURNER, I. M. 1992. Leaf fracture toughness and sclerophylly: their correlations and ecological implications. *New Phytologist*, 121, 597-610.
- CLEMENT, A. F. & HILLSON, S. W. 2013. 'Do larger molars and robust jaws in early hominins represent dietary adaptation?' A New Study in Tooth Wear. 2013, 16.
- CONKLIN-BRITTAIN, N. L., KNOTT, C. D. & WRANGHAM, R. W. 2001. The feeding ecology of apes. *The apes: challenges for the 21st century*. Brookfield Chicago Zoological Society.
- CONSTANTINO, P. J., LEE, J. J.-W., CHAI, H., ZIPFEL, B., ZISCOVICI, C., LAWN, B. R. & LUCAS, P. W. 2010. Tooth chipping can reveal the diet and bite forces of fossil hominins. *Biology Letters*.
- CONSTANTINO, P. J., LEE, J. J. W., MORRIS, D., LUCAS, P. W., HARTSTONE-ROSE, A., LEE, W.-K., DOMINY, N. J., CUNNINGHAM, A., WAGNER, M. & LAWN, B. R. 2011. Adaptation to hard-object feeding in sea otters and hominins. *Journal of Human Evolution*, 61, 89-96.
- CORLETT, R. & LUCAS, P. 1990. Alternative seed-handling strategies in primates: seed-spitting by long-tailed macaques (*Macaca fascicularis*). *Oecologia*, 82, 166-171.
- CROFTS, S. 2015. Finite element modeling of occlusal variation in durophagous tooth systems. *Journal of Experimental Biology*.
- CROFTS, S. B. & SUMMERS, A. P. 2014. How to best smash a snail: the effect of tooth shape on crushing load. *Journal of The Royal Society Interface*, 11.
- CROMPTON, A. W. & HIIEMAE, K. 1970. Molar occlusion and mandibular movements during occlusion in the American opossum, *Didelphis marsupialis* L. *Zoological Journal of the Linnean Society*, 49, 21-47.
- CUOZZO, F. P., HEAD, B. R., SAUTHER, M. L., UNGAR, P. S. & O'MARA, M. T. 2014. Sources of tooth wear variation early in life among known-aged wild ring-tailed lemurs (*Lemur catta*) at the Bezà Mahafaly Special Reserve, Madagascar. *American Journal of Primatology*, 76, 1037-1048.
- CUOZZO, F. P. & SAUTHER, M. L. 2006. Severe wear and tooth loss in wild ring-tailed lemurs (*Lemur catta*): A function of feeding ecology, dental structure, and individual life history. *Journal of Human Evolution*, 51, 490-505.
- CUOZZO, F. P., SAUTHER, M. L., GOULD, L., SUSSMAN, R. W., VILLERS, L. M. & LENT, C. 2010. Variation in dental wear and tooth loss among known-aged, older ring-tailed lemurs (*Lemur catta*): a comparison between wild and captive individuals. *American Journal of Primatology*, 72, 1026-1037.
- DAEGLING, D. J., MCGRAW, W. S., UNGAR, P. S., PAMPUSH, J. D., VICK, A. E. & BITTY, E. A. 2011. Hard-Object Feeding in Sooty Mangabeys (*Cercocebus atys*) and Interpretation of Early Hominin Feeding Ecology. *PLoS ONE*, 6, e23095.
- DARVELL, B. W., LEE, P. K. D., YUEN, T. D. B. & LUCAS, P. W. 1996. A portable fracture toughness tester for biological materials. *Measurement Science and Technology*, 7, 954.

- DECHOW, P. C. & CARLSON, D. S. 1990. Occlusal force and craniofacial biomechanics during growth in rhesus monkeys. *American Journal of Physical Anthropology*, 83, 219-237.
- DEMES, B. & CREEL, N. 1988. Bite force, diet, and cranial morphology of fossil hominids. *Journal of Human Evolution*, 17, 657-670.
- DENNIS, J. C., UNGAR, P. S., TEAFORD, M. F. & GLANDER, K. E. 2004. Dental topography and molar wear in *Alouatta palliata* from Costa Rica. *American Journal of Physical Anthropology*, 125, 152-161.
- DOMINY, N., VOGEL, E., YEAKEL, J., CONSTANTINO, P. & LUCAS, P. 2008. Mechanical Properties of Plant Underground Storage Organs and Implications for Dietary Models of Early Hominins. *Evolutionary Biology*, 35, 159-175.
- DOUNIAS, E. 2008. *Sacoglottis gabonensis* (Baill.) Urb. [Online]. Wageningen, Netherlands: PROTA (Plant Resources of Tropical Africa). [Accessed 26/05 2015].
- DUMONT, E. R. 1995. Enamel Thickness and Dietary Adaptation among Extant Primates and Chiropterans. *Journal of Mammalogy*, 76, 1127-1136.
- DUMONT, E. R. & HERREL, A. 2003. The effects of gape angle and bite point on bite force in bats. *Journal of Experimental Biology*, 206, 2117-2123.
- EDLUND, J. & LAMM, C. J. 1980. Masticatory efficiency. *Journal of Oral Rehabilitation*, 7, 123-130.
- ELGART-BERRY, A. 2004. Fracture toughness of mountain gorilla (*Gorilla gorilla beringei*) food plants. *American Journal of Primatology*, 62, 275-285.
- ELGART, A. A. 2010. Dental wear, wear rate, and dental disease in the African apes. *American Journal of Primatology*, 72, 481-491.
- EVANS, A. R. 2005. Connecting morphology, function and tooth wear in microchiropterans. *Biological Journal of the Linnean Society*, 85, 81-96.
- EVANS, A. R. 2013. Shape descriptors as ecometrics in dental ecology. *Hystrix, the Italian Journal of Mammalogy*, 24, 8.
- EVANS, A. R., HUNTER, J., FORTELIUS, M. & SANSON, G. D. 2005. The scaling of tooth sharpness in mammals. *Annales Zoologici Fennici*, 42, 603-613.
- EVANS, A. R. & SANSON, G. D. 1998. The effect of tooth shape on the breakdown of insects. *Journal of Zoology*, 246, 391-400.
- EVANS, A. R. & SANSON, G. D. 2003. The tooth of perfection: functional and spatial constraints on mammalian tooth shape. *Biological Journal of the Linnean Society*, 78, 173-191.
- EVANS, A. R. & SANSON, G. D. 2005a. Biomechanical properties of insects in relation to insectivory: cuticle thickness as an indicator of insect 'hardness' and 'intractability'. *Australian Journal of Zoology*, 53, 9-19.
- EVANS, A. R. & SANSON, G. D. 2005b. Correspondence between tooth shape and dietary biomechanical properties in insectivorous microchiropterans. *Evolutionary Ecology Research*, 7, 453-478.
- EVANS, A. R. & SANSON, G. D. 2006. Spatial and functional modeling of carnivore and insectivore molariform teeth. *Journal of Morphology*, 267, 649-662.
- EVANS, A. R., WILSON, G. P., FORTELIUS, M. & JERNVALL, J. 2007. High-level similarity of dentitions in carnivorans and rodents. *Nature*, 445, 78-81.
- FIGUEIRIDO, B., TSENG, Z. J. & MARTÍN-SERRA, A. 2013. Skull shape evolution in durophagous carnivorans. *Evolution*, 67, 1975-1993.
- FITTON, L. 2008. *The Form-Function Complex of the Primate Masticatory Apparatus*. Ph.D, University of Liverpool.
- FITTON, L., DICKINSON, E., SWAN, K. & COBB, S. 2015. Functional integration during development within the masticatory apparatus. *The FASEB Journal*, 29.
- FLEAGLE, J. G. 1988. *Primate adaptation & evolution*, San Diego, Academic Press.

- FLEAGLE, J. G. & MCGRAW, W. S. 1999. Skeletal and dental morphology supports diphyletic origin of baboons and mandrills. *Proceedings of the National Academy of Sciences*, 96, 1157-1161.
- FLEAGLE, J. G. & MCGRAW, W. S. 2002. Skeletal and dental morphology of African papionins: unmasking a cryptic clade. *Journal of Human Evolution*, 42, 267-292.
- FORTELIUS, M. 1985. Ungulate cheek teeth: developmental, functional, and evolutionary interrelations. *Acta Zoologica Fennica*, 180, 1-76.
- FRAZZETTA, T. 1988. The mechanics of cutting and the form of shark teeth (Chondrichthyes, Elasmobranchii). *Zoomorphology*, 108, 93-107.
- FREEMAN, P. W. 1979. Specialized Insectivory: Beetle-Eating and Moth-Eating Molossid Bats. *Journal of Mammalogy*, 60, 467-479.
- FREEMAN, P. W. & LEMEN, C. 2006. Puncturing ability of idealized canine teeth: edged and non-edged shanks. *Journal of Zoology*, 269, 51-56.
- FREEMAN, P. W. & WEINS, W. N. 1997. Puncturing ability of bat canine teeth: the tip. *Mammalogy Papers: University of Nebraska State Museum*.
- FRITZ, J., HUMMEL, J., KIENZLE, E., ARNOLD, C., NUNN, C. & CLAUSS, M. 2009. Comparative chewing efficiency in mammalian herbivores. *Oikos*, 118, 1623-1632.
- FRUNZA, M. C. & SUCIU, C. 2013. Cusp radius measurement through digital image analysis. *Acta Odontologica Scandinavica*, 71, 236-240.
- FRUTEAU, C., RANGE, F. & NOË, R. 2010. Infanticide risk and infant defence in multi-male free-ranging sooty mangabeys, *Cercocebus atys*. *Behavioural Processes*, 83, 113-118.
- GALBANY, J., ALTMANN, J., PÉREZ-PÉREZ, A. & ALBERTS, S. C. 2011a. Age and individual foraging behavior predict tooth wear in Amboseli baboons. *American Journal of Physical Anthropology*, 144, 51-59.
- GALBANY, J., DOTRAS, L., ALBERTS, S. C. & PÉREZ-PÉREZ, A. 2011b. Tooth Size Variation Related to Age in Amboseli Baboons. *Folia Primatologica; International Journal of Primatology*, 81, 348-359.
- GALBANY, J., ROMERO, A., MAYO-ALESÓN, M., ITSOMA, F., GAMARRA, B., PÉREZ-PÉREZ, A., WILLAUME, E., KAPPELER, P. M. & CHARPENTIER, M. J. E. 2014. Age-Related Tooth Wear Differs between Forest and Savanna Primates. *PLoS ONE*, 9, e94938.
- GIPPS, J. M. & SANSON, G. D. 1984. Mastication and digestion in *Pseudocheirus*. In: SMITH, A. & HUME, I. D. (eds.) *Possums and gliders*. Sydney: Surrey Beatty.
- GODFREY, L. R., WINCHESTER, J. M., KING, S. J., BOYER, D. M. & JERNVALL, J. 2012. Dental topography indicates ecological contraction of lemur communities. *American Journal of Physical Anthropology*, 148, 215-227.
- GOULD, S. J. 1975. On the Scaling of Tooth Size in Mammals. *American Zoologist*, 15, 353-362.
- GROVES, C. 1978. Phylogenetic and population systematics of the Mangabeys (primates: Cercopithecoidea). *Primates*, 19, 1-34.
- GUY, F., GOUVARD, F., BOISTEL, R., EURIAT, A. & LAZZARI, V. 2013. Prospective in (Primate) Dental Analysis through Tooth 3D Topographical Quantification. *PLoS ONE*, 8, e66142.
- HAMMER, Ø., HARPER, D. A. T. & RYAN, P. D. 2001. PAST: Paleontological statistics software package for education and data analysis. *Palaeontologia Electronica*, 4, 9.
- HAPPEL, R. 1988. Seed-eating by West African cercopithecines, with reference to the possible evolution of bilophodont molars. *American Journal of Physical Anthropology*, 75, 303-327.

- HARTSTONE-ROSE, A. & STYNDER, D. D. 2013. Hypercarnivory, durophagy or generalised carnivory in the Mio-Pliocene hyaenids of South Africa? *South African Journal of Science*, 109, 1-10.
- HARTSTONE-ROSE, A. & WAHL, S. 2008. Using radii-of-curvature for the reconstruction of extinct South African carnivoran masticatory behavior. *Comptes Rendus Palevol*, 7, 629-643.
- HERREL, A. & HOLANOVA, V. 2008. Cranial morphology and bite force in Chamaeleolis lizards – Adaptations to molluscivory? *Zoology*, 111, 467-475.
- HIEMAE, K. M. 2000. Feeding in mammals. In: SCHWENK, K. (ed.) *Feeding: Form, function, and evolution in tetrapod vertebrates*.
- HILL, D. A. & LUCAS, P. W. 1996. Toughness and fiber content of major leaf foods of Japanese macaques (*Macaca fuscata yakui*) in Yakushima. *American Journal of Primatology*, 38, 221-231.
- HILLSON, S. 2005. *Teeth*, USA, New York, Cambridge University Press.
- HYLANDER, W. L. 1975. Incisor size and diet in anthropoids with special reference to Cercopithecidae. *Science (New York, N.Y.)*, 189, 1095-1098.
- HYLANDER, W. L. 1979. The functional significance of primate mandibular form. *Journal of Morphology*, 160, 223-239.
- IWANO, T. 1991. An ecological and behavioral study of the aye-aye (*Daubentonia madagascariensis*). *African Study Monographs*, 12.
- KARASOV, W. H., PETROSSIAN, E., ROSENBERG, L. & DIAMOND, J. M. 1986. How do food passage rate and assimilation differ between herbivorous lizards and nonruminant mammals? *Journal of Comparative Physiology B*, 156, 599-609.
- KAY, R. F. 1973. *Mastication, molar tooth structure and diet in primates*. Ph.D., Yale University.
- KAY, R. F. 1975. The functional adaptations of primate molar teeth. *American Journal of Physical Anthropology*, 43, 195-215.
- KAY, R. F. 1978. Molar structure and diet in extant Cercopithecidae. In: BUTLER, P. M. & JOYSEY, K. A. (eds.) *Development, function and evolution of teeth*. London: Academic Press.
- KAY, R. F. 1981. The nut-crackers – a new theory of the adaptations of the Ramapithecinae. *American Journal of Physical Anthropology*, 55, 141-151.
- KAY, R. F. 1984. On the use of anatomical features to infer foraging behavior in extinct primates. In: RODMAN, P. S. & CANT, J. G. H. (eds.) *Adaptations for Foraging in Nonhuman Primates: Contributions to an Organismal Biology of Prosimians, Monkeys, and Apes*. New York: Columbia University Press.
- KAY, R. F. & COVERT, H. H. 1984. Anatomy and behavior of extinct primates. In: CHIVERS, D. J., WOOD, B. A. & BILSBOROUGH, A. (eds.) *Food Acquisition and Processing in Primates*. New York: Plenum Press.
- KAY, R. F. & HIEMAE, K. M. 1974. Jaw movement and tooth use in recent and fossil primates. *American Journal of Physical Anthropology*, 40, 227-256.
- KAY, R. F. & HYLANDER, W. L. 1978. The dental structure of mammalian folivores with special reference to Primates and Phalangerioidea (Marsupialia). In: MONTGOMERY, G. G. (ed.) *The biology of arboreal folivores*. Washington, D.C.: Smithsonian Institution Press.
- KENYON, K. W. 1969. The sea otter in the eastern Pacific Ocean. *North American Fauna*, 68, 1-352.
- KERR, A. 2010. *Introductory Biomechanics* Elsevier Limited.
- KING, S. J., ARRIGO-NELSON, S. J., POCHRON, S. T., SEMPREBON, G. M., GODFREY, L. R., WRIGHT, P. C. & JERNVALL, J. 2005. Dental senescence in a long-lived primate links infant survival to rainfall. *Proceedings of the*

- National Academy of Sciences of the United States of America*, 102, 16579-16583.
- KINZEY, W. G. 1992. Dietary and dental adaptations in the Pitheciinae. *American Journal of Physical Anthropology*, 88, 499-514.
- KINZEY, W. G. & NORCONK, M. A. 1990. Hardness as a basis of fruit choice in two sympatric primates. *American Journal of Physical Anthropology*, 81, 5-15.
- KRUUK, H. 1972. *The Spotted Hyena*, Chicago, University of Chicago.
- LAMBERT, J. E., CHAPMAN, C. A., WRANGHAM, R. W. & CONKLIN-BRITTAIN, N. L. 2004. Hardness of cercopithecine foods: Implications for the critical function of enamel thickness in exploiting fallback foods. *American Journal of Physical Anthropology*, 125, 363-368.
- LANYON, J. M. & SANSON, G. D. 1986. Koala (*Phascolarctos cinereus*) dentition and nutrition. II. Implications of tooth wear in nutrition. *Journal of Zoology*, 209, 169-181.
- LAWN, B. R., BUSH, M. B., BARANI, A., CONSTANTINO, P. J. & WROE, S. 2013. Inferring biological evolution from fracture patterns in teeth. *Journal of Theoretical Biology*, 338, 59-65.
- LAWN, B. R. & LEE, J. J. W. 2009. Analysis of fracture and deformation modes in teeth subjected to occlusal loading. *Acta Biomaterialia*, 5, 2213-2221.
- LAWN, B. R. & MARSHALL, D. B. 1979. Hardness, Toughness, and Brittleness: An Indentation Analysis. *Journal of the American Ceramic Society*, 62, 347-350.
- LEDOGAR, J. A., WINCHESTER, J. M., ST. CLAIR, E. M. & BOYER, D. M. 2013. Diet and dental topography in pitheciine seed predators. *American Journal of Physical Anthropology*, n/a-n/a.
- LEE, J. J.-W., KWON, J.-Y., CHAI, H., LUCAS, P. W., THOMPSON, V. P. & LAWN, B. R. 2009. Fracture Modes in Human Teeth. *Journal of Dental Research*, 88, 224-228.
- LIEBERMAN, D. 2011. *The Evolution of the Human Head*, Harvard University Press.
- LOGAN, M. & SANSON, G. D. 2002. The effect of tooth wear on the feeding behaviour of free-ranging koalas (*Phascolarctos cinereus*, Goldfuss). *Journal of Zoology*, 256, 63-69.
- LOVE, R. M. & JENKINSON, H. F. 2002. Invasion of Dentinal Tubules by Oral Bacteria. *Critical Reviews in Oral Biology & Medicine*, 13, 171-183.
- LUCAS, P. 1979. The dental-dietary adaptations of mammals. *Neues Jahrbuch für Geologie und Paläontologie, Monatshefte*, 8, 486-512.
- LUCAS, P., CONSTANTINO, P., WOOD, B. & LAWN, B. 2008. Dental enamel as a dietary indicator in mammals. *BioEssays*, 30, 374-385.
- LUCAS, P., CORLETT, R. & LUKE, D. 1986a. Postcanine tooth size and diet in anthropoid primates. *Zeitschrift für Morphologie und Anthropologie*, 253-276.
- LUCAS, P., LUKE, D., VOON, F., CHEW, C. & OW, R. 1986b. Food breakdown patterns produced by human subjects possessing artificial and natural teeth. *Journal of Oral Rehabilitation*, 13, 205-214.
- LUCAS, P. W. 1982. Basic principles of tooth design. In: KURTÉN, B. (ed.) *Teeth: Form, Function, and Evolution*. New York: Columbia University Press.
- LUCAS, P. W. 2004. *Dental Functional Morphology: How Teeth Work*, New York, Cambridge University Press.
- LUCAS, P. W., BETA, T., DARVELL, B. W., DOMINY, N. J., ESSACKJEE, H. C., LEE, P. K. D., OSORIO, D., RAMSDEN, L., YAMASHITA, N. & YUEN, T. D. B. 2001. Field Kit to Characterize Physical, Chemical and Spatial Aspects of Potential Primate Foods. *Folia Primatologica*, 72, 11-25.
- LUCAS, P. W., CONSTANTINO, P. J., CHALK, J., ZISCOVICI, C., WRIGHT, B. W., FRAGASZY, D. M., HILL, D. A., LEE, J. J. W., CHAI, H., DARVELL, B. W.,

- LEE, P. K. D. & YUEN, T. D. B. 2009. Indentation as a technique to assess the mechanical properties of fallback foods. *American Journal of Physical Anthropology*, 140, 643-652.
- LUCAS, P. W., COPEL, L., CONSTANTINO, P. J., VOGEL, E. R., CHALK, J., TALEBI, M., LANDIS, M. & WAGNER, M. 2012. Measuring the toughness of primate foods and its ecological value. *International Journal of Primatology*, 33, 598-610.
- LUCAS, P. W. & LUKE, D. A. 1983. Methods for analysing the breakdown of food in human mastication. *Archives of Oral Biology*, 28, 813-819.
- LUCAS, P. W. & LUKE, D. A. 1984. Chewing It over: Basic Principles of Food Breakdown. In: CHIVERS, D., WOOD, B. & BILSBOROUGH, A. (eds.) *Food Acquisition and Processing in Primates*. Springer US.
- LUCAS, P. W. & OMAR, R. 2012. New Perspectives on Tooth Wear. *International Journal of Dentistry*, 2012.
- LUCAS, P. W., OMAR, R., AL-FADHALAH, K., ALMUSALLAM, A. S., HENRY, A. G., MICHAEL, S., THAI, L. A., WATZKE, J., STRAIT, D. S. & ATKINS, A. G. 2013. Mechanisms and causes of wear in tooth enamel: implications for hominin diets. *Journal of The Royal Society Interface*, 10.
- LUCAS, P. W., PETERS, C. R. & ARRANDALE, S. R. 1994. Seed-breaking forces exerted by orang-utans with their teeth in captivity and a new technique for estimating forces produced in the Wild. *American Journal of Physical Anthropology*, 94, 365-378.
- LUCAS, P. W., PRINZ, J. F., AGRAWAL, K. R. & BRUCE, I. C. 2002. Food physics and oral physiology. *Food Quality and Preference*, 13, 203-213.
- LUCAS, P. W. & TEAFORD, M. F. 1994. Functional morphology of colobine teeth. *Colobine monkeys: Their ecology, behaviour and evolution*, 173-203.
- LUCAS, P. W., TURNER, I. M., DOMINY, N. J. & YAMASHITA, N. 2000. Mechanical Defences to Herbivory. *Annals of Botany*, 86, 913-920.
- LUKE, D. A. & LUCAS, P. W. 1983. The significance of cusps. *Journal of Oral Rehabilitation*, 10, 197-206.
- M'KIRERA, F. & UNGAR, P. S. 2003. Occlusal relief changes with molar wear in *Pan troglodytes troglodytes* and *Gorilla gorilla gorilla*. *American Journal of Primatology*, 60, 31-41.
- MATON, B., RENDELL, J., GENTIL, M. & GAY, T. 1992. Masticatory muscle fatigue: Endurance times and spectral changes in the electromyogram during the production of sustained bite forces. *Archives of Oral Biology*, 37, 521-529.
- MAYHALL, J. T. & KAGEYAMA, I. 1997. A new, three-dimensional method for determining tooth wear. *American Journal of Physical Anthropology*, 103, 463-469.
- MCGRAW, W. S. 1998. Comparative locomotion and habitat use of six monkeys in the Tai Forest, Ivory Coast. *American Journal of Physical Anthropology*, 105, 493-510.
- MCGRAW, W. S., PAMPUSH, J. D. & DA EGLING, D. J. 2012. Brief communication: Enamel thickness and durophagy in mangabeys revisited. *American Journal of Physical Anthropology*, 147, 326-333.
- MCGRAW, W. S., VICK, A. E. & DA EGLING, D. J. 2011. Sex and age differences in the diet and ingestive behaviors of sooty mangabeys (*Cercocebus atys*) in the Tai forest, Ivory coast. *American Journal of Physical Anthropology*, 144, 140-153.
- MCGRAW, W. S., VICK, A. E. & DA EGLING, D. J. 2014. Dietary variation and food hardness in sooty mangabeys (*Cercocebus atys*): Implications for fallback foods

- and dental adaptation. *American Journal of Physical Anthropology*, 154, 413-423.
- MCGRAW, W. S. & ZUBERBÜHLER, K. 2007. The monkeys of the Taï Forest: an introduction. In: MCGRAW, W. S., ZUBERBÜHLER, K. & NOË, R. (eds.) *Monkeys of the Taï Forest: An African Primate Community*. Cambridge: Cambridge University Press.
- MCGRAW, W. S., ZUBERBÜHLER, K. & NOË, R. (eds.) 2007. *The monkeys of the Taï Forest, Ivory Coast: an African primate community*, Cambridge: Cambridge University Press.
- MELANI, R. F. H., TURBINO, M. L., RAMOS, D. L. D. P., BOMBANA, A. C. & DIAS, P. E. M. 2012. Dental fracture and chocolate candies: Case report. *Journal of Forensic and Legal Medicine*.
- MELDRUM, D. J. & KAY, R. F. 1997. Nuciruptor rubricae, a new pitheciin seed predator from the Miocene of Colombia. *American Journal of Physical Anthropology*, 102, 407-427.
- MOLNAR, S. 1971. Human tooth wear, tooth function and cultural variability. *American Journal of Physical Anthropology*, 34, 175-189.
- MORSE, P. E., DA EGLING, D. J., MCGRAW, W. S. & PAMPUSH, J. D. 2013. Dental wear among cercopithecoid monkeys of the Taï forest, Côte d'Ivoire. *American Journal of Physical Anthropology*, 150, 655-665.
- MURIE, O. J. 1940. Notes on the Sea Otter. *Journal of Mammalogy*, 21, 119-131.
- MYERS, P., ESPINOSA, R., PARR, C. S., JONES, T., HAMMOND, G. S. & DEWEY, T. A. 2016. *The Animal Diversity Web* [Online]. Accessed at <http://animaldiversity.org>. 2016].
- NORCONK, M. A. & VERES, M. 2011a. Physical Properties of Fruit and Seeds Ingested by Primate Seed Predators with Emphasis on Sakis and Bearded Sakis. *The Anatomical Record: Advances in Integrative Anatomy and Evolutionary Biology*, 294, 2092-2111.
- NORCONK, M. A. & VERES, M. 2011b. Physical properties of fruit and seeds ingested by primate seed predators with emphasis on sakis and bearded sakis. *Anat Rec (Hoboken)*, 294, 2092-111.
- NORTON, S. F. 1988. Role of the Gastropod Shell and Operculum in Inhibiting Predation by Fishes. *Science*, 241, 92-94.
- O'HIGGINS, P. & COLLARD, M. 2002. Sexual dimorphism and facial growth in papionin monkeys. *Journal of Zoology*, 257, 255-272.
- O'HIGGINS, P. & JONES, N. 1998. Facial growth in *Cercocebus torquatus*: an application of three-dimensional geometric morphometric techniques to the study of morphological variation. *Journal of Anatomy*, 193 (Pt 2), 251-272.
- OLTHOFF, L. W., VAN DER BILT, A., BOSMAN, F. & KLEIZEN, H. H. 1984. Distribution of particle sizes in food comminuted by human mastication. *Archives of Oral Biology*, 29, 899-903.
- OLTHOFF, L. W., VAN DER BILT, A., DE BOER, A. & BOSMAN, F. 1986. Comparison of force-deformation characteristics of artificial and several natural foods for chewing experiments. *Journal of Texture Studies*, 17, 275-289.
- OSBORN, J. & LUMSDEN, A. 1978. An alternative to 'thegosis' and a re-examination of the ways in which mammalian molars work. *Neues Jahrbuch für Geologie und Paläontologie Abhandlungen*, 156, 371-392.
- PAHL, L. 1987. Survival, Age-Determination and Population Age Structure of the Common Ringtail Possum, *Pseudocheirus-Peregrinus*, in a Eucalyptus Woodland and a Leptospermum Thicket in Southern Victoria. *Australian Journal of Zoology*, 35, 625-639.

- PAMPUSH, J. D., DA EGLING, D. J., VICK, A. E., MCGRAW, W. S., COVEY, R. M. & RAPOFF, A. J. 2011. Technical note: Converting durometer data into elastic modulus in biological materials. *American Journal of Physical Anthropology*, 146, 650-653.
- PÉREZ-BARBERÍA, F. J. & GORDON, I. J. 1998. The influence of molar occlusal surface area on the voluntary intake, digestion, chewing behaviour and diet selection of red deer (*Cervus elaphus*). *Journal of Zoology*, 245, 307-316.
- PEYRON, M.-A., MISHPELLANY, A. & WODA, A. 2004. Particle Size Distribution of Food Boluses after Mastication of Six Natural Foods. *Journal of Dental Research*, 83, 578-582.
- PHILLIPS-CONROY, J. E., BERGMAN, T. & JOLLY, C. J. 2000. Quantitative assessment of occlusal wear and age estimation in Ethiopian and Tanzanian baboons. *Old world monkeys*.
- PILBEAM, D. & GOULD, S. J. 1974. Size and scaling in human evolution. *Science*, 186, 892-901.
- RANGE, F. & NOË, R. 2002. Familiarity and dominance relations among female sooty mangabeys in the Tai National Park. *American Journal of Primatology*, 56, 137-153.
- RICHARDS, L. C. 1984. Principal axis analysis of dental attrition data from two Australian Aboriginal populations. *American Journal of Physical Anthropology*, 65, 5-13.
- ROGERS, M. E., ABERNETHY, K., BERMEJO, M., CIPOLLETTA, C., DORAN, D., MCFARLAND, K., NISHIHARA, T., REMIS, M. & TUTIN, C. E. G. 2004. Western gorilla diet: A synthesis from six sites. *American Journal of Primatology*, 64, 173-192.
- ROSENBERGER, A. L. & KINZEY, W. G. 1976. Functional patterns of molar occlusion in platyrrhine primates. *American Journal of Physical Anthropology*, 45, 281-297.
- ROSS, C. F. 2000. Into the Light: The Origin of Anthrozoidea. *Annual Review of Anthropology*, 29, 147-194.
- ROSS, C. F. & IRIARTE-DIAZ, J. 2014. What does feeding system morphology tell us about feeding? *Evolutionary Anthropology: Issues, News, and Reviews*, 23, 105-120.
- ROWE, N. 1996. *The pictorial guide to the living primates*, Pogonias Press.
- ROWELL, T. E. & CHALMERS, N. R. 1970. Reproductive cycles of the mangabey, *Cercocebus albigena*. *Folia Primatologica*, 12, 264-272.
- RUDAS, M., QASIM, T., BUSH, M. B. & LAWN, B. R. 2005. Failure of curved brittle layer systems from radial cracking in concentrated surface loading. *Journal of Materials Research*, 20, 2812-2819.
- SANSON, G. 2006. The biomechanics of browsing and grazing. *American Journal of Botany*, 93, 1531-1545.
- SANTANA, S. E., GROSSE, I. R. & DUMONT, E. R. 2012. Dietary hardness, loading behavior, and the evolution of skull form in bats. *Evolution*, 66, 2587-2598.
- SCOTT, E. C. 1979a. Dental wear scoring technique. *American Journal of Physical Anthropology*, 51, 213-217.
- SCOTT, E. C. 1979b. Principal axis analysis of dental attrition data. *American Journal of Physical Anthropology*, 51, 203-211.
- SELIGSOHN, D. & SZALAY, F. S. 1978. Relationship between natural selection and dental morphology: tooth function and diet in *Lepilemur* and *Hapalemur*. In: BUTLER, P. M. & JOYSEY, K. A. (eds.) *Development, function and evolution of teeth*. New York: Academic Press.

- SHAHDAD, S. A., MCCABE, J. F., BULL, S., RUSBY, S. & WASSELL, R. W. 2007. Hardness measured with traditional Vickers and Martens hardness methods. *Dental Materials*, 23, 1079-1085.
- SINGLETON, M. 2002. Patterns of cranial shape variation in the Papionini (Primates: Cercopithecinae). *Journal of human evolution*, 42, 547-578.
- SLAGTER, A. P., VAN DER GLAS, H. W., BOSMAN, F. & OLTHOFF, L. W. 1992. Force-deformation properties of artificial and natural foods for testing chewing efficiency. *The Journal of Prosthetic Dentistry*, 68, 790-799.
- SMITH, B. H. 1984. Patterns of molar wear in hunter-gatherers and agriculturalists. *American Journal of Physical Anthropology*, 63, 39-56.
- SMITH, B. H. 1994. Sequence of emergence of the permanent teeth in *Macaca*, *Pan*, *Homo*, and *Australopithecus*: Its evolutionary significance. *American Journal of Human Biology*, 6, 61-76.
- SMITH, P. 1972. Diet and attrition in the natufians. *American Journal of Physical Anthropology*, 37, 233-238.
- SPEARS, I. R. & CROMPTON, R. H. 1996a. The mechanical significance of the occlusal geometry of great ape molars in food breakdown. *Journal of Human Evolution*, 31, 517-535.
- SPEARS, I. R. & CROMPTON, R. H. 1996b. The mechanical significance of the occlusal geometry of great ape molars in food breakdown. *Journal of Human Evolution*, 31, 517-536.
- SPENCER, M. A. 2003. Tooth-root form and function in platyrrhine seed-eaters. *American Journal of Physical Anthropology*, 122, 325-335.
- STRAIT, S. G. 1993. Molar Morphology and Food Texture among Small-Bodied Insectivorous Mammals. *Journal of Mammalogy*, 74, 391-402.
- STRAIT, S. G. 1997. Tooth use and the physical properties of food. *Evolutionary Anthropology: Issues, News, and Reviews*, 5, 199-211.
- SUI, Z., AGRAWAL, K. R., CORKE, H. & LUCAS, P. W. 2006. Biting efficiency in relation to incisal angulation. *Archives of Oral Biology*, 51, 491-497.
- SWINDLER, D. R. 2002. *Primate Dentition: An Introduction to the Teeth of Non-human Primates*, Cambridge University Press.
- TAYLOR, A. B., VOGEL, E. R. & DOMINY, N. J. 2008. Food material properties and mandibular load resistance abilities in large-bodied hominoids. *Journal of Human Evolution*, 55, 604-616.
- TEAFORD, M. F., UNGAR, P. & GRINE, F. E. 2013. Dental microwear and paleoecology. In: SPONHEIMER, M., LEE-THORP, J. A., REED, K. E. & UNGAR, P. (eds.) *Early Hominin Paleoecology*. University Press of Colorado.
- ULHAAS, L., KULLMER, O., SCHRENK, F. & HENKE, W. 2004. A new 3-d approach to determine functional morphology of cercopithecoid molars. *Annals of Anatomy - Anatomischer Anzeiger*, 186, 487-493.
- UNGAR, P. 1998. Dental allometry, morphology, and wear as evidence for diet in fossil primates. *Evolutionary Anthropology: Issues, News, and Reviews*, 6, 205-217.
- UNGAR, P. 2008. Materials science: Strong teeth, strong seeds. *Nature*, 452, 703-705.
- UNGAR, P. & WILLIAMSON, M. 2000. Exploring the effects of tooth wear on functional morphology: a preliminary study using dental topographic analysis. *Palaeontologia electronica*, 3, 17.
- UNGAR, P. S. 2010. *Mammal Teeth: Origin, Evolution, and Diversity*, Johns Hopkins University Press.
- UNGAR, P. S. 2015. Mammalian dental function and wear: A review. *Biosurface and Biotribology*, 1, 25-41.

- UNGAR, P. S. & M'KIRERA, F. 2003. A solution to the worn tooth conundrum in primate functional anatomy. *Proceedings of the National Academy of Sciences*, 100, 3874-3877.
- VAN DER BILT, A., OLTHOFF, L. W., VAN DER GLAS, H. W., VAN DER WEELLEN, K. & BOSMAN, F. 1987. A mathematical description of the comminution of food during mastication in man. *Archives of Oral Biology*, 32, 579-586.
- VAN VALKENBURGH, B. 1996. Feeding Behavior in Free-Ranging, Large African Carnivores. *Journal of Mammalogy*, 77, 240-254.
- VAN VALKENBURGH, B. 2007. Déjà vu: the evolution of feeding morphologies in the Carnivora. *Integrative and Comparative Biology*, 47, 147-163.
- VANDEVERE, J. E. Feeding Behaviour of the Southern Sea Otter. Proceedings of the Sixth Annual Conference on Biological Sonar and Diving Mammals, 1969 Stanford Research Institute, Biological Sonar Laboratory, Menlo Park, California.
- VENKATARAMAN, V. V., GLOWACKA, H., FRITZ, J., CLAUSS, M., SEYOUM, C., NGUYEN, N. & FASHING, P. J. 2014. Effects of dietary fracture toughness and dental wear on chewing efficiency in geladas (*Theropithecus gelada*). *American Journal of Physical Anthropology*, 155, 17-32.
- VINCENT, J. 1990. *Structural Biomaterials*, Princeton, Princeton University Press.
- VINCENT, J. F. V., JERONIMIDIS, G., KHAN, A. A. & LUYTEN, H. 1991. The wedge fracture test a new method for measurement of food texture *Journal of Texture Studies*, 22, 45-57.
- VOGEL, E. R., VAN WOERDEN, J. T., LUCAS, P. W., UTAMI ATMOKO, S. S., VAN SCHAİK, C. P. & DOMINY, N. J. 2008. Functional ecology and evolution of hominoid molar enamel thickness: *Pan troglodytes schweinfurthii* and *Pongo pygmaeus wurmbii*. *Journal of Human Evolution*, 55, 60-74.
- VOGEL, E. R., ZULFA, A., HARDUS, M., WICH, S. A., DOMINY, N. J. & TAYLOR, A. B. 2014. Food mechanical properties, feeding ecology, and the mandibular morphology of wild orangutans. *Journal of Human Evolution*, 75, 110-124.
- WIECZKOWSKI, J. 2009. Brief communication: Puncture and crushing resistance scores of Tana river mangabey (*Cercocebus galeritus*) diet items. *American Journal of Physical Anthropology*, 140, 572-577.
- WILLIAMS, S. H., WRIGHT, B. W., TRUONG, V. D., DAUBERT, C. R. & VINYARD, C. J. 2005. Mechanical properties of foods used in experimental studies of primate masticatory function. *American Journal of Primatology*, 67, 329-346.
- WINCHESTER, J. M., BOYER, D. M., ST. CLAIR, E. M., GOSSELIN-ILDARI, A. D., COOKE, S. B. & LEDOGAR, J. A. 2014. Dental topography of platyrrhines and prosimians: Convergence and contrasts. *American Journal of Physical Anthropology*, 153, 29-44.
- WRANGHAM, R. W., CONKLIN-BRITTAIN, N. L. & HUNT, K. D. 1998. Dietary response of chimpanzees and cercopithecines to seasonal variation in fruit abundance. I. Antifeedants. *International Journal of Primatology*, 19, 949-970.
- WRIGHT, B. W. 2005. Craniodental biomechanics and dietary toughness in the genus *Cebus*. *Journal of Human Evolution*, 48, 473-492.
- YAMAGIWA, J., MARUHASHI, T., YUMOTO, T. & MWANZA, N. 1996. Dietary and ranging overlap in sympatric gorillas and chimpanzees in Kahuzi-Biega National Park, Zaire. *Great ape societies*. Cambridge University Press, Cambridge, 82-98.

- YAMAGIWA, J., MWANZA, N., YUMOTO, T. & MARUHASHI, T. 1994. Seasonal change in the composition of the diet of eastern lowland gorillas. *Primates*, 35, 1-14.
- YAMASHITA, N. 1996a. *The Relationship Between Tooth Morphology and Mechanical Dietary Properties in Two Malagasy Lemur Families (Lemuridae and Indriidae)*, Northwestern University.
- YAMASHITA, N. 1996b. Seasonally and site specificity of mechanical dietary patterns in two malagasy lemur families (Lemuridae and Indriidae). *International Journal of Primatology*, 17, 355-387.
- YAMASHITA, N. 1998a. Functional dental correlates of food properties in five Malagasy lemur species. *American Journal of Physical Anthropology*, 106, 169-188.
- YAMASHITA, N. 1998b. Molar morphology and variation in two Malagasy lemur families (Lemuridae and Indriidae). *Journal of Human Evolution*, 35, 137-162.
- YAMASHITA, N. 2003. Food procurement and tooth use in two sympatric lemur species. *American Journal of Physical Anthropology*, 121, 125-133.
- YAMASHITA, N., CUOZZO, F. P. & SAUTHER, M. L. 2012. Interpreting food processing through dietary mechanical properties: A Lemur catta case study. *American Journal of Physical Anthropology*, 148, 205-214.
- YAMASHITA, N., VINYARD, C. J. & TAN, C. L. 2009. Food mechanical properties in three sympatric species of Hapalemur in Ranomafana National Park, Madagascar. *American Journal of Physical Anthropology*, 139, 368-381.
- ZUCCOTTI, L. F., WILLIAMSON, M. D., LIMP, W. F. & UNGAR, P. S. 1998. Technical note: Modeling primate occlusal topography using geographic information systems technology. *American Journal of Physical Anthropology*, 107, 137-142.

Appendix A: Chapter 2

Test programs used to control Mecmesin universal testing machine during compression tests.

Test program for hollow domes:

```
>ENTER@'CODE',string for V1
>ZERO value of load and displacement
>RUN@ 50mm/min until load=1.0N
>ZERO value of displacement
>CLEAR DATA

>RUN@5mm/min until load=2400.0N, or position from tared
zero=5.00mm, or break%=70%
```

Test program for solid domes:

```
>ENTER@'CODE',string for V1
>ZERO value of load and displacement
>RUN@ 50mm/min until load=1.0N
>ZERO value of displacement
>CLEAR DATA

>RUN@5mm/min until load=2400.0N, or position from tared
zero=5.00mm, or break%=10%
```

B60: Hollow hard object breakdown

Brittle failure occurred in only three of the ten hollow domes, whilst the majority exhibited large amounts of plastic deformation with no production of pieces. Due to this, tests were terminated based on having reached maximum displacement and resulted in specimens having a single indentation mark (Figure A.1-ii). Domes tended to lodge onto the cusp models and had to be physically removed. The domes that did fail broke into 3 pieces with occasional movement of pieces at fracture.

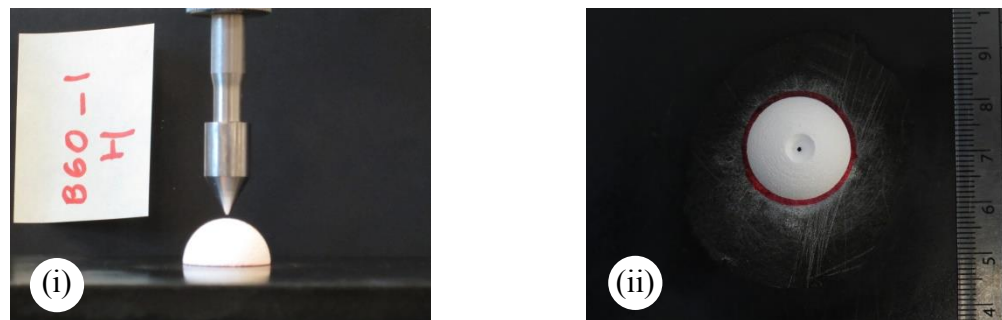


Figure A.1 B60 hollow hard object breakdown images: (i) B60 and hollow dome, (ii) post compression image showing the typical indentation mark left on the hollow dome after each test.

B60: Hollow

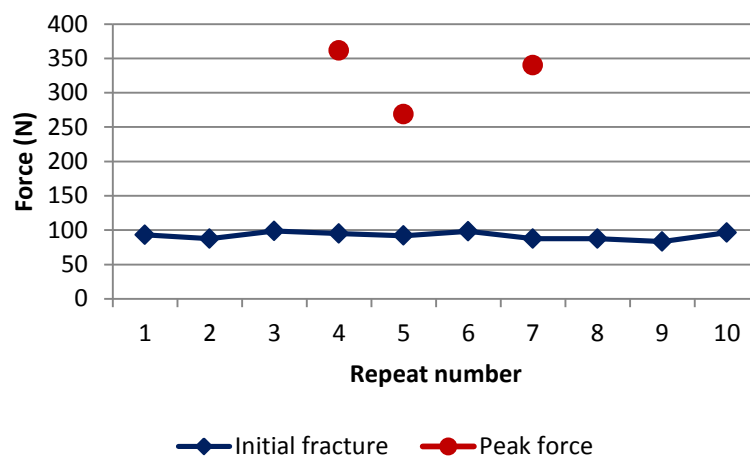


Figure A.2 Consistency of repeats for B60 based on force at initial fracture and peak force to break a hollow dome.

B60: Solid hard object breakdown

Brittle failure occurred in all solid domes and involved movement of pieces at breakage. The majority of domes fragmented into roughly 2 clean half pieces with very little production of fine fragments (Figure A.3-ii).

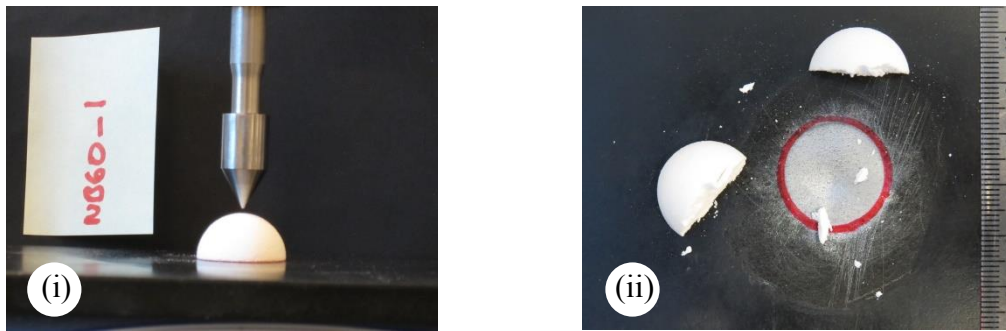


Figure A.3 B60 solid hard object breakdown images: (i) B60 and solid dome, (ii) post compression image. Domes typically split into 2 pieces and energetically moved apart at failure.

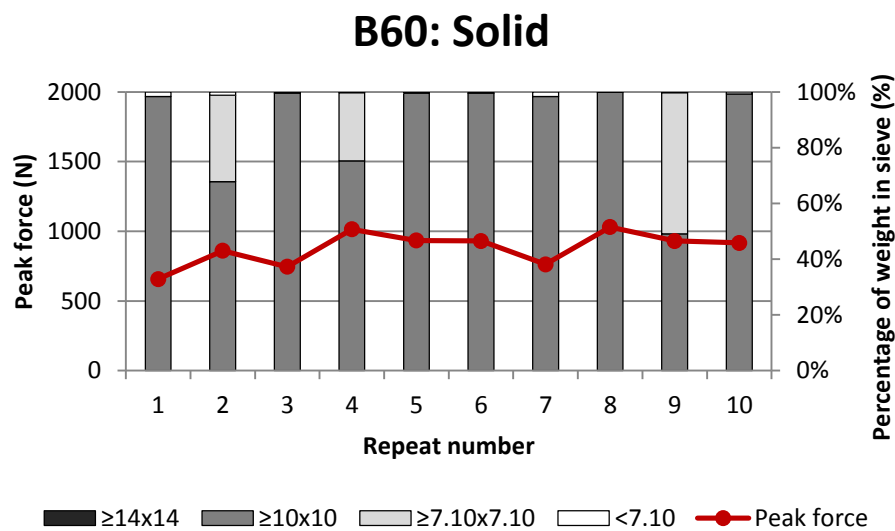


Figure A.4 Consistency of repeats for B60 to break down a solid dome in terms of peak force and fragmentation.

C60: Hollow hard object breakdown

In contrast to B60, brittle failure occurred in the entire hollow sample when compressed by C60, however not all domes fragmented at fracture. It should be noted that although these domes did not fragment they did exhibit lines of fracture that often led to them falling apart into pieces once moved (Figure A.5-ii). The ones that did fragment at fracture tended to involve movement of pieces that had broken into 2-3 main segments. Frequently the area of indentation would form a small sub-piece.

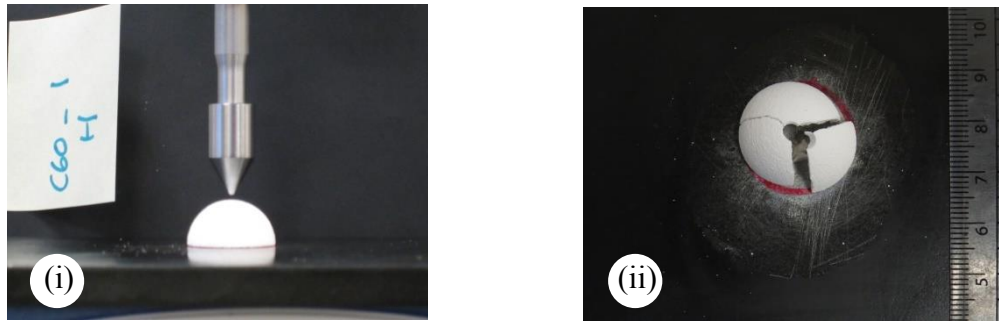


Figure A.5 C60 hollow hard object breakdown images: (i) C60 and hollow dome, (ii) post compression image. Domes typically split into 2-3 main pieces with the area of indentation forming a minor piece.

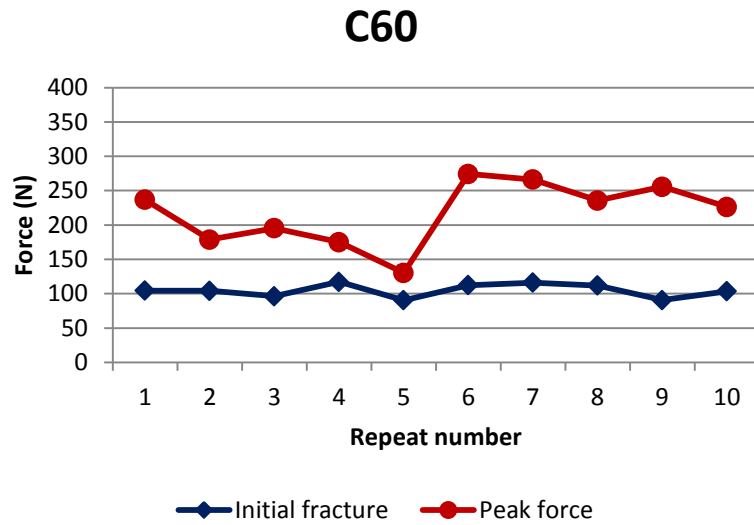


Figure A.6 Consistency of repeats for C60 based on force at initial fracture and peak force to break a hollow dome.

C60: Solid hard object breakdown

Similar to B60 the majority of solid domes broke into 2 pieces when compressed by C60 (Figure A.7-ii). Brittle failure occurred in all the domes, which was accompanied with an explosive movement of pieces. Three out of the original ten repeats were excluded from analysis due to a large amount of chipping with no brittle failure. This type of behaviour was found to be generally associated with the cusp tip being slightly off centre, which was more sensitive for cusps with a small radius of curvature. Therefore a further 3 repeats were used for data analysis.

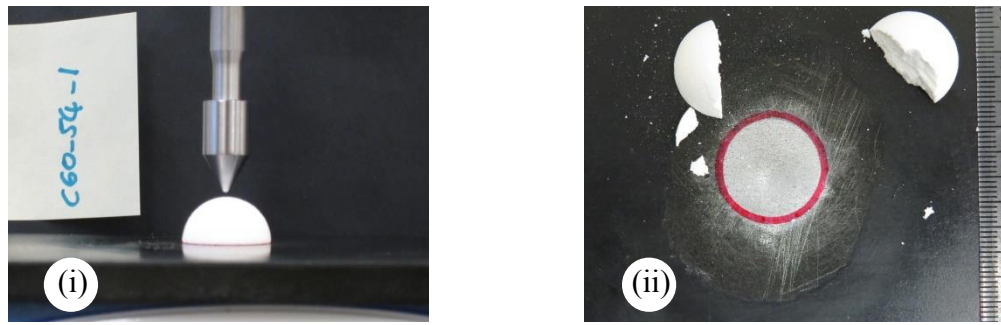


Figure A.7 C60 solid hard object breakdown images: (i) C60 and solid dome, (ii) post compression image. Domes typically split into 2 pieces and energetically moved apart at failure.

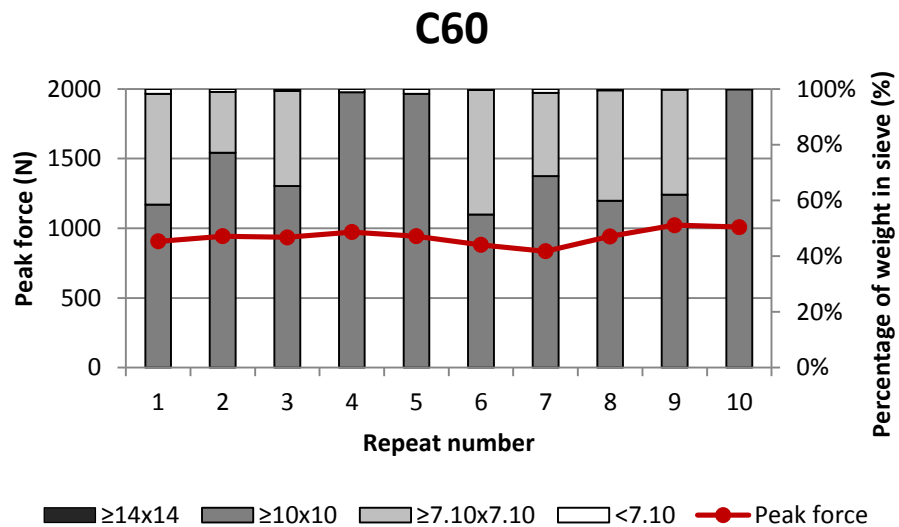


Figure A.8 Consistency of repeats for C60 to break down a solid dome in terms of peak force and fragmentation.

D60: Hollow hard object breakdown

Brittle failure occurred in most of the repeats where the pieces moved apart and formed 2-3 pieces (Figure A.9-ii). The exception to this was repeat 2, which did not fragment but did exhibit clear fracture lines. At failure, the area of indentation again formed a small sub-piece.

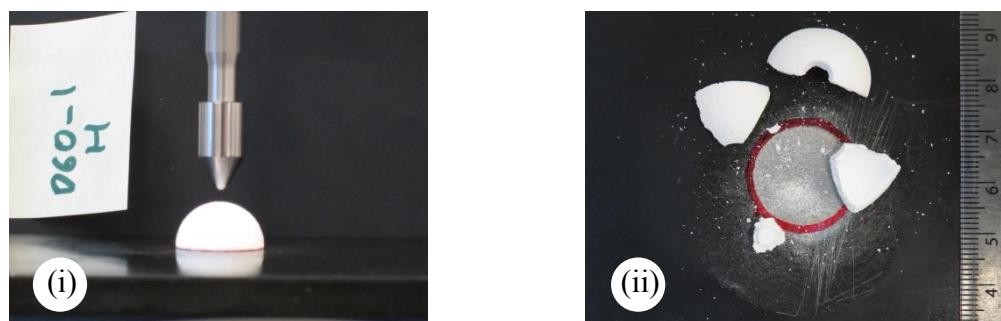


Figure A.9 D60 hollow hard object breakdown images: (i) D60 and hollow dome, (ii) post compression image. Domes typically split into 2-3 pieces and energetically moved apart at failure.

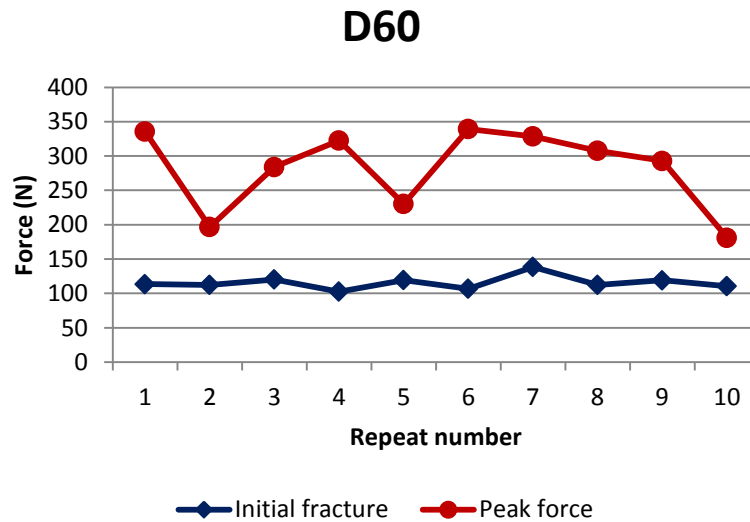


Figure A.10 Consistency of repeats for D60 based on force at initial fracture and peak force to break a hollow dome.

D60: Solid hard object breakdown

The majority of domes fractured in a fast brittle fashion and moved apart at fracture. At fragmentation all samples consistently split into 2 pieces and the area of indentation commonly formed a small sub-piece (Figure A.11-ii). 2 samples were excluded as brittle failure did not occur therefore 2 extra repeats were used for data analysis.

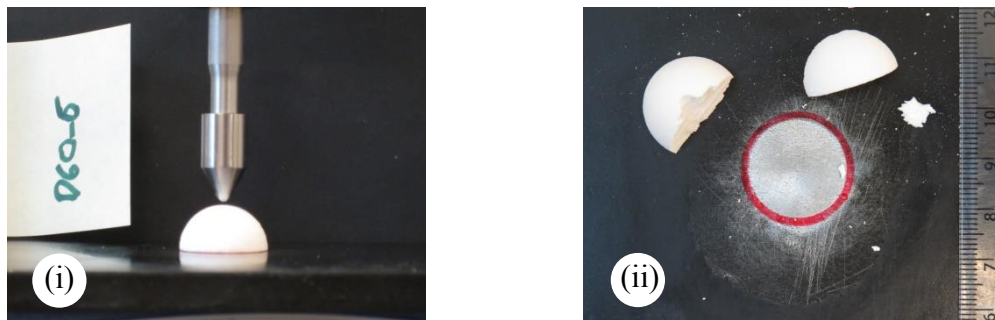


Figure A.11 D60 solid hard object breakdown images: (i) D60 and solid dome, (ii) post compression image. Domes typically split into 2 pieces and energetically moved apart at failure.

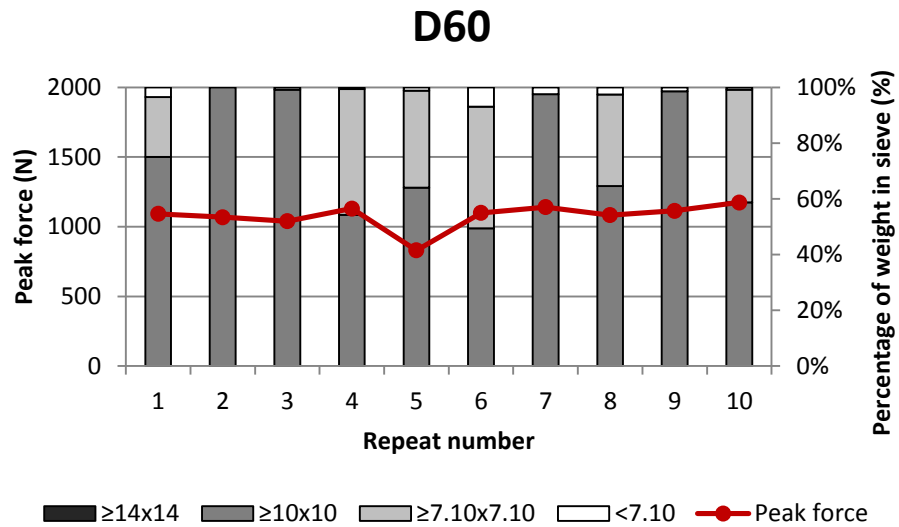


Figure A.12 Consistency of repeats for D60 to break down a solid dome in terms of peak force and fragmentation.

E60: Hollow hard object breakdown

In all samples brittle failure occurred which was accompanied with a movement of pieces except for two repeats where brittle failure occurred but the pieces were still connected. In the samples that did fragment at fracture, all domes split into 3 pieces (Figure A.13-ii). Again similar to the other models, the area of indentation tended to form a small sub-piece at fragmentation.

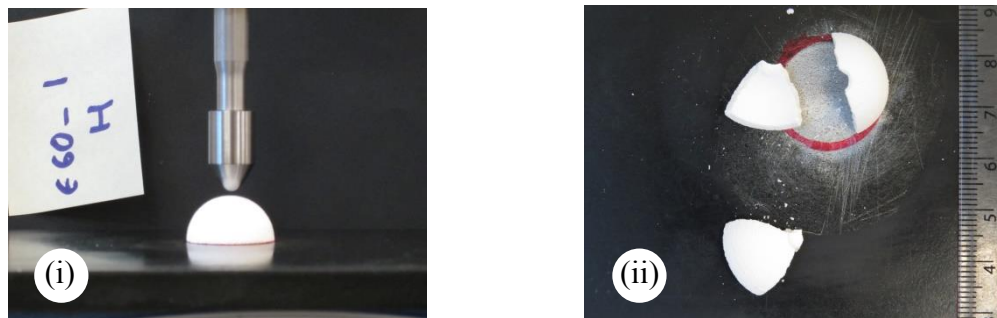


Figure A.13 E60 hollow hard object breakdown images: (i) E60 and hollow dome, (ii) post compression image. Domes typically split into 3 pieces and energetically moved apart at failure.

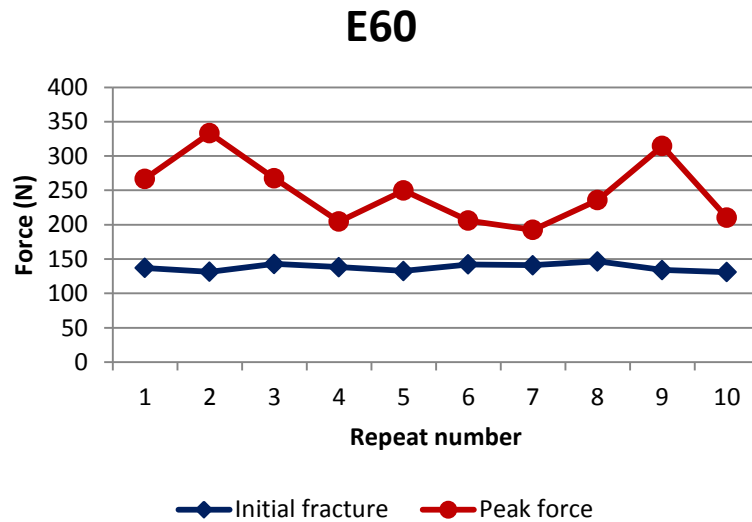


Figure A.14 Consistency of repeats for E60 based on force at initial fracture and peak force to break a hollow dome.

E60: Solid hard object breakdown

For all repeats fast explosive fracture occurred at failure that involved energetic movement of pieces. The domes broke into pieces that ranged in number from 2-4 (Figure A.15-ii).



Figure A.15 E60 solid hard object breakdown images: (i) E60 and solid dome, (ii) post compression image. Domes split into 2-4 pieces and energetically moved apart at failure.

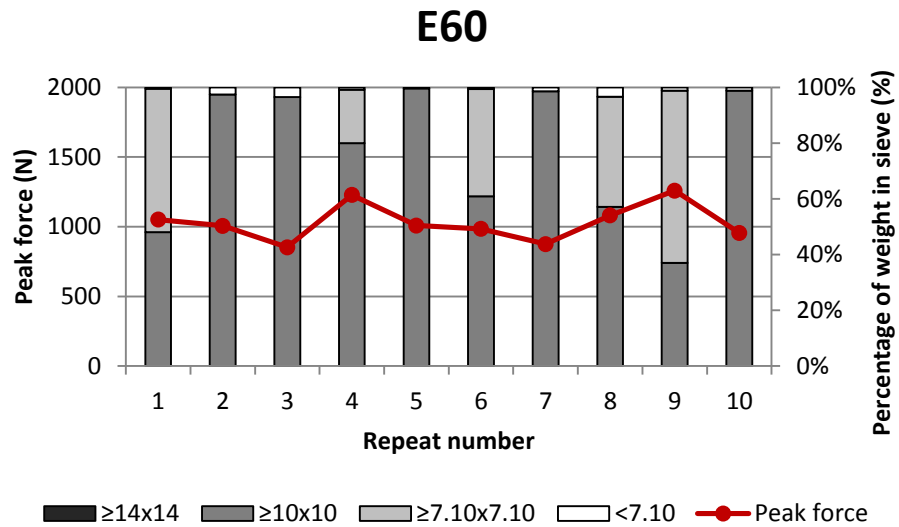


Figure A.16 Consistency of repeats for E60 to break down a solid dome in terms of peak force and fragmentation.

B90: Hollow hard object breakdown

Brittle failure and energetic movement of pieces occurred in all repeats. Number of pieces ranged from 2-4 (Figure A.17-ii). Again, the area of indentation tended to form a small sub-piece.



Figure A.17 B90 hollow hard object breakdown images: (i) B90 and hollow dome, (ii) post compression image. Domes split into 2-4 pieces and energetically moved apart at failure.

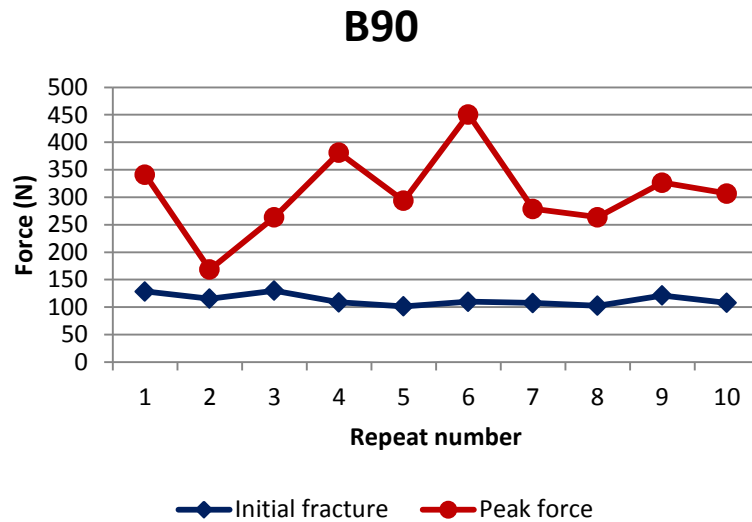


Figure A.18 Consistency of repeats for B90 based on force at initial fracture and peak force to break a hollow dome.

B90: Solid hard object breakdown

Fast explosive fracture occurred at failure in all samples of solid domes where pieces moved apart from each other. Number of pieces ranged from 2-4 (Figure A.19-ii). The first repeat was excluded from the sample as it appeared that the dome had slipped during compression thus producing a very off centre indentation. Therefore a further repeat was collected for data analysis.

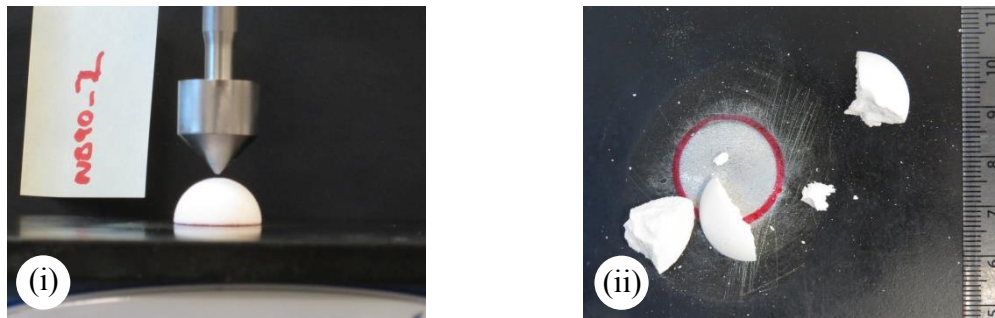


Figure A.19 B90 solid hard object breakdown images: (i) B90 and solid dome, (ii) post compression image. Domes split into 2-4 pieces and energetically moved apart at failure.

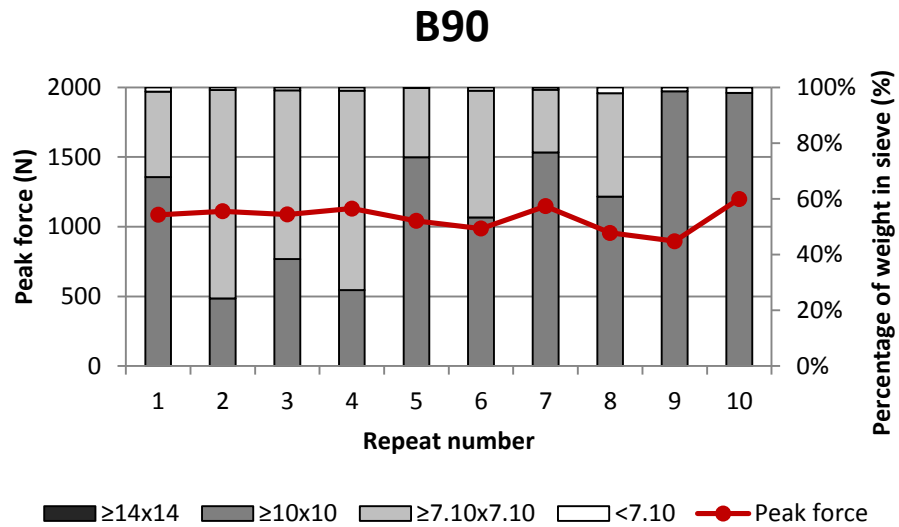


Figure A.20 Consistency of repeats for B90 to break down a solid dome in terms of peak force and fragmentation.

C90: Hollow hard object breakdown

All samples failed in a brittle fashion and the majority moved apart at fracture. Number of pieces ranged from 2-4 (Figure A.21-ii). However one of the samples did not fragment at failure but did fracture and later broke into pieces once sieved (repeat 2). The area of indentation tended to form a small sub-piece.

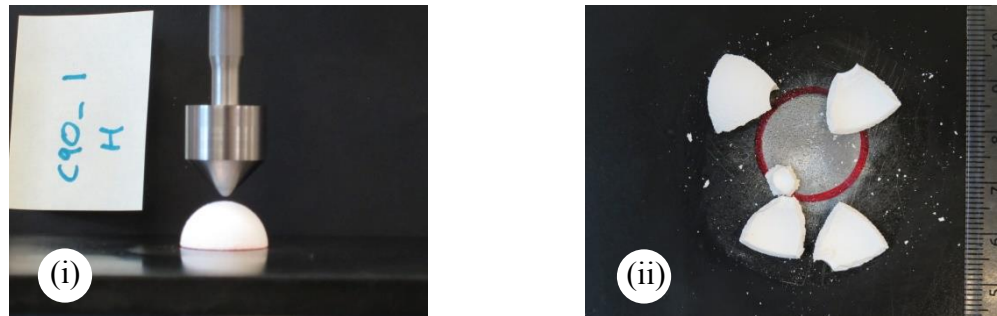


Figure A.21 C90 hollow hard object breakdown images: (i) C90 and hollow dome, (ii) post compression image. Domes split into 2-4 pieces and energetically moved apart at failure.

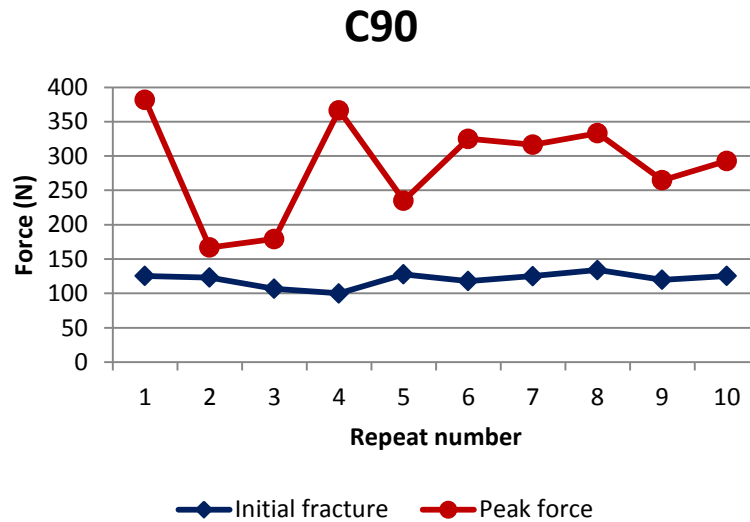


Figure A.22 Consistency of repeats for C90 based on force at initial fracture and peak force to break a hollow dome.

C90: Solid hard object breakdown

Fast explosive fracture occurred at failure in all samples where pieces energetically moved apart. The number of pieces ranged from 2-4 but the majority split into 2 pieces (Figure A.23-ii). The first repeat was excluded from data analysis as it appeared that the dome had slipped during compression. Therefore a further repeat was conducted.

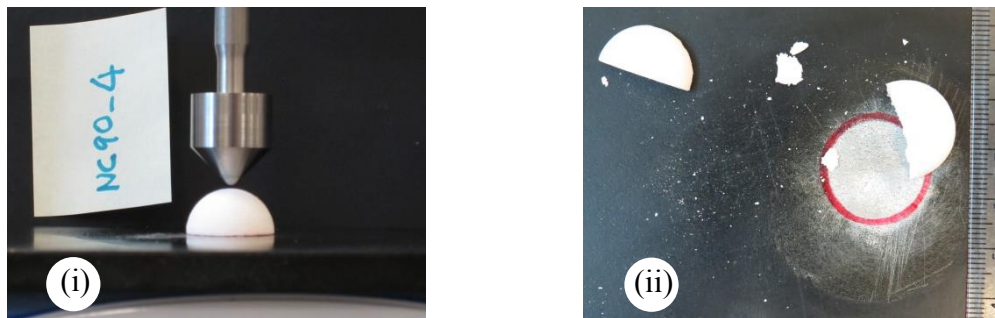


Figure A.23 C90 solid hard object breakdown images: (i) C90 and solid dome, (ii) post compression image. Domes split into 2-4 pieces and energetically moved apart at failure.

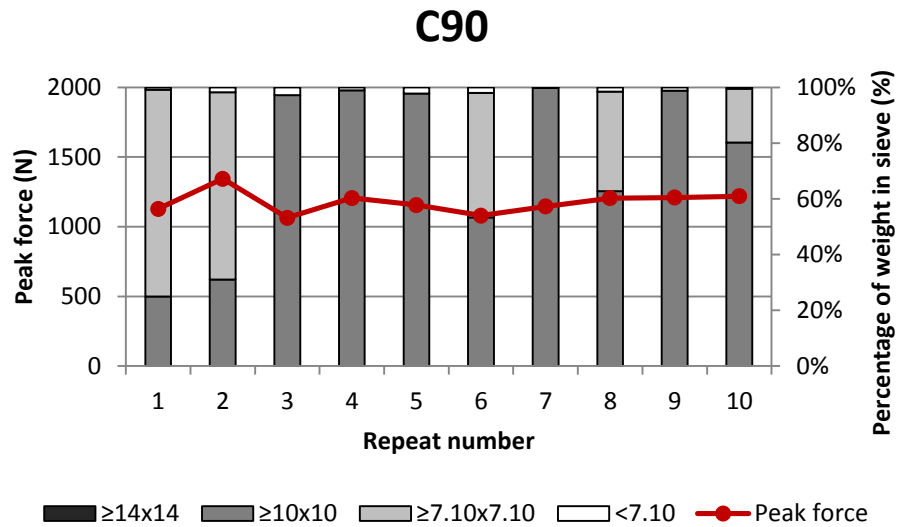


Figure A.24 Consistency of repeats for C90 to break down a solid dome in terms of peak force and fragmentation.

D90: Hollow hard object breakdown

All samples failed in brittle fashion and moved apart energetically. The majority of pieces fractured into 3 or 4 pieces (Figure A.25-ii). It was noted that although some of the domes did not fragment entirely at fracture they did tent to fall apart when moved due to fracture lines.



Figure A.25 D90 hollow hard object breakdown images: (i) D90 and hollow dome, (ii) post compression image. Domes split into 3-4 pieces and energetically moved apart at failure.

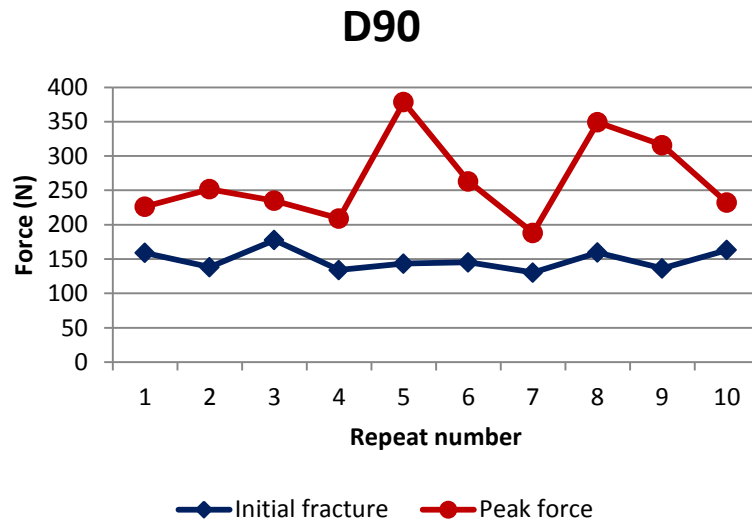


Figure A.26 Consistency of repeats for D90 based on force at initial fracture and peak force to break a hollow dome.

D90: Solid hard object breakdown

Fast brittle fracture occurred in all samples where pieces moved apart energetically. Again, the area of indentation formed a small sub-piece. The majority of domes fractured into 3 pieces (Figure A.27-ii), the remainder fractured into 2.



Figure A.27 D90 solid hard object breakdown images: (i) D90 and solid dome, (ii) post compression image. Domes typically split into 3 pieces and energetically moved apart at failure.

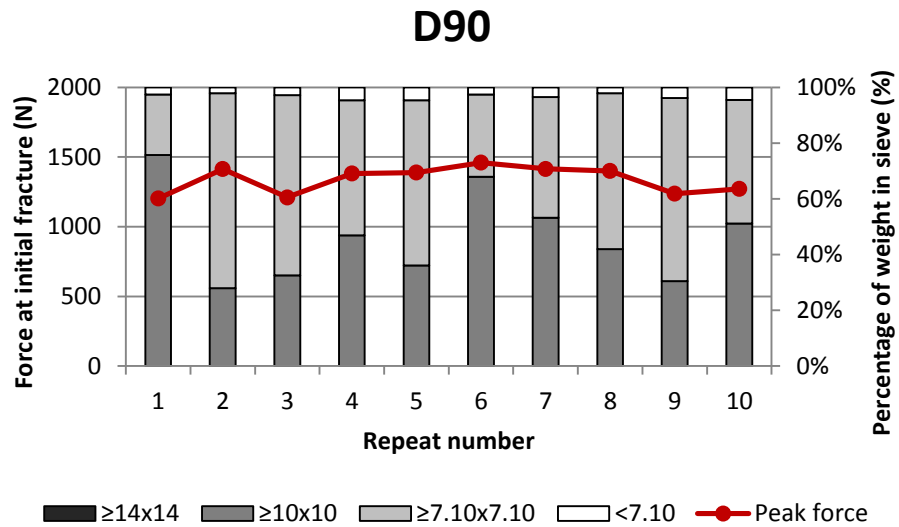


Figure A.28 Consistency of repeats for D90 to break down a solid dome in terms of peak force and fragmentation.

E90: Hollow hard object breakdown

All pieces failed in a brittle fashion although not all of the domes broke apart at fracture. For some, the top of the dome was compressed where fracture lines were visible around the dome which would later lead to fragmentation when moved (Figure A.29-ii). Number of pieces ranged from 2-4.



Figure A.29 E90 hollow hard object breakdown images: (a) E90 and hollow dome, (b) post compression image. Domes split into 2-4 pieces.

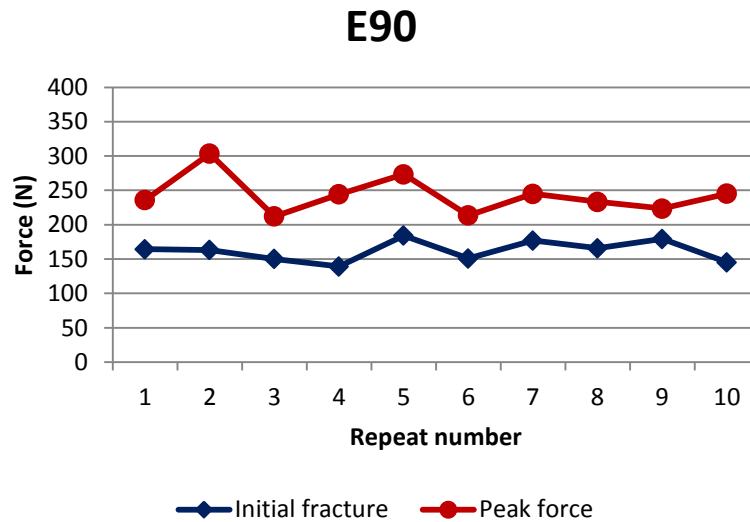


Figure A.30 Consistency of repeats for E90 based on force at initial fracture and peak force to break a hollow dome.

E90: Solid hard object breakdown

For all samples fast fracture occurred at failure, which was frequently accompanied by the movement of pieces. The central area of indentation tended to form a sub-piece. This piece was notably quite large compared to the sub-pieces created by the sharper cusp models. The number of pieces ranged from 2-4. Overall most domes split into 3 or 4 pieces (Figure A.31-ii).



Figure A.31 E90 solid hard object breakdown images: (i) E90 and solid dome, (ii) post compression image. Domes typically split into 3-4 pieces and energetically moved apart at failure.

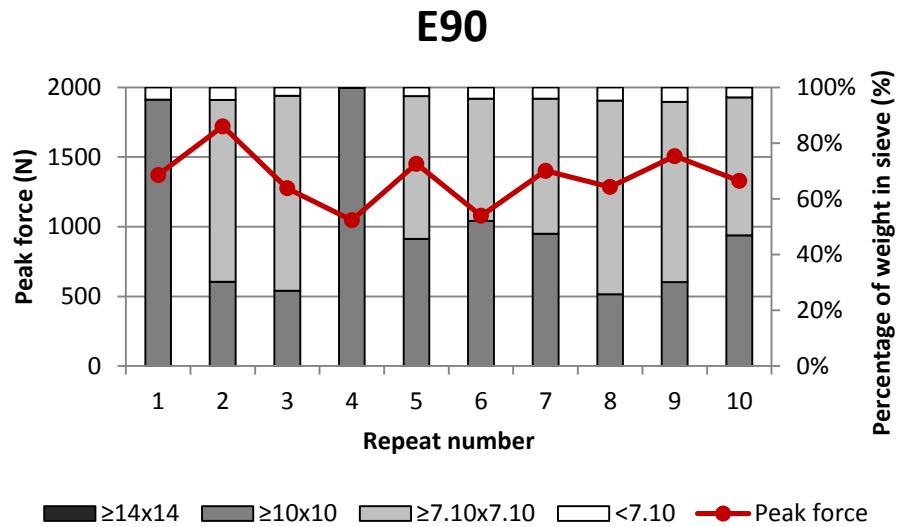


Figure A.32 Consistency of repeats for E90 to break down a solid dome in terms of peak force and fragmentation.

B120: Hollow hard object breakdown

Brittle failure occurred in all samples. Not all samples fragmented at fracture but did show visible fracture lines that would later lead to the fragmentation of the objects when moved (Figure A.33-ii). The domes that fragmented at fracture mostly broke into 2 or 3 pieces.

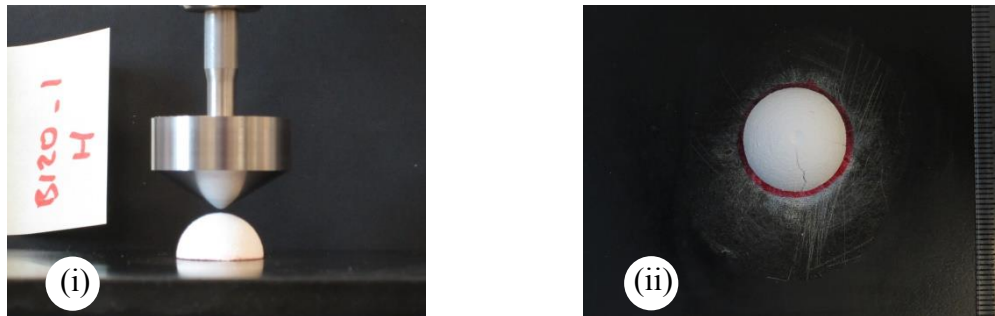


Figure A.33 B120 hollow hard object breakdown images: (i) B120 and hollow dome, (ii) post compression image. Domes typically split into 2-3 pieces.

B120

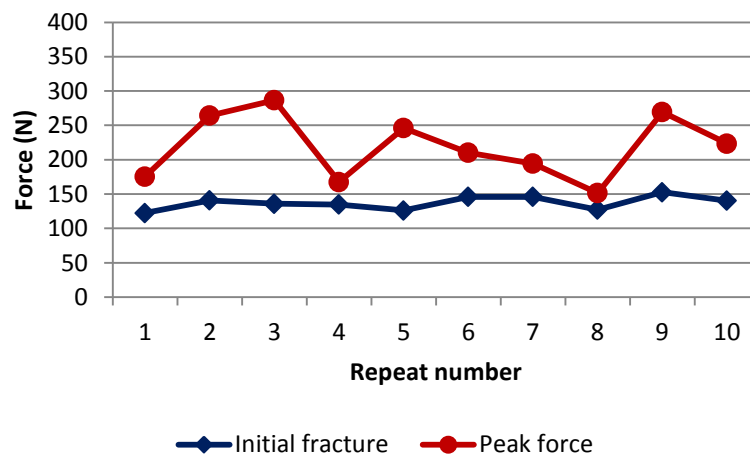


Figure A.34 Consistency of repeats for B120 based on force at initial fracture and peak force to break a hollow dome.

B120: Solid hard object breakdown

Brittle failure occurred in all the samples however interestingly in comparison to the narrower B models, there was less movement of pieces at fracture. In this case, the pieces were still connected by the central indentation mark (Figure A.35-ii). The domes fragmented into either 2 or 3 pieces and the central indentation area again frequently formed a small sub-piece.



Figure A.35 B120 solid hard object breakdown images: (i) B120 and solid dome, (ii) post compression image. Domes typically split into 2-3 pieces.

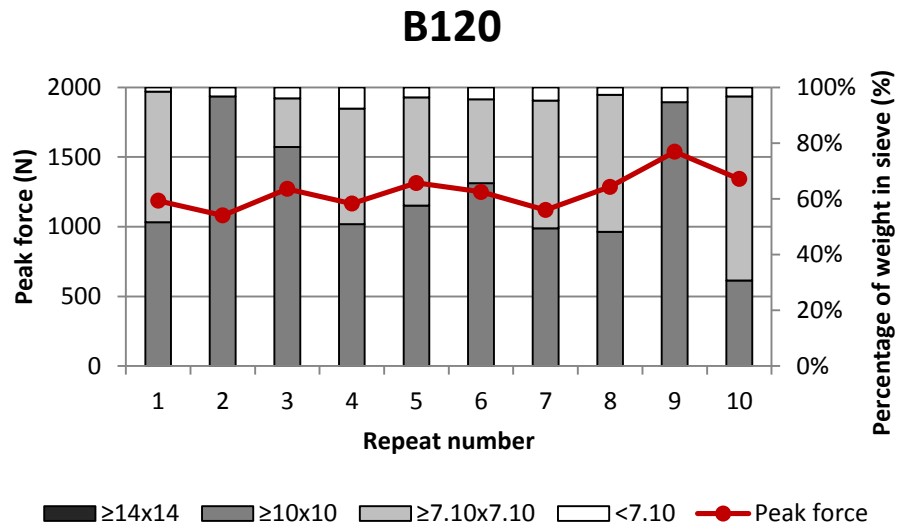


Figure A.36 Consistency of repeats for B120 to break down a solid dome in terms of peak force and fragmentation.

C120: Hollow hard object breakdown

Brittle failure occurred in all samples however similar to the B120 cusp, not all the samples fragmented at fracture but did exhibit clear fracture lines (Figure A.37-ii). Number of pieces ranged from 3-4. Repeat 9 was excluded from data analysis as the % break command did not capture the point of fracture therefore the machine continued compression after the dome had failed. Therefore an extra repeat was included for data analysis.

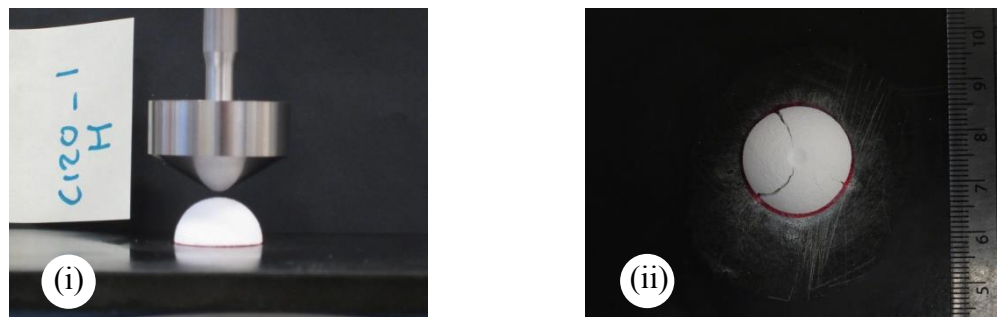


Figure A.37 C120 hollow hard object breakdown images: (i) C120 and hollow dome, (ii) post compression image. Domes typically split into 3-4 pieces.

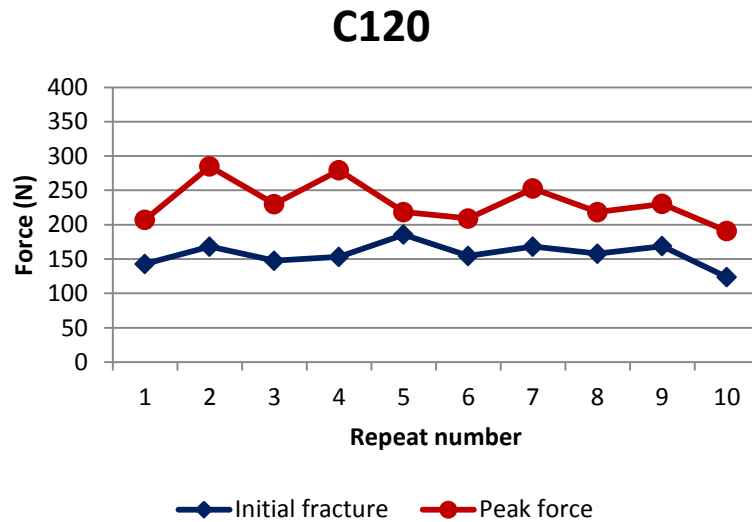


Figure A.38 Consistency of repeats for C120 based on force at initial fracture and peak force to break a hollow dome.

C120: Solid hard object breakdown

Fast fracture occurred at failure in all samples where the pieces fragmented and moved apart. The central indentation area formed a small sub-piece. Number of pieces ranged from 2-4 but the majority split into 2 or 3 pieces (Figure A.39-ii).

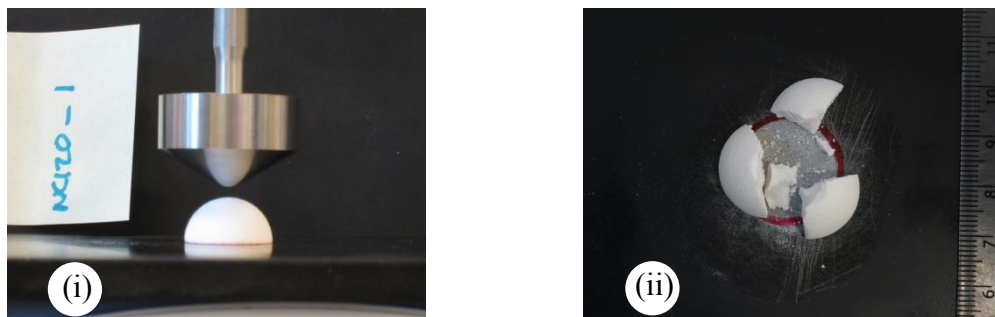


Figure A.39 C120 solid hard object breakdown images: (i) C120 and solid dome, (ii) post compression image. Domes typically split into 2-3 pieces and energetically moved apart at failure.

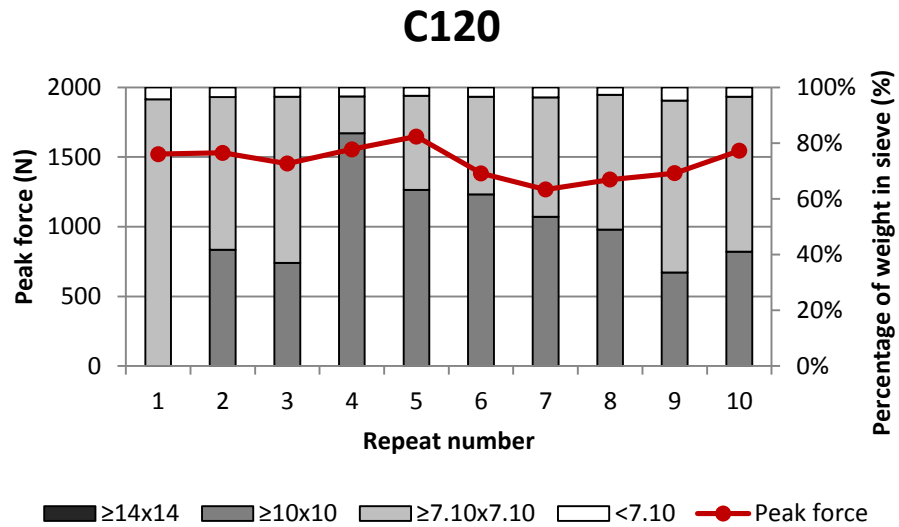


Figure A.40 Consistency of repeats for C120 to break down a solid dome in terms of peak force and fragmentation.

D120: Hollow hard object breakdown

Brittle failure occurred in all hollow domes, however not all moved at fracture or broke completely into pieces. The domes mostly split into 3 pieces at failure (Figure A.41-ii). The domes that did not fragment at fracture did exhibit clear fracture lines that would later lead to fragmentation.

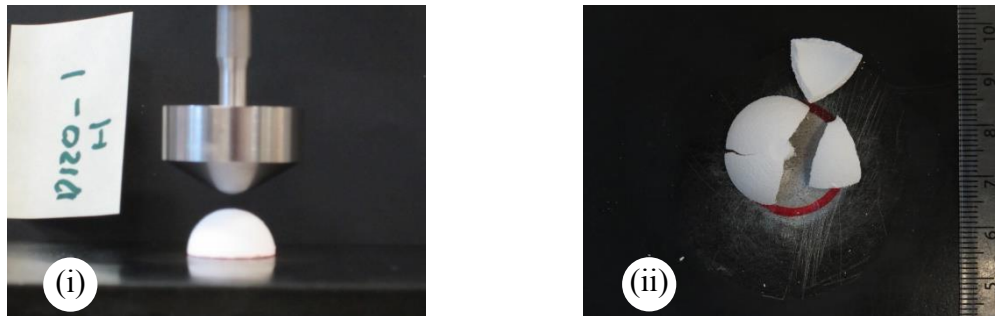


Figure A.41 D120 hollow hard object breakdown images: (i) D120 and hollow dome, (ii) post compression image. Domes typically split into 3 pieces.

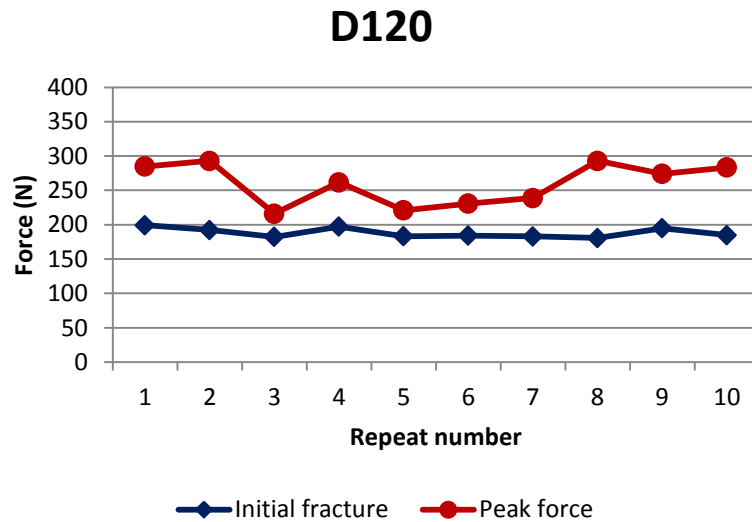


Figure A.42 Consistency of repeats for D120 based on force at initial fracture and peak force to break a hollow dome.

D120: Solid hard object breakdown

All samples failed in a brittle fashion however there was no movement of pieces at fracture and the pieces appeared to still be connected. The domes were quite compressed but had clear visible fracture lines (Figure A.43-ii). Number of pieces ranged from 2-4. Majority of pieces broke into 3.



Figure A.43 D120 solid hard object breakdown images: (i) D120 and solid dome, (ii) post compression image. Domes typically split into 3 pieces.

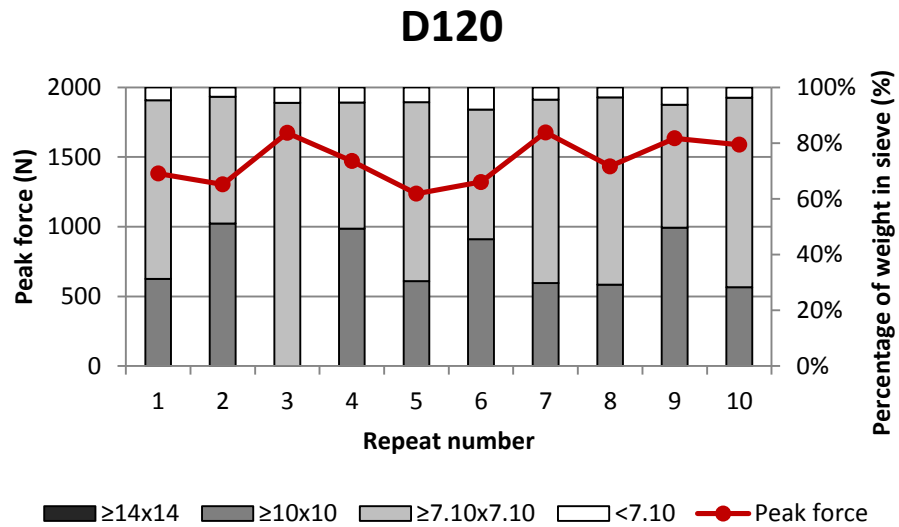


Figure A.44 Consistency of repeats for D120 to break down a solid dome in terms of peak force and fragmentation.

E120: Hollow hard object breakdown

Fast brittle failure occurred in all samples however not all moved or broke into pieces at fracture. In these samples, fracture lines were induced that would later fragment when moved (Figure A.45-ii). Taking this into account, most domes broke into 4 segments.

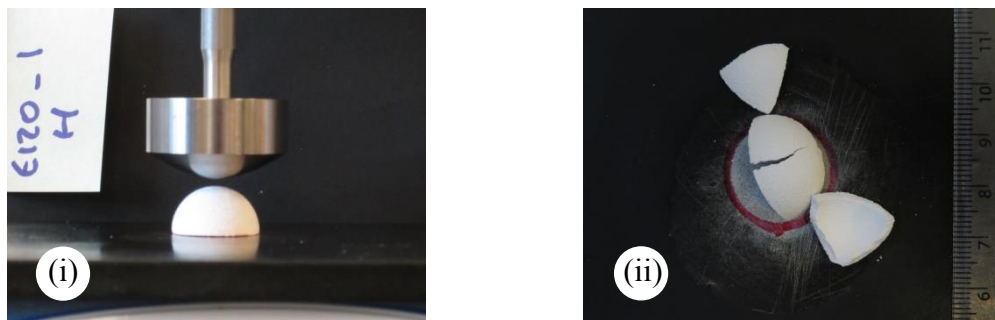


Figure A.45 E120 hollow hard object breakdown images: (i) E120 and hollow dome, (ii) post compression image. Domes typically split into 4 pieces.

E120

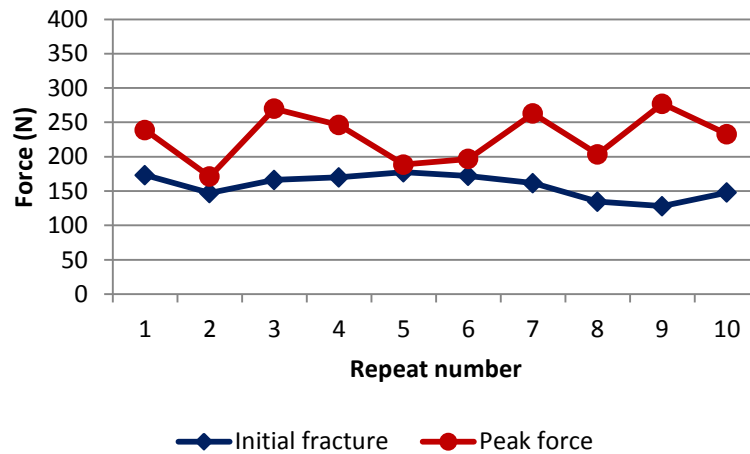


Figure A.46 Consistency of repeats for E120 based on force at initial fracture and peak force to break a hollow dome.

E120: Solid hard object breakdown

Brittle failure occurred but there was no movement of pieces in any of the repeats. The domes appeared very compressed after each test but exhibited clear fracture lines that would later lead to fragmentation when subjected to sieving (Figure A.47-ii). The majority of domes broke into 3 pieces although ranged from 2-4. Repeat 6 was excluded from sample as there was no brittle failure or audible fracture.

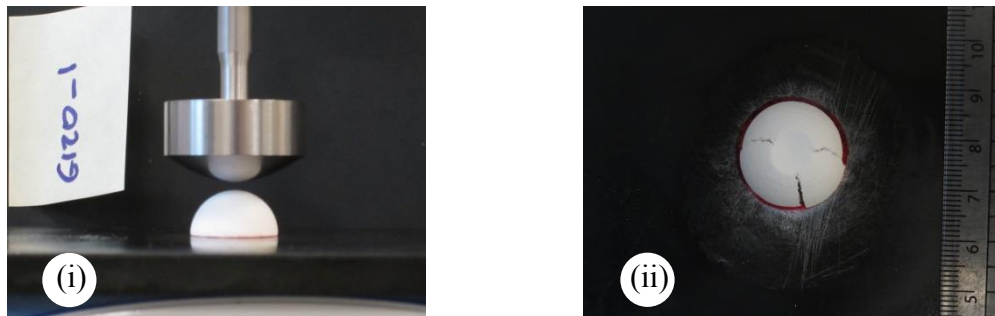


Figure A.47 E120 solid hard object breakdown images: (i) E120 and solid dome, (ii) post compression image. Domes typically split into 3 pieces.

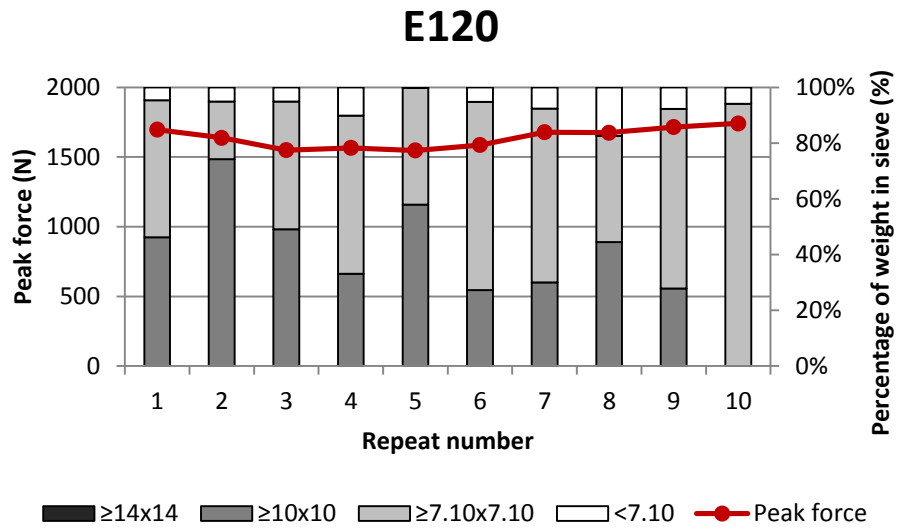


Figure A.48 Consistency of repeats for E120 to break down a solid dome in terms of peak force and fragmentation.

Table A.1 Averages and standard deviations of the surface area, displacement, force, energy and duration measurements at the point of initial fracture of the hollow hard objects for each cusp design (N=10).

Cusp design	Radius of curvature (mm)	Surface area (mm ²)		Displacement (mm)		Force (N)		Energy (mJ)		Duration (s)	
		Avg.	St. Dev.	Avg.	St. Dev.	Avg.	St. Dev.	Avg.	St. Dev.	Avg.	St. Dev.
B60	0.25	1.54	0.13	0.55	0.03	91.81	5.27	25.76	2.51	7.01	0.42
C60	0.50	2.02	0.23	0.47	0.04	104.73	9.85	23.19	3.66	5.86	0.59
D60	1.00	3.23	0.19	0.43	0.02	115.55	9.83	21.32	1.68	5.49	0.26
E60	2.00	5.76	0.40	0.42	0.03	137.73	5.44	24.62	2.00	5.23	0.33
B90	0.75	2.81	0.28	0.47	0.04	113.31	10.12	24.67	3.53	5.90	0.37
C90	1.50	4.21	0.25	0.40	0.02	120.55	10.14	21.01	2.27	5.00	0.26
D90	3.00	9.25	1.29	0.46	0.06	148.67	15.39	28.14	3.74	5.67	0.70
E90	6.00	15.82	1.60	0.41	0.04	161.89	15.25	26.80	3.92	5.07	0.44
B120	2.25	6.69	0.40	0.43	0.02	137.24	9.78	24.24	2.51	5.39	0.28
C120	4.50	12.79	0.83	0.43	0.03	156.99	17.07	28.41	4.59	5.35	0.32
D120	9.00	25.01	1.04	0.43	0.02	188.17	6.98	31.27	1.98	5.39	0.21
E120	18.00	50.02	3.37	0.44	0.03	157.78	17.32	28.02	3.86	5.45	0.36

Table A.2 Averages and standard deviations of the surface area, displacement, force, energy and duration measurements at peak force to break hollow hard objects for each cusp design (N=10).

Cusp design	Radius of curvature (mm)	Surface area (mm ²)		Displacement (mm)		Force (N)		Energy (mJ)		Duration (s)	
		Avg.	St. Dev.	Avg.	St. Dev.	Avg.	St. Dev.	Avg.	St. Dev.	Avg.	St. Dev.
B60	0.25	52.47	11.16	4.62	0.55	323.45	48.50	717.67	146.19	55.91	6.67
C60	0.50	27.00	13.73	2.82	0.87	217.44	46.23	352.72	173.13	34.15	10.44
D60	1.00	50.01	21.77	3.48	1.11	281.92	58.58	597.56	273.82	42.07	13.26
E60	2.00	27.17	15.58	1.58	0.73	248.21	48.05	244.34	170.47	19.13	8.73
B90	0.75	46.68	25.85	2.77	0.89	307.49	75.75	477.81	247.45	33.56	10.67
C90	1.50	39.56	21.09	2.18	0.85	286.29	73.86	371.81	201.74	26.45	10.26
D90	3.00	32.49	16.47	1.39	0.58	264.90	62.59	224.94	162.50	16.90	7.01
E90	6.00	31.11	5.56	0.77	0.13	242.98	27.76	95.76	27.35	9.51	1.53
B120	2.25	21.54	8.81	1.02	0.28	218.97	46.79	124.13	59.63	12.46	3.37
C120	4.50	26.97	5.47	0.86	0.15	232.11	31.05	105.31	34.80	10.56	1.83
D120	9.00	44.96	7.13	0.76	0.12	259.70	30.35	99.76	25.95	9.40	1.45
E120	18.00	80.96	13.49	0.70	0.12	228.75	36.85	76.98	24.06	8.64	1.40

Table A.3 Averages and standard deviations of the surface area, displacement, force, energy and duration measurements at peak force to break solid hard objects for each cusp design (N=10).

Cusp design	Radius of curvature (mm)	Surface area (mm ²)		Displacement (mm)		Force (N)		Energy (mJ)		Duration (s)	
		Avg.	St. Dev.	Avg.	St. Dev.	Avg.	St. Dev.	Avg.	St. Dev.	Avg.	St. Dev.
B60	0.25	30.24	2.91	3.44	0.18	878.40	121.10	1230.09	228.93	41.75	2.27
C60	0.50	29.71	2.00	3.08	0.12	938.88	55.83	1286.53	117.87	37.47	1.54
D60	1.00	32.08	3.19	2.66	0.18	1077.43	94.72	1317.30	190.24	32.38	2.24
E60	2.00	40.48	4.09	2.24	0.18	1029.90	132.81	1029.13	224.24	27.17	2.21
B90	0.75	47.13	4.15	2.89	0.14	1064.25	93.78	1292.70	168.05	35.21	1.70
C90	1.50	47.60	2.82	2.57	0.10	1175.70	80.50	1343.51	140.19	31.36	1.22
D90	3.00	58.65	4.71	2.30	0.14	1338.15	96.62	1397.52	178.21	28.09	1.73
E90	6.00	90.99	10.86	2.08	0.22	1346.96	197.63	1269.44	316.49	25.37	2.65
B120	2.25	78.93	9.34	2.32	0.16	1255.75	130.76	1270.79	218.42	28.33	1.99
C120	4.50	97.09	8.39	2.26	0.13	1462.36	117.22	1471.56	197.28	27.63	1.51
D120	9.00	125.94	13.80	1.98	0.18	1472.22	162.81	1296.30	254.48	24.34	2.24
E120	18.00	273.07	13.37	2.28	0.10	1639.26	72.23	1591.81	163.81	27.78	1.29

Appendix B: Chapter 3

Table B.1 Resolution of the CT scans used to reconstruct virtual dental models for each *C.atys* specimen.

Specimen	Scan resolution		
	x	y	z
C13.5	0.099	0.099	0.199
C13.41	0.117	0.117	0.117
C13.33	0.135	0.135	0.135
C13.43	0.115	0.115	0.230
C13.17	0.116	0.116	0.232
C13.28	0.136	0.136	0.136
C13.31	0.143	0.143	0.143
C13.35	0.143	0.143	0.143
C13.1	0.151	0.151	0.151
C13.3	0.116	0.116	0.232
C13.12	0.116	0.116	0.232
C13.13	0.116	0.116	0.232
C13.20	0.124	0.124	0.124
C13.26	0.110	0.110	0.110
C13.27	0.101	0.101	0.101
C13.2	0.122	0.122	0.488
C13.19	0.113	0.113	0.113
C13.21	0.121	0.121	0.121
C13.22	0.153	0.153	0.153
C13.29	0.143	0.143	0.143

Table B.2 Stage of eruption for both upper and lower dentition of each *C.atys* specimen included in chapter 3. Sex indicated where known.

Specimen	Sex		Dental eruption status												
			Deciduous					Permanent							
C13.41	?	Lower	I1	I2	C	P3	P4	I1	I2	C	P3	P4	M1	M2	M3
		Upper	I1	I2	C	P3	P4	I1	I2	C	P3	P4	M1	M2	M3
C13.33	F	Lower	I1	I2	C	P3	P4	I1	I2	C	P3	P4	M1	M2	M3
		Upper	I1	I2	C	P3	P4	I1	I2	C	P3	P4	M1	M2	M3
C13.36	F	Lower	I1	I2	C	P3	P4	I1	I2	C	P3	P4	M1	M2	M3
		Upper	I1	I2	C	P3	P4	I1	I2	C	P3	P4	M1	M2	M3
C13.42	F	Lower	I1	I2	C	P3	P4	I1	I2	C	P3	P4	M1	M2	M3
		Upper	I1	I2	C	P3	P4	I1	I2	C	P3	P4	M1	M2	M3
C13.43	?	Lower	I1	I2	C	P3	P4	I1	I2	C	P3	P4	M1	M2	M3
		Upper	I1	I2	C	P3	P4	I1	I2	C	P3	P4	M1	M2	M3
C13.17	M	Lower	I1	I2	C	P3	P4	I1	I2	C	P3	P4	M1	M2	M3
		Upper	I1	I2	C	P3	P4	I1	I2	C	P3	P4	M1	M2	M3
C13.28	F	Lower	I1	I2	C	P3	P4	I1	I2	C	P3	P4	M1	M2	M3
		Upper	I1	I2	C	P3	P4	I1	I2	C	P3	P4	M1	M2	M3
C13.31	M	Lower	I1	I2	C	P3	P4	I1	I2	C	P3	P4	M1	M2	M3
		Upper	I1	I2	C	P3	P4	I1	I2	C	P3	P4	M1	M2	M3
C13.35	F	Lower	I1	I2	C	P3	P4	I1	I2	C	P3	P4	M1	M2	M3

Table B.2 continued

Specimen	Sex		Dental eruption status												
			Deciduous					Permanent							
Unknown 1 ?	Upper		I1	I2	C	P3	P4	I1	I2	C	P3	P4	M1	M2	M3
	Lower		I1	I2	C	P3	P4	I1	I2	C	P3	P4	M1	M2	M3
	Upper		NP					NP							
C13.1	F	Lower	I1	I2	C	P3	P4	I1	I2	C	P3	P4	M1	M2	M3
		Upper	I1	I2	C	P3	P4	I1	I2	C	P3	P4	M1	M2	M3
C13.3	F	Lower	I1	I2	C	P3	P4	I1	I2	C	P3	P4	M1	M2	M3
		Upper	I1	I2	C	P3	P4	I1	I2	C	P3	P4	M1	M2	M3
C13.11	F	Lower	I1	I2	C	P3	P4	I1	I2	C	P3	P4	M1	M2	M3
		Upper	I1	I2	C	P3	P4	I1	I2	C	P3	P4	M1	M2	M3
C13.12	F	Lower	I1	I2	C	P3	P4	I1	I2	C	P3	P4	M1	M2	M3
		Upper	I1	I2	C	P3	P4	I1	I2	C	P3	P4	M1	M2	M3
C13.13	M	Lower	I1	I2	C	P3	P4	I1	I2	C	P3	P4	M1	M2	M3
		Upper	I1	I2	C	P3	P4	I1	I2	C	P3	P4	M1	M2	M3
C13.20	M	Lower	I1	I2	C	P3	P4	I1	I2	C	P3	P4	M1	M2	M3
		Upper	I1	I2	C	P3	P4	I1	I2	C	P3	P4	M1	M2	M3
C13.26	M	Lower	I1	I2	C	P3	P4	I1	I2	C	P3	P4	M1	M2	M3
		Upper	I1	I2	C	P3	P4	I1	I2	C	P3	P4	M1	M2	M3
C13.27	F	Lower	I1	I2	C	P3	P4	I1	I2	C	P3	P4	M1	M2	M3

Table B.2 continued

Specimen	Sex		Dental eruption status												
			Deciduous					Permanent							
C13.2	F	Upper	I1	I2	C	P3	P4	I1	I2	C	P3	P4	M1	M2	M3
		Lower	I1	I2	C	P3	P4	I1	I2	C	P3	P4	M1	M2	M3
		Upper	I1	I2	C	P3	P4	I1	I2	C	P3	P4	M1	M2	M3
C13.18	M	Lower	I1	I2	C	P3	P4	I1	I2	C	P3	P4	M1	M2	M3
		Upper	I1	I2	C	P3	P4	I1	I2	C	P3	P4	M1	M2	M3
C13.19	M	Lower	I1	I2	C	P3	P4	I1	I2	C	P3	P4	M1	M2	M3
		Upper	I1	I2	C	P3	P4	I1	I2	C	P3	P4	M1	M2	M3
C13.21	M	Lower	I1	I2	C	P3	P4	I1	I2	C	P3	P4	M1	M2	M3
		Upper	I1	I2	C	P3	P4	I1	I2	C	P3	P4	M1	M2	M3
C13.22	M	Lower	I1	I2	C	P3	P4	I1	I2	C	P3	P4	M1	M2	M3
		Upper	I1	I2	C	P3	P4	I1	I2	C	P3	P4	M1	M2	M3
C13.29	F	Lower	I1	I2	C	P3	P4	I1	I2	C	P3	P4	M1	M2	M3
		Upper	I1	I2	C	P3	P4	I1	I2	C	P3	P4	M1	M2	M3
Unknown 2	M	Lower	I1	I2	C	P3	P4	I1	I2	C	P3	P4	M1	M2	M3
		Upper	NP					NP							

Key: Tooth not yet erupted Deciduous tooth shed Tooth partially erupted Tooth fully erupted

Table B.3 Data on occlusal wear for each specimen. Information is presented on the dentine surface area and occlusal surface area, which was used to calculate occlusal wear as a percentage of dentine exposure (PDE). Unerupted teeth are indicated with '-' whereas teeth lost post-mortem or damaged are indicated with 'X'.

Specimen	Eruption stage	M1			M2		
		Dentine surface area (mm ²)	Occlusal surface area (mm ²)	Occlusal wear (PDE %)	Dentine surface area (mm ²)	Occlusal surface area (mm ²)	Occlusal wear (PDE %)
C13.41	0	-	-	-	-	-	-
C13.33	1	1.621	30.702	5.3	-	-	-
C13.36	1	0.099	34.828	0.3	-	-	-
C13.42	1	0.546	26.906	2.0	-	-	-
C13.17	2	3.411	31.962	10.7	0.247	37.395	0.7
C13.28	2	2.389	31.112	7.7	0	n/a	0
C13.31	2	3.483	31.730	11.0	0	n/a	0
C13.35	2	3.032	25.171	12.0	0	n/a	0
Unknown 1 (juvenile)	2	5.901	32.087	18.4	0.045	44.838	0.1
C13.1	3	4.496	27.452	16.4	0.311	33.799	0.9
C13.3	3	7.515	30.456	24.7	2.027	32.876	6.2
C13.11	3	6.464	29.209	22.1	0.350	37.365	0.9
C13.12	3	13.778	32.374	42.6	X	X	X
C13.20	3	5.681	36.680	15.5	0.363	38.063	1.0
C13.26	3	5.873	29.753	19.7	X	X	X
C13.27	3	9.143	30.334	30.1	2.754	33.020	8.3
C13.2	4	28.900	36.707	78.7	X	X	X
C13.18	4	26.514	41.805	63.4	14.866	51.156	29.1
C13.19	4	21.294	37.462	56.8	16.043	47.375	33.9
C13.21	4	11.425	32.361	35.3	6.957	37.672	18.5
C13.22	4	12.988	32.753	39.7	3.124	34.854	9.0
C13.29	4	10.931	33.478	32.7	4.551	36.202	12.6
Unknown 2 (adult)	4	26.493	42.105	62.9	17.724	53.307	33.2

C13.41

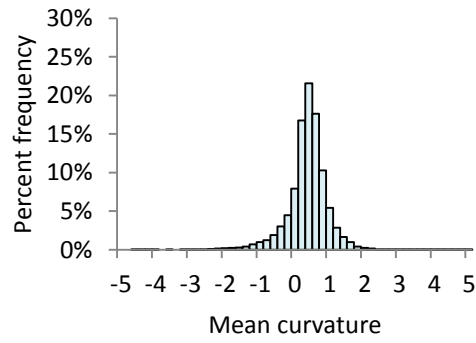
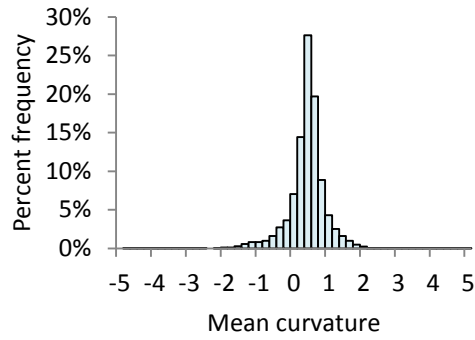


Figure B.1 Stage 0 mean curvature histogram.

C13.43



C13.33

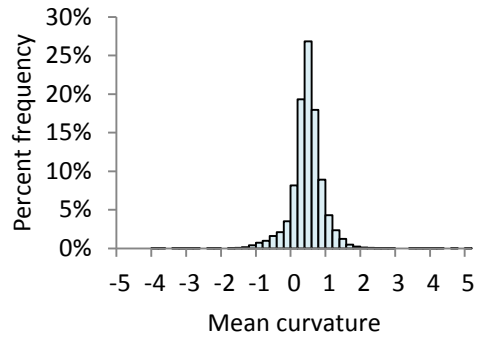
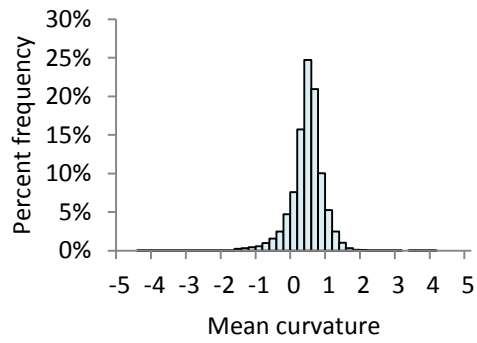
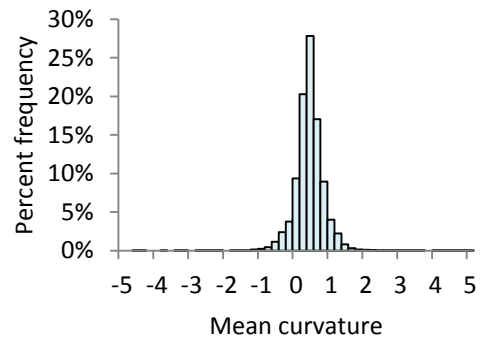


Figure B.2 Stage 1 mean curvature histograms. Specimen names indicated.

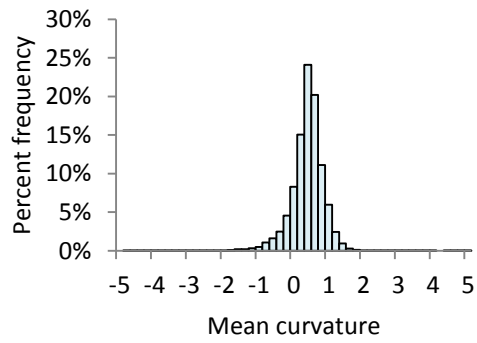
C13.28



C13.17



C13.31



C13.35

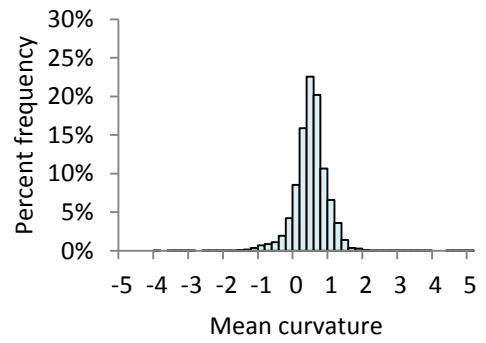
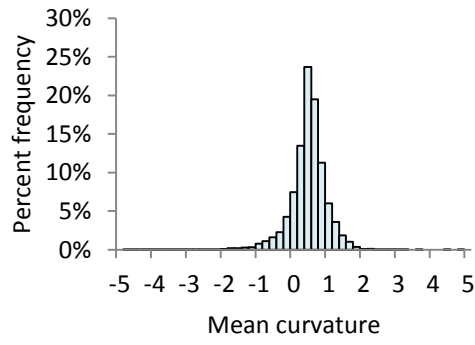
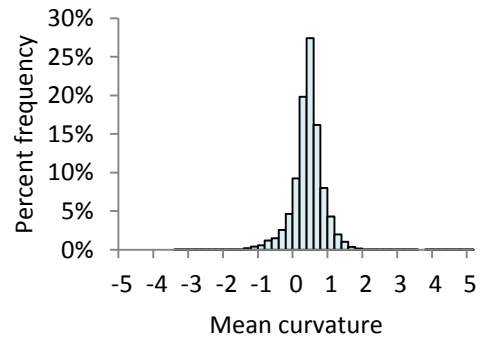


Figure B.3 Stage 2 mean curvature histograms. Specimen names indicated.

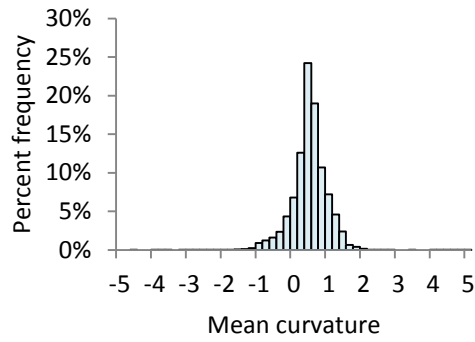
C13.13



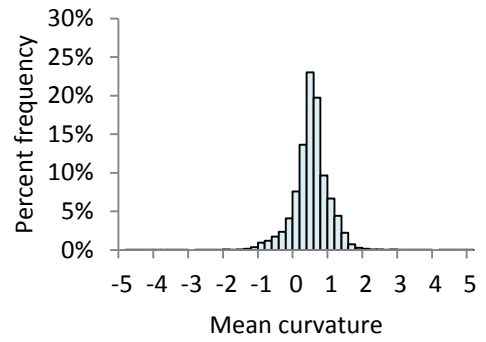
C13.20



C13.1



C13.3



C13.12

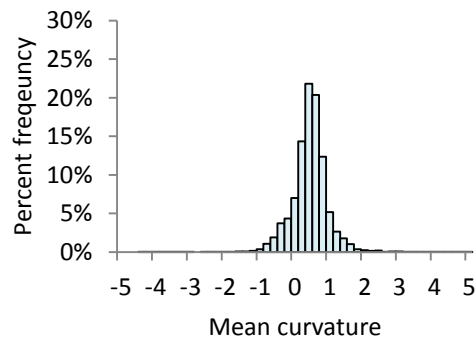
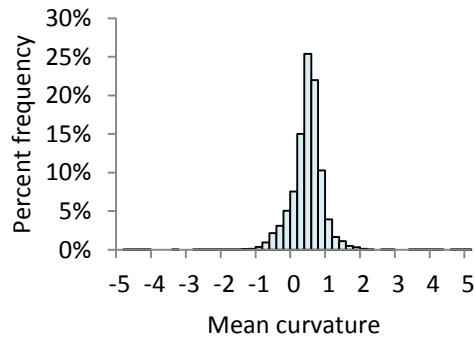
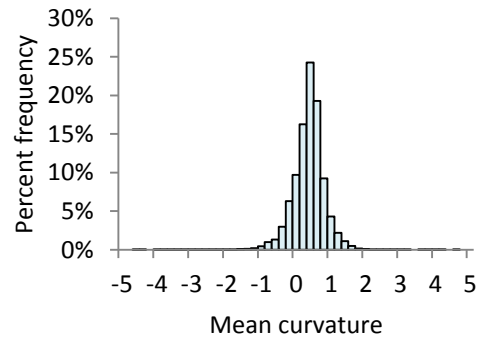


Figure B.4 Stage 3 mean curvature histograms. Specimen names indicated.

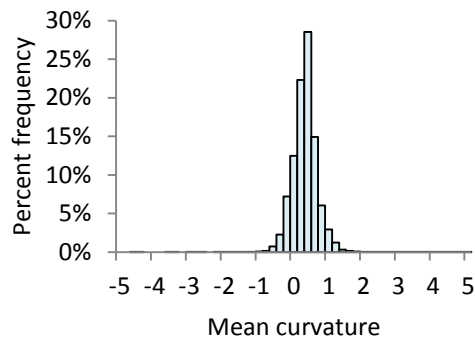
C13.29



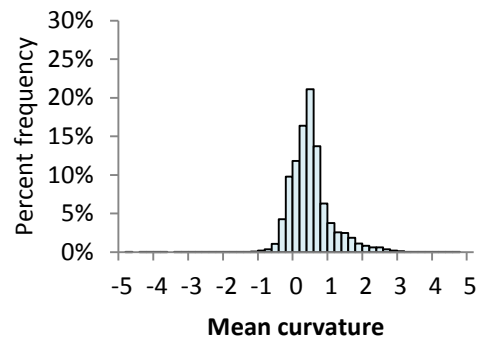
C13.21



C13.22



C13.19



C13.2

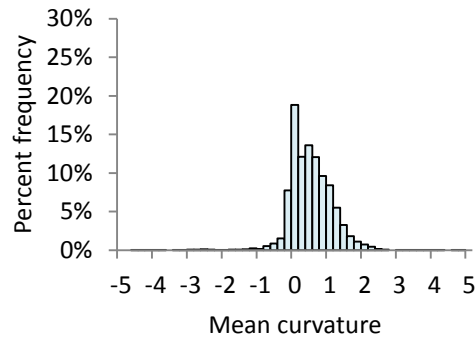


Figure B.5 Stage 4 mean curvature histograms. Specimen names indicated.

Appendix C: Chapter 4

C.atys cusp model: Hollow hard object breakdown

For the *C.atys* cusp model (Figure C.1-i), brittle failure occurred in all of the hollow domes. At the point of failure, the pieces broke apart from one another and typically broke into 4 pieces (Figure C.1-ii), with the exception of one (repeat 9) that broke into 2 pieces.

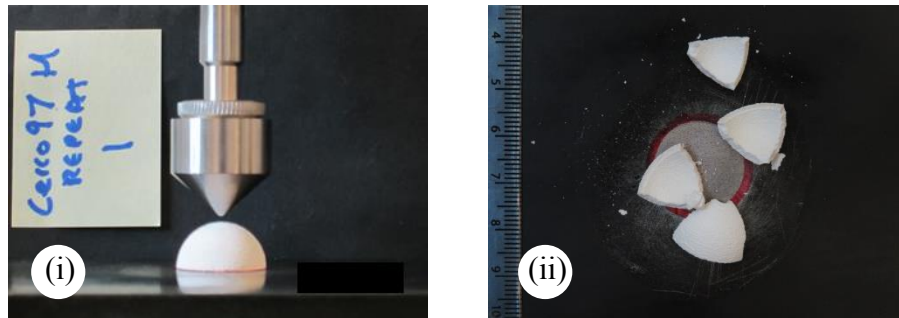


Figure C.1 *C.atys* cusp hollow hard object breakdown images: (i) *C.atys* cusp and hollow dome, (ii) post compression image. Domes split into 2-4 pieces and energetically moved apart at fracture.

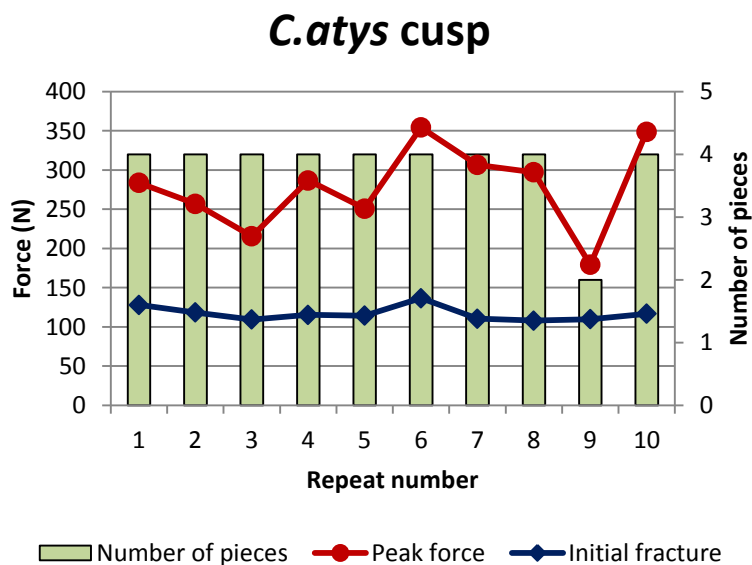


Figure C.2 Consistency of repeats for the *C.atys* cusp dental model to break down a hollow hard object. Results display values for peak force and number of pieces the dome was broken into for each repeat.

***C.atys* cusp model: Solid hard object breakdown**

For the *C.atys* model (Figure C.3-i), explosive fracture occurred at failure when breaking a solid hard object. At this point, the pieces would move energetically apart and typically split into 3 pieces (Figure C.3-ii). One of the repeats (repeat 4) was excluded from analysis due to malalignment of the dome; therefore an extra repeat was required.

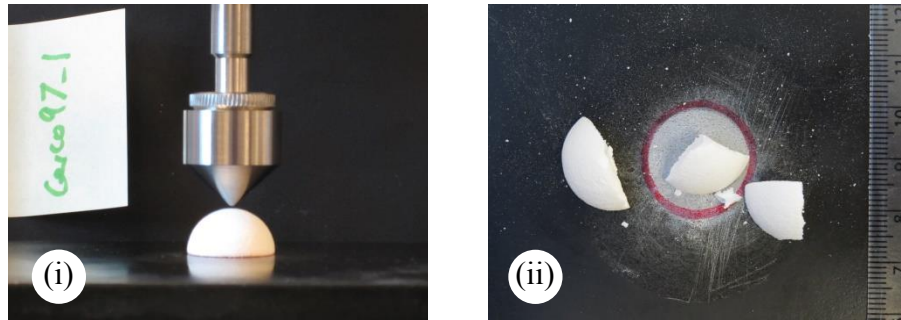


Figure C.3 *C.atys* cusp solid hard object breakdown images: (i) *C.atys* cusp and solid dome, (ii) post compression image. Domes typically split into 3 pieces and energetically moved apart at fracture.

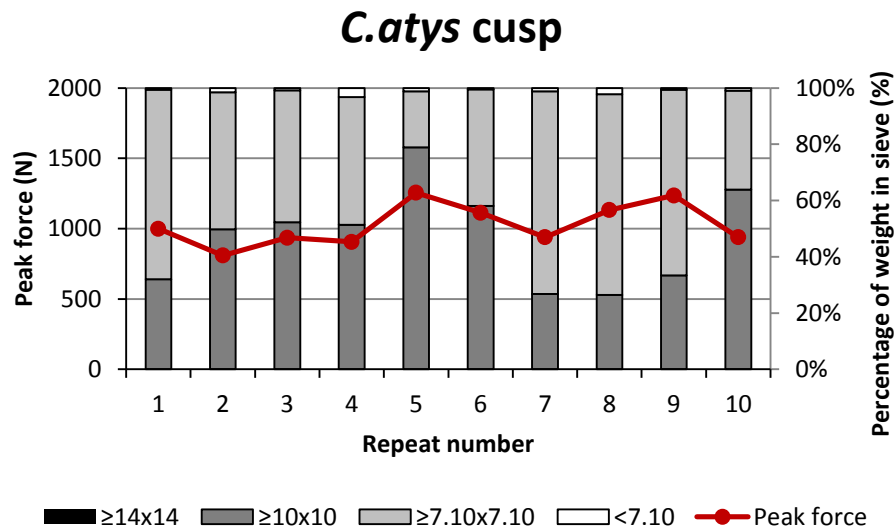


Figure C.4 Consistency of repeats for the *C.atys* cusp model to break down a solid hard object. Results display values for peak force and fragmentation for each repeat.

4 cusps: Hollow hard object breakdown

Brittle fracture occurred in all the repeats of the hollow domes when compressed by the 4 cusp model (Figure C.5-i). The force displacement graphs were single peaked therefore indicated that fracture and failure occurred at the same time. For the majority

of repeats the domes exhibited visible fracture lines at failure, without fragmenting into clear separate pieces (Figure C.5-ii,iii). However the domes did tend to fall into pieces once moved with the number of pieces ranging between 1-4 pieces (mode=2). For one of the repeats the dome shattered into 4 pieces at failure.

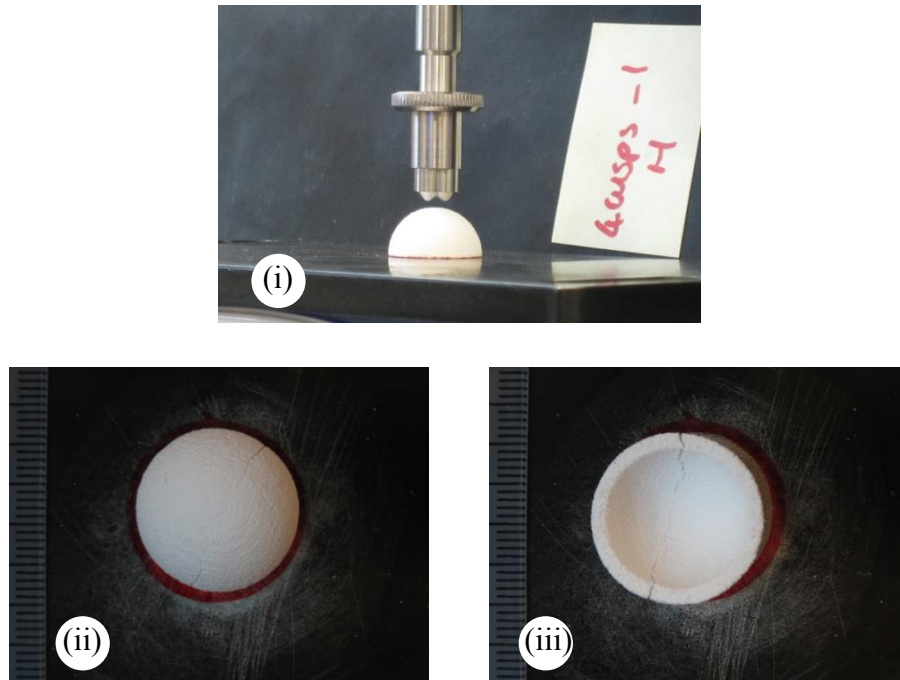


Figure C.5 4 cusps hollow hard object breakdown images: (i) 4 cusps and hollow dome, (ii) post compression image top view, (iii) post compression image bottom view.

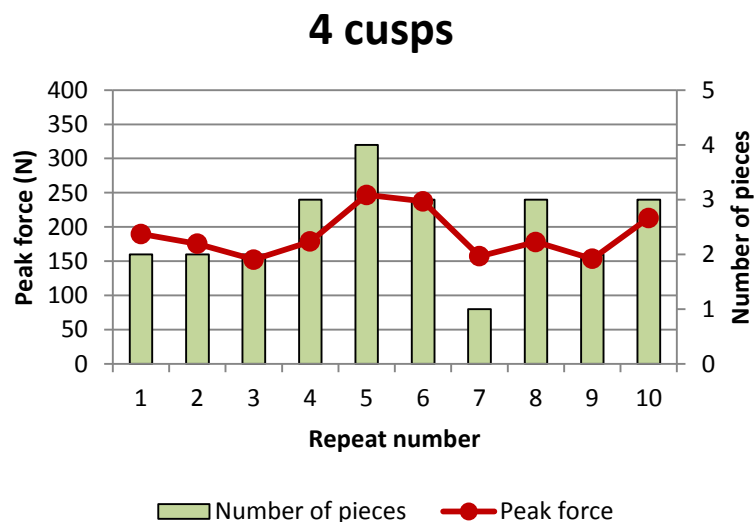


Figure C.6 Consistency of repeats for the 4 cusp dental model to break down a hollow hard object. Results display values for peak force and number of pieces the dome was broken into for each repeat.

4 cusps: Solid hard object breakdown

For the 4 cusp dental model brittle failure occurred in all the solid domes except for repeat 5, which did not fragment. From measurements taken on the top of the dome, the area of indentation was found to be off centre, therefore was excluded from the study. Repeat 6 was also excluded as the test specimen was dropped after compression and a considerable amount of fragments were lost. Therefore a further two repeats were used instead. In the sample used, the domes split into 2-4 main pieces that moved energetically apart at fracture. The area between the four cusps was also noted to form a small sub-piece at failure (Figure C.7-ii).



Figure C.7 4 cusps solid hard object breakdown images: (i) 4 cusps and solid dome, (ii) post compression image. Domes split into 2-4 pieces and energetically moved apart at fracture.

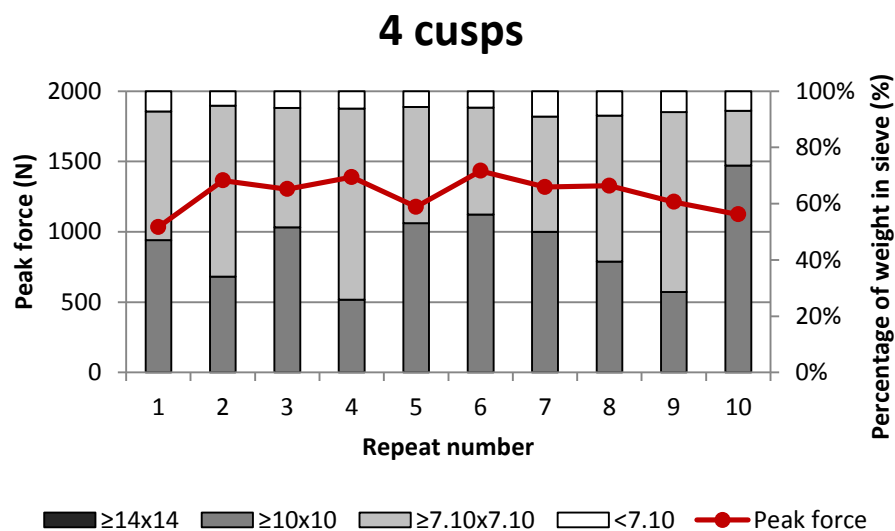


Figure C.8 Consistency of repeats for the 4 cusp dental model to break down a solid hard object. Results display values for peak force and fragmentation for each repeat.

3 cusps: Hollow hard object breakdown

For the 3 cusp dental model, fast brittle fracture occurred simultaneously with failure for all hollow domes. At this point, some of the domes moved apart at fracture whilst the majority exhibited clear fracture lines and fell apart once moved (Figure C.9-ii). Taking this into account, the number of pieces broken into ranged between 2-4 pieces with a mode value of 2.

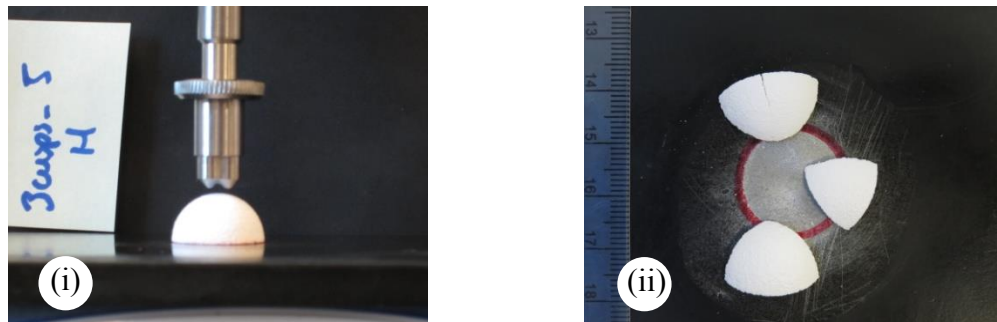


Figure C.9 3 cusps hollow hard object breakdown images: (i) 3 cusps and hollow dome, (ii) post compression image. Domes split into 2-4 pieces.

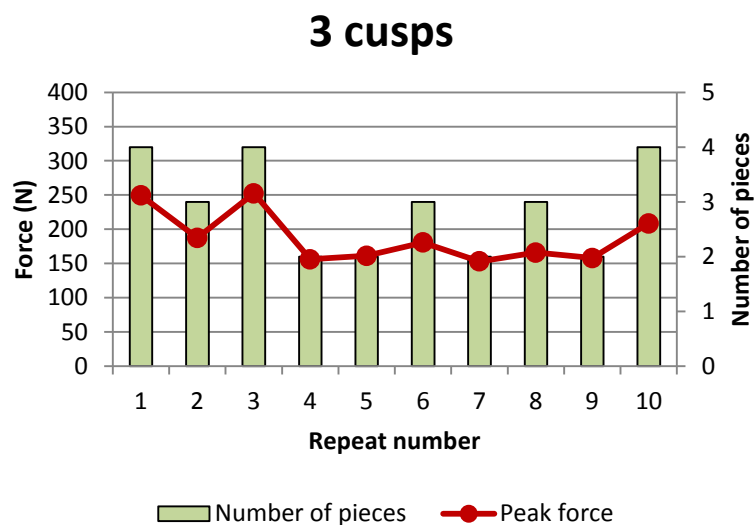


Figure C.10 Consistency of repeats for the 3 cusp dental model to break down a hollow hard object. Results display values for peak force and number of pieces the dome was broken into for each repeat.

3 cusps: Solid hard object breakdown

For the 3 cusp model, brittle failure occurred in most of the solid domes with the exception of repeats 3, 5 and 8. Further analysis indicated these to be off centre therefore were excluded from the study and 3 extra repeats were used instead. For the majority of test runs the solid domes fractured at failure but with little movement or

separation of pieces but did separate once moved (Figure C.11-ii). The majority of domes broke into 3 pieces with the area between the cusps forming a small piece.

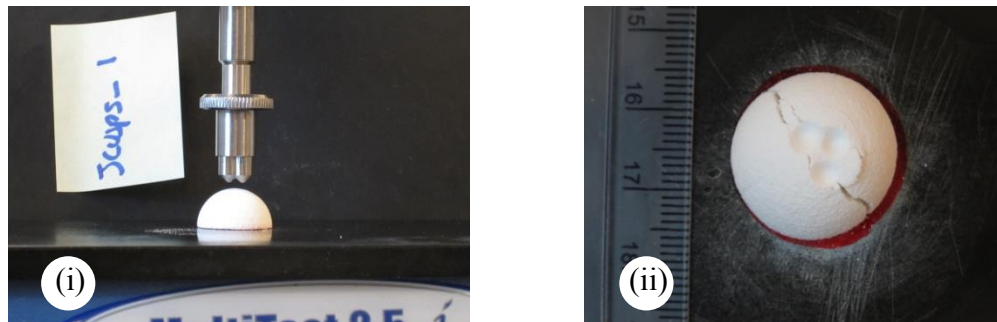


Figure C.11 3 cusps solid hard object breakdown: (i) 3 cusps and solid dome, (ii) post compression image. Domes split into 2-3 fragments.

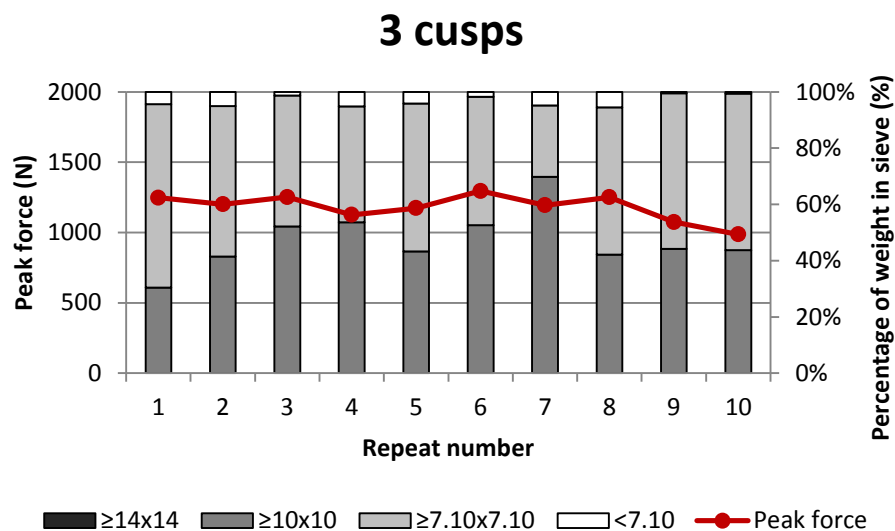


Figure C.12 Consistency of repeats for the 3 cusp dental model to break down a solid hard object. Results display values for peak force and fragmentation for each repeat.

2 cusps: Hollow hard object breakdown

Of the initial 10 repeats of the 2 cusp model; 4 of the hollow domes did not fracture at all and showed only very slight signs of indentation. On further examination the indentation marks of these domes were found to be off centre. It was postulated that a high incidence of this behaviour may have occurred due to the cusps being positioned laterally when compressed onto a curved surface. Coupled with the smooth surface of the platform with very little friction, the domes lacked stability when being compressed and thus are likely to have moved during the experiments. These domes were consequently excluded from the study and a further two repeats were used to provide a sample of 8. Of the sample used only two of the domes broke into pieces. For the

majority, the domes typically exhibited faint fracture lines and remained as a single piece (Figure C.13-ii.iii).

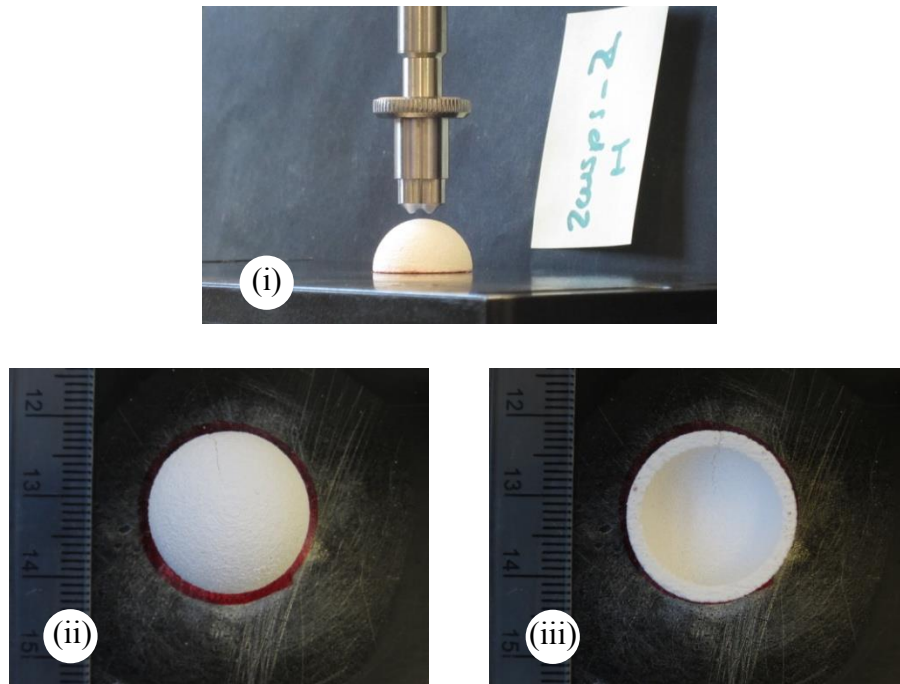


Figure C.13 2 cusps hollow hard object breakdown images: (i) 2 cusps and hollow dome, (ii) post compression image top view, (iii) post compression image bottom view.

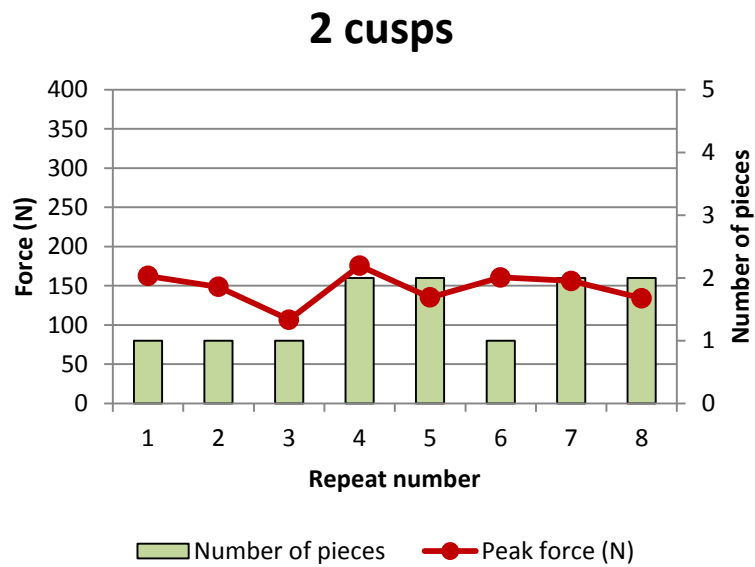


Figure C.14 Consistency of repeats for the 2 cusp dental model to break down a hollow hard object. Results display values for peak force and number of pieces the dome was broken into for each repeat.

2 cusps: Solid hard object breakdown

Brittle failure occurred in the majority of the solid domes when compressed by the two cusp model. At the point of fracture an audible crack occurred and the dome failed in a brittle fashion. Typically there was no movement of pieces at fracture but the domes did fragment easily when moved (Figure C.15-ii). Of the original 10 repeats one of domes (repeat 10) did not break into pieces, nor exhibit any line of fracture. It was also noted that there was no audible crack at the 10% drop in force when the graph terminated. By taking measurements on the top of the dome, the indentation marks were found to be off centre therefore it was decided to exclude this test run from the study and was replaced by a further repeat. This further repeat (11) did fracture however did not fragment into pieces when sieved.

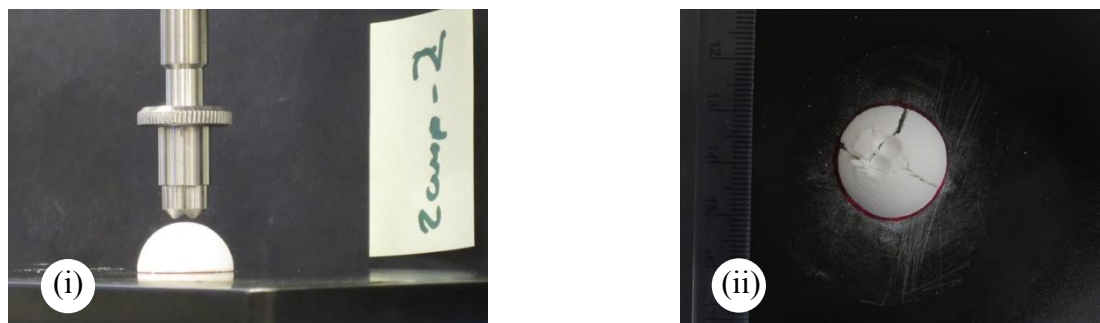


Figure C.15 2 cusps solid hard object breakdown images: (i) 2 cusps and solid dome, (ii) post compression image. Domes split into 2-4 fragments.

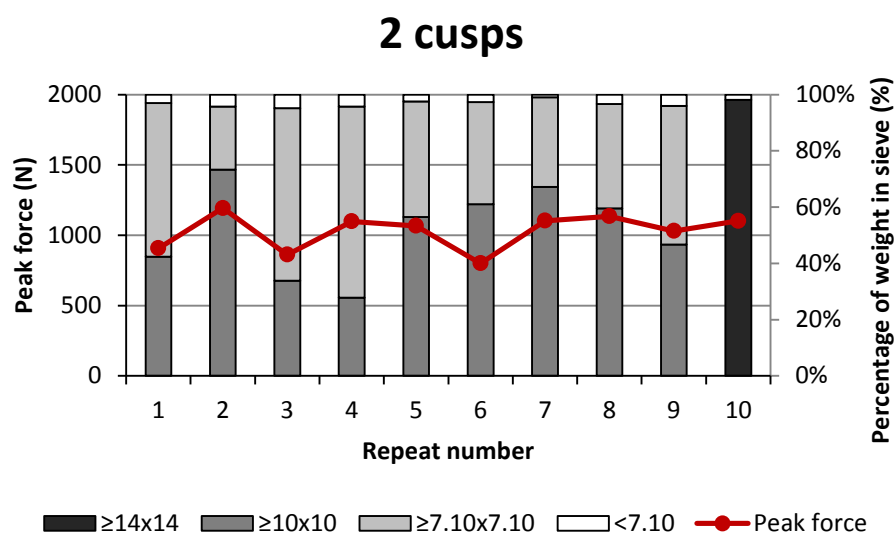


Figure C.16 Consistency of repeats for the 2 cusp dental model to break down a solid hard object. Results display values for peak force and fragmentation for each repeat.

1 cusp: Hollow hard object breakdown

Brittle failure occurred in all the hollow domes when compressed by the 1 cusp dental model. In contrast to many of the other dental models used in this chapter, the force displacement plots would often exhibit one or multiple peaks in force prior to failure. Therefore data for this model was recorded for both force at initial fracture (first peak of graph) and failure. Typically there was no fragmentation or movement of pieces at fracture but the domes exhibited one or several fracture lines (Figure C.17-ii,iii). For some of the domes, these fracture lines led to fragmentation once moved, breaking the domes into 2-3 pieces. One of the repeats (repeat 9) was excluded from analysis as it had an extremely large surface area of contact in comparison to the other repeats. This was due to the fact that the displacement level was above the height of the cusp therefore the flat areas of the crown were also in contact with the dome.

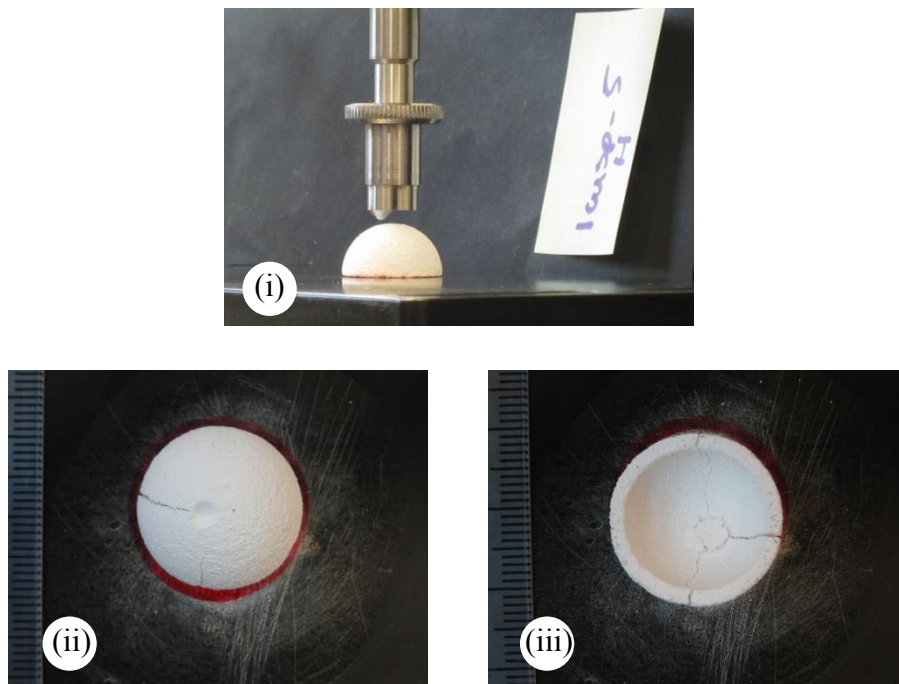


Figure C.17 1 cusp hollow hard object breakdown images: (i) 1 cusp and hollow dome, (ii) post compression image top view, (iii) post compression image bottom view.

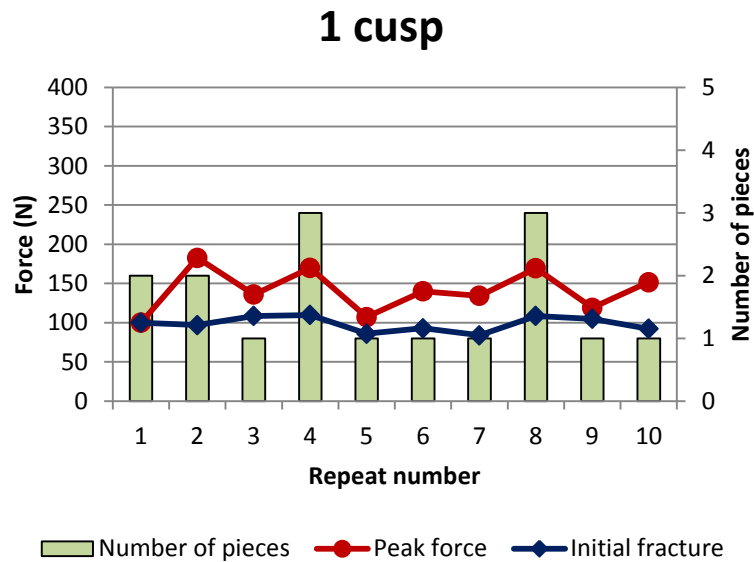


Figure C.18 Consistency of repeats for the 1 cusp dental model to break down a hollow hard object. Results display values for force at initial fracture, peak force, and number of pieces the dome was broken into for each repeat.

1 cusp: Solid hard object breakdown

The solid domes showed quite a different behaviour when compressed by the one cusp dental model in comparison to the other dental models. For these tests, the solid dome showed more of a ductile than brittle material response when compressed. For all of the tests the 3D print material was noted to lift outwards on the lateral side of the indentation area, which was to be expected as this chipping behaviour had previously been associated with single cusp models when positioned off centre (Figure C.19-ii). Fracture was very slow for all the tests and involved a lot of displacement and compacting of material (plastic deformation). In some cases the flat area of the model came into contact with the dome and “crushed” the material. Typically the dome did not fragment or move during the tests and tended to stay as one piece. However fracture lines were observed on the surface, which in some cases led to the fragmentation into pieces once sieved. There was no audible sound at fracture, however a delayed audible crack was noticed once the test had terminated.

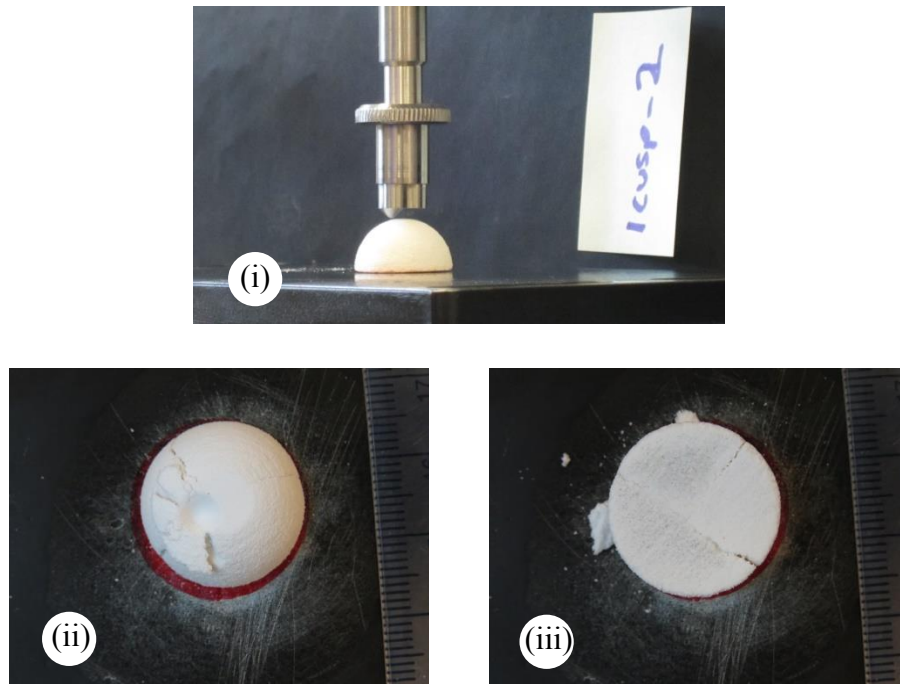


Figure C.19 1 cusp solid hard object breakdown images: (i) 1 cusp and solid dome, (ii) post compression image top view, (iii) post compression image bottom view.

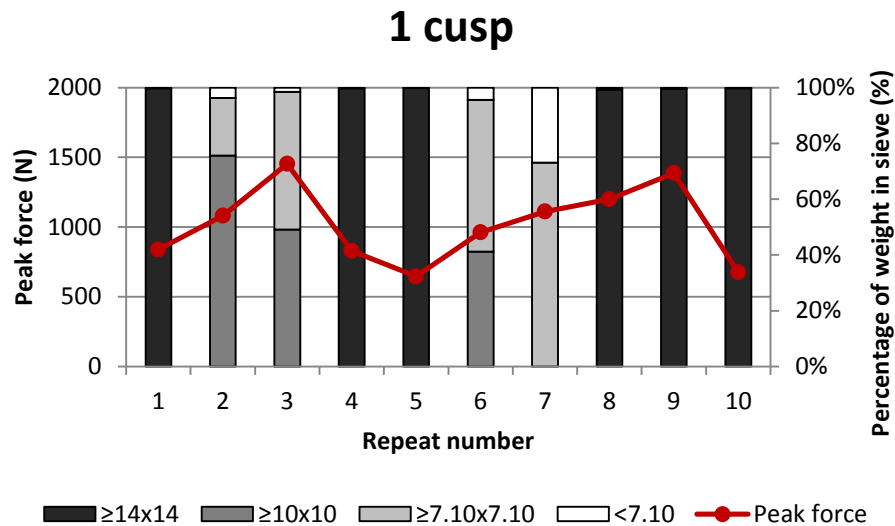


Figure C.20 Consistency of repeats for the 1 cusp dental model to break down a solid hard object. Results display values for peak force and fragmentation for each repeat.

0 cusps: Hollow hard object breakdown

Fast brittle fracture occurred simultaneously with failure for all of the hollow domes when compressed by the 0 cusp dental model. The method in which the hollow domes broke differed from that of the models with cusps, which indented the objects. In the case of the flat crown, the domes tended to break instantaneously by bending outward and collapsing in on itself. For the majority of the repeats the domes exhibited several

fracture lines at failure, which led to fragmentation when the dome was moved (Figure C.21-ii,iii). The number of pieces ranged from 2-4 with the modal value being 4.

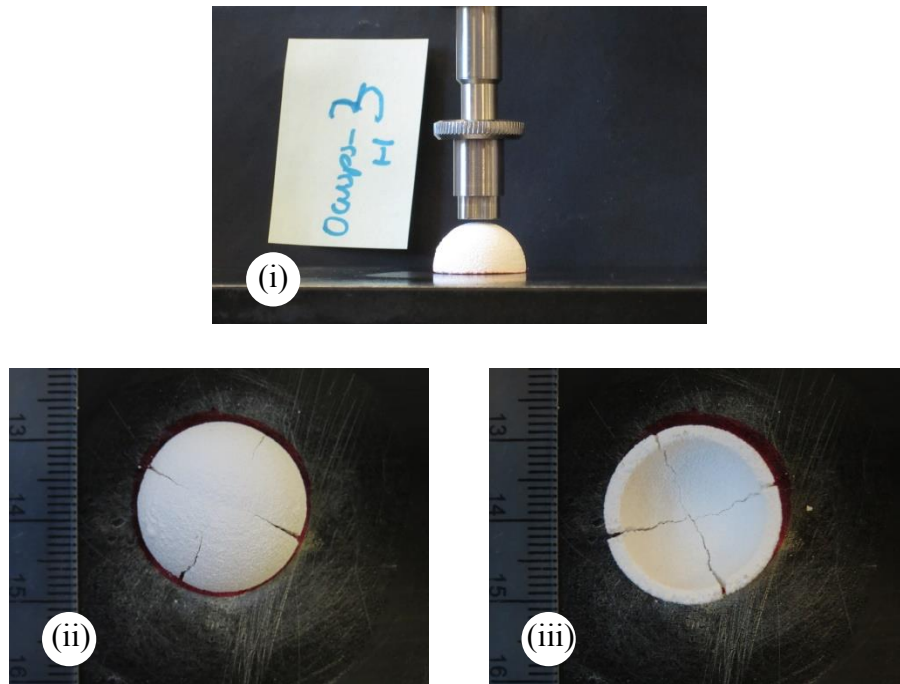


Figure C.21 0 cusps hollow hard object breakdown images: (i) 0 cusps and hollow dome, (ii) post compression image top view, (iii) post compression image bottom view.

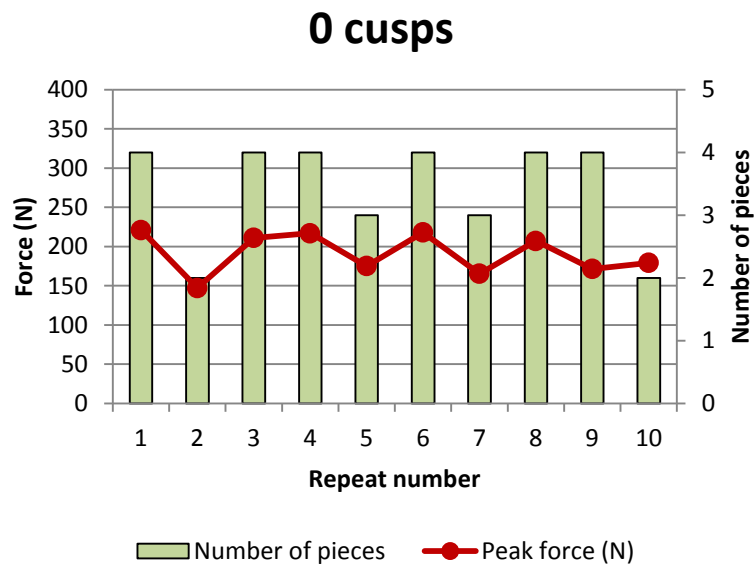


Figure C.22 Consistency of repeats for the 0 cusps dental model to break down a hollow hard object. Results display values for peak force and number of pieces the dome was broken into for each repeat.

0 cusps: Solid hard object breakdown

Much like the one cusp model, the solid domes behaved in largely a ductile manner when compressed by the 0 cusp model. This involved a lot of compacting of the 3D

print material which forced the material to fracture at the sides (Figure C.23-ii). Once sieved, the number of main pieces ranged from 2-5 with the most common numbers being 4 and 5. Two of the repeats were excluded from the study (1, 4) as these domes did not fragment and in comparison to the other repeats it may be the case that the tests were terminated too early. Further examination of these domes showed that the area of compression was off centre, thus these tests were replaced.

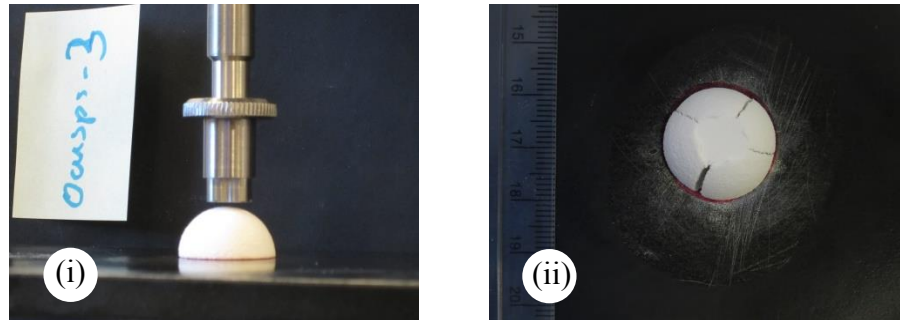


Figure C.23 0 cusps solid hard object breakdown images: (i) 0 cusps and solid dome, (ii) post compression image. Domes split into 2-5 fragments.

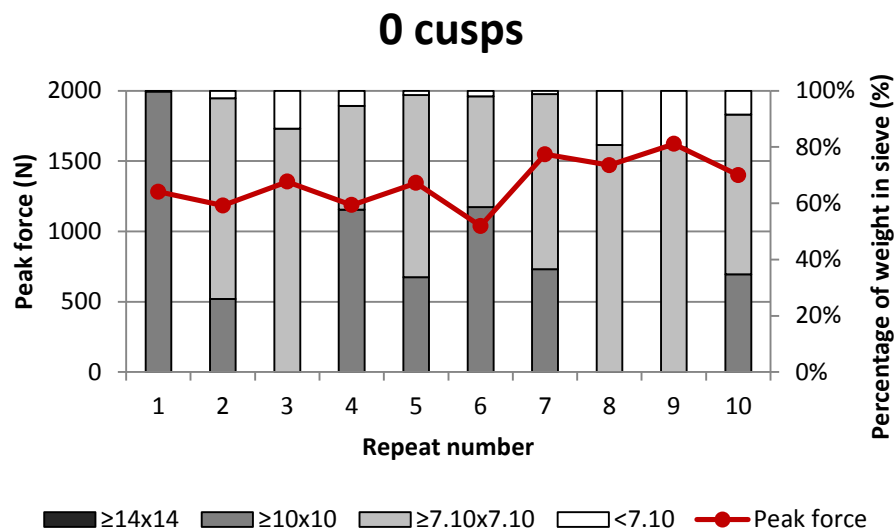


Figure C.24 Consistency of repeats for the 0 cusp dental model to break down a solid hard object. Results display values for peak force and fragmentation for each repeat.

0 ridge: Hollow hard object breakdown

Brittle failure occurred in all the hollow domes when compressed by the 0 ridge model. Although fragmentation did not occur at fracture, visible fracture lines were observed on the domes after each test, which led the domes to split into 2 or 4 pieces once moved (Figure C.25-ii,iii). Initial fracture and failure occurred simultaneously, therefore the force displacement graphs consisted of a single peak.

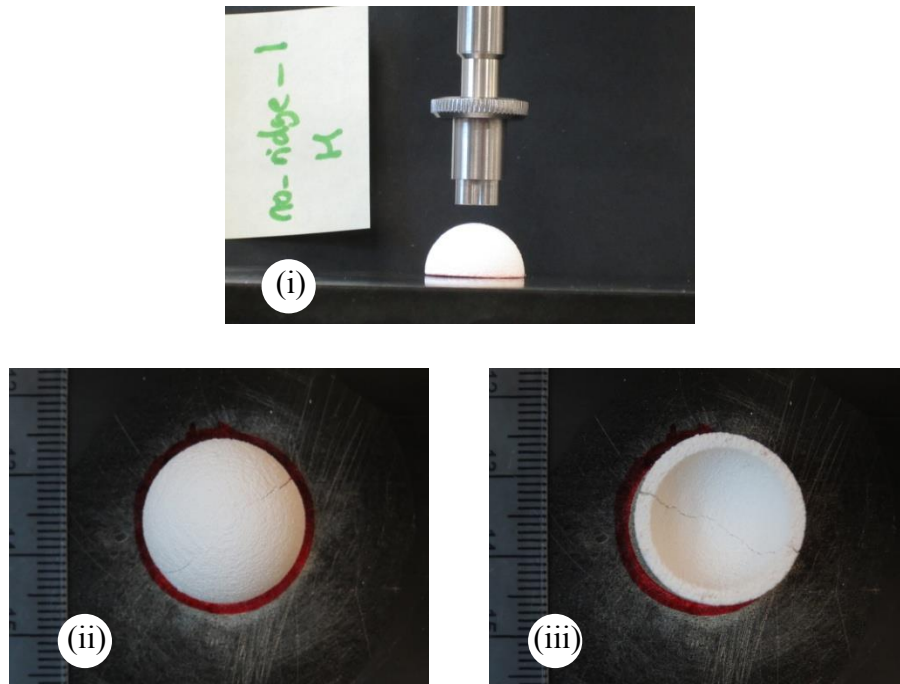


Figure C.25 0 ridge hollow hard object breakdown images: (i) 0 ridge and hollow dome, (ii) post compression image top view, (iii) post compression image bottom view.

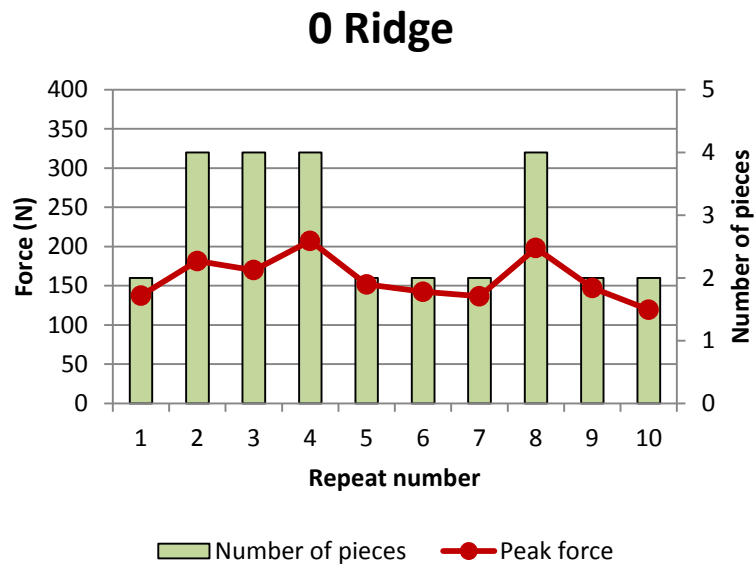


Figure C.26 Consistency of repeats for the 0 ridge dental model to break down a hollow hard object. Results display values for peak force and number of pieces the dome was broken into for each repeat.

0 ridge: Solid hard object breakdown

For the 0 ridge model, the solid domes fractured with the 3D print material being compacted with no movement i.e. the domes were crushed (Figure C.27-ii,iii). Similar to the other flat model (0 cusps); fractures radiated from the sides of the dome, which led to the fragmentation once the domes were sieved. For some, fracture was audible but

was not as loud in comparison to the cusped models. For two of the 10 repeats (8,9), fragmentation did not occur and the circular imprint on the top of the dome was found to be off centre. Therefore a further two repeats were used instead.

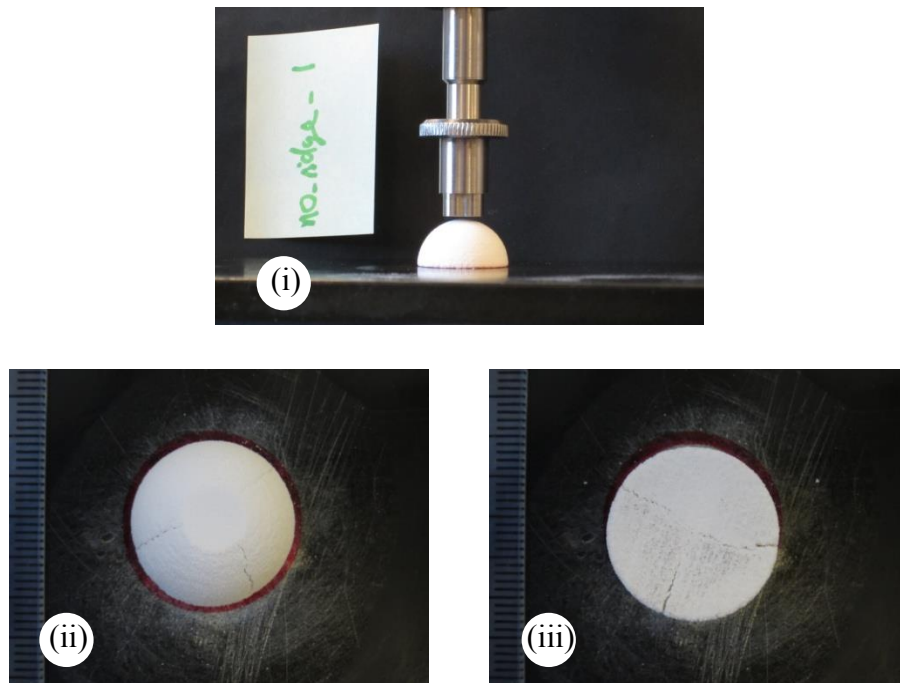


Figure C.27 0 ridge solid hard object breakdown images: (i) 0 ridge and solid dome, (ii) post compression image top view, (iii) post compression image bottom view.

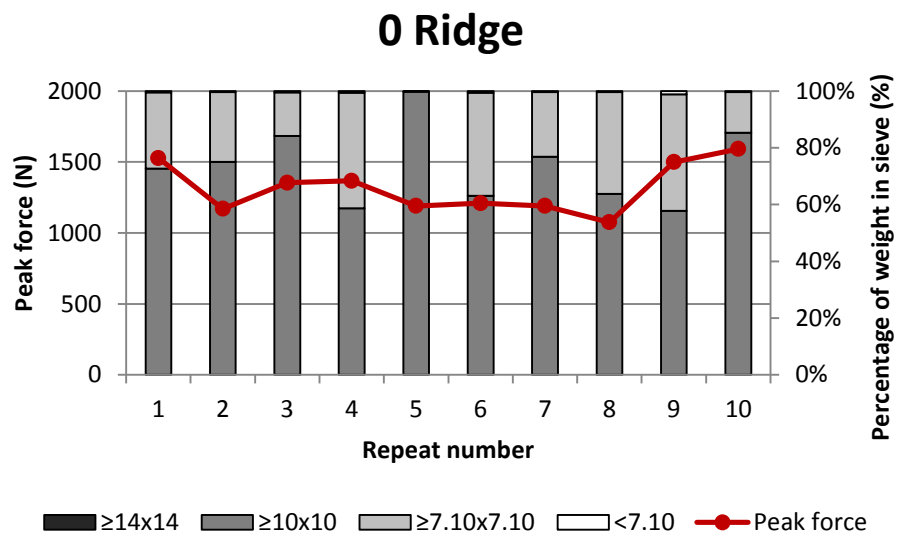


Figure C.28 Consistency of repeats for the 0 ridge dental model to break down a solid hard object. Results display values for peak force and fragmentation for each repeat.

Ridge: Hollow hard object breakdown

For the ridged dental model, brittle failure occurred in the hollow models at the point of fracture. After compression, fracture lines were visible on the surface of the domes and for some, the fractures led to fragmentation of pieces once moved (Figure C.29-ii,iii). If fragmented, the number of pieces ranged from 2-4. After the tests it was also noted that the domes often stuck to the dental model therefore had to be physically removed. Initially a 70% drop was used to terminate tests but it was found that this percentage was too large as frequently the dome continued to be fractured after breakage. Therefore a 10% drop was used instead. One of the repeats (10) was excluded from the study as there was no audible fracture and the dome did not exhibit any fracture lines. From the force/displacement data it seems that the 10% drop may have terminated the test too early for this specimen therefore an extra repeat was used instead.

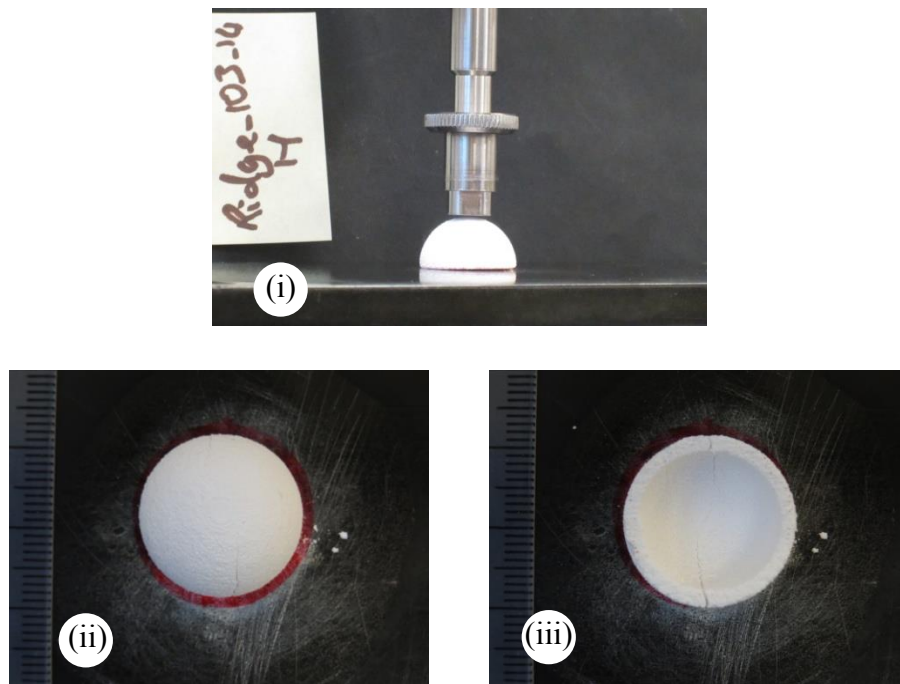


Figure C.29 Ridged hollow hard object breakdown images: (i) Ridged and hollow dome, (ii) post compression image top view, (iii) post compression image bottom view.

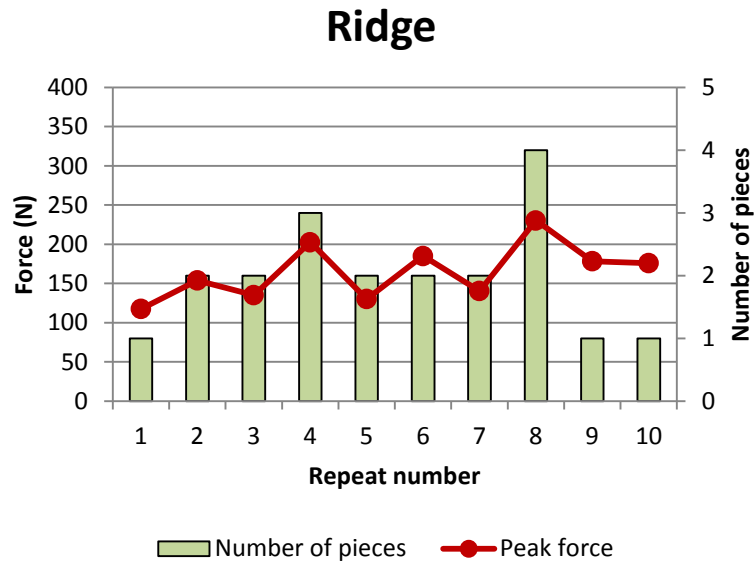


Figure C.30 Consistency of repeats for the ridge dental model to break down a hollow hard object. Results display values for peak force and number of pieces the dome was broken into for each repeat.

Ridge: Solid hard object breakdown

When compressed by the ridged tooth model, the solid domes showed a distinctive fracture pattern. The force displacement line graphs were considerably curved prior to failure indicating a large amount of plastic deformation. During the experiments the ridged outline was indented into the top of dome causing fractures to radiate outwards and break the outer material into pieces, which involved the movement of pieces. The central area was typically compacted into the dental model, forming a separate piece that had to be physically removed (Figure C.31-ii). For three of the repeats (2,5,8) there was no audible fracture and from the graphs there did not appear to be a brittle failure. Instead the dental model was slowly compressed into the 3D print material. The domes did however break into pieces.

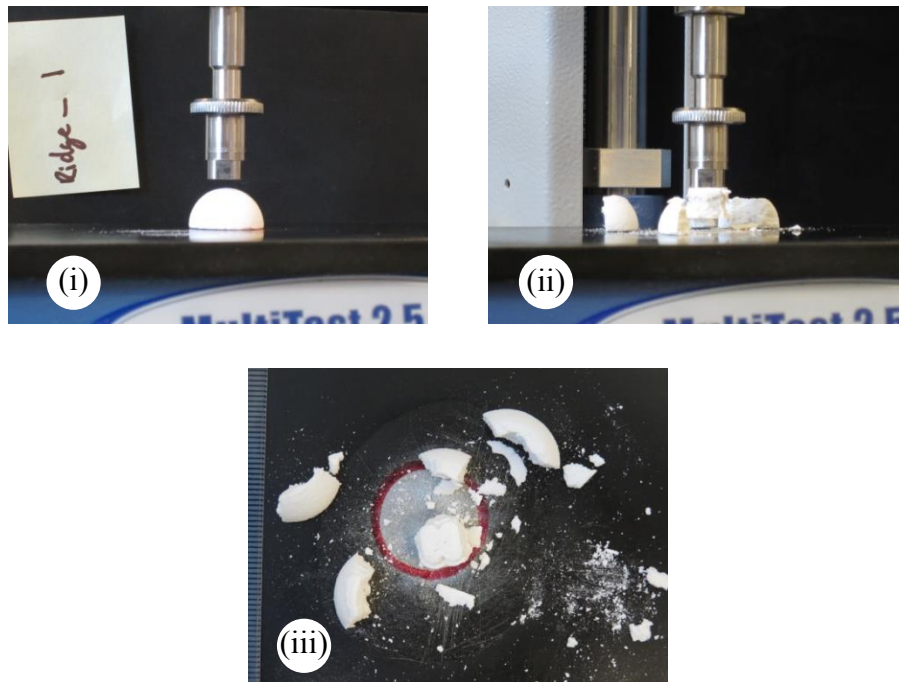


Figure C.31 Ridge solid hard object breakdown images: (i) Ridge model and solid dome prior to compression, (ii) Ridge model and solid dome subsequent to compression (note the large amount of 3D print material lodged within the model), (iii) post compression image.

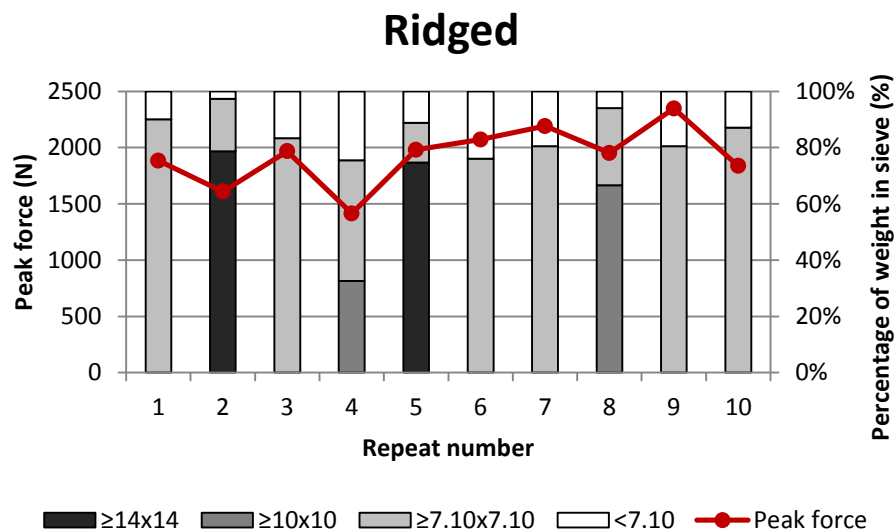


Figure C.32 Consistency of repeats for the ridged dental model to break down a solid hard object. Results display values for peak force and fragmentation for each repeat.

1 cusp (central): Hollow hard object breakdown

When the single cusp was centralised, brittle failure occurred at fracture for all of the hollow domes and was accompanied with an audible crack. Similarly to the 1 cusp model, one or multiple drops in force were observed prior to failure. Therefore data on force at initial fracture (first peak in graph) was also collected. For the majority of test

runs, the domes fractured without any movement or fragmentation but did break into pieces when moved with the mode number being 2 (Figure C.33-ii).

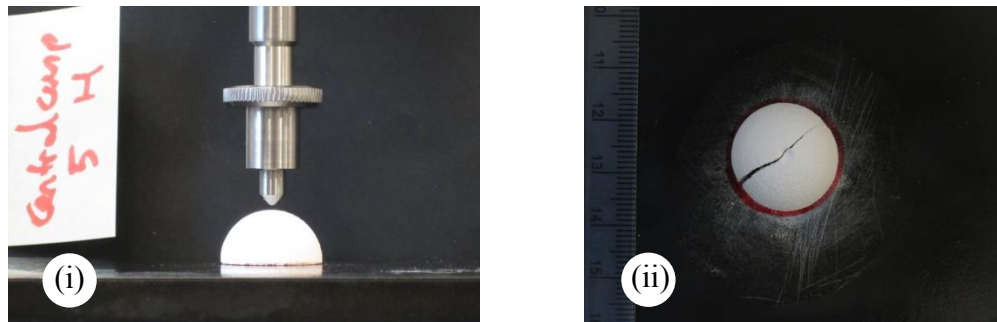


Figure C.33 1 cusp (central) hollow hard object breakdown images: (i) 1 cusp (central) and hollow dome, (ii) post compression image. Domes split into 2-3 fragments.

1 cusp central

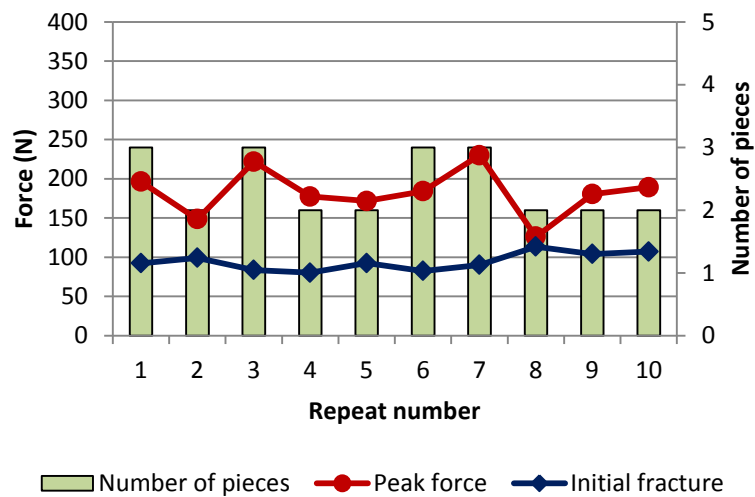


Figure C.34 Consistency of repeats for the 1 cusp (central) dental model to break down a hollow hard object. Results display values for force at initial fracture, peak force, and number of pieces the dome was broken into for each repeat.

1 cusp (central): Solid hard object breakdown

For the one cusp (central) model, brittle failure occurred at fracture for the solid domes and was accompanied with an audible crack. The point at fracture was often energetic with the pieces jumping apart and splitting into 2-4 pieces (mode=3) (Figure C.35-ii). Two of the domes (repeats 1,5) were excluded from the study as brittle failure did not occur and the point of indentation was found to be off centre.

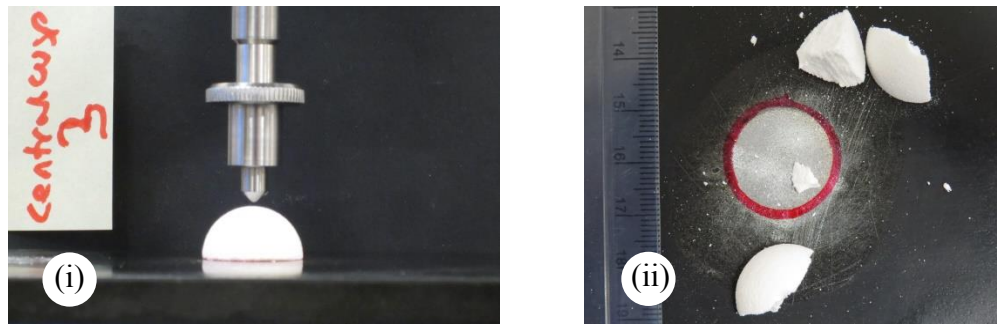


Figure C.35 1 cusp (central) solid hard object breakdown images: (i) 1 cusp (central) and solid dome, (ii) post compression image. Domes split into 2-4 fragments.

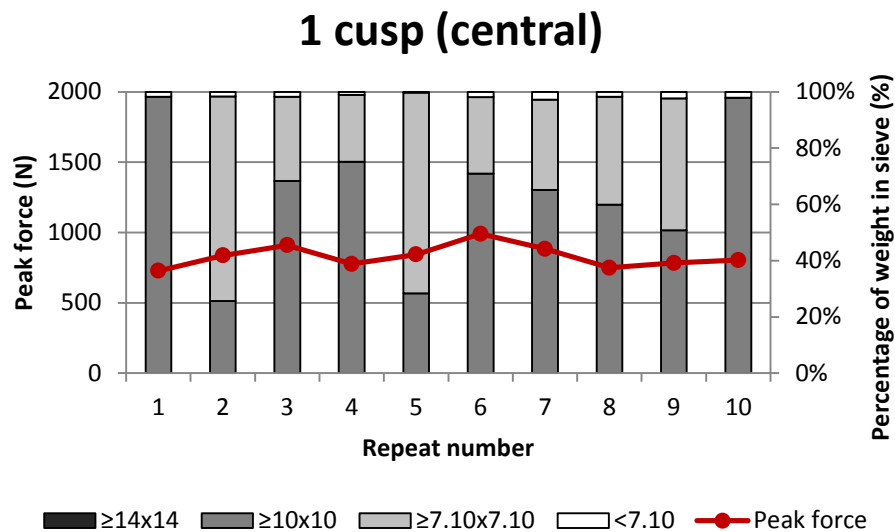


Figure C.36 Consistency of repeats for the 1 cusp (central) dental model to break down a solid hard object. Results display values for peak force and fragmentation for each repeat.

4 cusps (intercuspal distance): Hollow hard object breakdown

For the 4 cusp (intercuspal distance) model, brittle fracture occurred in all the hollow domes. Some of the domes moved apart energetically at fracture (Figure C.37-ii) whereas others had fractured and then fell into pieces once moved. One of the domes (repeat 7) fractured but did not fragment. For the rest of the domes the number of pieces broken into ranged from 2-4 with the mode being 3.

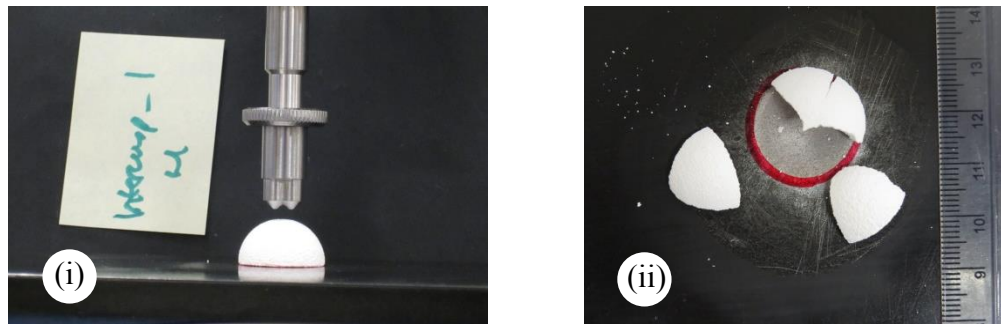


Figure C.37 4 cusps (intercuspal distance) hollow hard object breakdown images: (i) 4 cusps (intercuspal distance) and hollow dome, (ii) post compression image.

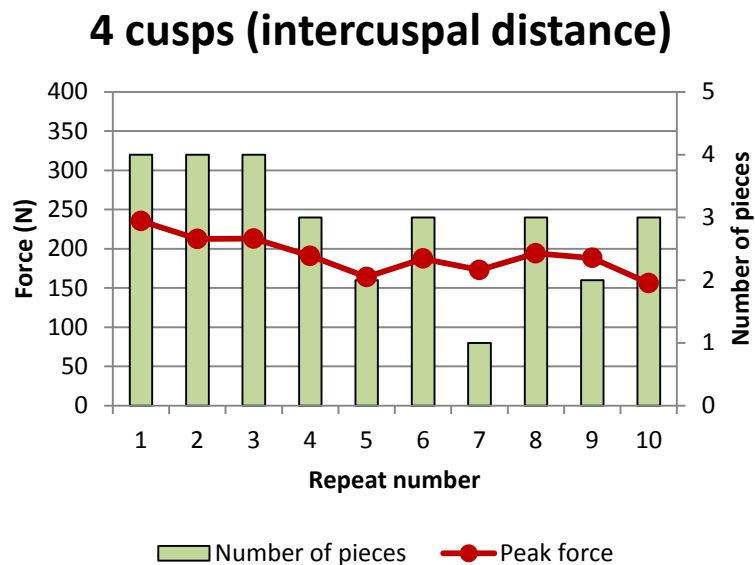


Figure C.38 Consistency of repeats for the 4 cusp (intercuspal) dental model to break down a hollow hard object. Results display values for peak force and number of pieces the dome was broken into for each repeat.

4 cusps (intercuspal distance): Solid hard object breakdown

For the 4 cusp (intercuspal distance) model, brittle failure occurred in the solid domes and was accompanied with an audible crack at fracture. For some of the repeats the domes moved apart at fracture whereas for others, the domes fractured but fell into pieces once moved (Figure C.39-ii,iii). The number of pieces ranged from 3-4 with the modal value being 3. Frequently a small sub-piece was formed from the area of indentation. Two of the repeats were excluded from the study (repeats 6, 7) as the points of indentation were found to be off centre therefore were replaced by two extra repeats.

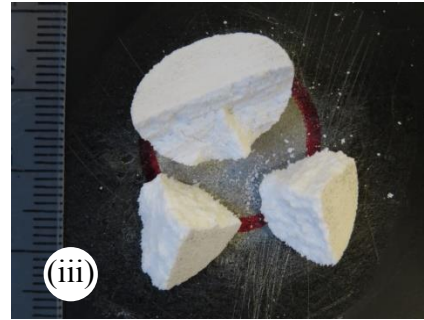
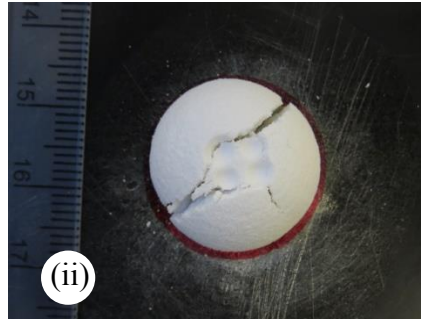
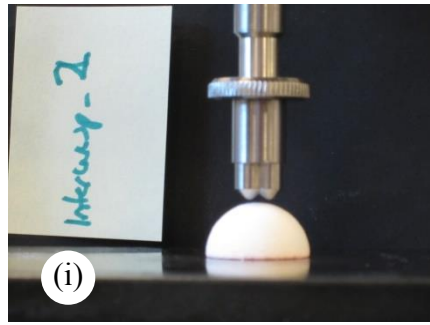


Figure C.39 4 cusps (intercuspal distance) solid hard object breakdown images: (i) 4 cusps (intercuspal distance) and solid dome, (ii) post compression image top view, (iii) post compression image bottom view. Dome fell apart into 3 pieces when moved.

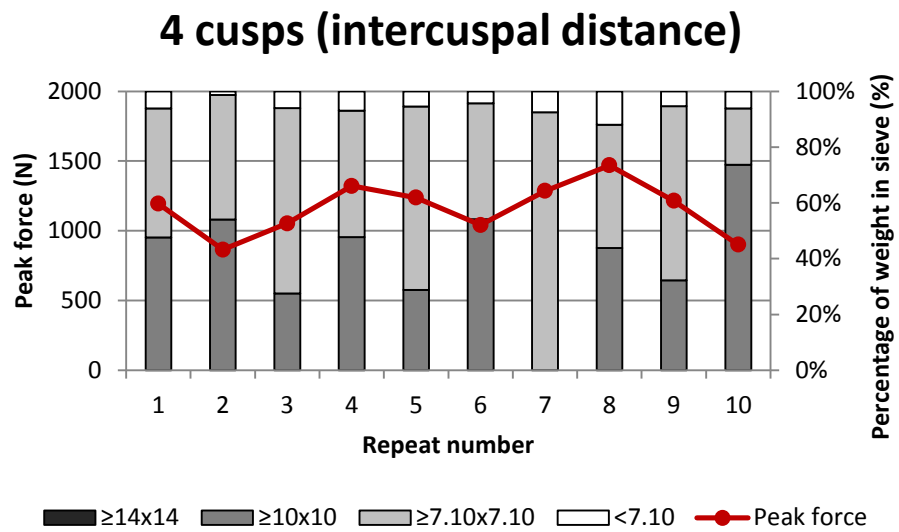


Figure C.40 Consistency of repeats for the 4 cusp (intercuspal distance) dental model to break down a solid hard object. Results display values for peak force and fragmentation for each repeat.

Table C.1 Averages and standard deviations of the results for each crown design to break a hollow hard object.

Crown design	Surface area (mm ²)		Displacement (mm)		Force (N)		Energy (mJ)		Duration (s)	
	Avg.	St. Dev.	Avg.	St. Dev.	Avg.	St. Dev.	Avg.	St. Dev.	Avg.	St. Dev.
4 cusps	13.98	2.13	0.48	0.06	188.25	33.82	31.97	9.79	5.94	0.73
3 cusps	11.60	1.57	0.52	0.06	187.24	37.61	35.06	10.81	6.43	0.69
2 cusps	7.09	0.95	0.48	0.05	147.38	21.52	27.33	6.09	5.95	0.68
1 cusp	10.34	4.03	1.02	0.28	141.02	27.60	79.89	36.96	12.41	3.40
0 cusps	87.71	3.52	0.46	0.10	191.23	26.51	36.23	13.60	5.75	1.29
0 ridge	87.29	1.88	0.41	0.06	159.09	28.80	26.94	10.15	5.03	0.67
Ridge	66.75	4.85	0.69	0.08	164.99	35.71	44.82	14.29	8.48	0.97
1 cusp (central)	20.28	10.08	1.58	0.52	182.57	30.74	160.61	82.75	19.22	6.21
4 cusps (intercusp)	14.47	1.49	0.49	0.04	191.38	24.04	33.51	7.27	6.07	0.52
<i>Initial fracture</i>										
1 cusp	3.58	0.36	0.49	0.04	98.42	9.53	20.08	2.98	6.03	0.47
1 cusp (central)	3.30	0.24	0.46	0.03	94.57	11.20	18.69	2.56	5.73	0.36

Table C.2 Averages and standard deviations of the results for each crown design to break a solid hard object.

Crown design	Surface area (mm ²)		Displacement (mm)		Force (N)		Energy (mJ)		Duration (s)		Fragmentation Index	
	Avg.	St. Dev.	Avg.	St. Dev.	Avg.	St. Dev.	Avg.	St. Dev.	Avg.	St. Dev.	Avg.	St. Dev.
4 cusps	97.55	4.58	2.08	0.12	1268.22	127.05	1143.69	169.59	25.36	1.44	0.39	0.06
3 cusps	94.87	7.27	2.16	0.11	1179.96	94.04	1092.21	135.80	26.34	1.25	0.64	0.05
2 cusps	92.08	16.58	2.30	0.24	1029.53	129.04	1086.16	233.95	27.97	2.87	0.31	0.12
1 cusp	112.59	17.02	3.00	0.51	1018.37	278.15	1235.55	512.42	36.34	6.19	0.16	0.23
0 cusps	147.45	12.62	2.27	0.38	1342.93	178.27	1641.39	519.69	27.55	4.63	0.41	0.18
0 ridge	128.77	4.55	1.69	0.14	1317.13	176.68	975.43	221.59	20.59	1.69	0.20	0.09
Ridge	228.56	10.82	3.16	0.34	1925.33	267.90	2697.32	724.60	38.41	4.15	0.48	0.16
1 cusp (central)	38.76	2.98	2.54	0.18	830.31	80.44	879.62	168.67	30.83	2.13	0.26	0.14
4 cusps (intercusp)	84.25	8.22	1.91	0.20	1158.04	190.90	970.93	264.26	23.36	2.39	0.40	0.08